



Πανεπιστήμιο Κύπρου
University of Cyprus

Search for a charged Higgs boson decaying to a W and a neutral Higgs boson in multilepton final states

Konstantinos Christoforou

Supervisor
Fotios Ptochos

September 2024

Abstract

The Standard Model of particle physics (SM) besides its great success it is known to be an incomplete theory. There are numerous problems, which can be understood if the SM is only an effective theory for low energies. In extended models, which include the SM, the Higgs sector is more complex, consisting of at least two Higgs doublet fields. These kind of models predict the existence of more than one Higgs boson, including electrically charged Higgs bosons H^+ . A search for charged Higgs bosons continues with the Large Hadron Collider (LHC), where several different final states are being investigated with data recorded at 7, 8 and 13 TeV center of mass energy of pp collisions. This study proposes a new channel in the searches: the charged Higgs boson decaying into a W and a neutral Higgs boson. The discussed channel is the first ever proposed to be searched for in HEP analyses. In this proposal only a specific final state is presented out of the many available configurations that when taken into account an increased sensitivity for the sought after signal can be achieved/reconstruct top quarks, and boosted neutral Higgs bosons decaying to pairs of tau-leptons. The report is based on the full Run-2 data of the LHC collider run and this will be the basis for a similar analysis for Run-3.

Contents

List of Figures	i
List of Tables	ix
1 Introduction	1
1.1 The Standard Model of Elementary Particles	1
1.1.1 Quarks and Leptons	1
1.1.2 Force carriers	2
1.1.3 Higgs boson	3
1.1.4 Is Standard Model the end of the road?	5
1.1.5 Standard Model limitations and shortcomings	6
1.1.5.1 "Naturalness" in the Higgs' mass and Hierarchy problem	7
1.2 The 2HDM as an expansion of the SM	8
1.3 Charged Higgs Boson	13
1.3.1 Charged Higgs Production Processes	13
1.3.2 Decaying modes	14
1.4 Neutral Higgs Bosons	15
1.4.1 Neutral Higgs Decaying modes	16
2 LHC and the CMS exmperiment	17
2.1 Large Hadron Collider	17
2.2 The CMS detector	19
2.2.1 Coordinate system of CMS	20
2.2.2 Superconducting Magnet	21
2.2.3 Tracking system	21
2.2.3.1 Silicon Pixel	22
2.2.3.2 Silicon Strip	23
2.2.4 Electromagnetic Calorimeter, ECAL	23
2.2.5 Hadronic Calorimeter, HCAL	25
2.2.6 Muon System	27
2.2.7 Trigger System	29
3 Particle Reconstruction and Identification	30
3.1 The Particle Flow Algorithm	31
3.2 Tracks and Vertices reconstruction	31
3.3 Electron Reconstruction	33
3.4 Muon Reconstruction	34
3.5 Photon Reconstruction	36
3.6 Jet Reconstruction	36
3.6.1 Cone Algorithms	37
3.6.2 Sequential Clustering Algorithms	37
3.7 B-tagging jets	38
3.8 τ -jet reconstruction	39
3.9 Missing Transverse Energy	40
3.10 Scalar Hadronic and Leptonic Transverse Momentum	41
4 Data and Simulation Samples	42
4.1 Collision data	42
4.2 Event Simulation	43
4.2.1 Hard Scattering	44

4.2.2	Parton Shower Generator	46
4.2.3	Hadronization Generators	47
4.2.4	Detector Simulation	47
4.2.5	Simulated samples	47
5	Corrections, filtering and reweighting	51
5.1	MET filters	51
5.2	Pileup reweighting	51
5.3	Data to MC scale factors	52
5.3.1	Electron trigger,identification and reconstruction	52
5.3.2	Muon trigger, identification and isolation	53
5.3.3	Tau identification	53
5.3.4	Electron energy corrections	53
5.3.5	MET corrections	53
5.3.6	B-tagging corrections	54
6	Analysis: Search for a charged Higgs boson	55
6.1	Object Identification and Selection	56
6.1.1	Primary vertices	56
6.1.2	Electrons	57
6.1.3	Muons	58
6.1.4	Hadronically decaying taus (τ_h)	59
6.1.5	Jets	60
6.1.6	B-jets	60
6.1.7	MET	60
6.1.8	Top tagging	61
6.1.9	Duplicate Removal	61
6.2	Event Selection	61
7	Trigger Efficiency Measurement	63
7.1	Description	63
7.2	Measurement of the Trigger Efficiency	63
7.2.1	Single electron trigger	64
7.2.2	Single muon trigger	66
8	Background Estimation	70
8.1	Strategy	70
8.1.1	Loose-to-Tight Extrapolation Method	70
8.2	Fake Rate Measurement	73
8.2.1	Electron Fake Rates	74
8.2.2	Muon Fake Rates	77
8.2.3	Tau Fake Rates	78
8.3	Closure Tests in CRs	80
8.4	Combined Closure Tests in VRs	82
8.4.1	Closure test in $\mu\mu e$ VR	83
8.4.2	Closure test in $\mu e \tau_h(0b)$ VR	83
8.5	Other backgrounds	84
9	DNN Classifier for Signal Extraction	85
9.1	DNN Input Variables	87
9.2	DNN Architecture and Features	90

9.3 DNN Performance and Response	90
9.4 Fit discriminant	91
10 Systematic Uncertainties	94
10.1 Luminosity uncertainty	94
10.2 Pileup reweighting uncertainty	94
10.3 Prefiring uncertainty	94
10.4 Trigger efficiency uncertainties	94
10.5 Lepton reconstruction and identification efficiency	95
10.6 Tau identification and energy scale uncertainties	95
10.7 JES, JER and UES uncertainties	95
10.8 B-tagging uncertainties	95
10.9 Misidentified ℓ ($e/\mu/\tau_h$) measurement uncertainty	96
10.10 Theoretical uncertainties	97
10.11 Summary of Systematic Uncertainties	97
11 Results	99
11.1 Pre-fit distributions in the SR	99
11.1.1 The $2\ell^{df}\tau_h$ final states	99
11.1.2 The $2\ell^{sf}\tau_h$ final states	99
11.2 Expected exclusion upper limits	112
11.2.1 Statistical method for calculating the expected exclusion upper limits for H^\pm production	112
11.2.2 Expected upper limits for $2\ell^{df}\tau_h$ - $2\ell^{sf}\tau_h$ combination	113
11.3 Impacts of the Nuisance Parameters	115
11.4 Goodness of fit	115
12 Conclusions	121
References	123
A DNN Input Variables	132
B Fit Discriminant in MuETau	134
C Fit Discriminant in EETau	138
D Fit Discriminant in MuMuTau	142
E Limits	146

List of Figures

1.1	Standard Model info-graphic of elementary particles and interactions [4].	1
1.2	A prototypical effective ‘Mexican hat’ potential that leads to ‘spontaneous’ symmetry breaking [10].	4
1.3	Diphoton invariant mass distribution with combining all categories used for the inclusive fiducial cross section measurement, with full Run2 data [3].	6
1.4	Charged Higgs Boson expected appearance through b to s decay channel, though photon emission.	13
1.5	Feynman Diagrams for $t\bar{t}$ (on the left plot), $t \rightarrow bH^+$ (middle plot and $t\bar{t} \rightarrow b\bar{b}H^+H^-$ (right hand-side plot).	14
1.6	Charged Higgs Boson production in association with a top quark, for the Heavy category.	14
1.7	Charged Higgs boson branching ratios (BR) as a function of m_{H^\pm} in different types of general 2HDM. Type-I and Type-X are shown on the <i>left</i> while Type-II and Type-Y are shown on the <i>right</i> . The top row shows the BRs for $\tan\beta = 3$ and the CP-conserving limit $\sin(\beta - \alpha) = 0.7$ while the bottom row shows the $\tan\beta = 30$ and the alignment limit $\sin(\beta - \alpha) = 0.7$. The masses of the two neutral Higgs bosons are set at $m_h = 125$ GeV and $m_H = 130$ GeV [15].	15
1.8	The decay branching ratios of the heavier (H^0) and lighter (h^0) CP-even MSSM h boson as a function of its mass for the two values $\tan\beta = 3$ (left) and $\tan\beta = 30$ (right) [16].	16
2.1	CERN Accelerator Complex.	17
2.2	The CMS Detector.	19
2.3	The CMS coordinate system.	20
2.4	Schematic down view of the CMS tracking system.	22
2.5	Electromagnetic Shower [26].	24
2.6	ECAL of CMS.	25
2.7	The CMS Hadron Calorimeter layout.	26
2.8	An $R - z$ cross-section of a quadrant of the CMS detector with the axis parallel to the beam (z) running horizontally and radius (R) increasing upward. The interaction point is at the lower left corner. The locations of the various muon stations and the steel disks (dark grey areas) are shown. The 4 drift tube (DT, in light orange) stations are labeled MB (“muon barrel”) and the cathode strip chambers (CSC, in green) are labeled ME (“muon endcap”). Resistive plate chambers (RPC, in blue) are in the barrel and the endcaps of CMS, labeled RB and RE, respectively. Figure and caption from [29].	28
3.1	Cross section of the CMS detector.	30
3.2	Reconstruction of a particle’s trajectory.	33

3.3	Effective electron resolution as a function of electron's momentum in the transverse plane, comparing ECAL only with combined ECAL-tracker information [36].	34
3.4	Muon transverse momentum resolution for tracker compared to its combination with muon system information [37].	35
3.5	A toy-model for a jet formation in CMS.	36
3.6	Schematic description for a b-hadron decay resulting to the formation of a b-jet, while additional jets directly emerge from the PV.	39
4.1	The NNPDF3.1 NNLO PDFs displayed are the next-to-next-to-leading order PDFs which describe the quark-gluon constituents of a proton, evaluated at $\mu^2 = 10 \text{ GeV}^2$ (left) and $\mu^2 = 10^4 \text{ GeV}^2$ (right) [45].	45
4.2	Example of a hard pp collision resulting to Z^0/γ^* production.	46
5.1	Simulated efficiency of different quark/gluon flavor jets to pass the medium b-tag wp of the DeepJet algorithm. Results are presented for (a) 2016 pre-VFP, (b) 2016 post-VFP, (c) 2017, and (d) 2018.	54
6.1	The LO Feynman diagram (<i>Left</i>) for heavy charged Higgs boson production at the LHC through $gg \rightarrow tbH^\pm$ in the 4FS, including the subsequent decay of the top quark and the decay of the charged Higgs boson into the neutral Higgs and W bosons. The breakdown and categorization of all possible final states after the leptonic or hadronic decay of the tau leptons and W bosons is visualized in a pie chart (<i>Right</i>).	55
7.1	The overall Single Electron HLT efficiency as a function of the p_T of the offline electron probe as determined with the $TnP_{\ell\ell}$ method for (a) 2016 pre-VFP, (b) 2016 post-VFP, (c) 2017 and (d) 2018.	65
7.2	The overall Single Electron HLT efficiency as a function of the p_T of the offline electron probe as determined with the $ODM_{\mu e}$ method for (a) 2016 pre-VFP, (b) 2016 post-VFP, (c) 2017 and (d) 2018.	66
7.3	Comparison of the single electron HLT trigger efficiency as a function of the offline probe electron p_T for the $TnP_{\ell\ell}$ and $ODM_{\mu e}$ for (a) 2016 pre-VFP, (b) 2016 post-VFP, (c) 2017 and (d) 2018.	67
7.4	The overall Single Muon HLT efficiency as a function of the p_T of the offline muon probe as determined with the $TnP_{\ell\ell}$ method for (a) 2016 pre-VFP, (b) 2016 post-VFP, (c) 2017 and (d) 2018.	67
7.5	The overall Single Muon HLT efficiency as a function of the p_T of the offline muon probe as determined with the $ODM_{\mu e}$ method for (a) 2016 pre-VFP, (b) 2016 post-VFP, (c) 2017 and (d) 2018.	69
7.6	Comparison of the single muon HLT trigger efficiency as a function of the offline probe muon p_T for the $TnP_{\ell\ell}$ and $ODM_{\mu e}$ for (a) 2016 pre-VFP, (b) 2016 post-VFP, (c) 2017 and (d) 2018.	69

8.1	The jet $\rightarrow e$ fake rates calculated in the μe CR using 2016 pre-VFP data, showing for the barrel (first row) and endcap (second row), in sip3d bins (various columns). The black circle and red square markers represent the fake factors obtained in data and simulations, respectively. The latter are solely shown for reference purposes.	75
8.2	The jet $\rightarrow e$ fake rates calculated in the μe CR using 2016 post-VFP data, showing for the barrel (first row) and endcap (second row), in sip3d bins (various columns). The black circle and red square markers represent the fake factors obtained in data and simulations, respectively. The latter are solely shown for reference purposes.	76
8.3	The jet $\rightarrow e$ fake rates calculated in the μe CR using 2017 data, showing for the barrel (first row) and endcap (second row), in sip3d bins (various columns). The black circle and red square markers represent the fake factors obtained in data and simulations, respectively. The latter are solely shown for reference purposes.	76
8.4	The jet $\rightarrow e$ fake rates calculated in the μe CR using 2018 data, showing for the barrel (first row) and endcap (second row), in sip3d bins (various columns). The black circle and red square markers represent the fake factors obtained in data and simulations, respectively. The latter are solely shown for reference purposes.	77
8.5	The jet $\rightarrow \mu$ fake rates calculated in the $e\mu$ CR with 2016 pre-VFP data, showing barrel (first row) and endcap (second row), in sip3d bins (various columns). The black circle and red square markers represent the fake factors obtained in data and simulations, respectively. The latter are solely shown for reference purposes.	78
8.6	The jet $\rightarrow \mu$ fake rates calculated in the $e\mu$ CR with 2016 post-VFP data, showing barrel (first row) and endcap (second row), in sip3d bins (various columns). The black circle and red square markers represent the fake factors obtained in data and simulations, respectively. The latter are solely shown for reference purposes.	78
8.7	The jet $\rightarrow \mu$ fake rates calculated in the $e\mu$ CR with 2017 data, showing barrel (first row) and endcap (second row), in sip3d bins (various columns). The black circle and red square markers represent the fake factors obtained in data and simulations, respectively. The latter are solely shown for reference purposes.	79

8.8	The jet $\rightarrow \mu$ fake rates calculated in the $e\mu$ CR with 2018 data, showing barrel (first row) and endcap (second row), in sip3d bins (various columns). The black circle and red square markers represent the fake factors obtained in data and simulations, respectively. The latter are solely shown for reference purposes.	79
8.9	The jet $\rightarrow \tau_h$ fake rates calculated in the $\mu\tau_h t^{\text{res}} p_T^{\text{miss}}$ CR, from left to right column, for 2016 pre-VFP, for 2016 post-VFP, for 2017 and 2018 respectively. The black circle and red square markers represent the fake factors obtained in data simulations, respectively. The latter are solely shown for reference purposes.	81
8.10	Electron FR Self-Closure tests showing the L_T distributions in the μe CR for (a) 2016 pre-VFP, (b) 2016 post-VFP, (c) 2017 and (d) 2018.	82
8.11	Muon FR Self-Closure tests showing the L_T distributions in the $e\mu$ CR for (a) 2016 pre-VFP, (b) 2016 post-VFP, (c) 2017 and (d) 2018.	82
8.12	Tau FR Self-Closure tests showing the L_T distributions in the $\mu\tau_h t^{\text{res}} p_T^{\text{miss}}$ CR for (a) 2016 pre-VFP, (b) 2016 post-VFP, (c) 2017 and (d) 2018. . . .	83
8.13	Closure tests showing the L_T distributions in the $\mu\mu e$ VR for (a) 2016 pre-VFP, (b) 2016 post-VFP, (c) 2017 and (d) 2018.	84
8.14	Closure tests showing the DNN output distributions in the $\mu e\tau_h(0b)$ VR for (a) 2016 pre-VFP, (b) 2016 post-VFP, (c) 2017 and (d) 2018.	84
9.1	Simple interpolation of a fully connected DNN, where individual networks are trained with a single value of parameter θ (<i>left</i>) and trained with the possible values of θ as input features (<i>right</i>), thus parameterized.	86
9.2	Schematic interpretation of the D_ζ variable, which is related to the momentum vector of a given light lepton (e/μ), the selected τ_h and the E_T^{miss}	88
9.3	Distributions of the input variables used for the parameterized DNN training, normalised in unity, presented for $m_{H^0(h^0)} = 200\text{GeV}$	89
9.4	Correlation matrices for input variables for $m_{H^0(h^0)} = 200\text{ GeV}$ in 2017+2018 training, presented for $m_{H^\pm} = 300\text{ GeV}$ (<i>left</i>), $m_{H^\pm} = 700\text{ GeV}$ (<i>middle</i>) and background (<i>right</i>).	90
9.5	ROC curves for the DNN that was trained using the 2017-2018 samples to be used in the 2016 analysis. Mass points in sub-plot labels are reported in GeV.	92
9.6	The DNN response for signal and background, shown for the $m_{H^0(h^0)} = 200\text{ GeV}$ - (a) $m_{H^\pm} = 300\text{ GeV}$, (b) 400 GeV , (c) 700 GeV and (d) 1 TeV signal samples, for both training and testing scenarios. The DNN was trained with the combination of 2017-2018 samples, in order to be used on 2016 samples.	93

9.7	The DNN response for signal and background, shown for the $m_{H^0(h^0)} = 90$ GeV - (a) $m_{H^\pm} = 400$ GeV, (b) 500 GeV, (c) 700 GeV and (d) 1 TeV signal samples, for both training and testing scenarios. The DNN was trained with the combination of 2017-2018 samples, in order to be used on 2016 samples.	93
9.8	The DNN response for signal and background, shown for the $m_{H^0(h^0)} = 90$ GeV - (a) $m_{H^\pm} = 185$ GeV, (b) 220 GeV and (c) 300 GeV, for both training and testing scenarios. The DNN was trained with the combination of 2017-2018 samples, in order to be used on 2016 samples.	93
11.1	Distributions of the parameterized DNN output in $2\ell^{df}\tau_h$ final state for $m_{H^0(h^0)} = 200$ GeV and all available m_{H^\pm} using 2016 pre-VFP data.	100
11.2	Distributions of the parameterized DNN output in $2\ell^{df}\tau_h$ final state for $m_{H^0(h^0)} = 200$ GeV and all available m_{H^\pm} using 2016 post-VFP data.	101
11.3	Distributions of the parameterized DNN output in $2\ell^{df}\tau_h$ final state for $m_{H^0(h^0)} = 200$ GeV and all available m_{H^\pm} using 2017 data.	102
11.4	Distributions of the parameterized DNN output in $2\ell^{df}\tau_h$ final state for $m_{H^0(h^0)} = 200$ GeV and all available m_{H^\pm} using 2018 data.	103
11.5	Distributions of the parameterized DNN output in $ee\tau_h$ final state for $m_{H^0(h^0)} = 200$ GeV and all available m_{H^\pm} using 2016 pre-VFP data.	104
11.6	Distributions of the parameterized DNN output in $ee\tau_h$ final state for $m_{H^0(h^0)} = 200$ GeV and all available m_{H^\pm} using 2016 post-VFP data.	105
11.7	Distributions of the parameterized DNN output in $ee\tau_h$ final state for $m_{H^0(h^0)} = 200$ GeV and all available m_{H^\pm} using 2017 data.	106
11.8	Distributions of the parameterized DNN output in $ee\tau_h$ final state for $m_{H^0(h^0)} = 200$ GeV and all available m_{H^\pm} using 2018 data.	107
11.9	Distributions of the parameterized DNN output in $\mu\mu\tau_h$ final state for $m_{H^0(h^0)} = 200$ GeV and all available m_{H^\pm} using 2016 pre-VFP data.	108
11.10	Distributions of the parameterized DNN output in $\mu\mu\tau_h$ final state for $m_{H^0(h^0)} = 200$ GeV and all available m_{H^\pm} using 2016 post-VFP data.	109
11.11	Distributions of the parameterized DNN output in $\mu\mu\tau_h$ final state for $m_{H^0(h^0)} = 200$ GeV and all available m_{H^\pm} using 2017 data.	110
11.12	Distributions of the parameterized DNN output in $\mu\mu\tau_h$ final state for $m_{H^0(h^0)} = 200$ GeV and all available m_{H^\pm} using 2018 data.	111
11.13	Combined expected upper limit of the $2\ell^{sf}\tau_h$ and $2\ell^{df}\tau_h$ final states with full Run2 data and $m_{H^0(h^0)} = 200$ GeV. The dotted black line shows the median expected limit, while the 68% and 95% confidence intervals are presented with the green and yellow bands, respectively.	114

11.14 Combined expected upper limit of the $2\ell^{sf}\tau_h$ and $2\ell^{df}\tau_h$ final states with full Run2 data. The dotted black line shows the median expected limit, while the 68% and 95% confidence intervals are presented with the green and yellow bands, respectively. The limits are presented for $m_{H^0(h^0)}$ values of (a) 80 GeV, (b) 90 GeV, (c) 125 GeV and (d) 300 GeV.	116
11.15 Pulls (left column) and Impacts (right column) for the $2\ell^{sf}\tau_h$ and $2\ell^{df}\tau_h$ combination and all three years, using the Asimov dataset. The signal assumption is the $m_{H^0(h^0)} = 200$ GeV and $m_{H^\pm} = 800$ GeV mass hypothesis, assuming 1pb signal cross section.	117
11.16 The Goodness-of-fit for the combination of all final states and eras obtained with the saturated algorithm, using pseudo-data for $m_{H^0(h^0)} = 80$ GeV and different m_{H^\pm} values.	118
11.17 The Goodness-of-fit for the combination of all final states and eras obtained with the saturated algorithm, using pseudo-data for $m_{H^0(h^0)} = 90$ GeV and different m_{H^\pm} values.	118
11.18 The Goodness-of-fit for the combination of all final states and eras obtained with the saturated algorithm, using pseudo-data for $m_{H^0(h^0)} = 125$ GeV and different m_{H^\pm} values.	119
11.19 The Goodness-of-fit for the combination of all final states and eras obtained with the saturated algorithm, using pseudo-data for $m_{H^0(h^0)} = 200$ GeV and different m_{H^\pm} values.	119
11.20 The Goodness-of-fit for the combination of all final states and eras obtained with the saturated algorithm, using pseudo-data for $m_{H^0(h^0)} = 300$ GeV and different m_{H^\pm} values.	120
A.1 Distributions of the input variables used for the parameterized DNN training, normalised in unity, presented for $m_{H^0(h^0)} = 80$ GeV and low $m_{H^\pm} (\leq 300$ GeV).	132
A.2 Distributions of the input variables used for the parameterized DNN training, normalised in unity, presented for $m_{H^0(h^0)} = 80$ GeV and high $m_{H^\pm} (> 300$ GeV).	133
B.1 Pre-fit distributions of the parameterized DNN output in $2\ell^{df}\tau_h$ final state, for $m_{H^0(h^0)} = 80$ GeV and various m_{H^\pm} using 2018 data.	134
B.2 Pre-fit distributions of the parameterized DNN output in $2\ell^{df}\tau_h$ final state, for $m_{H^0(h^0)} = 90$ GeV and various m_{H^\pm} using 2018 data.	135
B.3 Pre-fit distributions of the parameterized DNN output in $2\ell^{df}\tau_h$ final state, for $m_{H^0(h^0)} = 125$ GeV and various m_{H^\pm} using 2018 data.	136
B.4 Pre-fit distributions of the parameterized DNN output in $2\ell^{df}\tau_h$ final state, for $m_{H^0(h^0)} = 300$ GeV and various m_{H^\pm} using 2018 data.	137

C.1	Pre-fit distributions of the parameterized DNN output in $ee\tau_h$ final state, for $m_{H^0(h^0)} = 80$ GeV and various m_{H^\pm} using 2018 data.	138
C.2	Pre-fit distributions of the parameterized DNN output in $ee\tau_h$ final state, for $m_{H^0(h^0)} = 90$ GeV and various m_{H^\pm} using 2018 data.	139
C.3	Pre-fit distributions of the parameterized DNN output in $ee\tau_h$ final state, for $m_{H^0(h^0)} = 125$ GeV and various m_{H^\pm} using 2018 data.	140
C.4	Pre-fit distributions of the parameterized DNN output in $ee\tau_h$ final state, for $m_{H^0(h^0)} = 300$ GeV and various m_{H^\pm} using 2018 data.	141
D.1	Pre-fit distributions of the parameterized DNN output in $\mu\mu\tau_h$ final state, for $m_{H^0(h^0)} = 80$ GeV and various m_{H^\pm} using 2018 data.	142
D.2	Pre-fit distributions of the parameterized DNN output in $\mu\mu\tau_h$ final state, for $m_{H^0(h^0)} = 90$ GeV and various m_{H^\pm} using 2018 data.	143
D.3	Pre-fit distributions of the parameterized DNN output in $\mu\mu\tau_h$ final state, for $m_{H^0(h^0)} = 125$ GeV and various m_{H^\pm} using 2018 data.	144
D.4	Pre-fit distributions of the parameterized DNN output in $\mu\mu\tau_h$ final state, for $m_{H^0(h^0)} = 300$ GeV and various m_{H^\pm} using 2018 data.	145
E.1	Expected upper limit for $m_{H^0(h^0)} = 80$ GeV, per final state per data-taking year. The $ee\tau_h$, $\mu\mu\tau_h$, and $\mu e\tau_h$ limits are presented in the 1st, 2nd, and 3rd column, respectively, while the 2016 pre-VFP, 2016 post-VFP, 2017, and 2018 limits are in the 1st, 2nd, 3rd, and 4th row, respectively. The dotted black line shows the median expected limit, while the 68% and 95% confidence intervals are presented with the green and yellow bands, respectively. The non-smooth behavior observed, particularly for the 2016 pre- and post-VFP periods, is attributed to low statistics. Sensitivity tends to plateau or even degrade for $m_{H^\pm} > 1$ TeV, which is expected because, at high masses, the decay products become boosted and thus more collimated. In this scenario, an analysis incorporating boosted di-tau jets could potentially improve sensitivity. The slight bump at low masses is related to the performance of the DNN training (see Sec. 9.3).	147
E.2	Expected upper limit for $m_{H^0(h^0)} = 90$ GeV, per final state per data-taking year. The $ee\tau_h$, $\mu\mu\tau_h$, and $\mu e\tau_h$ limits are presented in the 1st, 2nd, and 3rd column, respectively, while the 2016 pre-VFP, 2016 post-VFP, 2017, and 2018 limits are in the 1st, 2nd, 3rd, and 4th row, respectively. The dotted black line shows the median expected limit, while the 68% and 95% confidence intervals are presented with the green and yellow bands, respectively. The unusual behavior observed in the limit plots is discussed in Fig. E.1, and the same explanation applies here as well.	148

E.3	Expected upper limit for $m_{H^0(h^0)} = 125$ GeV, per final state per data-taking year. The $ee\tau_h$, $\mu\mu\tau_h$, and $\mu e\tau_h$ limits are presented in the 1st, 2nd, and 3rd column, respectively, while the 2016 pre-VFP, 2016 post-VFP, 2017, and 2018 limits are in the 1st, 2nd, 3rd, and 4th row, respectively. The dotted black line shows the median expected limit, while the 68% and 95% confidence intervals are presented with the green and yellow bands, respectively. The unusual behavior observed in the limit plots is discussed in Fig. E.1, and the same explanation applies here as well.	150
E.4	Expected upper limit for $m_{H^0(h^0)} = 200$ GeV, per final state per data-taking year. The $ee\tau_h$, $\mu\mu\tau_h$, and $\mu e\tau_h$ limits are presented in the 1st, 2nd, and 3rd column, respectively, while the 2016 pre-VFP, 2016 post-VFP, 2017, and 2018 limits are in the 1st, 2nd, 3rd, and 4th row, respectively. The dotted black line shows the median expected limit, while the 68% and 95% confidence intervals are presented with the green and yellow bands, respectively. The unusual behavior observed in the limit plots is discussed in Fig. E.1, and the same explanation applies here as well.	151
E.5	Expected upper limit for $m_{H^0(h^0)} = 300$ GeV, per final state per data-taking year. The $ee\tau_h$, $\mu\mu\tau_h$, and $\mu e\tau_h$ limits are presented in the 1st, 2nd, and 3rd column, respectively, while the 2016 pre-VFP, 2016 post-VFP, 2017, and 2018 limits are in the 1st, 2nd, 3rd, and 4th row, respectively. The dotted black line shows the median expected limit, while the 68% and 95% confidence intervals are presented with the green and yellow bands, respectively. The unusual behavior observed in the limit plots is discussed in Fig. E.1, and the same explanation applies here as well.	153

List of Tables

3.1 Target τ_h identification efficiencies for the different working points defined for the three different discriminators, against electrons (D_e), muons (D_μ) and jets (D_{jet}). These efficiencies are evaluated with the $H \rightarrow \tau^+\tau^-$ event sample for $p_T^{th} \in [30, 70]$ GeV [42].	40
4.1 Dataset and run ranges used from the 2016 data-taking period, along with the corresponding integrated luminosity. The symbol † indicates data affected by a reduced hit efficiency in the Silicon strip detector, often called the HIP issue [48].	43
4.2 Dataset and run ranges used from the 2017 data-taking period, along with the corresponding integrated luminosity.	43
4.3 Dataset and run ranges used from the 2018 data-taking period, along with the corresponding integrated luminosity.	44
4.4 Summary of the available $m_{H^0(h^0)}$ and m_{H^\pm} combinations for the simulated signal samples used in the analysis.	48
4.5 Summary of the simulated signal samples used for the analysis. The production process $pp \rightarrow tbH^\pm$ with $H^\pm \rightarrow H^0(h^0)W^\pm$ and $H^0(h^0) \rightarrow \tau^+\tau^-$ refers to the 4FS scheme, with at least 1 lepton (e/μ) in the final state, while the notation X is shorthand for TuneCP5_13TeV-amcatnlo_pythia8.	49
4.6 Summary of the simulated background samples used for the analysis. The HT-binned versions of the $Z/\gamma^* +$ jets and $W +$ jets are used in the analysis, instead of their inclusive versions, because they more efficiently cover different regions of phase space, ensuring accurate event modeling and improving statistical precision, especially in low event rate regions.	50
5.1 Summary of all MET filters applied to events selected in data and simulation. A checkmark (\checkmark) indicates the filter is applied, while its absence is that it is not applied.	52
6.1 Summary of the PV selection criteria.	57
6.2 The τ_h DMs found by the mode finding algorithm.	59
6.3 Summary of the event selection criteria for the $2\ell^{sf}\tau_h$ and $2\ell^{df}\tau_h$ final state analyses. The p_T variables are reported in units of GeV. Selection criteria that depend on the year of data taking are presented in parentheses with the order corresponding to [2016 (pre-VFP, post-VFP), 2017, 2018].	62
7.1 List of the single lepton triggers used in the analysis for the three year eras of the LHC run 2 data taking.	63
7.2 Summary of selection criteria for the single electron trigger efficiency measurement with the $TnP_{\ell\ell}$ method.	65
7.3 Summary of selection criteria for the single electron trigger efficiency measurement using the $ODM_{\mu,e}$ method.	66

7.4	Summary of selection criteria for the single muon trigger efficiency measurement with the $TnP_{\ell\ell}$ method.	68
7.5	Summary of selection criteria for the single electron trigger efficiency measurement with the $ODM_{\mu,e}$ method.	68
8.1	All the CR and VR that are used in the fake rate measurement.	74
9.1	List of variables included in the training of the parameterized DNN.	88
9.2	Architecture and features of custom parameterized DNN.	90
9.3	Values of m_{H^\pm} given as input to the training the parameterized DNN. All values are reported in units of GeV.	91
10.1	The prefit systematic uncertainties (in %) for the background processes and the signal for $m_{H^0(h^0)} = 200$ GeV and $m_{H^\pm} = 900$ GeV, evaluated for the $\mu e \tau_h$ with 2018 data. Nuisance parameters with a checkmark (\checkmark) also affect the shape of the DNN output spectrum.	98
11.1	The $2\ell^{sf}\tau_h$ and $2\ell^{df}\tau_h$ combined upper limit for $m_{H^0(h^0)} = 200$ GeV, at 95% CL on $\sigma_{pp \rightarrow t(b)H^\pm} \times \mathcal{B}(H^+ \rightarrow H^0 W^+) \times (H^0 \rightarrow \tau^+ \tau^-)$ as a function of m_{H^\pm} , with full Run 2 data.	115
E.1	The $2\ell^{sf}\tau_h$ and $2\ell^{df}\tau_h$ combined upper limit for $m_{H^0(h^0)} = 80$ GeV, at 95% CL on $\sigma_{pp \rightarrow t(b)H^\pm} \times \mathcal{B}(H^+ \rightarrow H^0 W^+) \times (H^0 \rightarrow \tau^+ \tau^-)$ as a function of m_{H^\pm} , with full Run 2 data.	146
E.2	The $2\ell^{sf}\tau_h$ and $2\ell^{df}\tau_h$ combined upper limit for $m_{H^0(h^0)} = 90$ GeV, at 95% CL on $\sigma_{pp \rightarrow t(b)H^\pm} \times \mathcal{B}(H^+ \rightarrow H^0 W^+) \times (H^0 \rightarrow \tau^+ \tau^-)$ as a function of m_{H^\pm} , with full Run 2 data.	149
E.3	The $2\ell^{sf}\tau_h$ and $2\ell^{df}\tau_h$ combined upper limit for $m_{H^0(h^0)} = 125$ GeV, at 95% CL on $\sigma_{pp \rightarrow t(b)H^\pm} \times \mathcal{B}(H^+ \rightarrow H^0 W^+) \times (H^0 \rightarrow \tau^+ \tau^-)$ as a function of m_{H^\pm} , with full Run 2 data.	149
E.4	The $2\ell^{sf}\tau_h$ and $2\ell^{df}\tau_h$ combined upper limit for $m_{H^0(h^0)} = 200$ GeV, at 95% CL on $\sigma_{pp \rightarrow t(b)H^\pm} \times \mathcal{B}(H^+ \rightarrow H^0 W^+) \times (H^0 \rightarrow \tau^+ \tau^-)$ as a function of m_{H^\pm} , with full Run 2 data.	152
E.5	The $2\ell^{sf}\tau_h$ and $2\ell^{df}\tau_h$ combined upper limit for $m_{H^0(h^0)} = 300$ GeV, at 95% CL on $\sigma_{pp \rightarrow t(b)H^\pm} \times \mathcal{B}(H^+ \rightarrow H^0 W^+) \times (H^0 \rightarrow \tau^+ \tau^-)$ as a function of m_{H^\pm} , with full Run 2 data.	152

1 Introduction

1.1 The Standard Model of Elementary Particles

The Standard Model is unquestionably one of the greatest scientific achievements in human history, besides its limitations. As far as we understand, our world obeys the four fundamental forces of the universe, gravity, electromagnetism, weak, and strong interactions. Starting from pairing the electric with the magnetic forces into one single theory, electromagnetism, SM was built on the exact same idea, to combine electromagnetism, weak and strong interactions into one unified theory. As presented in Fig.1.1, SM predicts the existence of 3 generations of fermions, meaning particles of 1/2 spin, which are the building blocks of all visible matter in the universe. It predicts that there should be four vector bosons serving as the mediators of the three forces within the Standard Model framework and last but not least, the scalar Higgs boson.

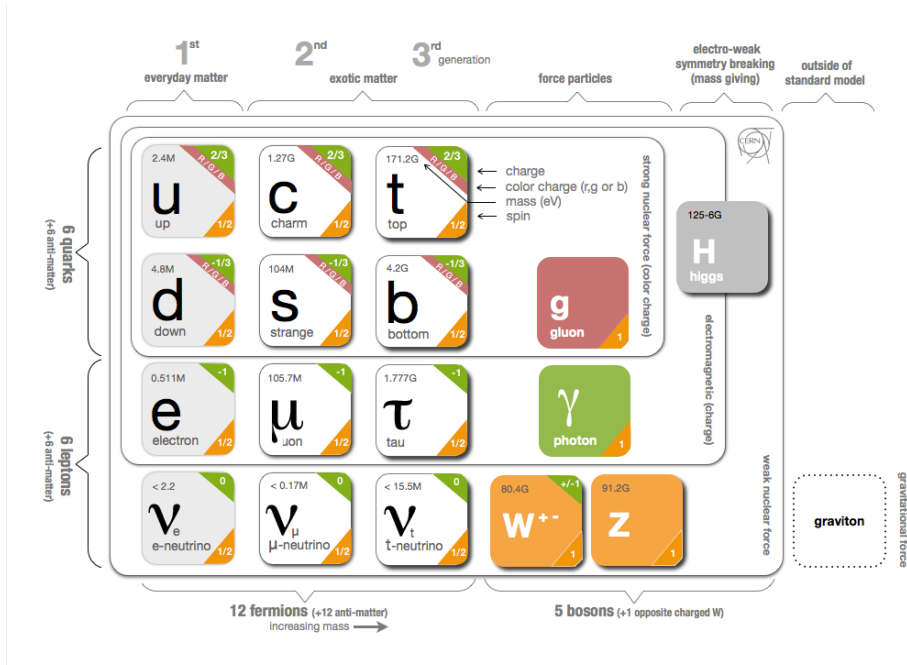


Figure 1.1: Standard Model info-graphic of elementary particles and interactions [4].

1.1.1 Quarks and Leptons

According to SM, all visible matter in the universe is constructed by these 12 fermions, each of which has its antiparticle, with the same mass and spin but of opposite charge. There are 6 quark flavours in total, namely up, down, charm, strange, top, and bottom, and 6 lepton flavours, electron, muon, tau, and the corresponding neutrinos. Both quarks and leptons are categorized into 3 generations where the first generation particles are the building blocks

of the matter that surround us. All matter we see and feel around us consists of atoms which subsequently consist of protons, neutrons, and electrons. Protons and neutrons are a combination of up and down quarks, more specifically, protons are made of 2 up and 1 down quarks and neutrons of 1 up and 2 down quarks. The second lepton of the first generation of fermions, the electron neutrino, is primarily produced through beta decay. In this type of radioactive decay, an atomic nucleus emits a beta particle (electron or positron) and an electron neutrino or antineutrino. In terms of fundamental particles, beta decay involves the transformation of a neutron into a proton or vice versa. This process occurs via the weak interaction, where a down quark in the neutron is converted into an up quark, emitting a W boson, which then decays into an electron (or positron) and an electron neutrino (or antineutrino) [5]. Besides the fact that SM has all neutrinos massless, recent studies have shown that they do have mass after all [11]. Even though precise measurements of neutrino masses have not yet been made, scientists have established upper limits on their masses. The mass differences between different neutrino types have been measured through their flavor oscillations because neutrinos can change from one flavor to another as they propagate. On the other hand, the second and third generations' fermions have the same properties as their analogous 1st generation fermions on the same column as shown in Fig.1.1 but are just heavier.

In contrast to leptons, which can exist freely in nature, quarks cannot move freely or be found free at rest due to a property known as color confinement. This phenomenon is a fundamental aspect of the strong interaction, the force that binds quarks together. The strength of the strong force varies with the coupling constant, which changes with the square of the momentum transfer, Q^2 . Quarks carry color charge and are bound together to form colorless states, such as protons and neutrons. As a result, quarks always exist within hadrons and cannot exist as free particles. There are 3 color charges in total, namely red ("r"), blue ("b"), and green ("g") along with their anti-colors, $r, \bar{r}, b, \bar{b}, g$ and \bar{g} . There are 2 categories of hadrons, namely mesons and baryons. The first are colorless bound states formed by a quark-antiquark pair, each of which has the anti-color charge of what the other one has, for the state to be colorless. Baryons on the other hand, consist of three quarks or three antiquarks each of which carries a different color charge to form a colorless state.

1.1.2 Force carriers

As noted, the Standard Model is a unified theory that describes three of the four fundamental forces (excluding gravity) governing the physical laws of the universe. Each force has its force carrier, 4 vector bosons in total, as presented in Fig.1.1. In general, all charged particles can interact with each other through electromagnetic forces by exchanging photons. Photons, being massless particles, are fundamental constituents in Quantum Electrodynamics (QED) [6], the quantum field theory that describes electromagnetic interactions. QED is renowned

for its comprehensive explanation of these interactions, characterized by an infinite range of applicability. This means that the electromagnetic force described by QED can act over arbitrarily large distances without diminishing strength, regardless of the spatial separation between charged particles.

For strong interactions, color charge plays the same role as electric charge in electromagnetic interactions. In other words, for 2 particles to interact through the strong force they both need to have color charge. Quarks are particles that interact with each other by exchanging a gluon, a dual color charge carrier, ensuring the overall color charge remains unchanged. Gluons are the strong force carriers and come in 8 different types, as is the number of all possible dual-color charge combinations. The range of applicability for strong interactions extends to orders of femtometers (10^{-15} m), just as much as needed to keep quarks together into bound states, forming hadrons, and nucleons into nuclei. Quantum chromodynamics, QCD [7], is the quantum field theory that describes the strong interactions, providing a comprehensive framework for understanding the behavior of particles ruled by the laws of strong force. Finally, all particles except gluons, can interact among themselves through the weak interactions, regardless of whether they have an electric or color charge. According to SM theory, all force carrier particles should be massless but that's not the case for the weak force mediators, W and Z bosons, which exist with surprisingly large mass. This phenomenon is tackled by introducing the electroweak symmetry "breaking", which is not exactly a break of the symmetry, symmetry is still there but it is just hidden in a non-linear way.

1.1.3 Higgs boson

The Brout-Englert-Higgs (BEH) mechanism [8]-[9] was introduced as the answer of SM on how the W and Z bosons, weak interaction's carriers, acquire mass. The whole idea is summarized by adding a Higgs field to the SM theory for the spontaneous electroweak symmetry breaking to be explained. Besides W and Z bosons, the Higgs mechanism is also responsible for giving mass to the fermions, through the Yukawa coupling between fermions' direct interactions with the Higgs field.

The Brout-Englert-Higgs mechanism suggests the existence of a Higgs field ϕ and a corresponding Higgs potential $V(\phi)$. The Higgs field is a $SU(2)_L$ doublet (Eq.1), where each component is a complex scalar field. On the other hand, the Higgs potential is symmetric with respect to the origin and has a non-trivial minimum, given by Eq.2, with $-\mu^2, \lambda > 0$.

$$\phi = \begin{pmatrix} \phi^+ \\ \phi^0 \end{pmatrix} \quad (1)$$

$$V(\phi) = \mu^2 |\phi|^2 + \lambda |\phi|^4 \quad (2)$$

The two-dimensional sketch of the Higgs potential is presented in Fig.1.2, which has a continuous minimum at the vacuum expectation value, given by Eq.3.

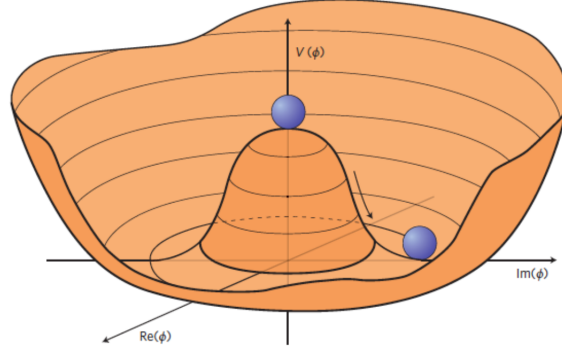


Figure 1.2: A prototypical effective ‘Mexican hat’ potential that leads to ‘spontaneous’ symmetry breaking [10].

$$\nu = |\phi|_{min} = \sqrt{\frac{-\mu^2}{2\lambda}} \quad (3)$$

In this case, the potential has two minima, implying the presence of two possible vacuum states. The choice of one of the two is known as spontaneous symmetry breaking, as it breaks the symmetry of the Lagrangian. By choosing the vacuum state of the potential to be the one given in Eq.4, the perturbation of the field around it can produce the excitations of the fields describing the particle states.

$$\phi = \frac{1}{\sqrt{2}} \begin{pmatrix} 0 \\ \nu \end{pmatrix} \quad (4)$$

By expanding the field in the radial direction, with the parametrization given by Eq.5 it can be shown that it generates the Higgs boson with a mass given by Eq.6.

$$\phi = \frac{1}{\sqrt{2}} \begin{pmatrix} 0 \\ \nu + H(x) \end{pmatrix} \quad (5)$$

$$m_H = \sqrt{2}\mu \quad (6)$$

Following the same procedure using a complex scalar field (Eq.7), the potential will have an infinite set of minima defined by Eq.8, which all lie on a circle in the complex ϕ plane, as shown in Fig.1.2.

$$\phi = \frac{1}{2}(\phi_1 + i\phi_2) \quad (7)$$

$$\phi_1 + \phi_2 = \frac{\mu^2}{2\lambda} \quad (8)$$

By expanding ϕ around the vacuum state, the mixing of vector boson fields results in a non-diagonal mass matrix. This implies that the observed bosons are linear combinations of the original fields present before symmetry breaking. The mixing between the Z boson and the photon is determined by a matrix involving the weak mixing angle, θ_W , which is the only free parameter needed to predict transition probabilities in electroweak processes. The masses of the W and Z bosons emerge from these mixed states, given by Eq.9, while the photon remains massless.

$$m_W = \frac{1}{2}g * \nu m_Z = \frac{m_W}{\cos\theta_W} \quad (9)$$

The g factor in the W boson mass definition refers to the electroweak coupling constant associated with the weak interaction, which determines the strength of the interaction between the W bosons and the particles they interact with, such as fermions. This process is a core aspect of the BEH mechanism, generating fermion masses as they arise through interactions with the Higgs field, described by the Yukawa interaction. However, the precise masses of the fermions are not predicted by the BEH mechanism and remain free parameters of the Standard Model.

The Higgs boson arises as an embodiment of the Higgs field's quantum fluctuations. It is a manifestation of the interactions between the field and the various particles, serving as a tangible confirmation of the presence and behavior of the underlying Higgs field. Higgs boson's experimental confirmation took place in 2012 at the European Organization for Nuclear Research (CERN), almost simultaneously by its two major multipurpose experiments, ATLAS and CMS [1, 2]. As shown in Fig.1.3, the mass of the Higgs boson was found to be equal to 125 GeV.

1.1.4 Is Standard Model the end of the road?

The Standard Model of particles as a theory describes in a very successful way how fundamental particles interact with each other through three out of the four fundamental interactions. Its latest experimental verification, the discovery of the Higgs boson, brought a lot of enthusiasm to the particle physics community because it was the last undiscovered piece of the theory. SM is an outcome of collective steps that were put together. Although it successfully explains most aspects of the particles and their interactions, the Standard Model still fails to account for many important elements of the broader framework of fundamental physics, such as the nature of dark matter, dark energy, the unification of all fundamental forces, the hierarchy problem, the neutrino masses, the non-inclusion of gravity, in its struc-

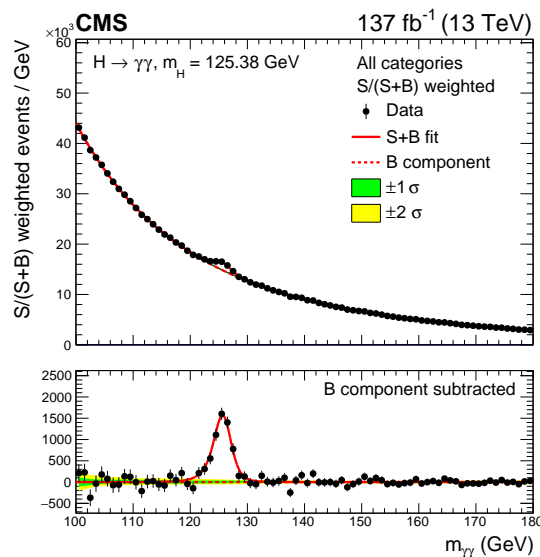


Figure 1.3: Diphoton invariant mass distribution with combining all categories used for the inclusive fiducial cross section measurement, with full Run2 data [3].

ture, and why an asymmetry between matter and antimatter exists in our universe.

Given that SM seems to be a satisfying theory on the low energy regime but many issues and questions start to pop out as we move to higher energy scales, SM must be a part of a more general theory which should be able to explain everything that SM fails to. Many Beyond Standard Model theories (BSM) have been produced in the last few decades, each trying to address some of the problems SM fails to explain. Unfortunately, no experimental evidence has been discovered yet to confirm or refute them.

1.1.5 Standard Model limitations and shortcomings

Despite the great success of the Standard Model (SM), it suffers from some significant drawbacks. The scientific community has identified several phenomena that the SM fails to address, describe, or accurately predict. These shortcomings suggest that the SM is an incomplete theory, though it still provides precise predictions within its range of applicability. Rather than being seen as a failure or an incorrect theory, it is viewed as effective within certain limits. Below are some of its limitations and shortcomings that scientists aim to resolve through a more comprehensive model.

- The inability to describe or unify one of the four fundamental forces of the universe, gravity. There is no prediction for the existence of graviton, the hypothesized force carrier of gravity, and therefore fails to account for any gravity-related effects in its calculations and predictions.
- Standard Model provides no explanation or reason for the existence of exactly three fermion generations, with the specific mass ordering and values. It also fails to predict

the values of any of the 18 free parameters that come with it, 3 coupling constants, 4 Cabibbo-Kobayashi-Maskawa (CKM) parameters, 9 fermion masses, and 2 boson masses for W and Z. However, these values have been determined through experimental precision measurements.

- Recent experiments have shown that neutrinos have mass [11], in contrast to what SM predicts. Moreover, recent measurements indicate that neutrinos change from one flavour to another, as they travel through space and time, a phenomenon known as neutrino oscillation [12]. The neutrino oscillation mechanism also implies that neutrinos should have non-zero masses, contrary to what SM theory stipulates. This particular fact, adds 9 additional free parameters to the model, raising their total number to 27.
- There is no explanation from the SM as to why there is observed matter-antimatter asymmetry in the universe or what exactly dark matter and dark energy are, that combine constitute almost 95% of the universe. This means that the SM is applied to just 5% of what we know that exists in nature. It doesn't even have a candidate to propose to serve as a potential dark matter particle.
- "Naturalness" in the Higgs' mass and the Hierarchy problem are also two of the crucial issues that the SM has to face. For that, a more extensive discussion takes place in the following subsection.

1.1.5.1 "Naturalness" in the Higgs' mass and Hierarchy problem

The term "Naturalness" in particle physics context, refers to a theoretical principle that suggests physical parameters or quantities in a theory, should not be much larger or smaller than unity unless there is a reason for it. In the case of the Higgs boson, the concept of naturalness is often invoked to address the question of why the mass of the Higgs boson is so much lighter than the Planck scale ($m_P \approx 10^{18}$ GeV), in which gravity becomes as strong as the other fundamental forces. Of course, as already noted, SM's effectiveness is in energy scales much lower than Planck's scale, where contributions due to gravitational forces are negligible. Nonetheless, even if we overlook this, electroweak symmetry breaking remains an issue, which takes place at 10^2 GeV, an energy that falls into the energy scale that SM is applicable. This huge difference between the two energy scales, at Planck, and at Electroweak Symmetry breaking, cannot be explained by SM.

The Hierarchy problem arises from considering higher-order quantum corrections, which significantly affect the Higgs boson's mass, especially due to virtual particles in loops, such as the top quark, which has a large Yukawa coupling to the Higgs field. These quantum corrections diverge quadratically, leading to an infinitely large Higgs mass as shown in Eq.10.

$$\delta m_H^2 = \mathcal{O} \left(\frac{\alpha}{\pi} \right) \Lambda^2 \quad (10)$$

If the cutoff scale Λ is close to the Planck scale, these quantum corrections become much larger than the small physical mass of the Higgs boson. The Planck scale represents the energy level where quantum effects of gravity become important, and where a theory of quantum gravity might be necessary to describe fundamental interactions. To reconcile this, a large bare Higgs mass ($m_H^2 = m_{\text{bare}}^2 - \delta m_H^2$) would be required, involving precise fine-tuning to achieve the observed Higgs mass of around 125 GeV. The naturalness principle suggests that the Higgs mass should be close to the scale at which new physics beyond the SM emerges, to avoid such fine-tuning or unnatural cancellations. Fine-tuning is considered "unnatural" because it demands precise adjustments of the fundamental parameters in order to obtain the observed Higgs mass, which seems unlikely without an underlying explanation.

Despite the discovery of the Higgs boson at around 125 GeV, the question of naturalness remains unresolved, as this mass is much smaller than the expected scale of new physics. This suggests that new physics may exist near Λ scale to stabilize the Higgs mass and resolve the hierarchy problem. However, the SM does not explain this, and it remains unclear at what value of Λ new physics will emerge.

Many theories have been proposed to address this issue and other shortcomings of the SM, but to date, none have been experimentally confirmed. The cutoff scale Λ is anticipated to define the energy threshold where a more fundamental theory replaces the SM. Two predominant scenarios are considered: one where Λ lies close to the Planck scale, which would not resolve the hierarchy problem, and another where Λ is much lower, at the TeV scale, within reach of current or near-future experiments. In this scenario, Λ is at least an order of magnitude greater than the energy scale in which the electroweak symmetry breaking occurs. In this context, the Hierarchy problem is completely tackled and a new theory, Super Symmetry [13] emerges as a leading candidate, offering solutions to most of the SM issues.

1.2 The 2HDM as an expansion of the SM

The Higgs sector of the SM is based on a simple structure, where the Higgs field is modeled as an SU(2) doublet, predicting the existence of a single neutral Higgs boson. However, given the numerous issues that the SM cannot fully address, the search for a new, Beyond Standard Model (BSM) theory has become essential. Most of them, are focusing on extending the SM by introducing additional singlets, doublets, or even triplets to the scalar part of the SM.

The simplest extension of the Standard Model (SM) is the Two-Higgs-Doublet Model (2HDM) [14], which introduces two complex scalar doublets instead of one. This model is not only simple but also offers significant advantages. One key feature is its flexible scalar mass spectrum, which refers to the ability to have multiple Higgs bosons with varying masses. This flexibility can be advantageous for addressing the baryon asymmetry of the Universe, as it allows for the possibility of new mechanisms for baryogenesis. In this

context, the 2HDM might explain the observed excess of baryons over antibaryons as the varying masses of the Higgs bosons can affect the dynamics of these mechanisms and contribute to the generation of baryon asymmetry through processes that violate baryon number conservation.

Moreover, many Supersymmetric theories, such as the Minimal supersymmetric Standard Model (MSSM), require the presence of an additional Higgs doublet. This extra doublet is essential for providing masses to both up-type and down-type quarks simultaneously. In supersymmetric models, scalar particles are organized into chiral multiplets, with their conjugates belonging to multiplets of opposite chirality. This requirement arises because multiplets with different chiralities cannot couple to each other in the same Lagrangian, necessitating the inclusion of additional Higgs doublets to properly account for the mass generation of all quark types.

As a first step, the 2 complex SU(2) scalars are defined with identical quantum numbers, as follows :

$$\Phi_\alpha = \begin{pmatrix} \phi_\alpha^\dagger \\ \frac{1}{\sqrt{2}}(v_\alpha + \rho_\alpha + i\eta_\alpha) \end{pmatrix}, \alpha = 1, 2 \quad (11)$$

In this definition, Φ_α represents the two Higgs doublets, with α indexing the first and second doublets. Each doublet contains two components, where the complex scalar field ϕ_α^\dagger denotes the charged components of the doublet, while $\frac{1}{\sqrt{2}}(v_\alpha + \rho_\alpha + i\eta_\alpha)$ represents the neutral component. Here, v_α is the vacuum expectation value (VEV) of the field, ρ_α is a real scalar field corresponding to physical Higgs bosons, and η_α is an imaginary scalar field that can represent either a physical Higgs boson or a Goldstone boson.

Given that the 2HDM introduces a total of 8 fields (2 components for each of the 2 doublets), the potential for these fields will involve fourteen free parameters, given by Eq.12.

$$\begin{aligned} V(\Phi_1, \Phi_2) = & m_{11}^2 \Phi_1^\dagger \Phi_1 + m_{22}^2 \Phi_2^\dagger \Phi_2 - m_{12}^2 (\Phi_1^\dagger \Phi_2 + \Phi_2^\dagger \Phi_1) + \frac{\lambda_1}{2} (\Phi_1^\dagger \Phi_1) + \frac{\lambda_2}{2} (\Phi_2^\dagger \Phi_2) \\ & + \lambda_3 \Phi_1^\dagger \Phi_1 \Phi_2^\dagger \Phi_2 + \lambda_4 \Phi_1^\dagger \Phi_2 \Phi_2^\dagger \Phi_1 + \frac{\lambda_5}{2} [(\Phi_1^\dagger \Phi_2)^2 + (\Phi_2^\dagger \Phi_1)^2] \\ & + \lambda_6 \Phi_1^\dagger \Phi_1 \Phi_1^\dagger \Phi_2 + \lambda_7 \Phi_2^\dagger \Phi_2 \Phi_1^\dagger \Phi_2 + h.c. \end{aligned} \quad (12)$$

The potential includes both quadratic and quartic terms, where the first describe the masses and VEVs of the Higgs fields, while the latter describe interactions between different field components. Specifically, the fourteen parameters arise from these mass terms, interaction strengths, and mixing angles, making the model more complex than the Standard Model,

which only includes a single Higgs doublet. The mass matrix elements m_{11}, m_{11} and the Higgs-self couplings $\lambda_1, \lambda_2, \lambda_3, \lambda_4$ are real parameters while $m_{12}, \lambda_5, \lambda_6, \lambda_7$ are complex. One of the most popular solutions that have been proposed in order to deal with this complexity is to impose some global symmetries by hand, to constrain the total number of free parameters. Specifically, the discrete \mathbb{Z}_2 symmetry is employed to achieve this goal, since it ensures that the CP is not spontaneously broken in order for the scalars and pseudo scalars to be distinguishable. This requirement enforces all free parameters to be real. The discrete \mathbb{Z}_2 symmetry is also essential for the elimination of tree-level flavor-changing neutral currents, which simplifies the model and avoids unwanted interactions between the Higgs fields. Under all these aforementioned assumptions the scalar potential for the 2 doublets can be defined as :

$$V(\Phi_1, \Phi_2) = m_{11}^2 \Phi_1^\dagger \Phi_1 + m_{22}^2 \Phi_2^\dagger \Phi_2 - m_{12}^2 (\Phi_1^\dagger \Phi_2 + \Phi_2^\dagger \Phi_1) + \frac{\lambda_1}{2} (\Phi_1^\dagger \Phi_1) + \frac{\lambda_2}{2} (\Phi_2^\dagger \Phi_2) + \lambda_3 \Phi_1^\dagger \Phi_1 \Phi_2^\dagger \Phi_2 + \lambda_4 \Phi_1^\dagger \Phi_2 \Phi_2^\dagger \Phi_1 + \frac{\lambda_5}{2} [(\Phi_1^\dagger \Phi_2)^2 + (\Phi_2^\dagger \Phi_1)^2] \quad (13)$$

This version of the potential contains 8 real free parameters, which is 6 fewer than the more general one, before imposing any assumptions. Specifically, the terms involving λ_6 and λ_7 are not present after imposing the discrete \mathbb{Z}_2 symmetry. The vacuum expectation values (vevs) of the 2 doublets are determined by minimizing this potential. The minimizing condition is expressed in Eq.14, which results in Eq.15-16. The vacuum expectation values are then given by Eq.17.

$$\frac{\partial V}{\partial u_1} = \frac{\partial V}{\partial u_2} = 0 \quad (14)$$

$$m_{11}^2 u_1 - \text{Re}(m_{12}^2) u_2 + u_1^3 \frac{\lambda_1}{2} + u_1 u_2^2 \frac{\lambda_{345}}{2} = 0, \quad \lambda_{345} = \lambda_3 + \lambda_4 + \lambda_5 \quad (15)$$

$$m_{22}^2 u_2 - \text{Re}(m_{12}^2) u_1 + u_2^3 \frac{\lambda_2}{2} + u_2 u_1^2 \frac{\lambda_{345}}{2} = 0 \quad (16)$$

$$\langle \Phi_\alpha \rangle_0 = \frac{1}{\sqrt{2}} \begin{pmatrix} 0 \\ v_\alpha \end{pmatrix}, \quad \alpha = 1, 2 \quad (17)$$

Keeping in mind that the SU(2) symmetry breaking leads to the appearance of 3 Goldstone bosons, 3 of the free parameters should be used for giving mass to Z and W^\pm bosons. That means the 5 remaining parameters should correspond to some kind of Higgs fields and indeed, as the electroweak breaking predicts, 5 new scalars, Higgs-like, physical fields must exist. So, having 5 Higgs bosons in total, two of them come with a charge (H^\pm), a light (h^0),

and a heavy (H^0) CP-even neutral Higgs bosons and one CP-odd neutral Higgs boson (A^0).

But how exactly are these free parameters related to the masses of these 5 newly introduced bosons? Using the vevs found above, the mass terms for the charged scalars can be written as :

$$\mathcal{L}_{\phi^\pm mass} = [m_{12}^2 - (\lambda_4 + \lambda_5)v_1v_2] \begin{pmatrix} \phi_1^- & \phi_2^- \end{pmatrix} \begin{pmatrix} \frac{v_2}{v_1} & -1 \\ -1 & \frac{v_1}{v_2} \end{pmatrix} \begin{pmatrix} \phi_1^+ \\ \phi_2^+ \end{pmatrix} \quad (18)$$

Assuming no CP violation, v_1 and v_2 are both taken to be real and not negative. As a result, the mass matrix has two eigenvalues, one null which corresponds to the charged Goldstone boson giving mass to the W^\pm and one non-zero which is used for defining the mass of the charged Higgs boson which is given by:

$$m_{H^\pm}^2 = \left[\frac{m_{12}^2}{v_1v_2} - \lambda_4 - \lambda_5 \right] (v_1^2 + v_2^2) \quad (19)$$

Similarly, since the part of the Lagrangian that corresponds to the pseudoscalars' mass term is given by:

$$\mathcal{L}_{Hmass} = \left[\frac{m_{12}^2}{v_1v_2} - \lambda_5 \right] + \begin{pmatrix} \eta_1 & \eta_2 \end{pmatrix} \begin{pmatrix} v_2^2 & -v_1v_2 \\ -v_1v_2 & v_1^2 \end{pmatrix} \begin{pmatrix} \eta_1 \\ \eta_2 \end{pmatrix}, \quad (20)$$

the Z boson gets its mass through the Goldstone boson, which corresponds to the null eigenvalue. Thus, the mass of the physical pseudoscalar can be expressed as a function of the non-zero eigenvalue:

$$m_A^2 = \left[\frac{m_{12}^2}{v_1v_2} - \lambda_5 \right] (v_1^2 + v_2^2) \quad (21)$$

Last but not least, Eq.22] represents the part with the mass terms for the neutral scalars.

$$\mathcal{L}_{\rho mass} = \begin{pmatrix} \rho_1 & \rho_2 \end{pmatrix} \begin{pmatrix} m_{11}^2 \frac{v_2}{v_1} + \lambda_1 v_1^2 & -m_{12}^2 + \lambda_{345} v_1 v_2 \\ -m_{12}^2 + \lambda_{345} v_1 v_2 & m_{22}^2 \frac{v_1}{v_2} + \lambda_2 v_2^2 \end{pmatrix} \begin{pmatrix} \rho_1 \\ \rho_2 \end{pmatrix} \quad (22)$$

The equations for the physical neutral scalars' masses are obtained by simultaneously performing a diagonalization of the three mass-squared matrices. One way to do this is by introducing 2 new parameters, the rotation angles α and β . Angle α is the one that performs the diagonalization of the mass-squared matrix for the neutral scalars and angle β performs the diagonalization of the mass-squared matrices of the charged and pseudo scalars, accordingly. By using this notation and the fact that the physical neutral scalars must

be orthogonal combinations of the ρ_i fields, the physical field H and h are:

$$h = \rho_1 \sin \alpha - \rho_2 \cos \alpha \quad (23)$$

$$H = -\rho_1 \cos \alpha - \rho_2 \sin \alpha \quad (24)$$

The masses of these fields are then determined by diagonalizing the mass-squared matrix for the neutral scalars, resulting in:

$$m_h^2 = \frac{1}{2} \left[m_{11}^2 + m_{22}^2 - \sqrt{(m_{11}^2 - m_{22}^2)^2 + 4 (\text{Re } m_{12}^2 + \lambda_{345} u_1 u_2)^2} \right] \quad (25)$$

$$m_H^2 = \frac{1}{2} \left[m_{11}^2 + m_{22}^2 + \sqrt{(m_{11}^2 - m_{22}^2)^2 + 4 (\text{Re } m_{12}^2 + \lambda_{345} u_1 u_2)^2} \right] \quad (26)$$

Concerning the rotation angle β , by taking into account the vevs of the scalar fields, the statement below is always true.

$$v_1 = v \cos \beta, v_2 = v \sin \beta, \quad (27)$$

Thus, a more useful way to interpret this angle is through the following definition:

$$\tan \beta = \frac{v_2}{v_1} \quad (28)$$

The parameters α and $\tan \beta$ play the most crucial role in the 2HDM, as they define how these Higgs fields interact with the fermions and the vector bosons. These two parameters plus m_{12}^2 and the 4 masses of the 5 Higgs bosons (H^+ and H^- should have the same mass in order for the theory to be self-consistent) form the set of the 7 free parameters of 2HDM.

Assuming that CP-symmetry is conserved in the extended Higgs sector as proposed by the general 2HDM, various 2HDMs can be categorized into 4 different types, according to the way that Higgs doublets couple to the fermions.

- **Type-I:** All quarks and charged leptons couple to only one of the Higgs doublets (conventionally Φ_2) while they do not couple with the other one. This is achieved by imposing \mathbb{Z}_2 symmetry, so $\Phi_1 \rightarrow -\Phi_1$ and $\Phi_2 \rightarrow \Phi_2$
- **Type-II:** up-type quarks are coupled to Φ_2 (same convention) but charged leptons and down-type quarks couple to the other Higgs doublet, Φ_1 . This is achieved by imposing $\Phi_1 \rightarrow -\Phi_1$ and $d_{right}^i \rightarrow -d_{right}^i$
- **Type-III (lepton-specific):** All quarks are coupled to the same doublet, Φ_2 , and charged leptons are coupled to the other one, Φ_1

- **Type-IV (flipped)** Same as Type-II but in this case, charged leptons couple with the same doublet as the up-type quarks (Φ_2), instead of the same as the down-type quarks

The couplings of the Higgs bosons (h^0, H^0, A^0 and H^\pm) to fermions vary depending on the model type, determined by the mixing angles and $\tan \beta$. The couplings to the neutral scalars h^0 and H^0 involve the factors $\frac{\cos\alpha}{\sin\beta}$ and $\frac{\sin\alpha}{\sin\beta}$ for up-type quarks, $\frac{\sin\alpha}{\cos\beta}$ and $\frac{\cos\alpha}{\cos\beta}$ for down-type quarks and leptons. The pseudoscalar A^0 couples to up-type quarks with $1/\tan \beta$ and to down-type quarks and leptons with $\tan \beta$. For the charged Higgs H^\pm , the couplings to fermions depend on the specific model, typically involving terms like $\tan \beta$ and $1/\tan \beta$, reflecting the different roles of the two Higgs doublets in providing mass to up-type versus down-type fermions.

1.3 Charged Higgs Boson

Even though in tree-level, the mass of H^\pm depends on the mass of Higgs boson A (Eq.29), higher order corrections could lead to large changes on the mass spectrum, cross sections and branching ratios of the charged Higgs boson.

$$m_{H^\pm}^2 = m_A^2 + m_W^2 \quad (29)$$

The reason behind this, is the comparatively large number of free parameters of the 2HDM, making the theory's predictions quite difficult and unstable. Furthermore, the SM is helicity suppressed. Mediated through a H^\pm is not helicity suppressed and can be large depending on the Yukawa couplings.

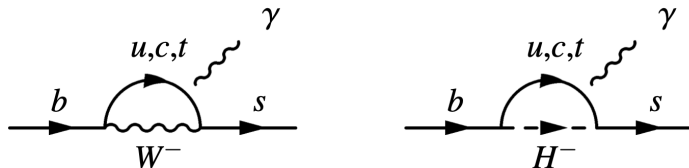


Figure 1.4: Charged Higgs Boson expected appearance through b to s decay channel, though photon emission.

1.3.1 Charged Higgs Production Processes

Many BSM models predict the existence of a charged Higgs boson. However, none of these models make predictions on the mass of the charged Higgs. Thus, experimental investigations categorize the charged Higgs boson into three different cases based on its mass relative to the masses of the top and bottom quarks, denoted as m_t and m_b , respectively.

- Light $H^\pm \rightarrow m_{H^\pm} < m_t - m_b$
- Intermediate $H^\pm \rightarrow m_{H^\pm} \sim m_t$
- Heavy $H^\pm \rightarrow m_{H^\pm} > m_t - m_b$

Depending on its mass, the processes that lead to the production of the charged Higgs are different. The low mass H^\pm is expected to appear in top-quark decays, as presented in Fig.1.5.

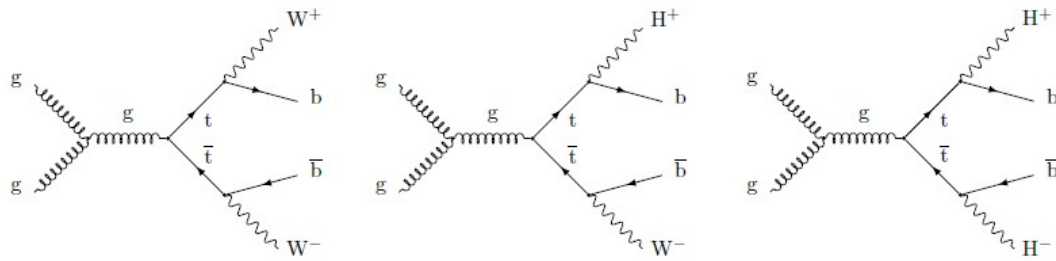


Figure 1.5: Feynman Diagrams for $t\bar{t}$ (on the left plot), $t \rightarrow bH^+$ (middle plot and $t\bar{t} \rightarrow b\bar{b}H^+H^-$ (right hand-side plot).

On the contrary, a heavier charged Higgs boson can mainly be produced in association with a top quark, as in Fig.1.6.

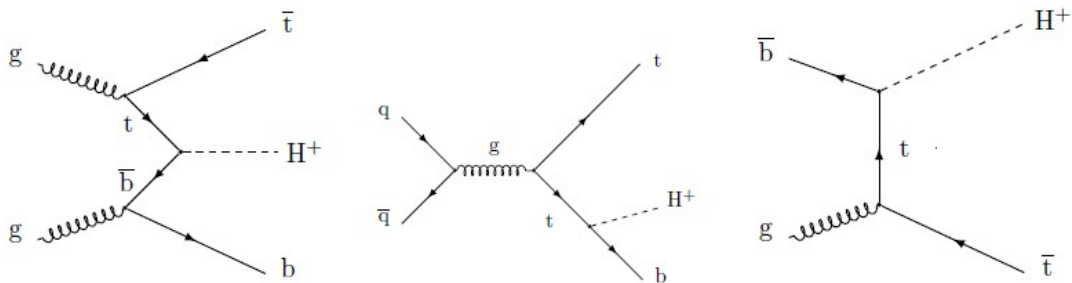


Figure 1.6: Charged Higgs Boson production in association with a top quark, for the Heavy category.

1.3.2 Decaying modes

As shown in Fig.1.7, at low masses, the $\tau\nu$ channel is the dominant one but rapidly falls as the mass of the charged Higgs increases. On the other hand, at large masses, the tb competes with the h^0W^\pm/H^0W^\pm channel but the last one seems to dominate in all types of 2HDMs, for both small and large values of $\tan\beta$. Thus, channel h^0W^\pm/H^0W^\pm allows searching for H^\pm in the most extensive way compared to any other mode, including the one which used to be the most promising of all the explored ones up to this moment, $H^\pm \rightarrow \tau^\pm\nu$. This project focuses on this particular decay mode and is quite promising in terms of enabling the probe of a large, unexplored region of the 2HDM parameter space.

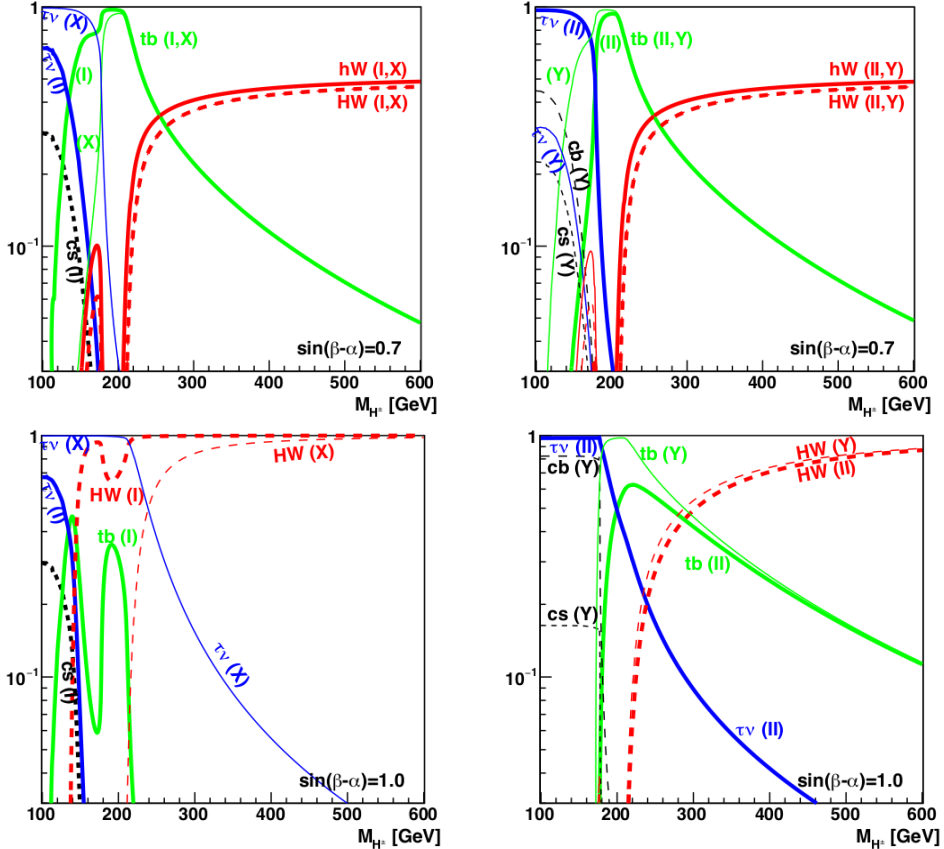


Figure 1.7: Charged Higgs boson branching ratios (BR) as a function of m_{H^\pm} in different types of general 2HDM. Type-I and Type-X are shown on the left while Type-II and Type-Y are shown on the right. The top row shows the BRs for $\tan\beta = 3$ and the CP-conserving limit $\sin(\beta - \alpha) = 0.7$ while the bottom row shows the $\tan\beta = 30$ and the alignment limit $\sin(\beta - \alpha) = 0.7$. The masses of the two neutral Higgs bosons are set at $m_h = 125$ GeV and $m_H = 130$ GeV [15].

1.4 Neutral Higgs Bosons

As discussed in Sec.1.2, the 2HDM predicts two neutral Higgs bosons, both CP-even and one heavier than the other one. The heavy neutral Higgs is symbolized with a capital H (H^0), while the light one with a lowercase h (h^0). Many believe that SM Higgs that was recently discovered should be the light one because if it were the heavy one, there should have been some hints of a lower mass resonant. The fact that no such neutral particle has been observed yet, leads to the assumption that the heavy neutral Higgs boson should have mass greater than the SM Higgs. Nevertheless, the scenario in which SM-like Higgs is the H^0 in 2HDM theory while the h^0 is yet to be discovered, should not be excluded, since there is no proof or undeniable piece of evidence that forbids it.

This study investigates both scenarios, by exploring the $H^\pm \rightarrow H^0(h^0)W^\pm$ decay channel, for five different mass points of neutral Higgs bosons. It considers scenarios where the SM-like Higgs is the H^0 boson, with m_{h^0} of 80 and 90 GeV. Additionally, it explores the scenario with m_{h^0} fixed at 125 GeV, independent of whether the SM-like Higgs is the heavy or the light Higgs boson. Finally, the $H^\pm \rightarrow H^0W^\pm$ is examined for two heavier m_{H^0} mass

hypotheses, namely 200 and 300 GeV.

1.4.1 Neutral Higgs Decaying modes

Branching Ratios for light h^0 and H^0 are presented in Fig.1.8, in which the $\tau\tau$ channel seems to dominate in all 2HDMs types, both in low and high m_{h^0/H^\pm} regimes. As shown in the two plots on the top row, for low neutral Higgs masses, the bb channel is the dominant one for h^0 with $\tau\tau$ being the second most significant one, for various $\tan\beta$ values. Similarly, for the H^0 decay modes, in high $\tan\beta$ scenarios (bottom right plot in Fig.1.8), again the dominant and subdominant channels are bb and $\tau\tau$ respectively, while for lower $\tan\beta$ values, things get a bit more complicated with many channels having a significant branching ratio share. However, $H^0(h^0) \rightarrow \tau\tau$ channel allows searching for H^\pm through its decay to $H^0(h^0)W^\pm$, in the most extensive way compared to any other mode, since the bb channel is experimentally challenging, due to the large QCD multijet background; in which case a different and more complex approach would be needed to tackle this kind of significant background to extract signal.

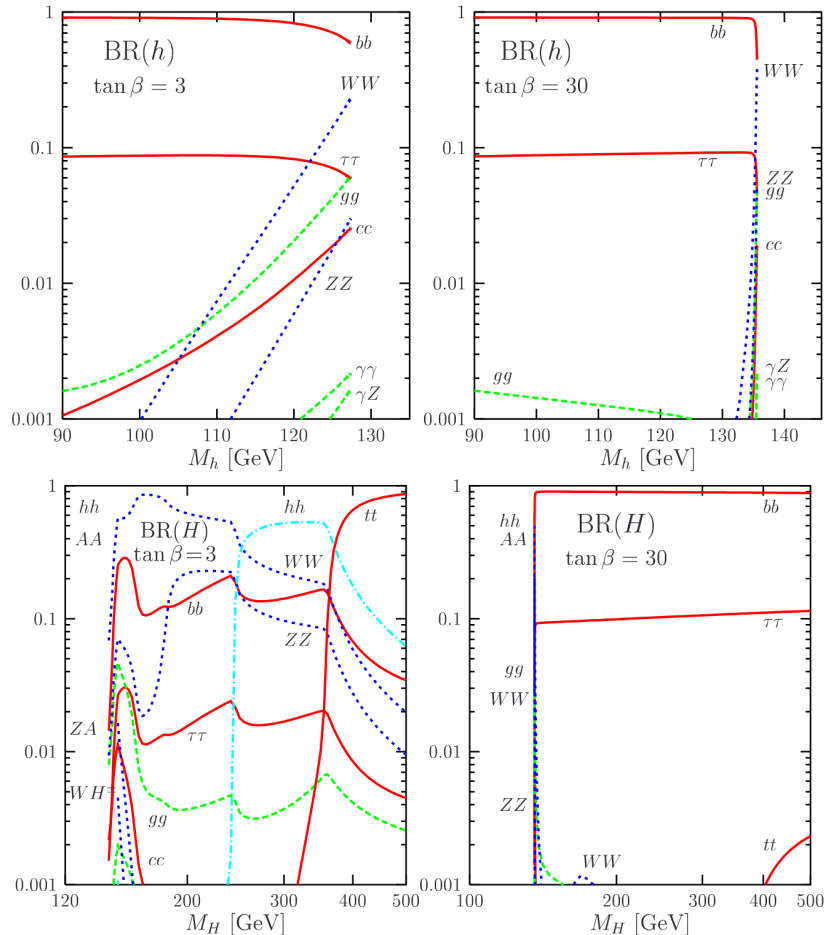


Figure 1.8: The decay branching ratios of the heavier (H^0) and lighter (h^0) CP-even MSSM h boson as a function of its mass for the two values $\tan\beta = 3$ (left) and $\tan\beta = 30$ (right) [16].

2 LHC and the CMS exmperiment

2.1 Large Hadron Collider

The Large Hadron Collider [17, 18] is the biggest and most powerful particle accelerator that has been ever build. It is located in Geneva, at the European Organization for Nuclear Research (CERN), 100 meters underground. In this 27 km circumference ring, particles get accelerated up to energies of 13 TeV center of mass and it is the most promising machine for revealing the most well-buried secrets of our universe, like what exactly is the Dark Matter and give an answer for whether extra dimensions exist or not.

The LHC is a circular accelerator system operating under ultra-high vacuum conditions. Within the system, two proton beams are guided by powerful magnetic fields and travel at speeds close the the speed of light. These beams are accelerated in opposite directions and they collide at four different interaction points along the collider. At the LHC, four major experiments (ATLAS, CMS, ALICE, and LHCb) exist, each having a distinct research focus and equipped with its own specialized detector, located at one of the four interaction points and designed to collect data relevant to their specific objectives.

But how is such tremendous acceleration achieved? At CERN, a complex system of accelerators is constructed to accomplish this and a schematic representation of it is shown in Fig.2.1.

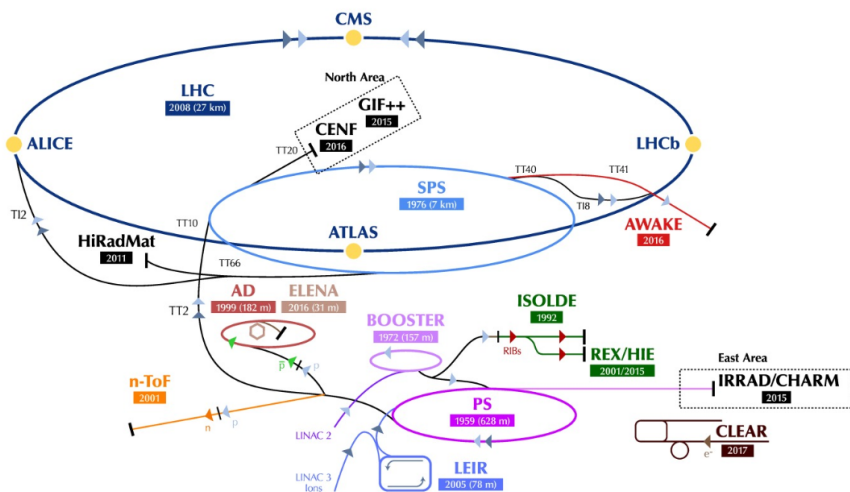


Figure 2.1: CERN Accelerator Complex.

The 2 proton beams, before reaching the LHC, follow a specific route through other, pre-acceleration systems. Their journey starts with hydrogen gas bottles, where their electron partners, forming the hydrogen atom, get extracted under the application of a strong electric field. The free protons are collected and guided into the LINAC2, a linear accelerator that

accelerates the protons up to energies of 50 MeV. After that, the protons are injected into the Proton Synchrotron Booster (PSB) and accelerated to an energy of 1.4 GeV. Then are moved to the next acceleration subsystem, the Proton Synchrotron (PS) which is the part where the protons get into bunches, gain energy up to 25 GeV and then pass to the last pre-acceleration subsystem of the accelerator complex, which is the Super Proton Synchrotron (SPS). The SPS is responsible for accelerating the protons to an energy of 450 GeV and injecting them into the LHC ring. Up to this point, protons travel for 4 minutes and 20 seconds. When in the LHC part, each proton gains extra energy of 485 keV per turn. Thus, a total time of 20 minutes is required for LHC to accelerate the protons to the desired energy of 6.5 TeV. At maximum speed, the revolution period, defined as the time it takes for a proton to complete one full orbit around the LHC ring, is approximately 89 microseconds.

To achieve the circular motion of the particles inside the LHC, a large number of superconducting magnets is needed. For the bending of the beams, 1232 dipole magnets are used so protons can keep their circular trajectory, and 392 quadrupole magnets are focusing and squeezing them right before they reach each of the interaction points. The magnets produce a magnetic field of 8.3 Tesla. To maintain superconductivity, the entire system is cooled to 1.9 K, using superfluid helium.

The proton beams consist of bunches which contain a specific number of protons. For the 2016 data-taking period, each beam consisted of 2208 bunches, whereas for the 2017 and 2018 data-taking periods, this number increased to 2556 bunches per beam. Each bunch contained approximately 2.8×10^{11} protons. The distance between successive bunches is known as bunch spacing and is set to 25 nanoseconds for collisions to occur at the designated interaction points and to balance the desired collision rates with the technical constraints of beam handling and detector performance.

Besides collision energy, luminosity is the most important parameter in a collider. The instantaneous luminosity can be expressed as follows:

$$\mathcal{L} = \gamma \frac{f_{rev} n_b N^2}{4\pi \beta^* \epsilon_n} R \quad (30)$$

where γ is the beam energy expressed in rest mass units, f_{rev} is the revolution frequency (11.2 kHz), n_b represents the total number of bunches inside the LHC, containing N protons each, β^* denotes the beam beta function at the collision point and represents the extend to which the beam is "squeezed". In other words, as this parameter decreases, the beam gets narrower. ϵ_n is the transverse normalized emittance and R is a geometrical correction factor for luminosity. The time integral of the instantaneous luminosity times the cross-section of an under study physical process gives the expected number of events per second for that specific process, generated by LHC pp collisions and is given by Eq.31.

$$N_{exp} = \sigma_{exp} \int \mathcal{L}(t) dt \quad (31)$$

2.2 The CMS detector

The Compact Muon Solenoid (CMS) [19] is one of the two large and general-purpose particle physics detectors that collect data from the collisions taking place inside LHC. It is a cylinder 21.6 m long with a diameter of 14.6 m and was built this way to maximize the detection and reconstruction of the particles emerging from the collisions that take place in the middle of the detector. The CMS detector design calls for an all-purpose detector that consists of concentric layers of sub-detectors, each optimized for measuring different particles and their properties.

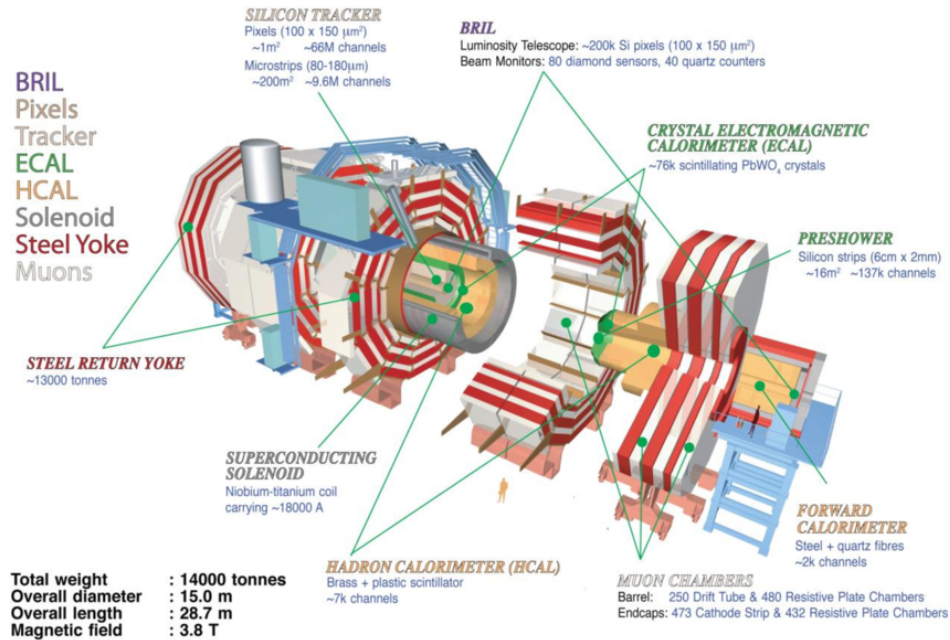


Figure 2.2: The CMS Detector.

The silicon tracker is the part of the detector that is closest to the interaction point. The tracker is the system that measures the momentum of the charged particles and is responsible for collecting the tracks from the traces they leave as they pass through the detector. The next layer after the tracker is the Electromagnetic Calorimeter (ECAL) which absorbs the incoming electrons and photons, measuring their energy with high precision. After that, the Hadronic Calorimeter (HCAL) is located. This part of the detector is responsible for absorbing and measuring the energy of the hadrons that are produced from the hadronization of the various quarks or gluons produced in the pp collisions. The silicon tracker, ECAL, and HCAL are enclosed inside a superconductive magnet which can generate a magnetic field of 4T, forcing all charged particles to bend, facilitating the measurement of their momentum. The last part of the detector components is the Muon system, which is a four-chamber sub-

detector where each station is separated from its neighbor ones by an iron "return yoke" plate. These plates are used to close the magnetic field lines. This sub-detector measures the muon momentum and produces its tracks. As a Minimum Ionizing Particle (MIP), a muon interacts weakly with matter, which facilitates its precise detection and energy measurement. In the CMS experiment, this characteristic is particularly advantageous, as the muon chambers, being the final sub-detector system, are optimized to accurately measure muons that have passed through all preceding detector layers. Neutrinos are the only SM particles that interact very weakly with matter and the detector is unable to stop them and measure their energy. However, since the energy in the transverse direction to the beam should be conserved, their energy can be estimated by calculating the vector sum of all visible energy in the detector's transverse plane and enforcing energy conservation.

The CMS detector was designed this way in order to maximize its capability to detect the Higgs golden channel, $H \rightarrow ZZ \rightarrow \mu\mu\mu\mu$. So a strong magnetic field is needed in order to bend as much as possible the μ tracks, thus a strong tracker. For the $H \rightarrow \gamma\gamma$ a good ECAL is needed as well. What was left of the budget was used to construct the HCAL, that's why is the worst sub-detector system.

2.2.1 Coordinate system of CMS

The CMS experiment uses a right-handed coordinate system by convention. As the origin of the system is selected to be the center of the detector, at the nominal collision point. The x-axis is pointing to the center of the LHC ring and the y-axis is perpendicular to the LHC plane, pointing up. Of course, the z-axis should be perpendicular to the other 2 and is selected to be along the anticlockwise beam direction, so the whole coordinate system will be consistent with the results of the cross product of any given pair of vectors. The ϕ (azimuthal) and θ (polar) angles are defined following the spherical coordinate system, meaning that the angle ϕ lies on the x-y plane and is measured from the positive x-axis with direction pointing to the positive y-axis. The polar angle θ is measured with respect to the positive z-axis.

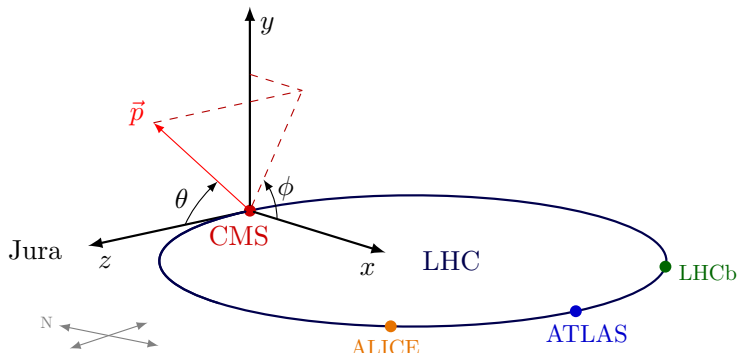


Figure 2.3: The CMS coordinate system.

A more convenient way to describe the angle between an outgoing particle and the z-axis instead of θ is the so-called "pseudorapidity", defined in Eq.33). That's because, in the relativistic limit, where the energy of the particle becomes much larger than its mass, this variable is approximately equal to the rapidity, defined in Eq.32), which remains the same under any Lorentz transformation.

$$y = \frac{1}{2} \ln \left(\frac{E + p_z}{E - p_z} \right) \quad (32)$$

$$\eta = -\ln \left[\tan \left(\frac{\theta}{2} \right) \right] \quad (33)$$

As shown in Eq.32, the E and p_z variables represent the energy and momentum of a given particle in the z-direction. The energy and momentum of the particle in the x-y plane are denoted with the symbols E_T and p_T , respectively. Lastly, a widespread and useful variable is the pseudo-solid angle ΔR , which represents the distance between 2 particles in the $\eta - \phi$ plane and is defined as:

$$\Delta R = \sqrt{(\Delta\eta)^2 + (\Delta\phi)^2} \quad (34)$$

2.2.2 Superconducting Magnet

One of the most crucial parts of the detector is the superconducting magnet [20] because the magnetic field that creates, necessary for precisely measuring the charged particles' properties. When a charged particle travels through a magnetic field, its trajectory bends based on the particle's momentum. The greater the momentum, the steeper the curve of the trajectory. The CMS magnet is a huge superconducting solenoid of 5.9 meters in diameter and 12.9 meters in length, operating at 4.5 Kelvin, and is built of NbTi with Cu sheathing. This magnet is designed to provide a magnetic field of up to 4 T. However, to increase its lifespan, it was decided to operate at 3.8 T.

2.2.3 Tracking system

The CMS tracking system is the innermost part of the CMS detector thus the closest part to the collision point. The tracking system is responsible for collecting all needed information for the track reconstruction of all particles passing through it. Due to the existence of the magnetic field (B), the momentum (p) of a charged particle with electric charge is possible to be measured using the radius of the track curvature (ρ) as presented in Eq.35.

$$pc = eB\rho \quad (35)$$

The Primary Vertex (PV) along with all additional interaction vertices of the scattering can be reconstructed by using the tracks of all charged particles in a given event. The tracking system is made of silicon, a semi-conducting material that favors the electron-positron pair production as charged particles pass through it, as a strong electric field is present inside the tracker due to the high voltage that is applied to the semiconducting material. The value of the electric field inside the silicon tracker can vary depending on the specific sensor configuration and operating conditions. Typically, in the CMS experiment, the bias voltage applied to the silicon sensors is around 100-600 V. Given that the thickness of the silicon sensors is usually in the range of 200-300 micrometers (μm), the resulting electric field can be estimated. Using an approximate bias voltage of 300 V and a thickness of 300 μm , the resulting electric field is approximately 1 MV/m. As a result, during the pass of a charged particle through the track system, several electron-positron pair productions take place which subsequently are collected by an electrical circuit for the track reconstruction to take place. The reason behind choosing this specific material is due to its unique property of suppressing the possibility of multiple scattering, Bremsstrahlung radiation, and other nuclear interactions to take place as the passing charged particle interacts with the sub-detector, maximizing the efficiency of track reconstruction.

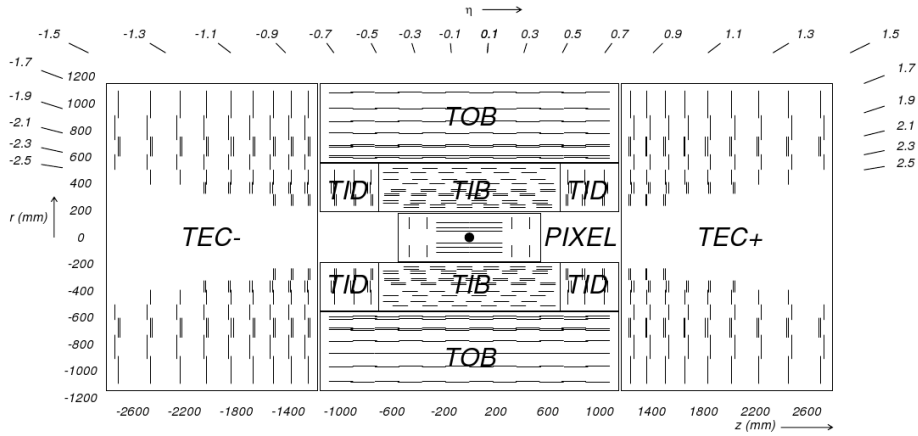


Figure 2.4: Schematic down view of the CMS tracking system.

In Fig.2.4 a down view of the CMS tracking system is presented. It covers a pseudo-rapidity range of $|\eta| < 2.5$ and is kept at low temperature conditions (-10°C) in order to protect it from the high radiation effects that is exposed to, expanding its lifespan. It consists of two subsystems, the "Silicon Pixel" and the "Silicon Strip".

2.2.3.1 Silicon Pixel

Silicon Pixel [22] is a sub-detector subsystem, characterized by high spatial resolution, allowing precise tracking of charged particles as they pass through the detector. It has 66

million pixels, with dimensions of $100 \times 150 \mu\text{m}^2$ and a total active surface of 1 square meter. This high resolution capability combined with its proximity to the interaction point makes it ideal for both track and PV-SV reconstruction. It has 3 impact points, at $r = 4.4, 7.3$, and 10.2 cm on its cylindrical part inside the barrel and another 2, disk-like, on each endcap at $|z| = 32.5$ and 46.5 cm), providing a coverage of $|\eta| < 2.5$.

2.2.3.2 Silicon Strip

Silicon Pixel is followed by Silicon Strip [23], the next subsystem of the Tracking System, whose main purpose is to define the trajectory of charged particles. Silicon Pixel is divided into four regions, two of which are inside the barrel. The central region hosts the Tracker Inner Barrel (TIB) and the forward regions host the inner discs of the system, the Tracker Inner Disks (TID). TIB consists of four cylindrical silicon layers covering the $25 \text{ cm} < r < 50 \text{ cm}$ region whereas TID consists of three disks, covering the region of $58 \text{ cm} < |z| < 124 \text{ cm}$. TIB and TID are enclosed inside the Tracker Outer Barrel (TOB), a 6 cylindrical silicon layers system covering the $50 \text{ cm} < r < 116 \text{ cm}$ region. Finally, two more parts of the Silicon Strip cover the regions defined by the beam direction, namely the Tracker Endcaps, TEC+, and TEC-), each of which consists of 9 discs, covering the $130 \text{ cm} < |z| < 270 \text{ cm}$. The first three discs have 7 rings, the subsequent 3 disks have 6 rings, while the following 2 disks have 5 rings and the last disk consists of 4 rings.

2.2.4 Electromagnetic Calorimeter, ECAL

The initial idea behind the design of the Electromagnetic Calorimeter (ECAL) [24] in CMS was the need for a powerful detector that would be able to "catch" and precisely measure the properties of the two photons from the neutral Higgs boson's decay. ECAL achieved its initial goal due to the very precise and careful work done during its construction. Having the entire tracking system enclosed to it, ECAL is an almost hermetic and homogeneous calorimeter, is approximately 25 radiation lengths deep, and is made of high density lead tungstate ($PbWO_4$) crystals, instrumented with photo-detectors. The selection of this material was mainly based on its high radiation tolerance, its fast scintillation, and its short radiation length. As a particle passes through, an electromagnetic shower is created, causing the emission of multiple photons that are subsequently gathered by photodiodes. Within 25 ns, is possible to collect up to 80% of the emitted photons. At the current LHC energy scales, the produced electrons are typically below the TeV range, meaning that only a small fraction of their electromagnetic shower penetrates into the HCAL. However, as LHC moves to higher energy collisions, ensuring that the shower is fully contained within the ECAL becomes challenging. If the shower is not fully contained, a significant portion of the energy could spill over into the HCAL, leading to non-negligible energy losses. Therefore, strategies must be developed to prevent the shower from penetrating through the entire ECAL and

entering the HCAL while minimizing energy leakage.

As an electron passes through a scintillator, it radiates photons through Bremsstrahlung, which subsequently interact with the detector's material through electron-positron pair production. These electrons and positrons radiate photons through Bremsstrahlung as well and so one, creating a particle shower inside the ECAL. The same effect appears as a photon enters the ECAL. The effect continues until all the energy of the initial particle is transformed into light, as it interacts with the scintillator and is absorbed by the photodiodes [25]. The ECAL energy resolution is measured to be :

$$\left(\frac{\sigma_E}{E}\right)^2 = \left(\frac{2.8\%}{\sqrt{E}}\right)^2 + \left(\frac{12.0\%}{E}\right)^2 + (0.3\%)^2 \quad (36)$$

The first term in Eq.36, is a stochastic one and is related to the fluctuations of the stored energy due to the high number of multiple interactions that simultaneously take place inside the detector. The second term is the uncertainty coming from the electronic background noise of the ECAL system and also from the pile-up events while the third term covers the detector's imperfections and non-perfect calibrations and misalignment. As an example, the energy of an electron of 100 GeV can be measured with a precision of $\simeq 0.4\%$.

Regarding electromagnetic showers, a simple interpretation is shown in Fig.2.5. Radiation length X_0 and Moliere radius R_M are the two main quantities that are used to define the development of a given electromagnetic shower. The first one is defined based on how far the shower has come inside the detector's material up to the point that most of the initial particle's energy is being absorbed and thus reduced by a factor of $1/e$. The Molière radius is defined as the characteristic distance over which a particle shower spreads laterally in the detector's material, containing approximately 95% of the shower's energy.

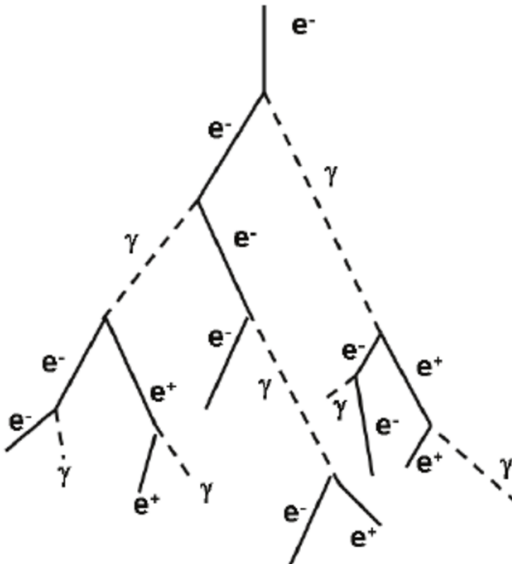


Figure 2.5: Electromagnetic Shower [26].

In Fig.2.6, a schematic outline of the ECAL is being shown. This sub-detector system is also split into two main parts, one in the barrel region (EB) and two identical parts, in each of the endcap regions (EE). The EB has a cylindrical shape and it covers a pseudorapidity range of $|\eta| < 1.48$. It consists of 61200 crystals of trapezoidal shape and dimensions of 0.0174×0.0174 in the $\eta - \phi$ plane. The selection of these dimensions was based on the expected Moliere radius value and regarding the length of the crystals, it was decided to be equal to 230 mm, which corresponds to $X_0 = 25.8$. On the other hand, the two EE are of a disc shape, having two "D" shaped parts combined and covering the $1.56 < |\eta| < 3.0$ region, placed at $z = 314$ cm. Each EE has 7324 crystals, with inner surface dimensions of 28.6 mm \times 28.6 mm and outer surface dimensions of 30 mm \times 30 mm per crystal. Furthermore, the value for the length of the crystals was chosen to be equal to 220 mm, which corresponds to $X_0 = 24.7$ radiation length.

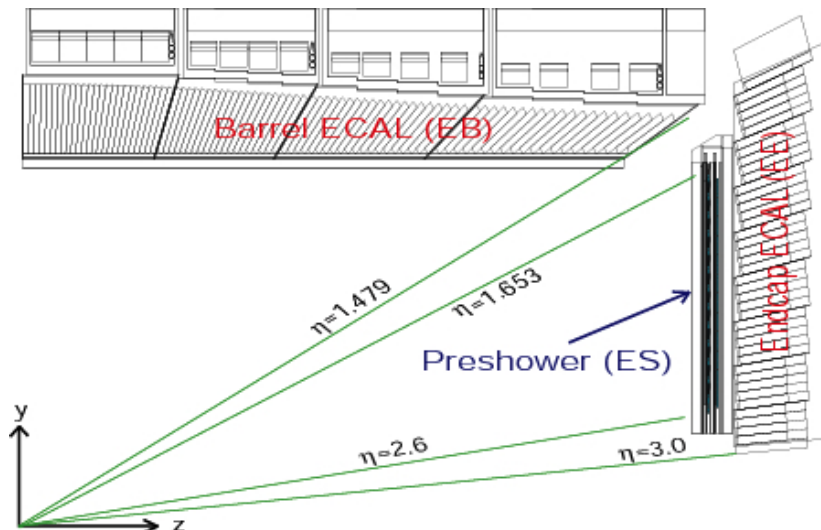


Figure 2.6: ECAL of CMS.

Finally, there is another part of the ECAL, placed right in front of the EE, covering the $1.65 < |\eta| < 2.6$ region, the so-called ECAL Preshower (ES). As its name suggests, is responsible for performing crucial measurements before the incoming particle interacts with the EE material and creates an electromagnetic shower. That is because of the poor resolution and capability of the ECAL endcaps, due to the way they were built and the size of the crystals that form them. The ES is to distinguish showers created by two or single photons reducing this way the $\pi^0 \rightarrow \gamma\gamma$ background to the $H^0 \rightarrow \gamma\gamma$ signal.

2.2.5 Hadronic Calorimeter, HCAL

The Hadronic Calorimeter (HCAL) of CMS encloses ECAL and all innermost parts of the detector in general. The HCAL is a sampling calorimeter and its main purpose is to measure the energy of hadrons produced during LHC collisions and of their decay products, through

their nuclear interactions with the HCAL's material. These interactions mainly lead to the creation of hadronic showers, analogous to the electromagnetic showers produced in the ECAL. Besides the energy measurement of an incoming particle, HCAL is also designed to record information of the particle's trajectory and time of entry into the calorimeter. For this, it was constructed by alternate layers of brass (an alloy of copper and zinc with high absorption rates) and a plastic scintillator, used as active material. As a hadron passes through the scintillator's layers and interacts with the material, it emits light which subsequently is absorbed by optical fibers, and then transmitted to the recording system where is amplified by photomultipliers, converting it to an electrical pulse that can then be analyzed. Thus, the initial energy of the hadron can be calculated after summing up all energies calculated by the various electrical pulses related to the hadronic shower that has been recorded.

The HCAL has 4 parts as shown in Fig.2.7, the HCAL Barrel, aka HB, the HCAL Endcap (HE), the HCAL Outer (HO), and the HCAL Forward (HF). The first two lie inside the solenoid while the other two are located outside of it, with the latter covering the forward region, up to $|\eta| = 5.19$.

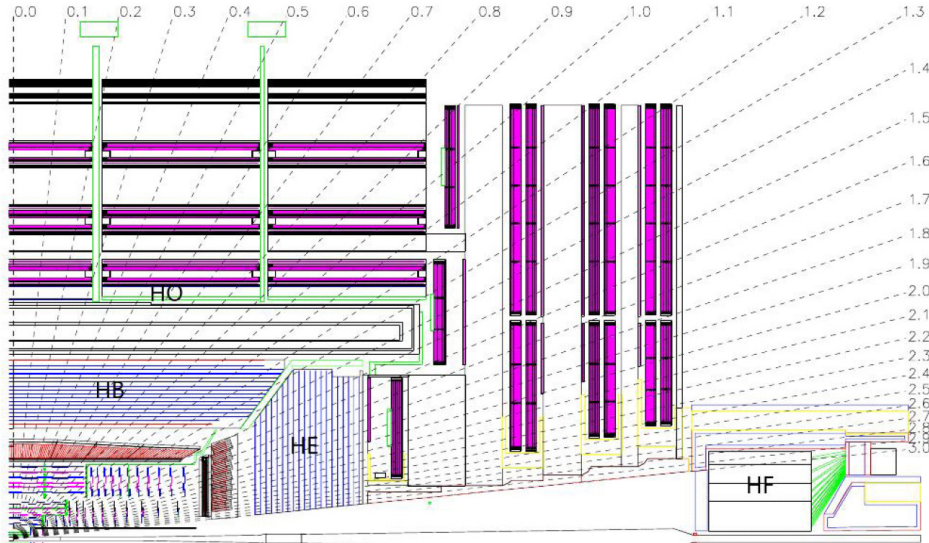


Figure 2.7: The CMS Hadron Calorimeter layout.

The HB is the part of HCAL that covers the barrel region of CMS, placed inside the superconducting magnet. The total number of plates used to create this sub-detector system is around 70000, each of which covers 0.087×0.087 in $\eta\phi$ space, covering cumulatively the region up to $|\eta| = 1.3$. Its inner and outer radius is 1.77 m and 2.88 m respectively, with an alternating thickness between different η regions, based on the corresponding radiation length, starting from $5.82\lambda_I$ for $\eta = 0$, increasing up to $10\lambda_I$ for $|\eta| = 1.3$. The other part of HCAL that lies inside the solenoid is the HE, which spans the region of $1.3 < |\eta| < 3.0$ and consists of 2 identical circular parts placed on the 2 Endcaps of the detector. Both the HE and HB are the last and outermost parts of CMS that are inside the solenoid and the superconducting magnet. Right after these parts, there is the HO, the third part of HCAL,

which surrounds the solenoid and its main purpose is to catch highly energetic particles that HB fails to do. The HF is placed at $|z| = \pm 11.2m$ from the interaction point to collect all outgoing particles that travel in small angles with respect to the initial beam direction. Being placed outside the Endcaps, it covers the $3.0 < |\eta| < 5.2$ region, where a large number of particles is expected. These particles are detected based on the Cherenkov radiation they emit as they traverse the HF material, which is also used to provide luminosity information. Due to the exposure of this sub-detector system to high numbers of particles, highly resistant materials were chosen to be used for its construction. For that, steel was chosen to be used as the absorber, and quartz fibers as active material, both having high durability to radiation exposure.

The HCAL energy resolution is computed via the parametric equation 37. The first term is stochastic and is related to the unevenness of the HCAL, while the second term is related to the background noise, possible miscalibration, and imperfections of this sub-detector system. A constant term is also taken into account but it turned out to be negligible with respect to the other two. The values of these parameters were measured using pion test beams, separately for barrel (HB) [27] and endcap regions (HE) [28]. For HB, using pions in an energy range of 20-300 GeV, the parameters were found to be $S = 115\%$ for the stochastic term and $N = 5.5\%$ for the noise term. Regarding the HE measurements, pions with energies between 5-300 GeV, the stochastic and noise related parameters were measured to be 106% and 4.0% respectively. Finally, it is also worth noting that hadronic showers' properties are described mainly by the quantity λ_I , the radiation length, in a similar way as X_0 is for electromagnetic showers. The Stochastic term of the HCAL is so poor in respect to the ECAL, because of the many different competing ways in the development of hadronic showers. The complexity of hadronic and nuclear processes produces a multitude of effects that determine the functioning and performance of the HCAL.

$$\left(\frac{\sigma_E}{E}\right)^2 = \left(\frac{S}{\sqrt{E/GeV}}\right)^2 \oplus (N)^2 \quad (37)$$

2.2.6 Muon System

Muon is the most important particle for CMS, as the detector acronym indicates. Muons are detected mostly through ionization and their identification can be used as a very powerful tool for signal extraction of interesting processes against background processes. It passes through most of the sub-detector systems without depositing almost any fraction of its initial energy. The CMS Muon System [29] is placed outside the solenoid, is the outmost part of the CMS detector and it consists of three subsystems. Most of the outgoing particles coming from the interaction point have already been detected and absorbed by the innermost

detector's layers but muon and neutrinos. The first are being collected by this sub-detector system while the latter are expected to leave the whole CMS without interacting with any of the CMS' layers. This is done so all particles emerging from the interaction to be absorbed in the earlier stages of the detectors and the muons which interact only weakly with matter to reach the detector.

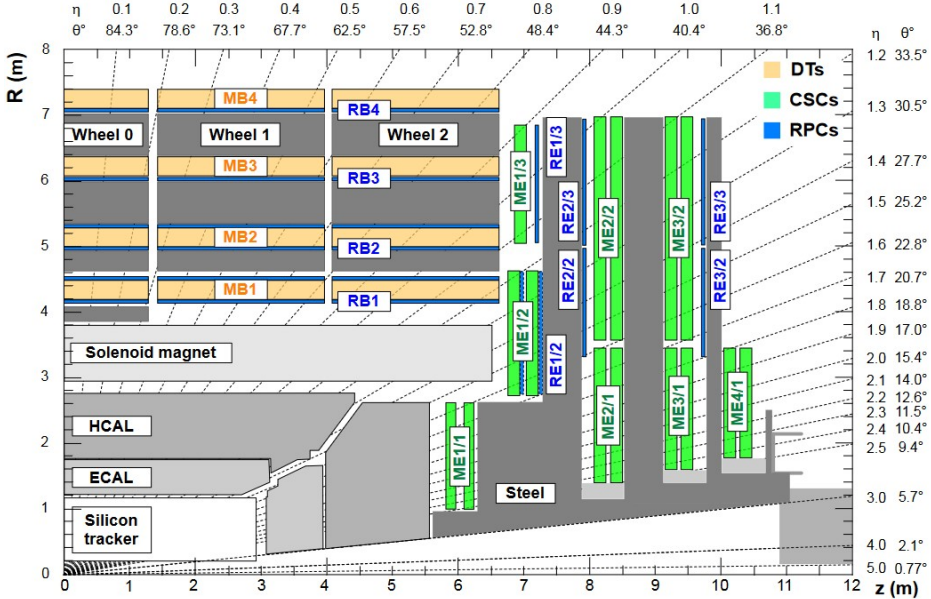


Figure 2.8: An $R - z$ cross-section of a quadrant of the CMS detector with the axis parallel to the beam (z) running horizontally and radius (R) increasing upward. The interaction point is at the lower left corner. The locations of the various muon stations and the steel disks (dark grey areas) are shown. The 4 drift tube (DT, in light orange) stations are labeled MB (“muon barrel”) and the cathode strip chambers (CSC, in green) are labeled ME (“muon endcap”). Resistive plate chambers (RPC, in blue) are in the barrel and the endcaps of CMS, labeled RB and RE, respectively. Figure and caption from [29].

The part of the Muon System in the barrel region is called Drift Tube (DT) and it consists of solenoid-like drift tubes, split into 4 regions, each of which has 250 tubes. The DT covers the $|\eta| < 1.2$ region while the part in the Endcap region is called Cathode Strip Chambers (CSC). Muon rates and background levels are higher with respect to the barrel and the magnetic field is strong and non-uniform. The CSC have fast response time and high radiation durability, thus can be finely segmented and can tolerate the non-uniformity of the magnetic field. Covering the $0.9 < |\eta| < 2.4$ region, there are 4 stations of chambers in each endcap, each of which consists of 6 layers, making feasible a precise measurement of muons' position in the $r\phi$ bending plane. Both CSC and DT are accompanied by the third part of the Muon System, the Resistive Plate Chambers (RPC) which cover the $|\eta| < 1.6$ region. RPC is being used mainly for triggering purposes since it has a fast timing response and exhibits time resolution of the order of nanoseconds.

All information needed for the muon identification and reconstruction is being obtained mostly from the Muon System but also from inner CMS layers and sub-detector systems and especially from the tracking system. That's because some low energetic muons interact

with the tracking system, the first sub-detector system that they face as they move away from the interaction point, resulting in significant energy losses and depositions before they even reach the Muon chambers. Nonetheless, in a 2010 study, the muon system performance for detecting and accurately reconstructing low p_T muons, of a few GeV, was found to reach 95%.

2.2.7 Trigger System

Considering that every 25 ns a bunch-crossing is taking place at the center of CMS, the detector produces a massive number of data at a rate of 40 MHz. By combining this with the fact that the expected number of proton-proton scatterings is around 40 per bunch crossing, the expected luminosity could reach the value of $10^{34} \text{cm}^{-2} \text{s}^{-1}$. Additionally, the detector has to contend with pileup, where several p-p interactions occur in the same bunch crossing, which significantly increases the complexity of event reconstruction and analysis. This leads to an extremely large number of data that the implemented Data Acquisition System (DAQ) is unable to handle in terms of both memory and effective processing. Besides that, the majority of these data are coming from physical processes that have been well studied in the past and they do not have any research interest. The above considerations led to the implementation of a trigger system that is responsible for exclusively selecting events of potential physics interest and at the same time keeping the output rate and CPU time under control.

The CMS uses a 2 stage trigger system, the Level 1 trigger (L1), and the High Level Trigger, HLT. The Level 1 trigger is a hardware system that drops the initial rate from 40 MHz to 100 kHz, reconstructing L1 objects using simple and fast algorithms, combining information from both calorimeters and muon systems. If the event at this point doesn't show any promising features, is thrown away. Otherwise, it is transferred to the HLT and is examined in more detail. This second stage of the trigger is a software system where the CMS offline reconstruction is run and more sophisticated selection algorithms are applied in order to determine whether a specific event has interesting features to offer. At this point, all the detected information from all sub-detectors is gathered and a more strict selection is taking place. The HLT provides a further rate reduction from 100 kHz to 1 kHz, a manageable amount of data that can be easily stored for a full offline reconstruction and further analysis.

3 Particle Reconstruction and Identification

Particle detection and identification is essential for performing physics analysis of pp collisions in CMS detector. Outgoing particles pass through the various sub-detector systems and deposit their energy in them, leaving also tracks in the tracking, if they are charged. Data collected from the CMS detector is a mixture of tracks and energy deposits, information that is crucial for particle reconstruction. For this purpose, precise and sophisticated object reconstruction methods and techniques have been developed, combining information from various parts of the detector, in most cases.

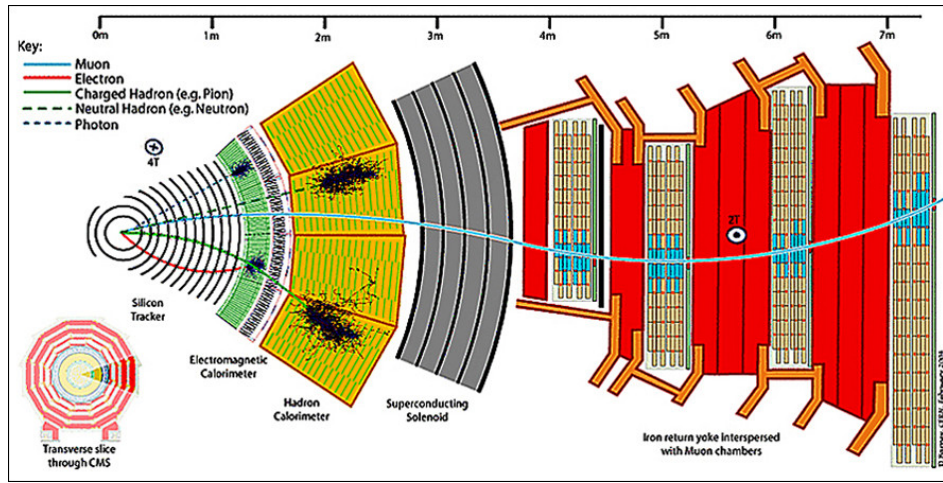


Figure 3.1: Cross section of the CMS detector.

Figure 3.1 shows how various types of particles interact with each subsystem of CMS. Charged particles leave hits into the tracking system and the tracking information is used to define their electric charge and to quantify their momentum. Electrons and photons are stopped at ECAL, depositing most of their energy into it, while both charged and neutral hadrons deposit their energy in HCAL. Muons are collected by the muon chambers, but they leave traces and some fraction of their initial energy behind them, as they move through the tracker and the calorimeters. Finally, neutrinos are the only outgoing particles that pass through the entire CMS detector without interacting with any of its sub-detectors and eventually escape. However, their energy can be measured indirectly, through the momentum imbalance in the transverse plane that is present when such particles are created by pp collisions.

Physics objects, like leptons and jets discussed later on, are reconstructed by gathering and merging the signals from particles detected in different areas of the detector. Initially, electronic signals in digitized form are collected from the sub-detectors to create reconstructed hits (RecHits), containing information about position, energy, and deposition time. These RecHits from various sub-detectors are then combined to form reconstructed tracks and primary vertices. Additionally, RecHits from the ECAL and HCAL are paired and summed

over to produce calorimeter towers known as CaloTowers. Muon RecHits obtained from the muon system are used to generate standalone muons. Finally, information from individual sub-detectors for each event is combined, using a comprehensive approach called Particle-Flow (PF) reconstruction algorithm.

3.1 The Particle Flow Algorithm

The Particle Flow (PF) Algorithm [30, 31], collects and combines all information needed for event reconstruction and particle identification from all sub-detector systems. The main collections of information are the reconstructed detector signals, the magnitude of the energy deposits in the calorimeters, and hits collected by the Muon System. The procedure employed by this algorithm can be decomposed into three main steps, namely the "Kalman filter" method, the "Calorimeter clustering" and finally the "linking algorithm". In the first step, particle trajectories are defined. Subsequently, during the "Calorimeter clustering", energy deposits are measured and categorized, allowing for discrimination between the energy depositions of neutral and charged particles. At this stage, electrons and corresponding Bremsstrahlung photons are also being reconstructed and identified. Finally, during the third and last stage of the PF algorithm, the so-called "linking algorithm", the various reconstructed trajectories are linked to the energy clusters formed from calorimeter information and to the potential muon candidates.

The various types of objects are reconstructed in a sequence that takes into account the geometry of the detector and the position each subsystem is placed. Initially, electrons and muons are reconstructed by combining the information from the track finder and the corresponding detector system, ECAL or Muon system respectively. Subsequently, charged and neutral hadrons are reconstructed, by pairing all the remaining identified trajectories in the tracker with all the collected HCAL information. Finally, all deposited energy in the ECAL that did not match with any trajectory, is used to define the photon candidates. Next, the list of all particle candidates, namely electrons, muons, hadrons, and photons, along with the related information, is passed to higher level algorithms in order to become a set of fully reconstructed and identified particles.

3.2 Tracks and Vertices reconstruction

The Primary Vertex (PV) of an event, is defined as the interaction point associated with the hardest scattering in each bunch crossing. Defining this PV with high precision can be quite challenging though, due to the presence of a large number of additional interactions that take place during the same bunch crossing. For example, in the 2016 LHC run, the mean value of such additional interactions was 27 per bunch crossing. All particles coming from any other

Vertex but the Primary one, are considered not to be interesting and all together compose the so-called Pile-up. The fact that each of these particles emerging from the additional interactions results in causing hits in the tracking system or energy deposits in the calorimeter makes the accurate reconstruction of each particle a difficult task.

During the trajectory reconstruction of a given particle, initially, various hits detected in the tracker are grouped and a preliminary version of the trajectory is reconstructed by the Combinatorial Track Finder (CTF). Rather than creating preliminary versions of all trajectories simultaneously, CTF starts from the cleanest and easiest to-form trajectory candidate and after each iteration, all remaining hits are used to define the next primary trajectory. This procedure is illustrated in Fig.3.2 and works as follows. First, 2-3 randomly selected hits from the tracker's inner layers are selected in order to be used as seeds for the algorithm. These hits are combined to form the "tracklet", the preliminary version of the trajectory. In the next step, this tracklet is expanded, seeking to add more hits that follow this trend in order to be added to it. If at least one additional hit is found, then this tracklet is temporarily labeled as a trajectory candidate with an open window for additional modifications and corrections at a later stage. At this point, Kalman filter [32] comes into play, a technique which essentially scans layer by layer the whole tracking system, in order to track down all hits that might be related to the trajectory candidate. After each update of the candidate, all parameters related to the trajectory are also updated until the latest version of the trajectory is established. Before moving forward and labeling this candidate as a real trajectory, it has to pass some quality tests based on the purity of each individual hit that is composed of, along with some preselection criteria, like transverse momentum above a threshold value and impact parameter cuts. The impact parameter refers to the shortest distance between the particle's trajectory and the collision point, helping to identify whether the particle originated from the primary vertex or a secondary decay. If all criteria are satisfied, the trajectory is marked as "real" and is added to the collection for later use, while all hits used to define it are excluded from the reconstruction process for the next trajectories. The same procedure goes on until the algorithm can not find any more additional suitable hits to use for a new tracklet. This algorithm provides fast trajectory reconstruction and also ranks all real trajectories based on their hits purity. The association of a trajectory to a given reconstructed particle is used to define the particle's position and momentum in the detector.

The reconstruction of the PV uses all information collected from the tracker and is divided into three main steps. At first, the algorithm attempts to cluster all real trajectories that seem to originate from a common vertex, through some preselection criteria. These clusters are then analyzed to determine the location of the PV, which serves as the reference point for further reconstruction steps. Subsequently, the Deterministic Annealing (DA) [33] algorithm is used to provide more information about the real trajectories that are not matched to the PV and groups them based on the Pile-up vertex they seem to originate from. After the comple-

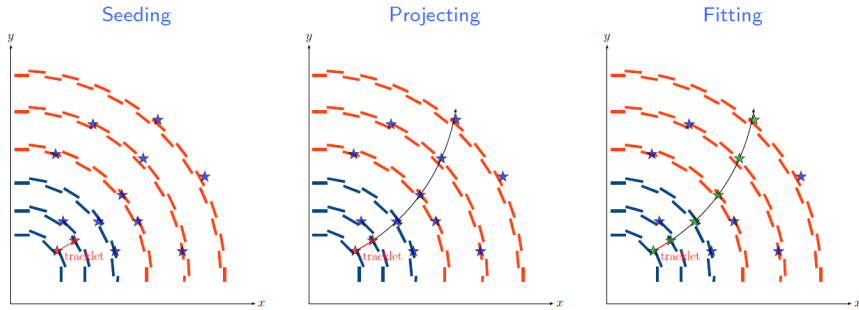


Figure 3.2: Reconstruction of a particle's trajectory.

tion of these 2 steps, there is just one last step left for the process to be complete, namely the translation of each found vertex to the CMS coordinate system, using the "Adaptive Vertex Fitter" (AVF) [34]. This algorithm uses all the trajectories that are associated with a given vertex and ranks them based on criteria such as their transverse momentum, impact parameter, and the quality of the track fit. Starting with the highest-ranked trajectory, precisely defines the vertex's position in space, performing adjustments and corrections as it uses more and more trajectories. For each vertex definition, at least two trajectories are needed and after determining all of them, the AVF creates the final list of all reconstructed vertices and the one with the highest transverse momentum (p_T) sum of the associated trajectories, is labeled as the Primary Vertex.

3.3 Electron Reconstruction

The electron reconstruction combines the information from the track finder and the ECAL sub-detectors. Ideally, an electromagnetic shower created by an electron deposits its energy to a narrow cone of neighboring ECAL crystals. However, the ECAL is positioned after the tracker, where electrons interact with the material, losing energy due to Bremsstrahlung radiation. This radiation results in photons being emitted, causing the electrons to enter the ECAL with less energy compared to their initial one. Additionally, these electrons become more susceptible to the strong magnetic field, which gradually increases the curvature of their trajectory. As a consequence, the electromagnetic shower spreads over a wider range of crystals along the φ -direction, making electron reconstruction more challenging.

The first version of a reconstructed electron is based on the hits that it leaves in the ECAL, where collective information from multiple crystals is clustered to give a first estimate of the electron's energy [36]. The clustering algorithm in the barrel and the endcap differs a bit but both use the $\eta-\varphi$ plane and E_T definitions with respect to the CMS center. For the barrel, the hybrid algorithm does the job, starting with a seed crystal, which contains most of the energy in a region of interest. Subsequently, arrays of 5x1 crystals in the $\eta-\varphi$ plane around the seed are added as long as they pass a certain predetermined minimum E_T threshold. Then, neighboring crystal arrays are grouped into clusters, each of which is required to have

a seed array with E_T greater than a given threshold in order to be included in the final global cluster, called supercluster (SC). On the contrary, for the endcap region, the "multi-5x5" algorithm is used to create the corresponding SC. In this case, the seed is selected based on the maximum energy deposited in a region of interest, compared to its four direct neighbors. Then, additional energy depositions are collected in clusters of 5x5 crystals, that can partly overlap, as long as they pass again a given E_T threshold. The effective resolution for electron reconstruction can be further improved by taking into account tracker information, as can be seen in Fig.3.3.

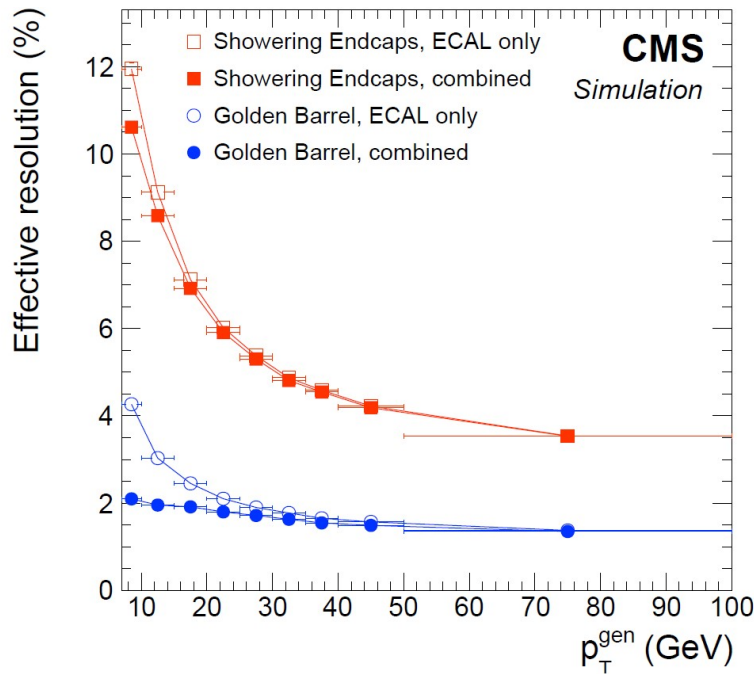


Figure 3.3: Effective electron resolution as a function of electron's momentum in the transverse plane, comparing ECAL only with combined ECAL-tracker information [36].

The second part of the electron reconstruction takes into consideration the electron hits in the tracker. These tracks are collected by a combinatorial Kalman Filter algorithm and then a Gaussian Sum Filter (GSF) [35] algorithm is used to fit them, taking into consideration the Gaussian energy fluctuations due to the emitted Bremsstrahlung photons in the tracker. Based on the volume of the emitted Bremsstrahlung radiation, electrons are categorized into three categories, "Golden", "Big-Brem" and "Showering" electrons, with little, large in a single step and large radiation all along the electron's trajectory, respectively.

3.4 Muon Reconstruction

Like electrons, muon reconstruction combines information from two sub-detector systems, the tracker and the muon system of CMS. The main reconstruction techniques are the "StandAlone Reconstruction", the "Global Reconstruction" and the "Tracker Muon Reconstruction" [37].

For the "StandAlone Reconstruction" technique, the "Kalman Filter" algorithm is used to create a preliminary version of the muon tracklet, using all hits detected in all layers of the muon system. Once the trajectory is successfully reconstructed, it is extrapolated to the center of the CMS. It is expected to match the PV within some acceptable distance, based on the uncertainty in the track's position and the PV location. "Global Reconstruction" on the other hand, can be seen as an extension of the "StandAlone" technique, meaning that it takes the muon tracklet and tries to match it with a tracker track within some uncertainty, typically on the order of a few hundred micrometers. At first, it tries to map the tracklet to the hits in the tracker and then establishes a "global" version of the track, an improved version of the preliminary one, taking into consideration all hits in both subsystems. Last but not least, the "Tracker Muon Reconstruction" technique does the job the other way around. Initially, takes the information from the tracking system of CMS, creates the tracklet from the corresponding hits, and then tries to map it to any hits in the muon system that follow its extrapolation. At the same time, any energy deposition in the calorimeters found all along the tracklet's way between the two systems, is also taken into consideration. Thus, this technique combines not only track information but also information related to any interactions the muon has with the material, such as multiple Coulomb scattering, and how they affect its trajectory as it travels through the various CMS layers.

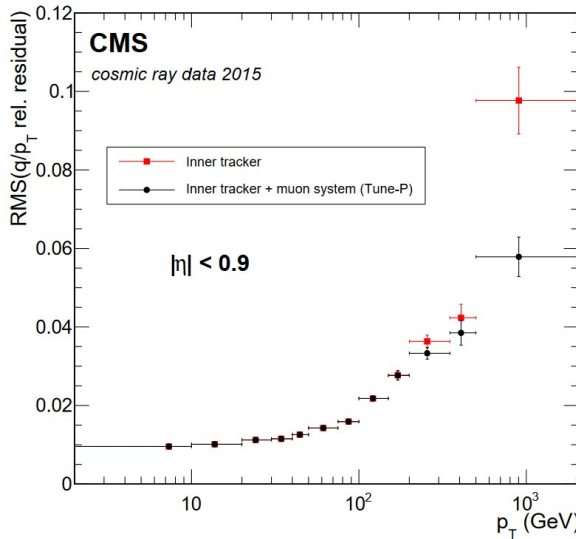


Figure 3.4: Muon transverse momentum resolution for tracker compared to its combination with muon system information [37].

The "Stand-Alone" technique performs best for muons with high transverse momentum values $p_T > 100$ GeV. The "Global Reconstruction" is more effective for medium momentum values ($p_T > 20$ GeV), while the "Tracker Muon Reconstruction" is more suitable for muons with a lower momentum ($p_T > 5$ GeV), as fewer such muons will essentially reach the muon chambers. However, the combination of the 3 techniques has the potential to successfully reconstruct muon with efficiency up to 99%.

3.5 Photon Reconstruction

After having electrons reconstructed and identified, photon reconstruction can be quite straightforward. Due to their zero electric charge, the magnetic field does not have any effect on their trajectory and combined with the fact that photons do not interact with the tracker's material at all, all information related to them is found in the ECAL. Thus, any detected energy deposition in the ECAL that was not associated with any trajectory is expected to come from the electromagnetic shower initiated by a photon as it interacts with the subdetector's material. A particular challenge in photon reconstruction arises when a photon converts into an electron-positron pair before it reaches the first layers of the tracker. In such cases, the electron and positron, having opposite electric charges, follow trajectories with opposite curvatures. This can result in a small ΔR separation (in the $\eta\text{-}\varphi$ space) between the two particles. To address this issue, the reconstruction algorithm carefully identifies and handles photon conversions. These conversions are detected and processed to ensure accurate reconstruction of the original photon. Photons in CMS are also reconstructed from the SC in ECAL [38], similar to electrons. In general, the photon shower is wider than the one created by electrons.

3.6 Jet Reconstruction

In most physics analysis in CMS, as in this one, the presence of quarks in the final state is expected. Therefore, the development of reconstruction algorithms is essential. Quarks, due to their color charge, interact with other color charged carriers through strong interactions and they obey to the color confinement rule. This rule dictates that they cannot exist free but must always be confined in colorless bound states, also known as hadrons. The rapid process in which outgoing quarks transform into hadrons is known as hadronization. As a quark travels in space and time, its interactions with matter generate a number of unstable hadrons, spread in a small area in $\eta\text{-}\varphi$ space. This high concentration of hadrons in a small area of the HCAL is called a jet. Thus, rather than reconstructing individual hadrons, algorithms are implemented to reconstruct these jets.

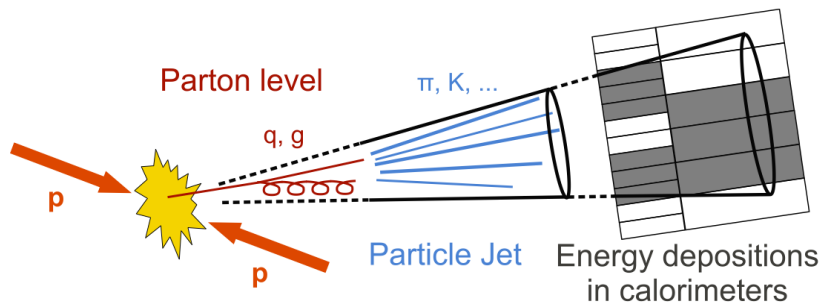


Figure 3.5: A toy-model for a jet formation in CMS.

There are two main jet reconstruction algorithms developed and used in high energy physics. The "Cone Algorithms", which offer high speed as an advantage but can be inefficient in jet reconstruction when a parton splits into two very closely in space particles or due to extensive radiation of high energetic particles. The second category, "Sequential Clustering Algorithms", are slower than the Cone Algorithms but they efficiently deal with the scenarios where Cone Algorithms fail.

3.6.1 Cone Algorithms

Cone algorithms are based on a specific sequence of steps that are repeated until all jets in an event are reconstructed and identified. The maximum radius R of the cone that a jet is spread along with the minimum energy in the transverse plane, $E_{T,min}^{seed}$, are defined to serve as threshold values given as preselections in order for such a cone to make it into the jet candidates set. For a given particle to be considered as part of a jet, the $\Delta R = \sqrt{(\Delta\eta)^2 + (\Delta\phi)^2} \leq R$ requirement should be satisfied, where ΔR stands for the distance in η - ϕ space between particle's trajectory and the axis of the evolving jet formation.

As a first step, all objects of a given jet candidate are sorted based on E_T . Afterward, a first version of the jet cone is reconstructed around the highest E_T object, of a radius R . Subsequently, a preliminary version of the jet, called "proto-jet", is formed which is reshaped and its properties are readjusted as additional objects are added to it. Next, the center axis of the proto-jet is readjusted, by weighting each object based on its E_T . In case the center axis of the proto-jet coincides with the one of the first version of the jet cone, within uncertainty, then the jet enters into the list of "confirmed" jets and all objects assigned to it are removed from the collection to prevent their reuse in reconstructing other jets. Alternatively, the sequence is repeated, using the proto-jet as the first version of the jet cone. Finally, if no additional objects are added with $E_T > E_{T,min}^{seed}$ and the two axes do not align, the procedure stops and the reconstruction of this specific jet is terminated.

3.6.2 Sequential Clustering Algorithms

Regarding Sequential Clustering Algorithms, as in Cone Algorithms, there is a sequence of repeated steps that the algorithm follows, with quantity d_{ij} (Eq.38) playing the leading role.

$$d_{ij} = \min(p_{T,i}^\alpha, p_{T,j}^\alpha) \frac{\Delta R_{i,j}^2}{R^2} \quad (38)$$

In Eq.38, " α " is a constant and can take 3 possible values, based on which algorithm someone chooses to use. For the k_T algorithm, " α " takes the value of 2, 0 for the Cambridge/Aachen (CA) algorithm and -2 for the anti- k_T algorithm. For this analysis, the latest

value is chosen to be used because of its better performance on jet reconstruction around the most important particles based on their purity and energy calculation, leading to the creation of a more cone-shaped jet of a circular base, compared to the other two algorithms.

Initially, all PF reconstructed particles are passed into the algorithm and then a random particle, i , is selected. The d_{ij} distance is calculated between particle i and all other PF particles individually. Starting from the $i - j$ pair with the d_{ij}^{min} , the algorithm checks if the $d_{ij} < p_{T,i}^2$ condition is satisfied. If satisfied, the two objects are merged into a single object called pseudo-jet, which is then used as the new object i , in order to calculate the new d_{ij} values, for all remaining j particles. If the condition is not satisfied, the sequence is repeated for all remaining j particles. When there are no more available j particles, the pseudo-jet gets into the list of jets, if some preselection requirements are satisfied and the procedure continues with all remaining particles. The whole procedure is repeated until all possible jets are reconstructed.

Once the list of all reconstructed jets is compiled, the next step involves calculating the four-vectors of these jets, which are crucial for physics analysis. This calculation is more complex than simply summing the four-vectors of the individual partons that make up the jet. The challenge arises because the detector has imperfections, non-uniformities, background electronic noise, and a high number of pile-up events, which can all affect the accuracy of the jet energy measurement. To address these issues, a set of four correction factors is applied to adjust the measured energy of the jets in the calorimeters [40]. These correction factors account for the various inefficiencies and improve the precision of the jet energy calculation.

3.7 B-tagging jets

Jets created by b quarks can be useful in many physics analyses in CMS. For this specific analysis, at least 1 b quark is expected in all examined final states, thus, the use of efficient b-tagging algorithms is important. What is so special about b-jets though? B-jets are formed by decays of b-hadrons which are originated in the hadronization of b-quarks. The long lifetime of b-hadrons can turn into a powerful tool for signal separation from background events and that is why a lot of effort has been made to construct highly efficient b-tagging algorithms.

The b-hadrons are unique because they have lifetimes long enough that they typically travel several millimeters from the PV before decaying. When these heavy hadrons decay, they produce a set of charged particles that form a b-jet, a distinct type of jet that originates from a location spatially separated from the PV. The point at which these decay products emerge is identified as a Secondary Vertex (SV). Inside a b-jet, there is a significant probability ($\sim 40\%$) for a low-energy electron or muon to be present. This can introduce challenges in accurately reconstructing the trajectories of the various objects within the jet. B-jets can

be identified by the presence of low-energy leptons within the jet, the existence of an SV due to b-hadron decays, and the high impact parameter values associated with the trajectories within the jet. B-tagging algorithms take as input the list of all reconstructed jets and they return a value between 0 and 1, known as the b-discriminator value, which embodies the corresponding probability of a given jet to be indeed a b-jet.

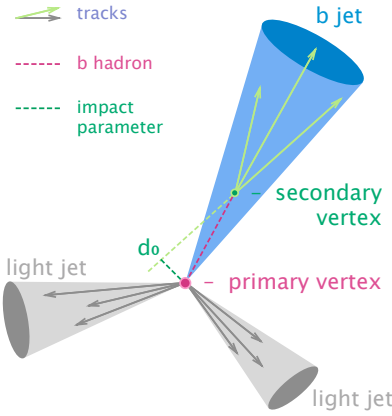


Figure 3.6: Schematic description for a b-hadron decay resulting to the formation of a b-jet, while additional jets directly emerge from the PV.

For this analysis, the b-tagging algorithm used is the DeepJet algorithm [41]. This algorithm is a Deep Neural Network (DNN) based-algorithm that takes as inputs various features related to information on the global variables of the jet and the event, on the charged and neutral PF candidates, and on the SVs. This algorithm falls into the multi-classifier category, meaning that it categorizes all input jets into six categories, three of which are related to b-flavor jets, and three more for jets originating either from charm, light quarks, or gluons. The three b-flavour categories refer to the scenarios where either the jet contains two b-hadrons, leptonically decaying b-hadrons, or hadronically decaying b-hadrons. Based on the specifics of a given analysis, one of the loose, medium, or tight working points (WP) is chosen to be used for b-tagging, having a light jet to b-jet misidentified efficiency of 10%, 1.0% and 0.1% respectively. For the needs of this analysis, the DeepJet medium WP is chosen as the most suited one to be used.

3.8 τ -jet reconstruction

In contrast to electrons and muons, τ -leptons are very unstable particles with very small life-time and a high probability to decay hadronically (~65%). If a τ -lepton decays hadronically, it forms τ -jet and because of its large branching fraction, various τ -jet reconstruction algorithms have been developed through the years in order to correctly identify and distinguish them from jets originating from ordinary quarks emerging in QCD processes. There are several properties of such jets that can be used to identify them, such as their relatively small radius R compared to normal jets. Additionally, its decay modes are very specific because

usually, it decays into 1 or 3 (or even 5 in some cases) charged kaons or pions, accompanied by a small number of neutral pions, resulting in a narrow jet constituted by a small number of tracks. The corresponding particles deposit their energies either in HCAL, for charged hadrons, or ECAL for neutral pions which subsequently decay into a pair of photons with 99% probability, without leaving any trace in the tracker.

The algorithm used for τ -jet (τ_h) identification in this analysis is the DeepTau [42], a τ_h identification algorithm that uses a deep neural network structure, with both particle-level and High-level inputs. The architecture of this algorithm is based on three main axes. It is a multiclass algorithm that was designed to simultaneously reject electrons, muons, quarks and gluon jets that are erroneously reconstructed as τ_h candidates, improving identification performance and reducing maintenance efforts in respect to older algorithms. The second axis is the usage of lower-level information than the MVA discriminators used previously. This also improves performance due to the incapability of the old MVA discriminators to perfectly describe jet hadronization and fragmentation which usually follow quite complex patterns, using higher-level information and limited statistics. A machine-learning algorithm, which uses a sufficiently large data set for the training and can exploit lower-level information, is expected to result in performance improvements. Last but not least, this DeepTau algorithm takes advantage of the "Domain knowledge". This means that higher-level input variables used as inputs in the previous MVA discriminators are also being used as additional information in order to reduce the number of training events needed and improve the convergence of the training, even though the same performance can be achieved without them.

The target τ_h identification efficiencies for the various DeepTau working points are shown in Table 3.1. These efficiencies are defined as the efficiency for genuine τ_h to be reconstructed as τ_h candidates for $p_T^{\tau_h} \in [30, 70]$ GeV and to pass the given discriminator.

	VVTight	VTight	Tight	Medium	Loose	VLoose	VVLoose	VVVLoose
D_e	60%	70%	80%	90%	95%	98%	99%	99.5%
D_μ	—	—	99.5%	99.8%	99.9%	99.95%	—	—
D_{jet}	40%	50%	60%	70%	80%	90%	95%	98%

Table 3.1: Target τ_h identification efficiencies for the different working points defined for the three different discriminators, against electrons (D_e), muons (D_μ) and jets (D_{jet}). These efficiencies are evaluated with the $H \rightarrow \tau^+\tau^-$ event sample for $p_T^{\tau_h} \in [30, 70]$ GeV [42].

3.9 Missing Transverse Energy

Particles interacting with matter just through weak interactions and have negligible mass are impossible to be detected by CMS because they don't leave any trace in any of its layers, not even hits in the tracker or in muon chambers to be used as seeds for reconstructing their trajectories. Such particles are the SM neutrinos, namely ν_e , ν_μ and ν_τ . These particles

escape the whole CMS system without being able to collect any sort of information about them. The beams before colliding have 0 momentum in the x-y (transverse) plane and from the energy-momentum conservation law, the vector sum of the total energy in the transverse plane should remain 0 after the hard scattering, as well. This means that by calculating this sum using all reconstructed particles of the final state, the sum should be equal to 0. If not, it is a sign that most probably a particle left the detector without being detected, maybe a sign of an outgoing neutrino. Missing Transverse Energy (MET) is defined as the negative vector sum of all PF particle's momentum in the transverse plane and the value of this variable is expected to be equal to the vector sum of the p_T of all neutrinos in the final state.

$$\vec{E}_T = - \sum_i^{N_{PF}} \vec{p}_{T,i}, \quad E_T^{miss} = |\vec{E}_T| \quad (39)$$

3.10 Scalar Hadronic and Leptonic Transverse Momentum

The hadronic scalar transverse momentum, H_T , is defined as the scalar sum of the transverse momenta of all reconstructed jets, except τ_h , while the leptonic scalar transverse momentum, L_T , is defined as the scalar sum of the transverse momenta of all reconstructed electrons, muons and τ_h jets in an event.

$$H_T = \sum_i^{jets} |\vec{p}_{T,i}| \quad (40)$$

$$L_T = \sum_i^{e,\mu,\tau_h} |\vec{p}_{T,i}| \quad (41)$$

Both H_T and L_T are measured after applying all identification criteria, event selections and lepton/jet-related corrections described in the following chapters.

4 Data and Simulation Samples

The collision data collected with the CMS detector with centre-of-mass energy of $\sqrt{s} = 13 \text{ TeV}$ are discussed in 4.1, and the corresponding simulated samples in 4.2.5.

4.1 Collision data

The certified collision data that were collected by the CMS detector during the 2016 - 2018 LHC running period (Run 2) at center of mass energy of $\sqrt{s} = 13 \text{ TeV}$ correspond to an integrated luminosity of 138 fb^{-1} . The certification of the data is a process that ensures the collected data is of high quality and no problems with various sub-detector systems or the trigger can affect or alter the outcome of the studies of the events.

The 2016 data were processed with the CMSSW_10_6_29 software, and with a Cert_271036-284044_13TeV_Legacy2016_Collisions16_JSON.txt certification file. The Global Tag (GT) 2016_106XULAPVdata or 2016_106XULdata was used in the analysis. The data collected in 2017 were processed with the CMSSW_10_6_29 software, and with a Cert_294927-306462_13TeV_UL2017_Collisions17_GoldenJSON.txt certification file. The GT 2017_106XULdata was used in the processing. The 2018 data were processed with the CMSSW_10_6_29 software, and with a Cert_314472-325175_13TeV_Legacy2018_Collisions18_JSON.txt certification file. The GT 2018_106XULdata was used in the processing. A summary of the collision data used in the analysis is shown in Tables 4.1, 4.2, 4.3 for the 2016, 2017, and 2018 data-taking periods, respectively.

During the 2016 data-taking period at CMS, the Silicon Strip Detector (SSD) faced a problem known as the High Irradiation Pressure (HIP) issue, leading to a dynamic loss in hit efficiency [48]. This issue arises when a large energy deposition, typically from a high-energy particle, causes the silicon sensor to briefly saturate, affecting its performance. As a result, certain particles passing through the detector during this saturation period might not be properly detected, leading to inefficiencies in the hit reconstruction. The impact of this issue was particularly pronounced during the 2016 run, where the rate of such occurrences increased. To mitigate this, specific corrections and re-calibrations were applied, which were optimized for the conditions during this period, coinciding with what is known as the Vertex-Finding Pixel (VFP) transition. The 2016 data was therefore split into two distinct periods, before and after VFP, referred to as "pre-VFP" and "post-VFP", with data collected during the post-VFP period labeled as "HIP Mitigated" (HIPM). In the pre-VFP period, the HIP issue was more pronounced, whereas, in the post-VFP period, detector performance improved due to the implementation of software and hardware updates that reduced the impact of the HIP issue. Consequently, the post-VFP data does not include any HIPM-related label, as

the improved conditions make such mitigation techniques less critical or unnecessary. By splitting the 2016 dataset into these categories, analysis consistency is ensured, accounting for varying detector performance throughout the data-taking period. This separation allows for more precise measurements, as different corrections and calibrations are applied to each dataset.

Dataset	Runs	$\mathcal{L} (pb^{-1})$
SingleElectron_Run2016B-ver2_HIPM_UL2016_MiniAODv2-v2 [†]	273150–275376	5828.415
SingleElectron_Run2016C-HIPM_UL2016_MiniAODv2-v2 [†]	275420–276283	2601.670
SingleElectron_Run2016D-HIPM_UL2016_MiniAODv2-v2 [†]	276315–276811	4285.851
SingleElectron_Run2016E-HIPM_UL2016_MiniAODv2-v5 [†]	276824–277420	4064.023
SingleElectron_Run2016F-HIPM_UL2016_MiniAODv2-v2 [†]	277932–278800	2717.345
SingleElectron_Run2016F-UL2016_MiniAODv2-v2	278801–278808	410.830
SingleElectron_Run2016G-UL2016_MiniAODv2-v2	278816–280385	7652.808
SingleElectron_Run2016H-UL2016_MiniAODv2-v2	281613–284044	8739.884
SingleMuon_Run2016B_ver2_HIPM_UL2016_MiniAODv2_v2 [†]	273150–275376	5824.236
SingleMuon_Run2016C_HIPM_UL2016_MiniAODv2_v2 [†]	275420–276283	2601.670
SingleMuon_Run2016D_HIPM_UL2016_MiniAODv2_v2 [†]	276315–276811	4285.851
SingleMuon_Run2016E_HIPM_UL2016_MiniAODv2_v2 [†]	276824–277420	4065.974
SingleMuon_Run2016F_HIPM_UL2016_MiniAODv2_v2 [†]	277932–278800	2701.321
SingleMuon_Run2016F_UL2016_MiniAODv2_v2	278801–278808	410.830
SingleMuon_Run2016G_UL2016_MiniAODv2_v2	278816–280385	7652.808
SingleMuon_Run2016H_UL2016_MiniAODv2_v2	281613–284044	8739.884

Table 4.1: Dataset and run ranges used from the 2016 data-taking period, along with the corresponding integrated luminosity. The symbol † indicates data affected by a reduced hit efficiency in the Silicon strip detector, often called the HIP issue [48].

Dataset	Runs	$\mathcal{L} (pb^{-1})$
SingleElectron_Run2017B_UL2017_MiniAODv2_v1	297050–299329	4803.363
SingleElectron_Run2017C_UL2017_MiniAODv2_v1	299368–302029	9572.184
SingleElectron_Run2017D_UL2017_MiniAODv2_v1	302031–302663	4247.682
SingleElectron_Run2017E_UL2017_MiniAODv2_v1	303825–304797	9313.642
SingleElectron_Run2017F_UL2017_MiniAODv2_v1	305044–306460	13539.222
SingleMuon_Run2017B_UL2017_MiniAODv2_v1	297050–299329	4803.363
SingleMuon_Run2017C_UL2017_MiniAODv2_v1	299368–302029	9572.498
SingleMuon_Run2017D_UL2017_MiniAODv2_v1	302031–302663	4247.682
SingleMuon_Run2017E_UL2017_MiniAODv2_v1	303825–304797	9312.832
SingleMuon_Run2017F_UL2017_MiniAODv2_v1	305044–306460	13538.886

Table 4.2: Dataset and run ranges used from the 2017 data-taking period, along with the corresponding integrated luminosity.

4.2 Event Simulation

Both theoretical and experimental physicists benefit from Monte Carlo (MC) simulations, which are crucial tools for studying the behavior and evolution of systems, particularly in

Dataset	Runs	$\mathcal{L} (pb^{-1})$
EGamma_Run2018A_UL2018_MiniAODv2_v1	315257–316995	14026.725
EGamma_Run2018B_UL2018_MiniAODv2_v1	317080–319310	7060.617
EGamma_Run2018C_UL2018_MiniAODv2_v1	319337–320065	6894.771
EGamma_Run2018D_UL2018_MiniAODv2_v2	320413–325172	31834.116
SingleMuon_Run2018A_UL2018_MiniAODv2_v3	315257–316995	14027.047
SingleMuon_Run2018B_UL2018_MiniAODv2_v2	317080–319310	7060.622
SingleMuon_Run2018C_UL2018_MiniAODv2_v2	319337–320065	6891.747
SingleMuon_Run2018D_UL2018_MiniAODv2_v3	320413–325172	31834.889

Table 4.3: Dataset and run ranges used from the 2018 data-taking period, along with the corresponding integrated luminosity.

High Energy Particle Physics. MC simulations incorporate theoretical models and analytical solutions, such as those for the hard scattering processes, to generate predictions on how events unfold. They are fundamental to any physics analysis conducted with LHC data, as they allow scientists to model not only the expected behavior of different physical processes but also to simulate the response of sub-detector systems. This dual role helps compare the experimental data collected by detectors with theoretical predictions, enabling a more accurate and comprehensive understanding of the underlying physics.

4.2.1 Hard Scattering

The simulation of an event involves several steps. The first step in the process is the simulation of the Hard Scattering of the pp beams, a quite challenging procedure, hard to predict due to the composite nature of the protons. In high-energy collisions, the variable " x " represents the momentum fraction of the proton carried by one of its constituent partons. As the collision energy increases, the momentum transfer (Q) also increases, resulting in different ranges of x being probed. The value of x can vary from near 0, indicating a parton that carries only a small fraction of the proton's momentum, to values close to 1, where a parton carries nearly all the proton's momentum. The Parton Distribution Function (PDF) describes the probability of finding a parton with a specific momentum fraction x when the proton is probed at an energy scale Q^2 . The momentum scale Q^2 is chosen to match the mass of the proton ($Q^2 = \mu^2$), serving as the factorization scale in the PDF evolution equations.

The evolution of parton distributions is described by the Dokshitzer-Gribov-Lipatov-Altarelli-Parisi (DGLAP) equations, which dictate how the PDFs change with variations in Q and x [45]. At low values of x , corresponding to high-energy scales, the gluon density within the proton dominates, contributing significantly to the proton's momentum, as shown in Fig. 4.1. This is because, at high energies, the proton's structure is increasingly described by contributions from the quark-gluon sea rather than just the valence quarks (up and down

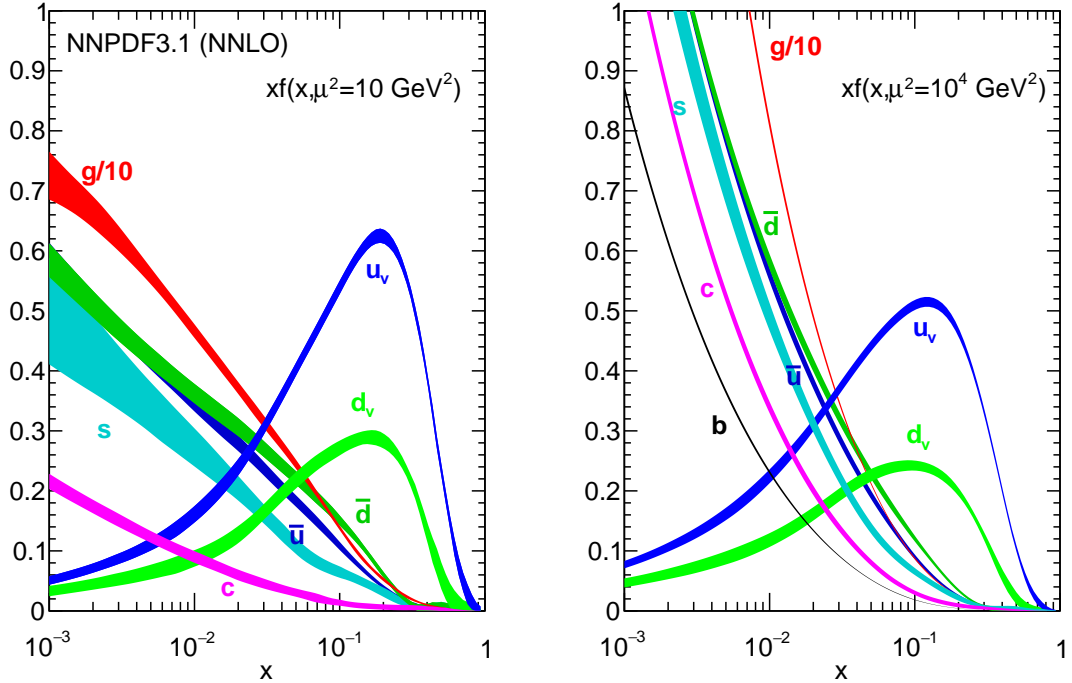


Figure 4.1: The NNPDF3.1 NNLO PDFs displayed are the next-to-next-to-leading order PDFs which describe the quark-gluon constituents of a proton, evaluated at $\mu^2 = 10 \text{ GeV}^2$ (left) and $\mu^2 = 10^4 \text{ GeV}^2$ (right) [45].

quarks). On the other hand, at higher values of x , valence quarks play a more dominant role. Up to this moment, the most precisely determined PDF over most of the experimentally accessible range of x is now the gluon.

The region of interest for seeking signs of new physics lies in high energy scales, thus the most interesting processes are those in which the two partons carrying the highest fraction of each of their respective protons' kinetic energy are the ones that collide and scattered. Ideally, partons with momentum fractions closer to 1 are more relevant because they represent scenarios where the protons' energy is transferred almost entirely to the colliding partons. However, in practice, these partons are less common and thus less likely to participate in a typical collision. Therefore, partons with momentum fractions around 0.3 to 0.4 also contribute significantly because their x value corresponds to a relatively higher parton density. Nonetheless, the probability of two protons colliding in such a way that a "hard scattering" occurs is quite low in each bunch crossing.

In every single bunch crossing, the possibility for two protons to collide as perfectly centrally as needed for a "hard scattering" to occur is almost zero. As a result, most of the protons either continue their journey without interacting at all with the protons of the other bunch or they are scattered elastically. This means that most of the collisions that take place inside CMS are of zero interest. Therefore, substantial effort is focused on identifying and

analyzing hard scatterings, which are collisions where partons with high momentum fractions interact with each other, increasing the likelihood of producing rare and significant processes. To optimize this search, MC simulations are specifically tuned to predict and model these hard scattering events. An example of a hard process that might appear in one of the pp collisions is shown in Fig.4.2.

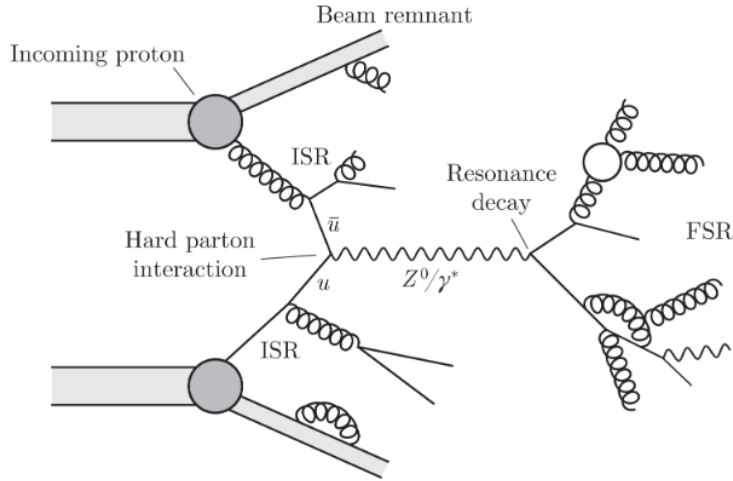


Figure 4.2: Example of a hard pp collision resulting to Z^0/γ^* production.

The first step for simulating a hard process is to calculate its PDF and apply Perturbation Theory to calculate the related cross section for the interaction. The cross section quantifies the likelihood of the scattering process occurring between the partons in the colliding protons.

4.2.2 Parton Shower Generator

After simulating the hard scattering process, the next step is the parton shower simulation. This models how the partons involved in the initial scattering event undergo further interactions, leading to the emission of additional particles. The parton shower simulation is based on the Altarelli-Parisi equations, which provide the probability for a quark or gluon branching into other partons. These equations provide a quantitative framework for predicting how initial partons will split into more particles during the parton shower.

Parton showers include two key components: Initial-State Radiation (ISR) and Final-State Radiation (FSR). ISR refers to the radiation emitted by partons before the hard scattering event, while FSR describes the radiation emitted after the scattering. In the shower process, gluons can decay into quark-antiquark pairs or emit additional gluons, while quarks can emit gluons or undergo other branching processes. Both types of radiation contribute to the cascading effect of particles, which results in a dense shower inside the detector. More about Parton Shower event generators can be found in Ref. [46].

4.2.3 Hadronization Generators

Partons, as already noted, as color carries, cannot exist freely in nature but they are confined in colorless bound states with other partons, forming hadrons. The process in which a parton shower transforms into a hadron shower, is called Hadronization. Perturbation theory here is not effective, due to the gradually increasing distance between particles, resulting in the increase of the value of the strong coupling constant leading to the failure of the validity of the perturbation theory. Phenomenological models based on QCD characteristics on the other hand, are more suited for this job, like String and Cluster Models, that are produced by PYTHIA [55] and HERWIG [47] event generators, respectively.

4.2.4 Detector Simulation

Final state particles, produced through Hard Scattering, Parton Showers and Hadronization, have lifetime long enough (> 90 psec) that can enter the detector volume and interact with the detector material. The interaction of those particles with matter is simulated with the "GEometry ANd Tracking" (GEANT4) [43] simulation package that includes all electromagnetic and hadronic interactions of particles with matter. The simulation of each particle's interactions as it traverses the detector material is an intense and costly computational process. For this reason, a faster version of it was designed for simulating just a very small number of particular MC simulations that the CMS group is interested in. This software, called "Fast Simulation" (FastSim) [44], is approximately 10^3 times faster than GEANT4 because it takes advantage of the detector's geometry and simplifies certain aspects of particles' interactions with the detector's materials.

4.2.5 Simulated samples

The simulation samples used in this analysis will be detailed in the following. The matrix element calculations of the various processes of interest are done using the MADGRAPH5_AMC@NLO [49] and POWHEG v2 [50, 51, 52] MC generators. The centre-of-mass energy for proton-proton collisions was set to $\sqrt{s} = 13$ TeV, and full detector simulation was done with GEANT4 [53, 54] for all samples used. The parton shower and hadronization are simulated using PYTHIA8 [55] using the tune CP5 [56] for all 3 years. The CP5 tune is one of several tuning options available in PYTHIA8, and it is used to adjust the parameters of the simulation to better match experimental data. It was optimized to improve the agreement between simulation results and measurements from the LHC, taking into account various aspects of the parton shower and hadronization. The tune employed for POWHEG v2 is CUETP8M1 [57].

The samples involving the process of single top production and decay are generated at

Next-to-leading order (NLO) precision in the four flavour scheme (4FS), for the t -channel process [58], using POWHEG v2 interfaced with MADSPIN [59] for simulating the top quark decay. The s -channel process is simulated using MADGRAPH5_AMC@NLO v2.2.2, while the production of single top quark events via the tW channel is simulated at NLO in the five flavour scheme (5FS) using POWHEG v1 [60]. The production of $t\bar{t}$ in association with W, Z or γ is simulated at NLO using MADGRAPH5_AMC@NLO v2.2.2. For the $t\bar{t}H$ production, separate samples simulating the H^0 decay to bb or non-bb final state are generated using POWHEG v2 at NLO [61].

The samples are normalised to the most precise available cross section calculations, corresponding most often to next-to-next-to-leading order (NNLO) in QCD and NLO in electroweak corrections.

The 2016 simulated samples used were centrally produced with GT 106X_mcRun2_asymptotic_preVFP_v11 and the RunIISummer20UL16MiniAODAPVv2 or with 106X_mcRun2_asymptotic_v17 and the RunIISummer20UL16MiniAODv2 production campaign. The 2017 simulated samples used were centrally produced with GT 106X_mc2017_realistic_v9 and the RunIISummer20UL17MiniAODv2 production campaign. Finally, the 2018 simulated samples used were also centrally produced with GT 106X_upgrade2018_realistic_v16_L1v1 and the RunIISummer20UL18MiniAODv2 production campaign. The MC analysis was performed using the CMSSW_10_6_29 software.

The signal samples with charged Higgs bosons were simulated with MADGRAPH5_AMC@NLO event generator and decayed with MadSpin. All the available $m_{H^0(h^0)}$ and m_{H^\pm} combinations are summarized in Table 4.4 while the corresponding signal samples used are summarised in Table 4.5. The $\tan\beta$ and $\sin(b-a)$ values of the 2HDM, used to produce the signal samples were the following. For $m_{H^0(h^0)} = 125, 200, \text{ and } 300 \text{ GeV}$, $\tan\beta$ is set to be equal to 10 and $\sin(b-a)$ to 1, while for $m_{H^0(h^0)} = 80 \text{ and } 90 \text{ GeV}$, the values of the $\tan\beta$ and $\sin(b-a)$ are equal to 5 and 0, respectively. The background samples used for the analysis are summarised in Table 4.6 and are the same across all three years of Run 2.

$m_{H^0(h^0)}$ (GeV)	m_{H^\pm} (GeV)
80	170, 185, 200, 220, 250, 300, 400, 500, 600, 700, 800, 900, 1000, 1250, 1500, 2000
90	185, 200, 220, 250, 300, 400, 500, 600, 700, 800, 900, 1000, 1250, 1500, 2000
125	220, 250, 300, 400, 500, 600, 700, 800, 900, 1000, 1250, 1500, 2000
200	300, 400, 500, 600, 700, 800, 900, 1000, 1250, 1500, 2000
300	400, 500, 600, 700, 800, 900, 1000, 1250, 1500, 2000

Table 4.4: Summary of the available $m_{H^0(h^0)}$ and m_{H^\pm} combinations for the simulated signal samples used in the analysis.

Process	Generator	ME accuracy	Events	Dataset
$m_{h^0} = 80 \text{ GeV}$	MADGRAPH5_AMC@NLO	NLO	4 000 000	ChargedHiggsToHW_HToTauTau_M-V1_MH1_M-80_1L_X
$m_{h^0} = 80 \text{ GeV}$	MADGRAPH5_AMC@NLO	NLO	1 500 000	ChargedHiggsToHW_HToTauTau_M-V2_MH1_M-80_1L_X
$m_{h^0} = 80 \text{ GeV}$	MADGRAPH5_AMC@NLO	NLO	500 000	ChargedHiggsToHW_HToTauTau_M-V3_MH1_M-80_1L_X
$m_{h^0} = 90 \text{ GeV}$	MADGRAPH5_AMC@NLO	NLO	4 000 000	ChargedHiggsToHW_HToTauTau_M-W1_MH1_M-90_1L_X
$m_{h^0} = 90 \text{ GeV}$	MADGRAPH5_AMC@NLO	NLO	1 500 000	ChargedHiggsToHW_HToTauTau_M-W2_MH1_M-90_1L_X
$m_{h^0} = 90 \text{ GeV}$	MADGRAPH5_AMC@NLO	NLO	500 000	ChargedHiggsToHW_HToTauTau_M-W3_MH1_M-90_1L_X
$m_{h^0} = 125 \text{ GeV}$	MADGRAPH5_AMC@NLO	NLO	4 000 000	ChargedHiggsToHW_HToTauTau_M-X1_MH1_M-125_1L_X
$m_{h^0} = 125 \text{ GeV}$	MADGRAPH5_AMC@NLO	NLO	2 500 000	ChargedHiggsToHW_HToTauTau_M-300_MH1_M-125_1L_X
$m_{h^0} = 125 \text{ GeV}$	MADGRAPH5_AMC@NLO	NLO	2 000 000	ChargedHiggs_HplusTB_HplusToHW_M-300_MH1_M-125_X
$m_{h^0} = 125 \text{ GeV}$	MADGRAPH5_AMC@NLO	NLO	1 500 000	ChargedHiggsToHW_HToTauTau_M-X2_MH1_M-125_1L_X
$m_{h^0} = 125 \text{ GeV}$	MADGRAPH5_AMC@NLO	NLO	1 000 000	ChargedHiggsToHW_HToTauTau_M-700_MH1_M-125_1L_X
$m_{h^0} = 125 \text{ GeV}$	MADGRAPH5_AMC@NLO	NLO	2 000 000	ChargedHiggs_HplusTB_HplusToHW_M-700_MH1_M-125_X
$m_{h^0} = 125 \text{ GeV}$	MADGRAPH5_AMC@NLO	NLO	500 000	ChargedHiggsToHW_HToTauTau_M-X3_MH1_M-125_1L_X
$m_{H^0} = 200 \text{ GeV}$	MADGRAPH5_AMC@NLO	NLO	2 500 000	ChargedHiggsToHW_HToTauTau_M-300_MH2_M-200_1L_X
$m_{H^0} = 200 \text{ GeV}$	MADGRAPH5_AMC@NLO	NLO	2 000 000	ChargedHiggs_HplusTB_HplusToHW_M-300_MH2_M-200_X
$m_{H^0} = 200 \text{ GeV}$	MADGRAPH5_AMC@NLO	NLO	1 500 000	ChargedHiggsToHW_HToTauTau_M-600_MH2_M-200_1L_X
$m_{H^0} = 200 \text{ GeV}$	MADGRAPH5_AMC@NLO	NLO	1 000 000	ChargedHiggsToHW_HToTauTau_M-Y2_MH2_M-200_1L_X
$m_{H^0} = 200 \text{ GeV}$	MADGRAPH5_AMC@NLO	NLO	2 000 000	ChargedHiggs_HplusTB_HplusToHW_M-Y2_MH2_M-200_X
$m_{H^0} = 200 \text{ GeV}$	MADGRAPH5_AMC@NLO	NLO	500 000	ChargedHiggsToHW_HToTauTau_M-Y3_MH2_M-200_1L_X
$m_{H^0} = 300 \text{ GeV}$	MADGRAPH5_AMC@NLO	NLO	1 500 000	ChargedHiggsToHW_HToTauTau_M-Z2_MH2_M-300_1L_X
$m_{H^0} = 300 \text{ GeV}$	MADGRAPH5_AMC@NLO	NLO	500 000	ChargedHiggsToHW_HToTauTau_M-Z3_MH2_M-300_1L_X
$V^* = m_{H^\pm}(\text{GeV}), V1 = [170, 185, 200, 220, 250, 300], V2 = [400, 500, 600, 700, 800, 900, 1000], V3 = [1250, 1500, 2000]$				
$W^* = m_{H^\pm}(\text{GeV}), W1 = [185, 200, 220, 250, 300], W2 = [400, 500, 600, 700, 800, 900, 1000], W3 = [1250, 1500, 2000]$				
$X^* = m_{H^\pm}(\text{GeV}), X1 = [220, 250], X2 = [400, 500, 600, 800, 900, 1000], X3 = [1250, 1500, 2000]$				
$Y^* = m_{H^\pm}(\text{GeV}), Y2 = [400, 500, 700, 800, 900, 1000], Y3 = [1250, 1500, 2000]$				
$Z^* = m_{H^\pm}(\text{GeV}), Z2 = [400, 500, 700, 800, 900, 1000], Z3 = [1250, 1500, 2000]$				

Table 4.5: Summary of the simulated signal samples used for the analysis. The production process $pp \rightarrow tbH^\pm$ with $H^\pm \rightarrow H^0(h^0)W^\pm$ and $H^0(h^0) \rightarrow \tau^+\tau^-$ refers to the 4FS scheme, with at least 1 lepton (e/μ) in the final state, while the notation X is shorthand for TuneCP5_13TeV_amcatnlo_pythia8.

Process	Cross section (pb)	Generator	ME accuracy	Dataset
$Z/\gamma^* + \text{jets}$	6077.22 [66]	MADGRAPH5@NLO	NNLO	/DYJetsToLL_M-50_TuneCP5_13TeV-amcatnloFXFX-pythia8
$Z/\gamma^* + \text{jets HT binned}$	158.172 [66, 67]	MADGRAPH5_AMC@NLO	NNLO	/DYJetsToLL_M-50_HT-70to100_TuneCP5_PSweights_13TeV-madgraphMLM-pythia8
$Z/\gamma^* + \text{jets HT binned}$	157.268 [66, 67]	MADGRAPH5_AMC@NLO	NNLO	/DYJetsToLL_M-50_HT-100to200_TuneCP5_PSweights_13TeV-madgraphMLM-pythia8
$Z/\gamma^* + \text{jets HT binned}$	43.384 [66, 67]	MADGRAPH5_AMC@NLO	NNLO	/DYJetsToLL_M-50_HT-200to400_TuneCP5_PSweights_13TeV-madgraphMLM-pythia8
$Z/\gamma^* + \text{jets HT binned}$	5.846 [66, 67]	MADGRAPH5_AMC@NLO	NNLO	/DYJetsToLL_M-50_HT-400to600_TuneCP5_PSweights_13TeV-madgraphMLM-pythia8
$Z/\gamma^* + \text{jets HT binned}$	1.421 [66, 67]	MADGRAPH5_AMC@NLO	NNLO	/DYJetsToLL_M-50_HT-600to800_TuneCP5_PSweights_13TeV-madgraphMLM-pythia8
$Z/\gamma^* + \text{jets HT binned}$	0.632 [66, 67]	MADGRAPH5_AMC@NLO	NNLO	/DYJetsToLL_M-50_HT-800to1200_TuneCP5_PSweights_13TeV-madgraphMLM-pythia8
$Z/\gamma^* + \text{jets HT binned}$	0.147 [66, 67]	MADGRAPH5_AMC@NLO	NNLO	/DYJetsToLL_M-50_HT-1200to2500_TuneCP5_PSweights_13TeV-madgraphMLM-pythia8
$Z/\gamma^* + \text{jets HT binned}$	0.011 [66, 67]	MADGRAPH5_AMC@NLO	NNLO	/DYJetsToLL_M-50_HT-2500toInf_TuneCP5_PSweights_13TeV-madgraphMLM-pythia8
$W + \text{jets}$	20508.9 $\times 3.0$ [66]	MADGRAPH5@NLO	NNLO	/WJetsToLNu_TuneCP5_13TeV-amcatnloFXFX-pythia8
$W + \text{jets HT binned}$	1463.455 [66, 67]	MADGRAPH5@NLO	NNLO	/WJetsToLNu_HT-70to100_TuneCP5_13TeV-madgraphMLM-pythia8
$W + \text{jets HT binned}$	1418.970 [66, 67]	MADGRAPH5@NLO	NNLO	/WJetsToLNu_HT-100to200_TuneCP5_13TeV-madgraphMLM-pythia8
$W + \text{jets HT binned}$	385.312 [66, 67]	MADGRAPH5@NLO	NNLO	/WJetsToLNu_HT-200to400_TuneCP5_13TeV-madgraphMLM-pythia8
$W + \text{jets HT binned}$	51.249 [66, 67]	MADGRAPH5@NLO	NNLO	/WJetsToLNu_HT-400to600_TuneCP5_13TeV-madgraphMLM-pythia8
$W + \text{jets HT binned}$	12.764 [66, 67]	MADGRAPH5@NLO	NNLO	/WJetsToLNu_HT-600to800_TuneCP5_13TeV-madgraphMLM-pythia8
$W + \text{jets HT binned}$	5.619 [66, 67]	MADGRAPH5@NLO	NNLO	/WJetsToLNu_HT-800to1200_TuneCP5_13TeV-madgraphMLM-pythia8
$W + \text{jets HT binned}$	1.314 [66, 67]	MADGRAPH5@NLO	NNLO	/WJetsToLNu_HT-1200to2500_TuneCP5_13TeV-madgraphMLM-pythia8
$W + \text{jets HT binned}$	0.030 [66, 67]	MADGRAPH5@NLO	NNLO	/WJetsToLNu_HT-2500toInf_TuneCP5_13TeV-madgraphMLM-pythia8
WW	118.7 [66]	pythia8	NNLO	/WW_TuneCP5_13TeV-pythia8
WZ	47.13 [66]	pythia8	NLO	/WZ_TuneCP5_13TeV-pythia8
ZZ	16.523 [66]	pythia8	NLO	/ZZ_TuneCP5_13TeV-pythia8
WWW	0.2158 [67]	MADGRAPH5_AMC@NLO	NLO	/WWW_4F_TuneCP5_13TeV-amcatnlo-pythia8
WWZ	0.1707 [67]	MADGRAPH5_AMC@NLO	NLO	/WWZ_4F_TuneCP5_13TeV-amcatnlo-pythia8
WZZ	0.05079 [67]	MADGRAPH5_AMC@NLO	NLO	/WZZ_TuneCP5_13TeV-amcatnlo-pythia8
ZZZ	0.01476 [67]	MADGRAPH5_AMC@NLO	NLO	/ZZZ_TuneCP5_13TeV-amcatnlo-pythia8
$t, s \text{ channel}$	10.32×0.676 [63]	MADGRAPH5_AMC@NLO	NLO	/ST_s-channel_4F_hadronicDecays_TuneCP5_13TeV-amcatnlo-pythia8
$t, s \text{ channel}$	10.32×0.324 [63]	MADGRAPH5_AMC@NLO	NLO	/ST_s-channel_4F_leptonDecays_TuneCP5_13TeV-amcatnlo-pythia8
$t, tW \text{ channel}$	35.85 [63]	POWHEG v2	NLO	/ST_tW_antitop_5f_inclusiveDecays_TuneCP5_13TeV-powheg-pythia8
$t, tW \text{ channel}$	35.85 [63]	POWHEG v2	NLO	/ST_tW_antitop_5f_inclusiveDecays_TuneCP5_13TeV-powheg-pythia8
$t, t \text{ channel (4FS)}$	136.02/2 [63]	POWHEG v2	NLO	/ST_t-channel_top_4F_InclusiveDecays_TuneCP5_13TeV-powheg-madspin-pythia8
$t, t \text{ channel (4FS)}$	80.95/2 [63]	POWHEG v2	NLO	/ST_t-channel_antitop_4F_InclusiveDecays_TuneCP5_13TeV-powheg-madspin-pythia8
$t, t \text{ channel (5FS)}$	136.02/2 [63]	POWHEG v2	NLO	/ST_t-channel_top_5f_InclusiveDecays_TuneCP5_13TeV-powheg-pythia8
$t, t \text{ channel (5FS)}$	80.95/2 [63]	POWHEG v2	NLO	/ST_t-channel_antitop_4F_InclusiveDecays_TuneCP5_13TeV-powheg-madspin-pythia8
$t\bar{t}(2L2Nu)$	$833.9 \times 0.3259 \times 0.3259$ [62]	POWHEG v2	NNLO	/TTTo2LNu_TuneCP5_13TeV-powheg-pythia8
$t\bar{t} \text{ Semileptonic}$	$833.9 \times 0.6741 \times 0.3259$ [62]	POWHEG v2	NNLO	/TTToSemiLeptonic_TuneCP5_13TeV-powheg-pythia8
$t\bar{t} \text{ Hadronic}$	$833.9 \times 0.6741 \times 0.6741$ [62]	POWHEG v2	NNLO	/TTToHadronic_TuneCP5_13TeV-powheg-pythia8
$t\bar{t}\bar{t}$	8.091×10^{-3} [67]	MADGRAPH5_AMC@NLO	NLO	/TTT_TuneCP5_13TeV-amcatnlo-pythia8
$t\bar{t}W + \text{jets}$	0.55 $\times 0.3259$ [66, 67]	MADGRAPH5_AMC@NLO	NLO	/TTWJetsToLNu_TuneCP5_13TeV-amcatnloFXFX-madspin-pythia8
$t\bar{t}W + \text{jets}$	0.55 $\times 0.6741$ [66, 67]	MADGRAPH5_AMC@NLO	NLO	/TTWJetsToQQ_TuneCP5_13TeV-amcatnloFXFX-madspin-pythia8
$t\bar{t}Z + \text{jets}$	0.86 $\times 0.69911$ [66, 67]	MADGRAPH5_AMC@NLO	NLO	/TTZToQQ_TuneCP5_13TeV-amcatnlo-pythia8
$t\bar{t}Z + \text{jets}$	0.2439 [66, 67]	MADGRAPH5_AMC@NLO	NLO	/TTZToLLNu_M-10_TuneCP5_13TeV-amcatnlo-pythia8
$t\bar{t}\gamma + \text{jets}$	3.697 [67]	MADGRAPH5_AMC@NLO	NLO	/TTGJets_TuneCP5_13TeV-amcatnloFXFX-madspin-pythia8
$t\bar{t}W^{h^0}$	1.349×10^{-3} [67]	MADGRAPH5@NLO	NLO	/TTWH_TuneCP5_13TeV-madgraph-pythia8
$t\bar{t}Z^{h^0}$	1.349×10^{-3} [67]	MADGRAPH5@NLO	NLO	/TTWH_TuneCP5_13TeV-madgraph-pythia8
$t\bar{t}h^0 \rightarrow h^0bb$	0.5071×0.4176 [68, 67]	POWHEG v2	NLO	/ttHToNonbb_M125_TuneCP5_13TeV-powheg-pythia8
$t\bar{t}h^0 \rightarrow h^0bb$	0.5071×0.5824 [68, 67]	POWHEG v2	NLO	/ttHTobb_M125_TuneCP5_13TeV-powheg-pythia8

Table 4.6: Summary of the simulated background samples used for the analysis. The HT-binned versions of the $Z/\gamma^* + \text{jets}$ and $W + \text{jets}$ are used in the analysis, instead of their inclusive versions, because they more efficiently cover different regions of phase space, ensuring accurate event modeling and improving statistical precision, especially in low event rate regions.

5 Corrections, filtering and reweighting

Certain imperfections in data modeling are addressed through the corrections outlined in the following subsections. Unless specified otherwise, these corrections are exclusively applied to simulated samples. All corrections and reweightings are applied according to the guidelines provided by the relevant CMS Physics Object Group (POG).

5.1 MET filters

The JetMET POG recommendations [69] guide the application of specific filters on the selected data and simulated events. These filters are responsible for event cleaning based on criteria such as the presence of good vertices, beam halos, and various sources of detector noise. Both data and simulation undergo the same filtering process. As detailed in Table 5.1, all filters are applied across the full Run2 period, except for the `Flag_eeBadCalibFilter`, which is exclusive to 2017 and 2018 UL events. This filter was introduced to address issues related to calibration problems in the ECAL, specifically affecting the endcap regions.

The beam halos are machine-induced particles which are flying with the beam. They are mainly produced via beam-gas and beam-pipe interactions. In particular, high-energy halo muons have a non-negligible probability of interacting in the calorimeters, causing clusters of up to several hundreds of GeV in energy. Such events are suppressed with the `Flag_globalSuperTightHalo2016Filter` filter, which ensures that detector activity originates from the hard pp collision. Events with significant noise in the HCAL, HB, and HE, are also filtered since it is known to record sporadic anomalous signals at a fixed rate, independent of beam conditions. For this reason, the `Flag_HBHENoiseFilter` filter is used, with the loose WP, as defined by the JetMET POG. The ECAL dead cell trigger primitive filter, `Flag_EcalDeadCellTriggerPrimitiveFilter`, is employed to combat noisy ECAL crystals which are masked in the event reconstruction and can thus cause missing energy in case of an overlap with a jet. Trigger primitive information is used to assess how much energy is lost and if energy loss is found to be significant, the event is discarded. Finally, the `Flag_eeBadScFilter` is a bad EE supercluster filter that is used to reject events with anomalously high energies in EE superclusters.

5.2 Pileup reweighting

The number of additional pp interactions in the same or nearby bunch crossings is known as Pile-Up (PU) and varies between simulation and data. In simulated events generated with PYTHIA v8.212, pileup is superimposed on the hard collisions using a distribution with a fixed average number of interactions. In real data, pileup changes as a function of instanta-

Filter	2016(APV/FPV)	2017	2018
Flag_goodVertices	✓	✓	✓
Flag_globalSuperTightHalo2016Filter	✓	✓	✓
Flag_HBHENoiseFilter	✓	✓	✓
Flag_HBHENoiseIsoFilter	✓	✓	✓
Flag_EcalDeadCellTriggerPrimitiveFilter	✓	✓	✓
Flag_BadPFMuonFilter	✓	✓	✓
Flag_BadPFMuonDzFilter	✓	✓	✓
Flag_eeBadScFilter	✓	✓	✓
Flag_ecalBadCalibFilter		✓	✓

Table 5.1: Summary of all MET filters applied to events selected in data and simulation. A checkmark (✓) indicates the filter is applied, while its absence is that it is not applied.

neous luminosity. To address this variation, events in simulated samples are reweighted to match the true distribution observed in the data. This ensures that simulated events accurately reflect the pileup distribution in data, considering factors such as the measured luminosity profile and average measured total inelastic pp cross section. The number of interactions in the data is estimated from the measured luminosity in each bunch crossing times the average total inelastic cross section. The mean number of interactions per bunch crossing for the 2016, 2017, and 2018 pp run at 13 TeV was 23, 32, and 32, respectively [70].

5.3 Data to MC scale factors

A Scale Factor (SF) is an event weight used to multiply a simulated event in order to make a certain distribution in simulated samples to match with the distribution in data. It is usually defined as the ratio of efficiencies, evaluated from data to that evaluated from simulation, and unless otherwise stated they are independently calculated and applied separately for each year.

5.3.1 Electron trigger,identification and reconstruction

For the single electron trigger, the SFs are calculated for each year of data-taking and applied bins of electron p_T and η . They are defined as the ratio of the efficiencies from data and simulations. The trigger SFs are calculated as described in Sec.7.2.1. For the identification and reconstruction of the related SFs, the EGamma POG recommendations are followed, as described in [81].

5.3.2 Muon trigger, identification and isolation

For the single muon trigger, the SFs are calculated and applied in bins of muon p_T and η . The trigger SFs are calculated as described in Sec.7.2.2. For the identification and isolation of the related SFs, the Muon POG recommendations are followed, as described in [84].

5.3.3 Tau identification

The Tau POG provides SFs and energy scale corrections for each of the Run 2 data-taking periods individually. The efficiency of hadronically decaying τ to pass the τ_h identification criteria of the DeepTau algorithm has been measured using $Z/\gamma\gamma^* \rightarrow \tau_h\tau_h$ events [71]. The ratio of the efficiency measured in data to that measured in simulation, depends on the τ_h p_T and the τ_h identification discriminant used, i.e. VSjet, VSe and VSmu. More specifically, there are three types of corrections applied; corrections to genuine taus (VSjet), corrections to genuine electrons misidentified as taus (VSe), and corrections to genuine muons misidentified as taus (VSmu). For the VSjet corrections the identification SFs are applied in p_T bins for each year separately, and their values depend on the DeepTau discriminator WP used. The SFs on the VSe discriminator are split into barrel and endcap regions and applied for each year separately while the SFs on the VSmu discriminator are applied as a function of the τ_h pseudorapidity only, the binning of which was determined by the muon sub-detector and tracker geometries. In addition, a tau energy correction is applied as a function of the Decay Mode (DM), for each year separately. The values and supporting documents for all quoted SFs can be found in [72] and [85], respectively.

5.3.4 Electron energy corrections

E/gamma POG provides residual corrections to scale the data to the MC and smear the MC to match the data resolution for both electrons and photons. This analysis uses electron energy corrections along with their systematic errors. The corrected trk-ECAL combined energy (E_T) and four-momentum (p4) are used, as presented in [73]. Systematic variations on scale and smearing, are applied only to the MC, as recommended by POG.

5.3.5 MET corrections

Raw MET is the negative vector sum of all reconstructed particles. Thus, it is systematically different from the true MET, which is carried by invisible particles, due to various factors, such as possible detector misalignments, non-isotropic detector responses, the non-compensating nature of the calorimeters, possible inactive calorimeter cells or tracking regions and beam spot displacements. The JetMET POG provides corrections [74] which im-

prove the true MET estimation. In this analysis, the xy-shift correction is used to reduce the MET-phi modulation. True MET has no dependence on phi due to the rotational symmetry of the collisions around the beam axis. However, it is observed that the reconstructed MET does depend on phi. The amplitude of the modulation increases roughly linearly with the number of pile-up interactions. Shifting the coordinate origin in the transverse momentum plane as a function of different particle species and eta bins helps to reduce this modulation. The correction takes as inputs the number of vertices in the offlineSlimmedPrimaryVertices collection and the corrections are derived per run era.

5.3.6 B-tagging corrections

The simulated events are corrected for the difference between data and simulation derived b-tagging efficiencies, by calculating and applying a suitable SF for each event. This per-event SF can be calculated by applying different per-jet SFs to each jet in the event. The per-event SFs used in this analysis are derived from Method 1a [75]. The per-jet difference in b-tagging efficiency has been quantified by the BTV POG [76]. The results are summarized in payload files containing per-jet SFs to be applied on jets in simulated events, as a function of p_T , η , and jet flavour [78]. The jet flavors are separated into b , c , g , and uds categories. The c flavor jets are assumed to perform like the b flavor jets while gluon jets and jets for which the flavor matching failed are taken to be jets of light (uds) flavor. The dependence on jet η is assumed to be small compared to other effects, so it is neglected. The difference in b-(mis)tagging efficiency of a jet can be expressed as per-jet scale factor, defined as f_{tag} and f_{mistag} , respectively. These efficiencies are measured for the DeepJet b-tagging algorithm used to select b-jets in Signal Regions (defined in Section 6.2). Simulation efficiencies for the medium b-tagging WP are presented in Fig 5.1, as a function of the jet's p_T . Data and simulation efficiencies are subsequently used to determine the per-event SFs for reweighting the simulated events.

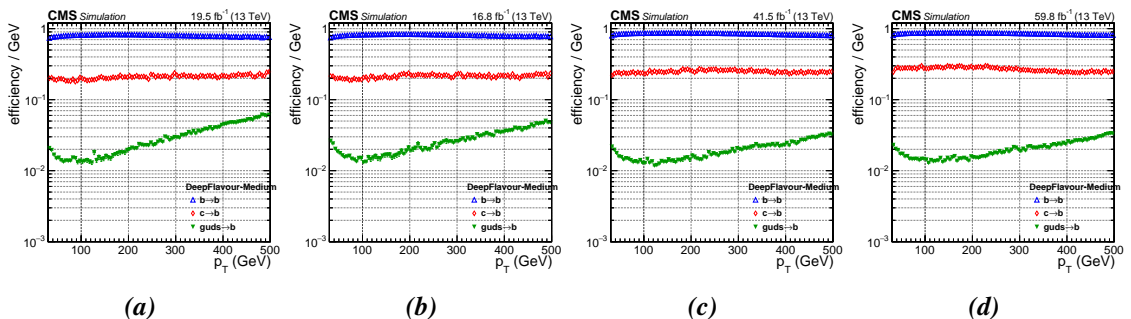


Figure 5.1: Simulated efficiency of different quark/gluon flavor jets to pass the medium b-tag wp of the DeepJet algorithm. Results are presented for (a) 2016 pre-VFP, (b) 2016 post-VFP, (c) 2017, and (d) 2018.

6 Analysis: Search for a charged Higgs boson

In this thesis, heavy charged Higgs bosons are searched through the $pp \rightarrow tbH^\pm$ production and the $H^\pm \rightarrow H^0(h^0)W^\pm$ decay mode, in final states where $H^0(h^0) \rightarrow \tau\tau$, with a representative Feynman Diagram shown in Fig6.1. The H^0 identifies with the heavy (non-SM) CP-even Higgs boson and has a mass of $m_{H^0} = 200$ GeV or $m_{H^0} = 300$ GeV. The h^0 identifies with the light (non-SM) CP-even Higgs boson and has a mass of $m_{h^0} = 80$ GeV or $m_{h^0} = 90$ GeV. Additionally, another mass point at 125 GeV for the CP-even neutral Higgs boson is been used, for the SM-like Higgs case, which could either be the heavy or light CP-even Higgs boson. The presence of two taus in the final state results in sixteen different possible final states, the majority of which include the presence of a hadronically decaying tau lepton (τ -jet or τ_h). This work targets the final states of hadronic tau plus 2 same flavoured light leptons ($2\ell^{sf}\tau_h = 2\ell^{os}\tau_h + 2\ell^{ss}\tau_h$) and one hadronic tau plus 2 different flavoured light leptons ($2\ell^{df}\tau_h$) final states, which amount to $\sim 16.5\%$ of all possible final states, as shown in Fig6.1. Final states with one and two hadronically decaying τ_h s plus one light lepton were studied in a previously published analysis, referred through this study as HIG-21-010 [79].

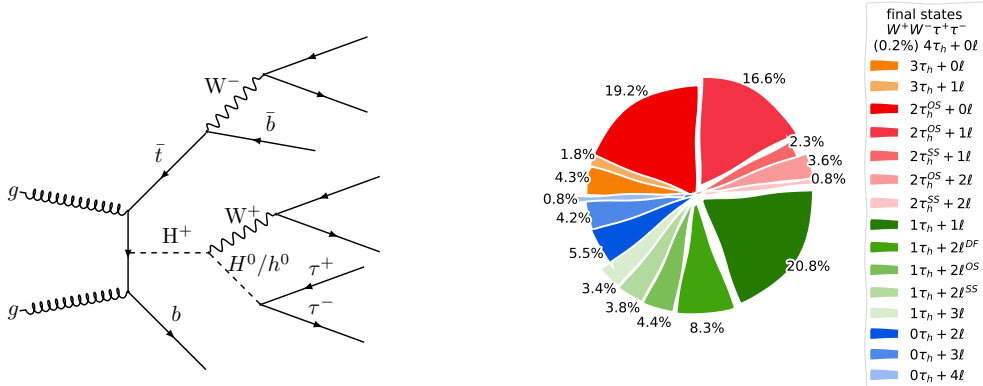


Figure 6.1: The LO Feynman diagram (Left) for heavy charged Higgs boson production at the LHC through $gg \rightarrow tbH^\pm$ in the 4FS, including the subsequent decay of the top quark and the decay of the charged Higgs boson into the neutral Higgs and W bosons. The breakdown and categorization of all possible final states after the leptonic or hadronic decay of the tau leptons and W bosons is visualized in a pie chart (Right).

The final state observables for the $2\ell^{sf}\tau_h$ are either two muons or two electrons, a hadronically decaying tau lepton, missing E_T from the neutrinos, and at least three jets with at least one of them tagged as a b-jet. For the $2\ell^{df}\tau_h$ the observables are similar to the $2\ell^{sf}\tau_h$, but instead of two same flavoured leptons, a muon, and an electron are required.

The events are triggered with either a single muon trigger or with a single electron trigger for the final states with muons or electrons respectively. For the $2\ell^{df}\tau_h$ events are selected via single muon or single electron trigger, performing the appropriate cross-cleaning, as

explained later on. Events with two muons or two electrons, one identified τ_h and at least two additional hadronic jets, with at least one of which should be tagged as b-jet, are selected in the $2\ell^{sf}\tau_h$ analysis. Same for $2\ell^{df}\tau_h$ analysis, but instead of two same flavoured leptons, events with exactly one muon and exactly one electron are selected instead. Events with isolated electrons are rejected in the di-muon final state analysis to ensure the orthogonality with the electron final state analysis. For the same reason, muons are rejected in the di-electron final state analysis.

For the $2\ell^{sf}\tau_h$ and $2\ell^{df}\tau_h$ final states, the limits are extracted by performing a maximum likelihood (MLHD) fit to data on the output of a dedicated parameterized Deep Neural Network (DNN).

Throughout this study, charge conjugate states are implied, the cross section $\sigma(pp \rightarrow \bar{t}(b)H^+)$ denotes the sum $\sigma(pp \rightarrow \bar{t}(b)H^+) + \sigma(pp \rightarrow t(\bar{b})H^-)$, and the branching fractions $\mathcal{B}(H^+ \rightarrow X)$ stands for $\mathcal{B}(H^\pm \rightarrow X)$.

The main backgrounds for this channel arise from the $t\bar{t}$ and $t\bar{t}X$ processes. Smaller backgrounds from single top production, $W + jets$, $Z/\gamma^* + jets$, diboson (WW,ZZ,WZ) and triboson (WWW,WWZ,WZZ,ZZZ) events are also taken into account. As no SUSY (Supersymmetry) particles have been discovered, potential SUSY backgrounds are not taken into account in this analysis. The SM backgrounds with misidentified muons, electrons, and/or hadronic taus referred to as misidentified- ℓ , are measured with a Loose-to-Tight Extrapolation Method (LTEM), a Fake Rate (FR) based method, thoroughly explained in Sec. 8. The remaining backgrounds with prompt/genuine light leptons and taus, isolated electrons, and muons faking taus are estimated directly from simulation.

6.1 Object Identification and Selection

The following subsections describe the criteria applied to select the events used in this analysis. The selection criteria are optimized using simulated signal and background samples, as described in Sec. 8. The search strategy for signal extraction is described in Sec. 9.

6.1.1 Primary vertices

The PV for this analysis is determined using the criteria depicted in Table 6.1. There is likely more than one PV in an event due to the additional interactions in the same bunch crossing. In this case, the vertex with the largest value of the sum of all transverse momenta squared $\sum_i p_{T,i}^2$ of the associated tracks is considered to be the primary pp interaction vertex. All other PVs are considered to be pile-up vertices.

Selection	Description
$d.o.f > 4$	minimum number of associated degrees of freedom ($d.o.f$)
$ \rho = \sqrt{x^2 + y^2} < 2$ cm	maximum distance from the origin (0, 0, 0) in the $x - y$ plane
$ z < 24$ cm	the PV z -coordinate should be within 24 cm from the CMS detector

Table 6.1: Summary of the PV selection criteria.

6.1.2 Electrons

An MVA algorithm which relies on the expected shower shape created by electrons, as well as matching criteria between the shower and tracking clusters, is used to identify suitable electron candidates reconstructed with the *GSF* method [36]. The algorithm, provided by the EGAMMA POG [81], is based on a dedicated Boosted Decision Tree (BDT), a machine learning algorithm, specifically trained to discriminate electrons from jets. The training is performed using prompt electrons as signal and unmatched plus non-prompt electrons as background in DY+jets ($Z/\gamma^* + jets$) MC samples.

The training was performed in low- p_T and high- p_T bins ($p_T = 5 - 10$ GeV and $p_T > 10$ GeV), as well as in three η regions (inner barrel, outer barrel, endcap). Two independent identification discriminators are trained, one denoted as "iso" and the other as "noIso". When using the "noIso" discriminator, additional electron isolation requirements are applied based on the PF isolation value (pf-iso), to ensure proper isolation. The pf-iso is a value produced by using the three PF isolation components (tracker, ECAL, HCAL) and reflects the surrounding activity. Four distinct WPs are defined based on PF isolation, loose ($pf\text{-iso} \leq 0.25$), medium ($pf\text{-iso} \leq 0.20$), tight ($pf\text{-iso} \leq 0.15$), and very-tight ($pf\text{-iso} \leq 0.10$). For each identification discriminator, three WPs are defined based on the BDT output score, $wpLoose$, $wp90$ and $wp80$, corresponding to 98%, 90%, and 80% signal efficiency, respectively. The BDT cuts associated with these WPs are outlined in [82].

The significance of the impact parameter in 3D (sip3d) is an important variable used to improve the identification of prompt (produced at the PV) electrons and muons while suppressing backgrounds from non-prompt leptons. The sip3d is the ratio of the 3D impact parameter to its uncertainty $\frac{IP^{3d}}{\sigma_{IP}^{3d}}$. A low sip3d value indicates that the lepton is more likely to be prompt, whereas a high sip3d suggests a displaced origin, non-prompt. Applying cuts on sip3d helps to reduce backgrounds from non-prompt sources, especially those coming from heavy-flavor jets (like b -jets), which would otherwise be incorrectly identified as signal leptons. Therefore, selected electrons are required to pass a sip3d cut.

An electron candidate is selected as a good candidate for the analysis if it satisfies the following criteria

- $p_T > 10.0$ GeV or $p_T > [28, 35, 35]$ GeV if trigger matching is required.

- $|\eta| < 2.1$, $\text{sip3d} \leq 10$.
- passed mvaEleID_Fall17_noIso_V2_wp90, PF isolation (pf-iso) < 0.15 .

Additionally, if a selected electron is required to fire the trigger, then a trigger threshold-dependent p_T requirement is applied, as noted above, and the offline selected electron is matched to the HLT trigger electron by requiring:

$$\Delta R(e, e_{\text{HLT}}) < 0.1 \quad (42)$$

Similarly, an electron candidate is vetoed if satisfies the following:

- $p_T > 10.0$ GeV and $|\eta| < 2.5$.
- passed mvaEleID_Fall17_noIso_V2_wpLoose, $\text{pf-iso} < 0.25$.

Events with additional loosely isolated electrons with $p_T > 10.0$ and $|\eta| < 2.5$ are excluded to ensure that no overlapping events are used between various Signal Regions (SRs, defined in Section 6.2).

To measure the background from misidentified electrons, appropriate regions should be defined. These regions are called Control Regions and are defined by inverting the isolation selection criterion. More details are given in Sec. 8.

6.1.3 Muons

The standard muon reconstruction is used, which relies on the linking of track segments reconstructed in the silicon tracking detector with those in the muon system [83]. Muon candidates used in the analysis are identified with the PF CutBasedID identification provided by Muon POG [84], which is designed to be highly efficient for prompt muons. A muon candidate is selected for the analysis if satisfies all of the following criteria:

- $p_T > 10.0$ GeV or $p_T > [26, 28, 26]$ GeV if trigger matching is required.
- $|\eta| < 2.4$, $\text{sip3d} \leq 10$.
- passed Tight wp of CutBasedID, $\text{pf-iso} < 0.15$.

Additionally, as for the electron selection, if a selected muon is required to fire the trigger, then a trigger threshold-dependent p_T requirement is applied, as noted above, and the offline selected muon is matched to the HLT muon by requiring:

$$\Delta R(\mu, \mu_{\text{HLT}}) < 0.1 \quad (43)$$

A muon candidate is vetoed if it satisfies all of the following criteria:

- $p_T > 10.0$ GeV and $|\eta| < 2.4$.

- passed loose WP of CutBasedID, passed pf-iso<0.25.

Events with additional loosely isolated muons satisfying $p_T > 10.0$ and $|\eta| < 2.4$ are excluded to ensure orthogonality among SRs.

As for the case of the electrons, in order to measure the background arising from misidentified muons, appropriate CRs are defined by inverting the muon isolation requirement. More details are given in Sec. 8.

6.1.4 Hadronically decaying taus (τ_h)

The hadronic decays of τ leptons (τ_h) are reconstructed and identified as presented in Sec. 3.8. For this study, the Tau POG recommendations are followed [85]. The τ_h candidates used in this analysis are required to be consistent with 1 or 3 prong decays, reconstructed with the decayModeFinding which defines the Decay Mode (DM) as an integer between 0 and 11, as shown in Table 6.2.

		DM = $5 \cdot (N_{\pi^\pm} - 1) + N_{\pi^0}$							
		0	1	2	5	6	7	10	11
N_{π^\pm}	1	1	1	2	2	2	3	3	
	N_{π^0}	0	1	2	0	1	2	0	1

Table 6.2: The τ_h DMs found by the mode finding algorithm.

Additionally, the following selection criteria are applied for selecting τ_h used in the analysis:

- $DM = [0,1,2,10,11]$, $p_T > 30$ GeV, $|\eta| < 2.4$.
- byMediumDeepTau2017v2p1VSe and byTightDeepTau2017v2p1VSmu.
- byMediumDeepTau2017v2p1VSjet.

The selected τ_h s are also required to be separated from other τ_h but also electron and muon objects by requiring

$$\Delta R(\tau_h, \tau_h/\mu/e) > 0.5 \quad (44)$$

As in the electron and muon case, for the selection of the CR with inverted tau isolation for the measurement of the background from events with misidentified τ_h , the isolation criterion is loosened compared to the nominal analysis, i.e. if any τ_h candidate passes the VVVLooseDeepTau2017v2p1VSjet isolation criterion, the event is accepted.

6.1.5 Jets

Jets are reconstructed by clustering all particles reconstructed by the PF event reconstruction, with the anti- k_T algorithm implemented in *Fastjet*, as explained in Sec. 3.6. The jets selected for this study are required to satisfy the following criteria, in accordance with the JetMET POG [86] recommendations:

- $p_T > 30 \text{ GeV}$, $|\eta| < 2.4$, $\Delta R < 0.4$
- PF-jetID Tight (fake jet suppression)

The PF-jetID provided by the JetMET POG is a set of selection criteria used to identify jets reconstructed with the PF algorithm and ensure they are of good quality. The goal of PF-jetID is to reject fake jets while retaining genuine physics objects. The PF-jetID has different WPs based on the strictness of the requirements, however, the JetMET POG recommends using the Tight working point for most analyses, as it provides a good balance between signal efficiency and background rejection.

The energy of the reconstructed jets is corrected as a function of their p_T and η and additional Jet Energy Corrections (JEC) are applied to tackle contributions coming from pileup events [87]. Corrections related to the Jet Energy Scale (JES) are also applied [88].

The two leading jets used in the analysis are required to pass a higher p_T threshold of 40 GeV. The collection of jets is cleaned for any overlapping with the selected τ_h , muon and electron candidates by requiring:

$$\Delta R(\text{jet}, \tau_h/\mu/e) > 0.5. \quad (45)$$

6.1.6 B-jets

At least one of the selected jets are required to be identified as b-tagged with the DeepJet algorithm described in Sec. 3.7. All selected bjets are required to pass the medium WP of the DeepJetID. Taking into account the differences between data and simulation in terms of tagging efficiency, a per-event Scale Factor (SF) is applied to simulated events as described in Sec. 5.3.6.

6.1.7 MET

The vector of the missing transverse momentum (\vec{p}_T^{miss}) represents the projection of the negative vector sum of all reconstructed PF candidates' momenta in the transverse to the beam axis plane. Its magnitude is referred to as $|\vec{E}_T|$ or simply as E_T^{miss} (see Sec. 3.9). Quality requirements are also applied to remove events in which detector effects, such as electronic

noise, can affect the MET reconstruction. Type-1 corrections are applied for this analysis, which propagate the jet energy corrections (JEC) to the MET. Type-1 corrections on MET refer to adjustments applied to account for the mismeasurement of jet energy in the detector. If jets are mismeasured, the MET will also be inaccurate. After the jets are corrected, the difference between the corrected jet energy and the uncorrected jet energy is used to adjust the MET, as shown in Eq.46.

$$\vec{E}_T^{\text{miss, Type-I}} = \vec{E}_T^{\text{miss, unc.}} - \sum_{\text{jets}} (\vec{p}_T^{\text{JEC}} - \vec{p}_T^{\text{unc.}}) \quad (46)$$

No type-1 PF E_T^{miss} requirement is applied for any of the Signal Regions explored in this study. However, since it is used as input for the extraction of the final fit discriminant (Sec. 9.1), the MET is corrected further by applying the "x-y corrections" described in Sec. 5.3.5.

6.1.8 Top tagging

Although top quark is produced in association with the H^\pm , no top tagging is applied in the search because of reduced efficiency of the top taggers. However, to test the τ_h fake rates a CR is defined using events requiring the presence of a top candidate (for details see Sec. 8), and is worth noting the algorithm that is used. The analysis uses a home developed tagging algorithm for top quarks of moderate pt, in order to identify top quarks decaying hadronically to well separated products (resolved top tagging) as described in [89].

6.1.9 Duplicate Removal

For the search in the $2\ell^{df}\tau_h$ category, events are selected requiring two non-orthogonal to each other triggers, SingleMuon and SingleElectron triggers. In order to reject duplicate events, a careful procedure is followed. Events are initially selected with the SingleMuon trigger and if and only if the event failed to pass the SingleMuon trigger, then the SingleElectron trigger is examined. Thus, for data, events from primary SingleMuon dataset are selected only if they passed the SingleMuon trigger while the ones from SingleElectron/EGamma primary datasets are selected only if they failed the SingleMuon trigger but passed the SingleElectron one.

6.2 Event Selection

The complete set of the criteria used to select $2\ell^{sf}\tau_h$ ($\mu\mu\tau_h$ and $ee\tau_h$) and $2\ell^{df}\tau_h$ events are summarised in Table 6.3.

Selection	$ee\tau_h$	$\mu\mu\tau_h$	$\mu e\tau_h$
Trigger	At least 1 isolated $\ell = e, \mu$		
	electrons		
N_e	= 2	= 0	= 1
p_T^e	≥ 10.0	≥ 10.0	≥ 10.0
$p_T^{e,trg}$	$\geq [28, 35, 35]$	-	$\geq [28, 35, 35]$
$ \eta^e $	≤ 2.1	≤ 2.5	≤ 2.1
$\frac{IP^{3d}}{\sigma_{IP}^{3d}}$ (SIP3D)	≤ 10.0	-	≤ 10.0
muons			
N_μ	= 0	= 2	= 1
p_T^μ	≥ 10.0	≥ 10.0	≥ 10.0
$p_T^{\mu,trg}$	-	$\geq [26, 28, 26]$	$\geq [26, 28, 26]$
$ \eta^\mu $	≤ 2.4	≤ 2.4	≤ 2.4
$\frac{IP^{3d}}{\sigma_{IP}^{3d}}$ (SIP3D)	-	≤ 10.0	≤ 10.0
τ_h object			
N_{τ_h}	= 1	= 1	= 1
$p_T^{\tau_h}$	≥ 30.0	≥ 30.0	≥ 30.0
$ \eta^{\tau_h} $	≤ 2.3	≤ 2.3	≤ 2.3
τ_h DM	0, 1, 2, 10, 11	0, 1, 2, 10, 11	0, 1, 2, 10, 11
jets			
N_{jets}	≥ 2	≥ 2	≥ 2
$p_T^{jets_{1,2}}$	≥ 40.0	≥ 40.0	≥ 40.0
$p_T^{jets_{\geq 3}}$	≥ 30.0	≥ 30.0	≥ 30.0
$ \eta^{jets} $	≤ 2.4	≤ 2.4	≤ 2.4
bjets			
N_{bjets}	≥ 1	≥ 1	≥ 1

Table 6.3: Summary of the event selection criteria for the $2\ell^{sf}\tau_h$ and $2\ell^{df}\tau_h$ final state analyses. The p_T variables are reported in units of GeV. Selection criteria that depend on the year of data taking are presented in parentheses with the order corresponding to [2016 (pre-VFP, post-VFP), 2017, 2018].

7 Trigger Efficiency Measurement

This analysis selects events that have been collected using the single muon and electron triggers. The triggers are briefly described in Sec. 7.1 and the measurement of the efficiency of each one is presented in Sec. 7.2.1 and in Sec. 7.2.2 for the electron and the muon respectively.

7.1 Description

The light lepton (e or μ) in all final state categories of the analysis, namely $ee\tau_h, \mu\mu\tau_h$ and $\mu e\tau_h$, used to trigger, could originate either from the leptonic decay of the tau lepton or any of the 2 W bosons decay.

The trigger paths used in different years of the data taking period are listed in Table 7.1. The single muon and single electron triggers remained unprescaled during the full Run 2 data taking. For 2017, HLT_Ele32_WPTight_Gsf is reconstructed from HLT_Ele32_WPTight_Gsf_L1DoubleEG by following the related EGamma POG recommendations [90].

To ensure that the lepton used in the analysis is the one that triggered the event, it is further required the distance in η - φ space between the trigger lepton and the offline lepton to be $\Delta R(\ell, \ell_{\text{HLT}}) < 0.1$.

Primary Dataset	HLT Path		
	2016	2017	2018
SingleMuon	HLT_IsoMu24_v*	HLT_IsoMu27_v*	HLT_IsoMu24_v*
	HLT_IsoTkMu24		
SingleElectron	HLT_Ele27_WPTight_Gsf_v*	HLT_Ele32_WPTight_Gsf_v*	—
EGamma	—	—	HLT_Ele32_WPTight_Gsf_v*

Table 7.1: List of the single lepton triggers used in the analysis for the three year eras of the LHC run 2 data taking.

7.2 Measurement of the Trigger Efficiency

The trigger efficiencies are measured with two different approaches. The first one is the original Tag-and-Probe (TnP) method generally used for trigger efficiency measurements and the second is the orthogonal-dataset-method (ODM). In the former one, same-flavour ($TnP_{\ell\ell}$) and in the latter one different-flavour ($ODM_{\mu e}$) leptons are used.

The $TnP_{\ell\ell}$ method utilizes a known mass resonance, such as the Z^0 boson, to select particles of a specific type and probe the efficiency with which a particular selection criterion

is successfully applied. In general, the tag is an object that passes a set of tight selection criteria, designed to be satisfied by the target particle type. Consequently, the fake rate for passing the tag selection criteria is normally quite small. The probe is of the same type as the probe on which the criterion whose efficiency is to be determined and a loose selection is applied. The probe particle is selected in conjunction with the tag particle so they give the invariant mass of the resonance. The probe efficiency is then measured by counting the number of probe particles that pass the desired selection criteria as

$$\varepsilon = \frac{N_{\text{probes}}^{\text{pass}}}{N_{\text{probes}}} \quad (47)$$

where $N_{\text{probes}}^{\text{pass}}$ is the number of probes passing the desirable selection and N_{probes} is the total number of probes counted using the resonance. In general, a probe object may also pass the tag selection criteria. In this case, it will appear in both the tag and the probe lists and produce a double pairing in the same event, in which case the definition in Eq. 47 must account for the double pairing. However, in this study, the two same-flavoured leptons are selected to be distinguishable, based on the sign of their electric charge, as explained later on.

The same definition in Eq. 47 stands for $ODM_{\mu e}$ as well. The only difference is that the tag and the probe are of a different particle type, which means particle types are distinguishable. Also, it avoids a possible bias from the definition of a selection criterion that applies both to the tag and the probe particles.

The efficiency measurement is performed as a function of the transverse momentum of the probe lepton and for three different η - regions, separately for data and simulation for each year. Their ratio defines the trigger-specific SFs that are applied to simulation samples used in the analysis. Here an inclusive version is presented for simplicity. The SFs uncertainties are defined as a systematic error, calculated as the difference between the trigger SFs of the two methods.

7.2.1 Single electron trigger

The selection criteria used to measure the single electron trigger with the $TnP_{\ell\ell}$ method are summarised in Table 7.2. The tag object is required to match the trigger electron, have positive charge, by convention, be within the tracker acceptance ($|\eta| < 2.4$), and to have p_T larger than 30, 35, and 35 GeV for 2016, 2017, and 2018 respectively. Furthermore, tight identification and isolation criteria are imposed. The probe object is required to be of opposite charge (negative) and satisfy identical selection criteria as with the tag object, with the exception of a lower p_T threshold of 10 GeV. The dielectron system is also required to be well separated in $\eta - \phi$ space with $\Delta R(e^+, e^-) > 0.5$ and be within an invariant mass

window of ± 15 GeV from the Z^0 pole mass, in order to select $Z/\gamma^* \rightarrow e^+e^-$ events. A muon veto ensures that the selected events do not contain muons with $p_T > 10$ GeV and $|\eta| < 2.4$, that pass the loose selection criteria of CutBasedID and pf-iso.

Selection	Tag e	Probe e
$\Delta R(e, e_{HLT})$	≤ 0.1	-
p_T	$\geq [30, 35, 35]$ GeV	≥ 10 GeV
$ \eta $	< 2.4	< 2.4
Charge (Q)	$=+1$	$=-1$
Relative pf isolation	< 0.15	< 0.15
Identification	mvaEleID_Fall17_noIso_V2_wp90	mvaEleID_Fall17_noIso_V2_wp90
$\Delta R(e^+, e^-)$		> 0.5
$m_{e^+e^-}$		$\in (75, 105)$ GeV

Table 7.2: Summary of selection criteria for the single electron trigger efficiency measurement with the $TnP_{\ell\ell}$ method.

The overall HLT efficiency for the single electron trigger with the $TnP_{\ell\ell}$ method is shown in Fig. 7.1 as a function of the p_T of the probe electron for all three years. The same procedure has been tested vice-versa (tag is negatively charged and probe positively charged) to make sure no charge dependence is introduced in the measurement.

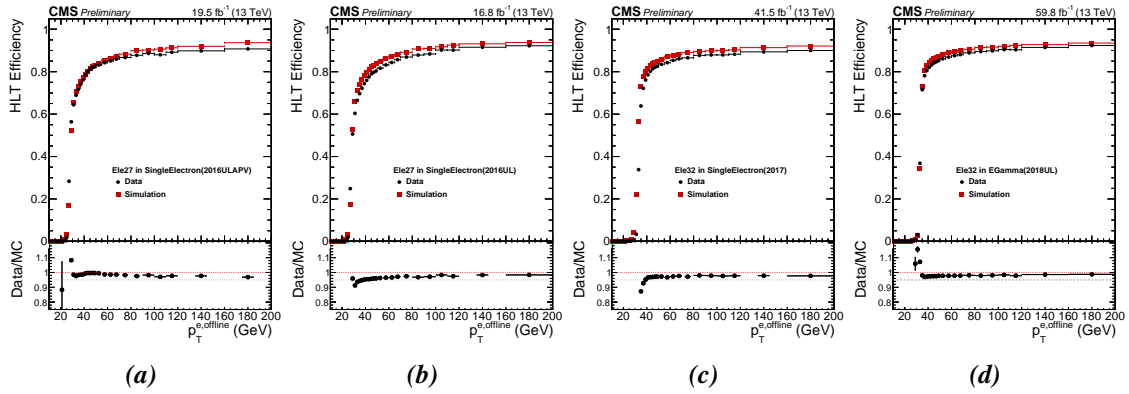


Figure 7.1: The overall Single Electron HLT efficiency as a function of the p_T of the offline electron probe as determined with the $TnP_{\ell\ell}$ method for (a) 2016 pre-VFP, (b) 2016 post-VFP, (c) 2017 and (d) 2018.

The selection criteria used to measure the single electron trigger with the $ODM_{\mu e}$ method are summarised in Table 7.3. The tagged muon object is required to match the trigger muon, to be within the tracker acceptance ($|\eta| < 2.4$), and to have p_T larger than 26, 28, and 26 GeV, for 2016, 2017, and 2018, respectively. It is also required to pass the tight cut-based identification and relative isolation criteria are also imposed. The probe electron is required to pass the selection criteria required for the probe electrons in the $TnP_{\ell\ell}$ method.

Selection	Tag μ	Probe e
$\Delta R(\mu, \mu_{\text{HLT}})$	≤ 0.1	-
p_T	$\geq [26, 29, 26] \text{ GeV}$	$\geq 10 \text{ GeV}$
$ \eta $	< 2.4	< 2.4
Relative Isolation	< 0.15	< 0.15
Identification	isCutBasedIDTight	mvaEleID_Fall17_noIso_V2_wp90
$\Delta R(e, \mu)$		> 0.5

Table 7.3: Summary of selection criteria for the single electron trigger efficiency measurement using the $ODM_{\mu,e}$ method.

The overall HLT efficiency for the single electron trigger with the $ODM_{\mu,e}$ method is shown in Fig. 7.2 as a function of the p_T of the probe electron for all three years.

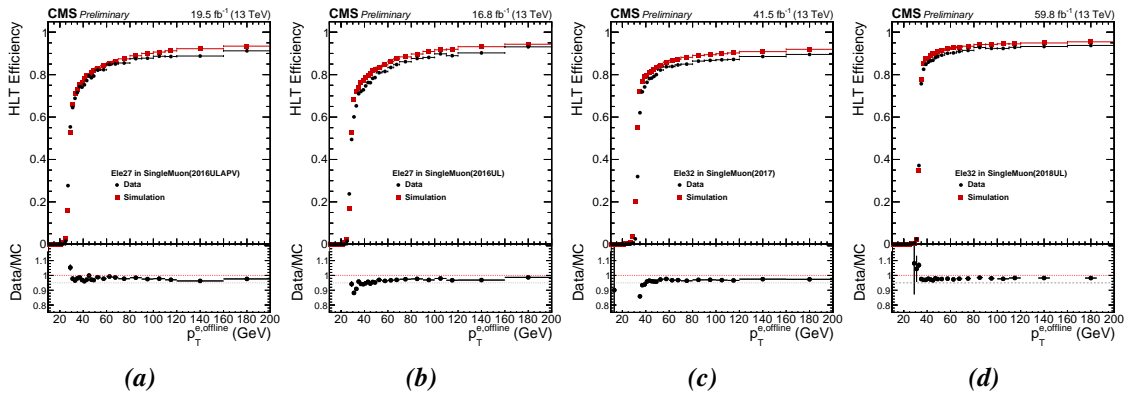


Figure 7.2: The overall Single Electron HLT efficiency as a function of the p_T of the offline electron probe as determined with the $ODM_{\mu,e}$ method for (a) 2016 pre-VFP, (b) 2016 post-VFP, (c) 2017 and (d) 2018.

A comparison of the results from the two methods, $TnP_{\ell\ell}$ and $ODM_{\mu,e}$, is presented in Fig. 7.3 for each year of the collider running. The p_T resolution of the electrons defines the extent of the turn-on curves, where the efficiency changes quickly and background contamination can be important. A quasi-plateau region appears to establish at about 120 GeV for 90-95% efficiency. The two methods are found to be in agreement in terms of the turn-on shapes and their associated SFs. In this analysis, the trigger SFs evaluated with the $TnP_{\ell\ell}$ method are adopted since it offers better statistics. The SFs uncertainties are defined as a systematic error, calculated as the difference between the trigger SFs of the two methods.

7.2.2 Single muon trigger

The selection criteria used to measure the single muon trigger with the $TnP_{\ell\ell}$ method are summarised in Table 7.4. The tag object is required to match the trigger muon, have positive charge, by convention, to be within the tracker acceptance ($|\eta| < 2.4$), and to have p_T

7.2 Measurement of the Trigger Efficiency

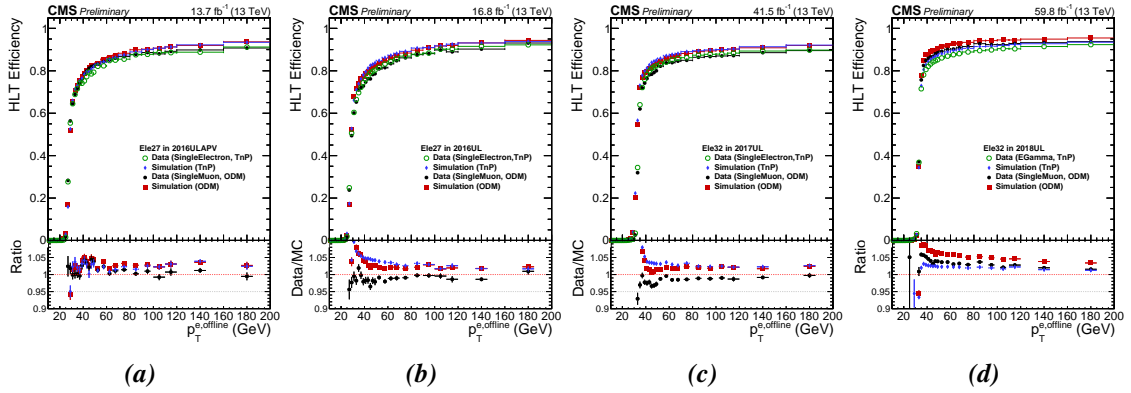


Figure 7.3: Comparison of the single electron HLT trigger efficiency as a function of the offline probe electron p_T for the $TnPE\ell$ and $ODM_{\mu e}$ for (a) 2016 pre-VFP, (b) 2016 post-VFP, (c) 2017 and (d) 2018.

larger than 26, 29 and 26 GeV, for 2016, 2017 and 2018, respectively. Furthermore, tight identification criteria are imposed along with tight relative isolation. The probe object is required to be of opposite charge (negative) and satisfy identical selection criteria as with the tag object, with the exception of a lower p_T threshold of 10 GeV. The system is also required to be well separated in $\eta - \phi$ space with $\Delta R(\mu^+, \mu^-) > 0.5$. In addition, for 2016 data-taking period, an additional requirement of $\Delta\phi(\mu^+, \mu^-) > 1.23$ (or not in the same endcap) is used to take care of a known bug in Endcap Muon Track Finder (EMTF), (run < 278167) causing inefficiencies for muons in close proximity. The dimuon system is also required to be within an invariant mass window of ± 15 GeV from the Z^0 pole mass, in order to select $Z/\gamma^* \rightarrow \mu^+ \mu^-$ events. An electron veto ensures that the selected events do not contain electrons loose selection criteria, with $p_T > 10$ GeV, $|\eta| < 2.4$ and pf isolation < 0.25 . The overall HLT efficiency for the single muon trigger with the $TnPE\ell$ method is shown in Fig. 7.4 as a function of the p_T of the probe muon for each of the three running periods of the LHC running. The same procedure has been tested vice-versa (tag is negatively- and probe positively-charged) to make sure there is no charge bias in the method.

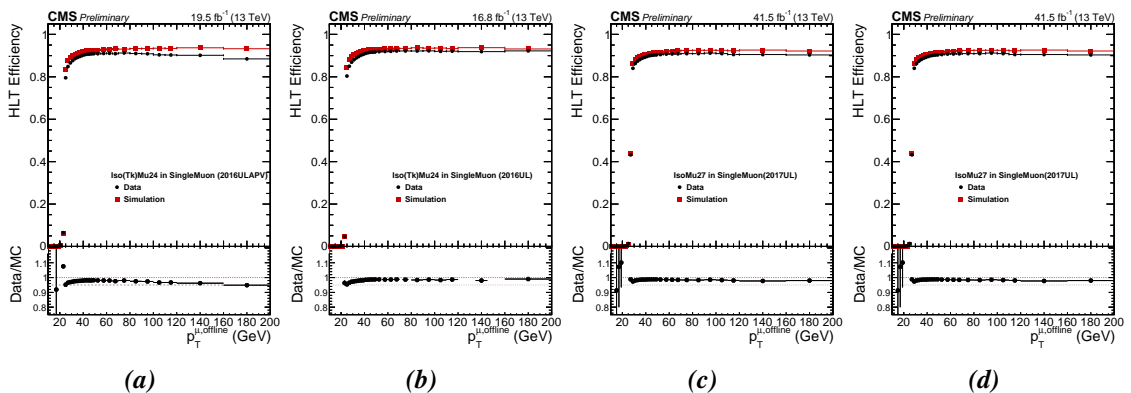


Figure 7.4: The overall Single Muon HLT efficiency as a function of the p_T of the offline muon probe as determined with the $TnPE\ell$ method for (a) 2016 pre-VFP, (b) 2016 post-VFP, (c) 2017 and (d) 2018.

Selection	Tag μ	Probe μ
$\Delta R(\mu, \mu_{HLT})$	≤ 0.1	-
p_T	$\geq [26, 29, 26] \text{ GeV}$	$\geq 10 \text{ GeV}$
$ \eta $	< 2.4	< 2.4
Charge (Q)	$=+1$	$=-1$
Relative pf isolation	< 0.15	< 0.15
Identification	CutBasedIDTight	CutBasedIDTight
$\Delta\phi(\mu^+\mu^-)$	> 1.23 or not in same endcap (2016)	
$\Delta R(\mu^+, \mu^-)$		> 0.5
$m_{\mu^+\mu^-}$		$\in (75, 105) \text{ GeV}$

Table 7.4: Summary of selection criteria for the single muon trigger efficiency measurement with the $TnP_{\ell\ell}$ method.

The selection criteria used to measure the single muon trigger with the $ODM_{\mu e}$ method are summarised in Table 7.5. The tagged electron object is required to match the trigger electron, to have a p_T of at least 30, 35, or 35 GeV for 2016, 2017, and 2018, respectively, and be within the tracker acceptance ($|\eta| < 2.4$). Furthermore, tight MVA identification WP and pf isolation are imposed. The selection criteria for the probe muon are identical to the ones used for the $TnP_{\ell\ell}$ method (see Table 7.4). The overall HLT efficiency for the single muon trigger with the $ODM_{\mu e}$ method is shown in Fig. 7.5 as a function of the p_T of the probe muon for each of the three years of the LHC running.

Selection	Tag e	Probe μ
$\Delta R(e, e_{HLT})$	≤ 0.1	-
p_T	$\geq [30, 35, 35] \text{ GeV}$	$\geq 10 \text{ GeV}$
$ \eta $	< 2.4	< 2.4
Relative pf isolation	< 0.15	< 0.15
Identification	mvaEleID_Fall17_noIso_V2_wp90	CutBasedIDTight
$\Delta R(e, \mu)$		> 0.5

Table 7.5: Summary of selection criteria for the single electron trigger efficiency measurement with the $ODM_{\mu e}$ method.

A comparison of the results from the two methods, $TnP_{\ell\ell}$ and $ODM_{\mu e}$, is presented in Fig. 7.6 for all three years. Due to a better p_T resolution, the turn-on curves are much smaller when compared to that obtained for the electrons. The fast turn-on reaches a steady plateau at about 40 GeV, corresponding to an efficiency of about 90-95% efficiency. The two methods are found to be in agreement in terms of the turn-on shapes, as shown in Fig. 7.6, and their associated SFs. As with the single electron case described in the previous sub-section, in this analysis, the trigger SFs evaluated with the $TnP_{\ell\ell}$ method are adopted since it offers better

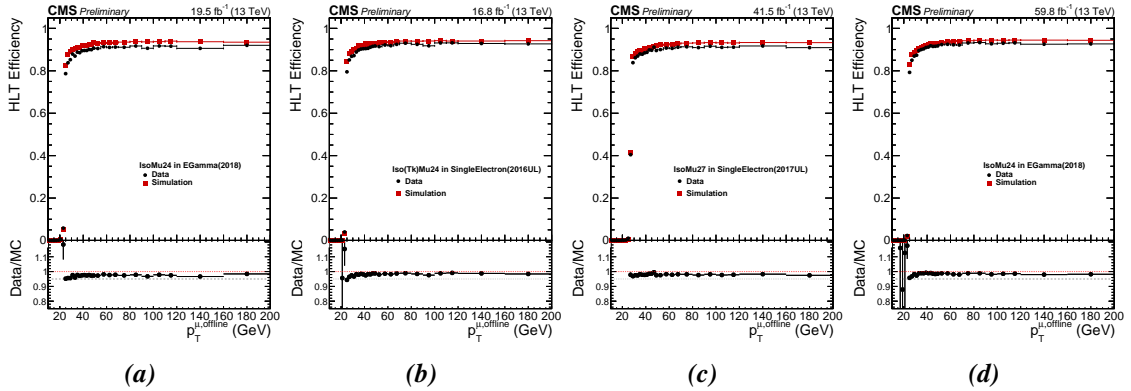


Figure 7.5: The overall Single Muon HLT efficiency as a function of the p_T of the offline muon probe as determined with the $ODM_{\mu e}$ method for (a) 2016 pre-VFP, (b) 2016 post-VFP, (c) 2017 and (d) 2018.

statistics. The SFs uncertainties are defined as a systematic error, calculated as the difference between the trigger SFs of the two methods.

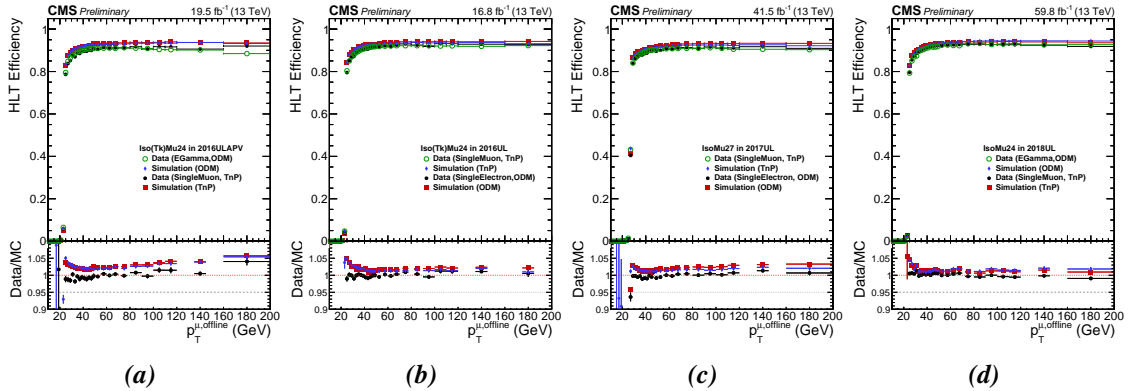


Figure 7.6: Comparison of the single muon HLT trigger efficiency as a function of the offline probe muon p_T for the $TnP_{\ell\ell}$ and $ODM_{\mu e}$ for (a) 2016 pre-VFP, (b) 2016 post-VFP, (c) 2017 and (d) 2018.

8 Background Estimation

The main backgrounds for all the final states considered, namely the $2\ell^{sf}\tau_h$ and $2\ell^{df}\tau_h$ can be decomposed into events containing genuine leptons (e, μ, τ_h), or events with an electron, a muon, or a jet being misidentified as a τ_h ($\ell \rightarrow \tau_h$ and jet $\rightarrow \tau_h$) and/or with a jet being misidentified as an electron or a muon (jet $\rightarrow e/\mu$). In this analysis, we consider as “genuine” or “prompt” leptons the ones that emerge from the decay of gauge bosons or τ -leptons. However, leptons can appear in decays of long-lived objects like, B- or C-mesons, k, π decays in flight, as by-products of the interaction of the photons, and also ordinary QCD jets (light quarks or gluons) that mimic the lepton signature. This type of lepton is called “non-prompt” and is the dominant source of misidentified leptons, or misID- ℓ in short. Other important background concerns SM processes containing prompt leptons and include $t\bar{t}$, $t\bar{t}X$, Single-t, DY+jets, Dibosons (WW, WZ, ZZ), Tribosons and W+jets production.

8.1 Strategy

The background estimation strategy involves the measurement of non-prompt leptons with data-driven technique known as Loose-to-Tight Extrapolation Method (LTEM) [91]. LTEM , which is described in Sec. 8.1.1, uses the fake rate method (see Sec. 8.2) in dedicated Control Regions (CRs) and Application Regions (ARs) in order to provide a reliable estimation of misID- ℓ background for multilepton final states. The measurements of the Fake Rates (FRs) jet $\rightarrow e$ jet $\rightarrow \mu$ and jet $\rightarrow \tau_h$ are presented in Sec. 8.2.1, Sec. 8.2.2 and Sec. 8.2.3, respectively. In order to validate the method, the fake rates are applied in the samples used to derive the fake rate. This step is done for self-consistency of the method and consists the “self-closure” tests, presented in Sec.8.3. The prompt e, μ, τ_h and minor $\ell \rightarrow \tau_h$ background is modeled using simulation as described in Sec. 8.5.

8.1.1 Loose-to-Tight Extrapolation Method

LTEM is a data-driven method which assumes that the prompt(p) and non-prompt(f) probabilities of prompt and non-prompt leptons to pass a tight lepton isolation given they satisfy a looser version of the same lepton isolation, can be described as a function of the lepton’s properties and event-topology related parameters. This approach reduces the dependence of p and f from the specific process the lepton originates from and allows the measurement of these probabilities in control regions with low signal contamination and their successful application to the signal region.

The LTEM is presented for the single lepton case while for the two and three lepton cases, the procedure is the same but more mathematically involved. A set of a total number of

events (N_{tot}) can be produced for a given single lepton event selection criteria with loose lepton isolation and can be categorized based on whether the lepton passed the tight version of the given lepton isolation, N_T , or not N_L (loose-not-tight). N_{tot} can also be decomposed to 2 subsets based on whether or not the lepton is prompt (N_P) or non-prompt (N_F), as shown in Eq. 48.

$$N_{tot} = N_T + N_L = N_P + N_F \quad (48)$$

The tight lepton isolation region consists of events with prompt and non-prompt leptons. Assuming that p and f are the rates for prompt and non-prompt leptons (e/μ or τ_h), the number of tight and loose-not-tight lepton events can be written as in Eq. 49 and Eq. 50, respectively. The p and f can be functions of lepton p_T , η , and sip3d, while for the τ_h case, can also be a function of the τ_h DM (or number of prongs).

$$N_T = pN_P + fN_F \quad (49)$$

$$N_L = (1 - p)N_P + (1 - f)N_F \quad (50)$$

Equations 49 and 50 can be written in a matrix form, as shown in Eq. 51. In this format, the isolation-based categorization is converted to an origin-based one by multiplying it with a transformation matrix, whose elements are the p and f rates. To simplify the notation, let $\hat{p} = 1 - p$ and $\hat{f} = 1 - f$.

$$\begin{pmatrix} p & f \\ \hat{p} & \hat{f} \end{pmatrix} \begin{pmatrix} N_P \\ N_F \end{pmatrix} = \begin{pmatrix} N_T \\ N_L \end{pmatrix} \quad (51)$$

Under the assumption that $f \neq p$, the inverse transformation of Eq. 51 is more useful, since the measurable subsets are the isolation-based ones, as already noted. This transformation leads to Eq. 52.

$$\begin{pmatrix} N_P \\ N_F \end{pmatrix} = \frac{1}{(f - p)} \begin{pmatrix} -\hat{f} & f \\ \hat{p} & -p \end{pmatrix} \begin{pmatrix} N_T \\ N_L \end{pmatrix} \quad (52)$$

Thus, the number of non-prompt leptons can be expressed as shown in Eq. 53.

$$N_F = \frac{\hat{p}}{f - p} N_T - \frac{p}{f - p} N_L \quad (53)$$

Under the assumption that the contribution of prompt leptons that fail the tight selection is negligible with respect to the contributions of non-prompt leptons, therefore $p = 1$ and $\hat{p} = 0$, Eq. 49 and Eq. 53 can be simplified and give :

$$N_T = MC^{prompt} + \frac{f}{1-f} N_L \quad (54)$$

In the case of 2 leptons present in the event, the same procedure is followed but the prompt and non-prompt rates for both leptons should be taken into account. Therefore the equations will include $p1$, $p2$, $f1$, and $f2$, the prompt and non-prompt rate for the first and second lepton. For example, in the case of two electrons, the first index could represent the leading in p_T electron while the second one the sub-leading. In the 2 lepton case, there are 4 isolation-based subcategories and 4 origin-based subcategories. Events with both leptons failing the tight isolation fall into the N_{LL} subset while events with both leptons passing it, contribute to the TT subset. In the case of one lepton passing and the other one failing the tight isolation, the event is classified either as an LT or a TL event, based on the convention that was used to distinguish the 2 leptons. Thus, Eq. 51 for the single lepton will be written as in Eq. 55 for the dilepton case.

$$\begin{pmatrix} \hat{f}_1 \hat{f}_2 & \hat{f}_1 \hat{p}_2 & \hat{p}_1 \hat{f}_2 & \hat{p}_1 \hat{p}_2 \\ \hat{f}_1 f_2 & \hat{f}_1 p_2 & \hat{p}_1 f_2 & \hat{p}_1 p_2 \\ f_1 \hat{f}_2 & f_1 \hat{p}_2 & p_1 \hat{f}_2 & p_1 \hat{p}_2 \\ f_1 f_2 & f_1 p_2 & p_1 f_2 & p_1 p_2 \end{pmatrix} \begin{pmatrix} N_{FF} \\ N_{FP} \\ N_{PF} \\ N_{PP} \end{pmatrix} = \begin{pmatrix} N_{LL} \\ N_{LT} \\ N_{TL} \\ N_{TT} \end{pmatrix} \quad (55)$$

After following analogous procedure and assumptions as in the single lepton scenario, the final form for N_{TT} is given by Eq. 56.

$$N_{TT} = MC^{prompt} + \frac{f_1}{1-f_1} N_{LT} + \frac{f_2}{1-f_2} N_{TL} - \frac{f_1 f_2}{(1-f_1)(1-f_2)} N_{LL} \quad (56)$$

As a result, events with a single lepton failing the tight isolation criterion enter in the estimation weighted by the factor $f_i/(1-f_i)$, while events with both leptons failing the tight isolation criteria, enter with a negative weight, $-f_i f_j/(1-f_i)(1-f_j)$. It's important to note that the minus sign is a result of the inversion of the matrix that multiplies the column matrices.

The method can be expanded in the same way for the cases of high lepton multiplicities. The transformation equation takes the form shown in Eq. 57:

$$\begin{pmatrix} \hat{f}_1 \hat{f}_2 \hat{f}_3 & \dots & \hat{p}_1 \hat{p}_2 \hat{p}_3 \\ \dots & \dots & \dots \\ f_1 f_2 f_3 & \dots & p_1 p_2 p_3 \end{pmatrix} \begin{pmatrix} N_{FFF} \\ N_{FFP} \\ N_{FPF} \\ N_{PFF} \\ N_{FPP} \\ N_{PFP} \\ N_{PPF} \\ N_{PPP} \end{pmatrix} = \begin{pmatrix} N_{LLL} \\ N_{LLT} \\ N_{LTL} \\ N_{TLL} \\ N_{LTT} \\ N_{TLT} \\ N_{TTL} \\ N_{TTT} \end{pmatrix} \quad (57)$$

Following analogous procedure and assumptions as in the single and double lepton scenarios, the final form for N_{TTT} is given in Eq. 58.

$$N_{TTT} = MC^{prompt} + \frac{f_1}{1-f_1} N_{LTT} + \frac{f_2}{1-f_2} N_{TLT} + \frac{f_3}{1-f_3} N_{TTL} - \frac{f_1 f_2}{(1-f_1)(1-f_2)} N_{LLT} - \frac{f_1 f_3}{(1-f_1)(1-f_3)} N_{LTL} - \frac{f_2 f_3}{(1-f_2)(1-f_3)} N_{TLL} + \frac{f_1 f_2 f_3}{(1-f_1)(1-f_2)(1-f_3)} N_{LLL} \quad (58)$$

8.2 Fake Rate Measurement

The probability for a jet to fake an electron ($f_{jet \rightarrow e}$), a muon ($f_{jet \rightarrow \mu}$) or a τ_h ($f_{jet \rightarrow \tau_h}$), is measured by the ratio of the number of non-prompt tight-isolated lepton candidates over the number of non-prompt candidates passing the loose isolation criterion, as shown in Eq.59.

$$f_{jet \rightarrow e/\mu/\tau_h} = \frac{N_{\text{tight}}^{\text{t}}}{N_{\text{loose}}} = \frac{N_{\text{data}}^{\text{tight}} - \sum_i^{\text{MC samples}} N_{\text{prompt}, i}^{\text{tight}}}{N_{\text{data}}^{\text{loose}} - \sum_i^{\text{MC samples}} N_{\text{prompt}, i}^{\text{loose}}} \quad (59)$$

The fake rate measurement is performed in CRs and tested in Verification Regions (VRs), which mimic closely the kinematics, topology, and sample composition of the various SRs. All CRs and VRs are defined to be orthogonal to all SRs while having minimal signal contamination.

The analysis selects events with 3 leptons (two light leptons and a τ_h) while the major source of background is $t\bar{t}$. Thus, each lepton flavor's fake rate measurement is performed in dedicated CRs enriched in $t\bar{t}$, as summarised in Table 8.1. The electron FRs are measured in a CR enriched in μe events and presented in Sec. 8.2.1, the muon FRs are measured in a CR enriched in $e\mu$ events, selected requiring an electron to trigger the event, and is presented in Sec. 8.2.2, while the τ_h FRs are measured in a CR defined by requiring the presence of

$\mu\tau_h t^{\text{res}} p_T^{\text{miss}}$ and is presented in Sec. 8.2.3.

Selection	Control Regions (CRs)			Verification Regions (VRs)		
	μe	$e\mu$	$\mu\tau_h t^{\text{res}} p_T^{\text{miss}}$	$\mu\mu e$	$\mu e\tau_h(0b)$	
Trigger	At least 1 isolated $\ell = e, \mu$ electrons					
N_e	= 1	= 1	= 0	= 1	= 1	
p_T^e	≥ 10.0	$\geq [32.0, 35.0, 35.0]$	≥ 10.0	≥ 10.0	≥ 10.0	
$p_T^{e,\text{trg}}$	—	$\geq [32.0, 35.0, 35.0]$	—	—	—	
$ \eta^e $	≤ 2.1	≤ 2.1	≤ 2.5	≤ 2.1	≤ 2.1	
$ \frac{IP^{3d}}{\sigma_{IP}^{3d}} $	≤ 10.0	≤ 4.0	—	≤ 10.0	≤ 10.0	
muons						
N_μ	= 1	= 1	= 1	= 2	= 1	
p_T^μ	$\geq [26.0, 28.0, 26.0]$	≥ 10.0	≥ 10.0	≥ 10.0	$\geq [26.0, 28.0, 26.0]$	
$p_T^{\mu,\text{trg}}$	$\geq [26.0, 28.0, 26.0]$	—	$\geq [26.0, 28.0, 26.0]$	$\geq [26.0, 28.0, 26.0]$	$\geq [26.0, 28.0, 26.0]$	
$ \eta^\mu $	≤ 2.4	≤ 2.4	≤ 2.4	≤ 2.4	≤ 2.4	
$ \frac{IP^{3d}}{\sigma_{IP}^{3d}} $	≤ 4.0	≤ 10.0	≤ 10.0	≤ 10.0	≤ 10.0	
τ_h objects						
N_{τ_h}	= 0	= 0	= 1	= 0	= 1	
$p_T^{\tau_h}$				≥ 20.0		
$ \eta^{\tau_h} $				≤ 2.3		
τ_h DMs				[0,1,2,10,11]		
jets						
N_{jets}	≥ 1	≥ 1	≥ 3	≥ 1	≥ 2	
p_T^{jet}				≥ 30.0		
$ \eta^{\text{jet}} $				≤ 2.4		
b-jets						
N_{bjets}	≥ 1	≥ 1	≥ 1	≥ 1	≥ 0	
p_T^{bjet}				≥ 30.0		
$ \eta^{\text{bjet}} $				≤ 2.4		
event-based variables						
$ Q_{e\mu} $	$\neq 0$	$\neq 0$	-	-	-	
p_T^{miss}	—	—	≤ 40	—	—	
$N_{t^{\text{res}}}$	—	—	= 1	—	—	
$m_{t^{\text{res}}}$	—	—	$120 \leq m_{t^{\text{res}}} \leq 230$	—	—	

Table 8.1: All the CR and VR that are used in the fake rate measurement.

8.2.1 Electron Fake Rates

The $f_{\text{jet} \rightarrow e}$ are measured in the CR μe as presented in Eq. 59, as a function of transverse momentum (p_T), pseudorapidity (η) and sip3d ($|\frac{IP^{3d}}{\sigma_{IP}^{3d}}|$) of the electron candidate. The tight and loose terms refer to the nominal electron candidate selection with a tight pf isolation cut (< 0.15) and very very loose pf isolation cut (< 1.0), respectively. The amount of prompt electrons in the CR is estimated from simulation and subtracted from the data to correct for the imperfect sample purity and thus ensure that these events do not introduce a systematic bias in our measurement. The fake rate measurement is performed separately for each year. The event selections for the CR μe are summarised in Table 8.1. Events are selected in a

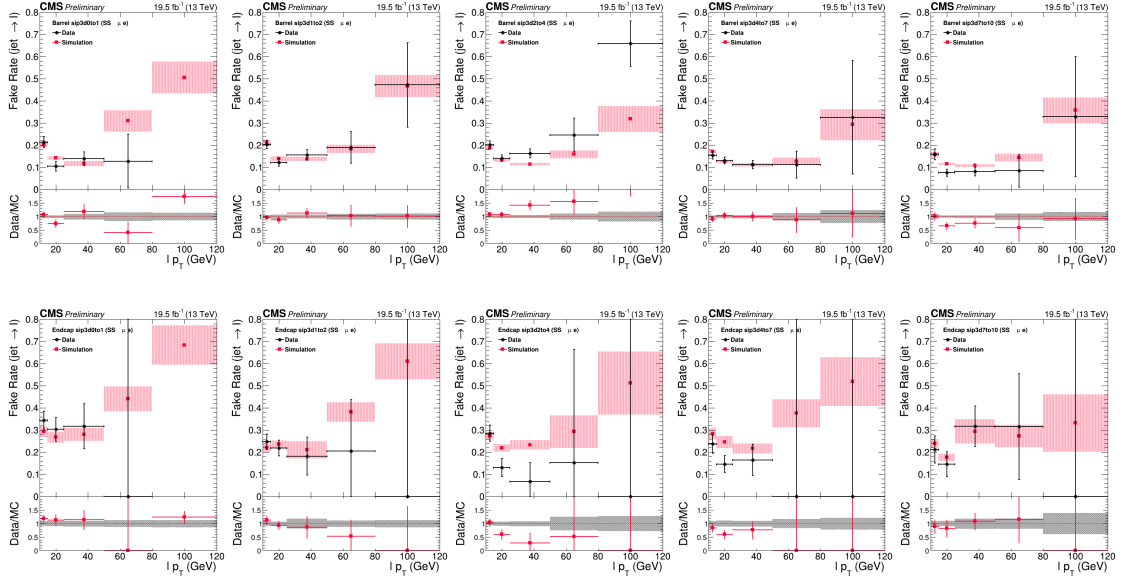


Figure 8.1: The jet $\rightarrow e$ fake rates calculated in the μe CR using 2016 pre-VFP data, showing for the barrel (first row) and endcap (second row), in sip3d bins (various columns). The black circle and red square markers represent the fake factors obtained in data and simulations, respectively. The latter are solely shown for reference purposes.

way to be orthogonal to all SRs of the analysis and close enough in terms of kinematics and sample composition. A τ_h veto is introduced to accommodate the orthogonality requirement while the criterion of at least one b-tagged jet increases the $t\bar{t}$ contribution, making it the dominant process, as in the SRs. In order to increase the statistics and make the measurement more accurate, the jet multiplicity is dropped down to at least one and the p_T threshold to 30 GeV, in contrast to SRs selections (see Table 6.3). Finally, to increase the non-prompt contributions, the same sign requirement for electron and muon is introduced.

The $f_{\text{jet} \rightarrow e}$ are measured as a function of the electron p_T , separately for barrel and endcap and in 5 different sip3d bins. This takes into account any possible effects on these rates of the various electron candidates' kinematic properties. After optimization and tests, the phase space was split into 5 p_T bins, two η -bins, and 5 sip3d bins as shown below, resulting to a total of 50 different bins.

- $p_T = [10, 15, 25, 50, 80, \infty]$ GeV.
- $|\eta| < 1.5$ (barrel) and $|\eta| \geq 1.5$ (endcaps).
- $\text{sip3d} = [0, 1, 2, 4, 7, 10]$.

The measured $f_{\text{jet} \rightarrow e}$ are shown in Figs. 8.1-8.4 for each year of the data taking period. 2016-preVFP and 2016-postVFP eras are measured and presented separately.

8.2 Fake Rate Measurement

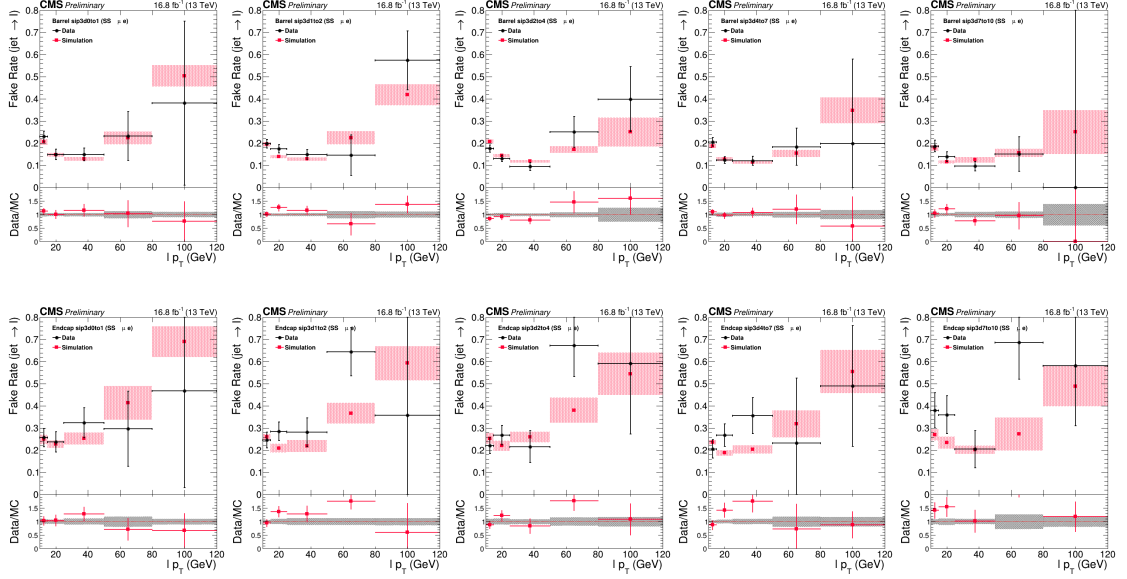


Figure 8.2: The jet $\rightarrow e$ fake rates calculated in the μe CR using 2016 post-VFP data, showing for the barrel (first row) and endcap (second row), in sip3d bins (various columns). The black circle and red square markers represent the fake factors obtained in data and simulations, respectively. The latter are solely shown for reference purposes.

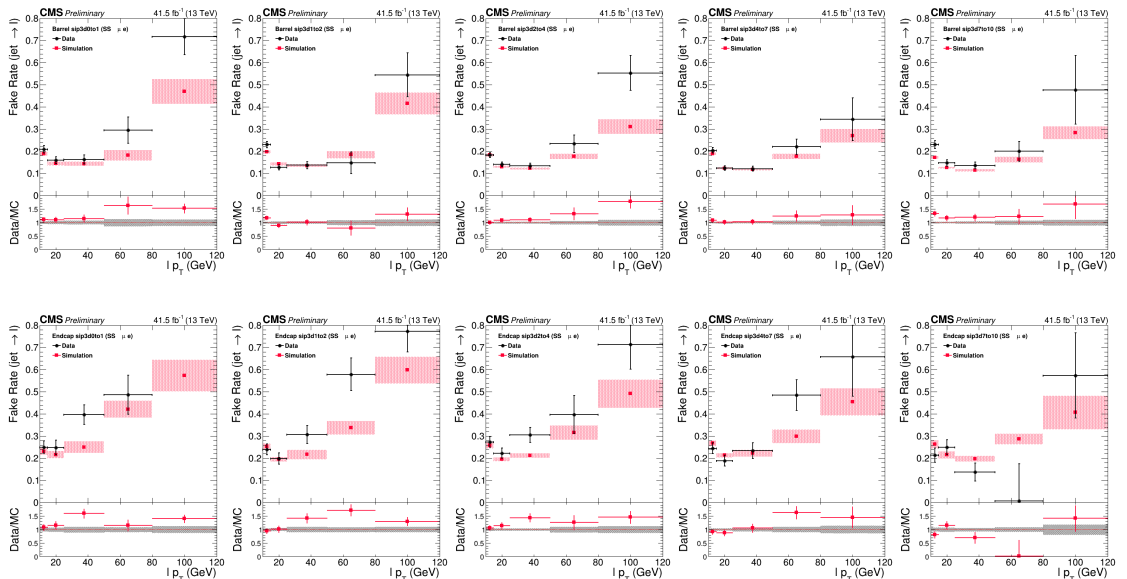


Figure 8.3: The jet $\rightarrow e$ fake rates calculated in the μe CR using 2017 data, showing for the barrel (first row) and endcap (second row), in sip3d bins (various columns). The black circle and red square markers represent the fake factors obtained in data and simulations, respectively. The latter are solely shown for reference purposes.

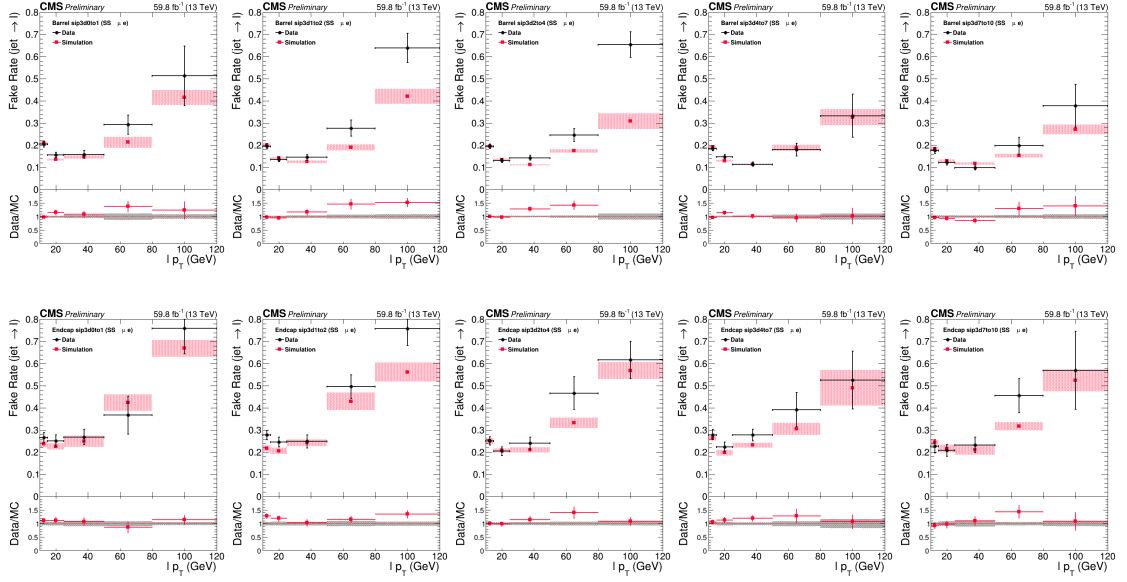


Figure 8.4: The jet $\rightarrow e$ fake rates calculated in the μe CR using 2018 data, showing for the barrel (first row) and endcap (second row), in sip3d bins (various columns). The black circle and red square markers represent the fake factors obtained in data and simulations, respectively. The latter are solely shown for reference purposes.

8.2.2 Muon Fake Rates

The probability of a jet faking a muon ($f_{\text{jet} \rightarrow \mu}$) is measured in the CR $e\mu$, as presented in Eq. 59, as a function of transverse momentum (p_T), pseudorapidity (η) and sip3d of the muon candidate. As in the $f_{\text{jet} \rightarrow e}$ case, the tight and loose terms refer to the nominal muon candidate selection with a tight pf isolation cut (< 0.15) and very very loose pf isolation cut (< 1.0), respectively. The amount of prompt muons in the CR is estimated from simulation and subtracted from the data to correct for the imperfect sample purity and thus ensure that these events do not introduce a systematic bias in our measurement. The measurement of the fake rats is performed separately for each year of the data taking period.

The event selections for the CR $e\mu$ are summarised in Table 8.1. Events are selected based on the same criteria as in the CR μe , in which the $f_{\text{jet} \rightarrow e}$ are measured, for the same reasons as explained in the Eq. 8.2.1, thus the event selections are the same except on the requirement on the type of trigger lepton.

Similarly to the electron fake rate measurement, $f_{\text{jet} \rightarrow \mu}$ are measured in the same transverse momentum (p_T), pseudorapidity (η) and sip3d bins.

The measured $f_{\text{jet} \rightarrow \mu}$ are shown in Figs. 8.5-8.8 for all three years of the data taking period. The 2016-preVFP and 2016-postVFP eras are measured and presented separately.

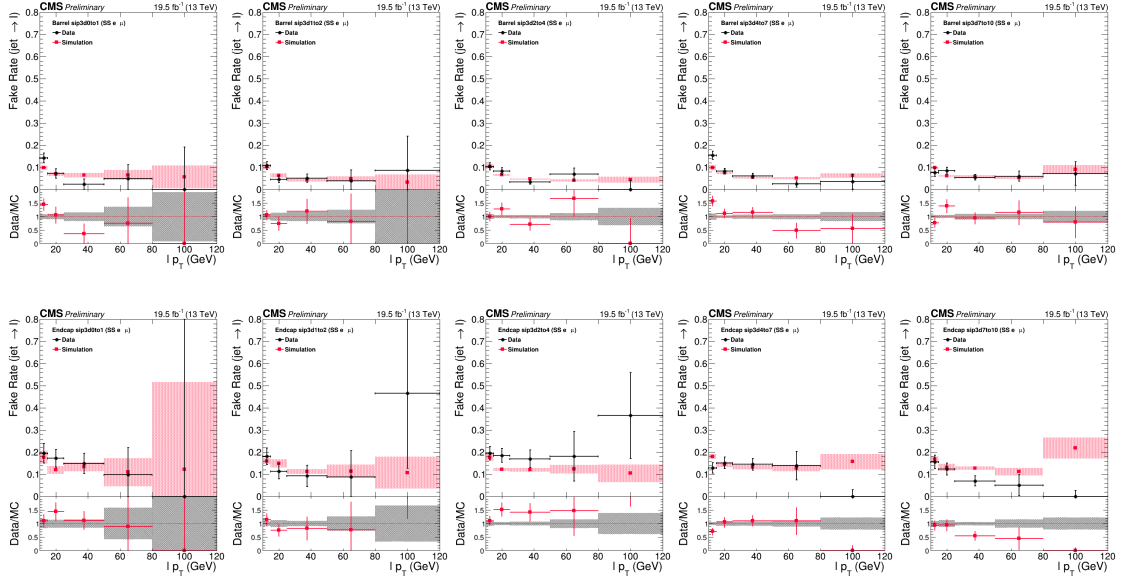


Figure 8.5: The jet $\rightarrow \mu$ fake rates calculated in the $e\mu$ CR with 2016 pre-VFP data, showing barrel (first row) and endcap (second row), in sip3d bins (various columns). The black circle and red square markers represent the fake factors obtained in data and simulations, respectively. The latter are solely shown for reference purposes.

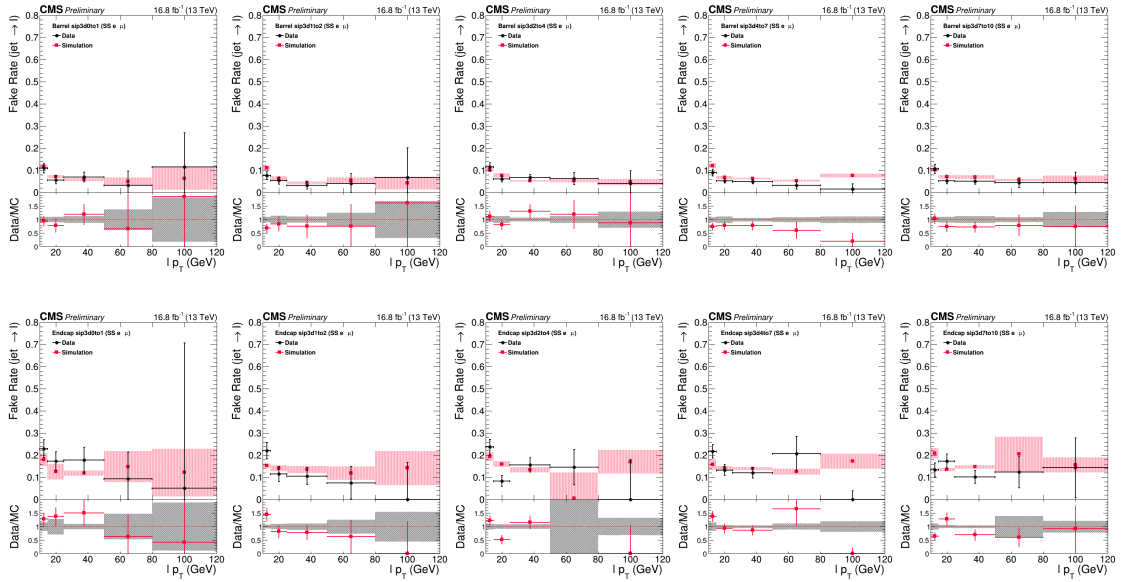


Figure 8.6: The jet $\rightarrow \mu$ fake rates calculated in the $e\mu$ CR with 2016 post-VFP data, showing barrel (first row) and endcap (second row), in sip3d bins (various columns). The black circle and red square markers represent the fake factors obtained in data and simulations, respectively. The latter are solely shown for reference purposes.

8.2.3 Tau Fake Rates

The τ_h fake rates are measured in the same CR as in HIG-21-010 and the same strategy is followed. The $f_{\text{jet} \rightarrow \tau_h}$ are measured as a function of transverse momentum (p_T) and pseudorapidity (η) of the τ_h candidate and for three different DMs or charged-track multiplicity (n-prong). The tight τ_h and loose τ_h terms refer to the nominal τ_h candidate selection with

8.2 Fake Rate Measurement

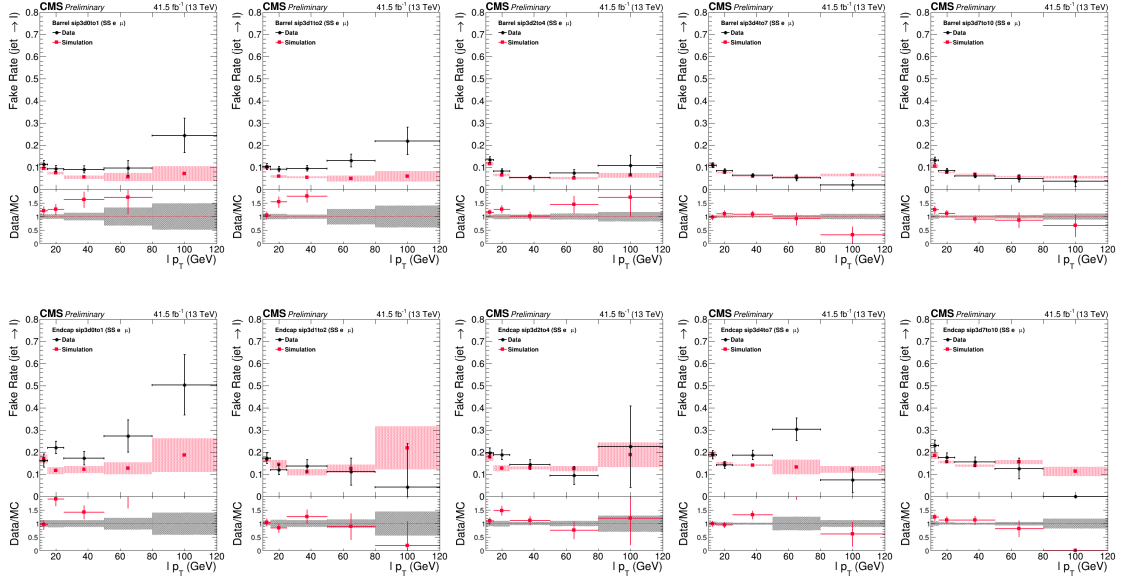


Figure 8.7: The jet $\rightarrow \mu$ fake rates calculated in the $e\mu$ CR with 2017 data, showing barrel (first row) and endcap (second row), in sip3d bins (various columns). The black circle and red square markers represent the fake factors obtained in data and simulations, respectively. The latter are solely shown for reference purposes.

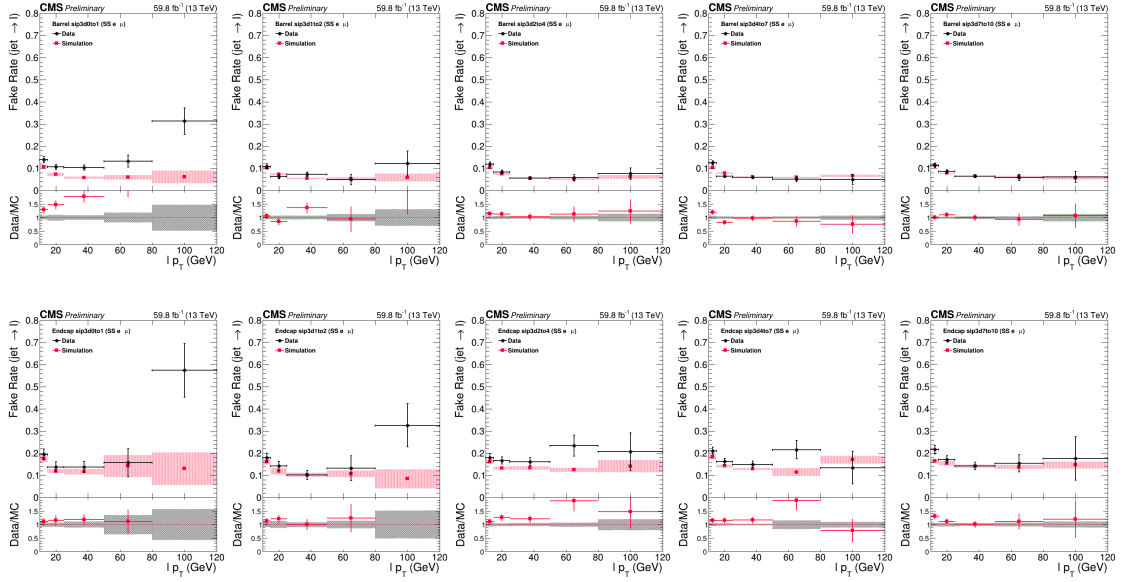


Figure 8.8: The jet $\rightarrow \mu$ fake rates calculated in the $e\mu$ CR with 2018 data, showing barrel (first row) and endcap (second row), in sip3d bins (various columns). The black circle and red square markers represent the fake factors obtained in data and simulations, respectively. The latter are solely shown for reference purposes.

the byMediumDeepTau2017v2p1VSjet and byVVVLooseDeepTau2017v2p1VSjet discriminator WP, respectively.

The genuine τ_h contributions in the CR are estimated from simulation and subtracted from the data to correct for the imperfect sample purity and thus ensure that these events do not introduce a systematic bias in the measurement. The fake rate measurement is performed

separately for each year of the data taking period.

The CR $\mu\tau_h t^{\text{res}} p_T^{\text{miss}}$ is selected with the nominal criteria used in defining the $\tau_h + \ell$ SR studied in HIG-21-010, but with a few modifications. The p_T^{miss} criterion is inverted such that $p_T^{\text{miss}} < 40$ GeV, while the requirement of exactly one t^{res} object is also introduced to suppress electroweak contributions with additional jets. The motivation for these selections is twofold; to enforce orthogonality with the $\tau_h + \ell$ SR studied in HIG-21-010 and to ensure the obtained region is enriched in $t\bar{t}$ production. The complete set of event selections for the $\mu\tau_h t^{\text{res}} p_T^{\text{miss}}$ CR is summarised in Table 8.1.

The misidentification rates are measured as a function of the $\tau_h p_T$, separately for one-prong and three-prong decays, and individually for the barrel and endcap regions of the detector. To account for the dependence of the jet $\rightarrow \tau_h$ probability on the kinematics properties of the τ_h candidate, the fake rates are evaluated in different transverse momentum (p_T), pseudorapidity (η), and n-prong bins:

- $p_T = [20, 23, 27, 44, 65, \infty]$ GeV.
- $|\eta| < 1.5$ (barrel) and $|\eta| > 1.5$ (endcaps).
- n-prong = [1, 3].

The measured $f_{\text{jet} \rightarrow \tau_h}$ are shown in Fig. 8.9, for each year of the data taking period. 2016-preVFP and 2016-postVFP eras are measured and presented separately.

8.3 Closure Tests in CRs

The extracted fake rates were used to predict the misidentified ℓ ($e/\mu/\tau_h$) contribution in the various CRs used. This self-consistency test defines a so-called self-closure test. Events with loose-not-tight (anti-loose) leptons ℓ ($e/\mu/\tau_h$) candidates are used to predict the shape and normalization of events with tight ℓ candidates in the CR, as shown in Eq. 60, based on the one lepton scenario presented in LTEM (see Sec. 8.1.1).

$$N_{\text{jet} \rightarrow e/\mu/\tau_h}^{\text{tight } \ell} = \sum_i^{p_T, \eta, \text{n-prong(sip3d)}} \left(N_{\text{data}, i}^{\text{anti-loose } \ell} - \sum_j^{\text{MC samples}} N_{\text{prompt}, ij}^{\text{anti-loose } \ell} \right) \cdot \frac{f_{\text{jet} \rightarrow e/\mu/\tau_h, i}}{1 - f_{\text{jet} \rightarrow e/\mu/\tau_h, i}} \quad (60)$$

The tight $N_{\text{jet} \rightarrow e/\mu/\tau_h}$ calculated in Eq. 60 is a more analytic expression of the second term in Eq. 54.

By definition, the aforementioned test should give good agreement when comparing data and predictions since it employs fake factors that are evaluated in the CR itself. For example,

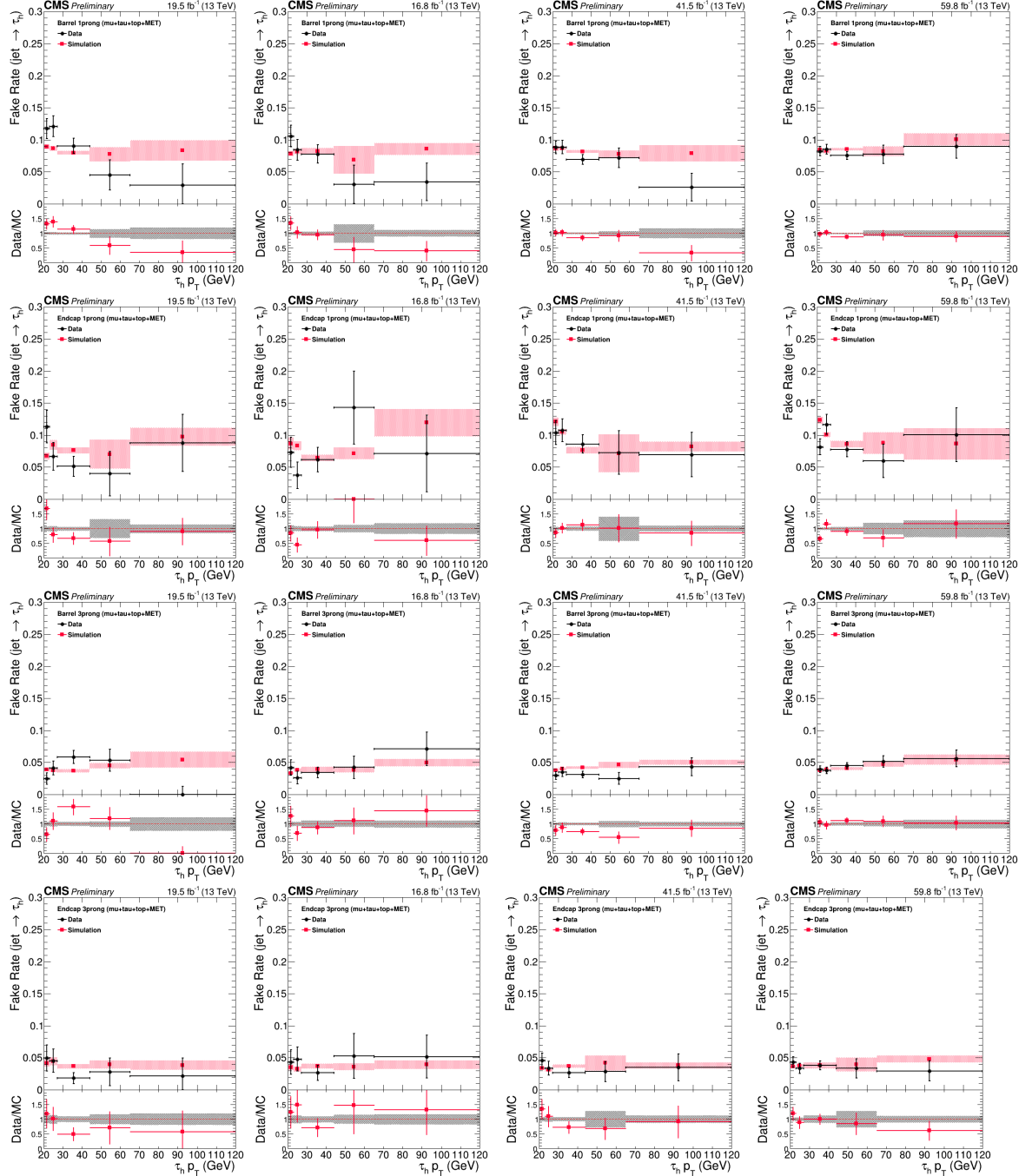


Figure 8.9: The jet $\rightarrow \tau_h$ fake rates calculated in the $\mu\tau_h t^{res} p_T^{\text{miss}}$ CR, from left to right column, for 2016 pre-VFP, for 2016 post-VFP, for 2017 and 2018 respectively. The black circle and red square markers represent the fake factors obtained in data simulations, respectively. The latter are solely shown for reference purposes.

as shown in the self-closure distributions in Fig. 8.10, besides some small disagreements, a quite good agreement between data and predictions is observed and the discrepancies are within statistical uncertainties. The closure test conducted in μe CR for validating the $f_{jet \rightarrow e}$ are presented in Fig. 8.10, for $e\mu$ CR and $f_{jet \rightarrow \mu}$ in Fig. 8.11 and for $\mu\tau_h t^{\text{res}} p_T^{\text{miss}}$ CR and $f_{jet \rightarrow \tau_h}$ in Fig. 8.12.

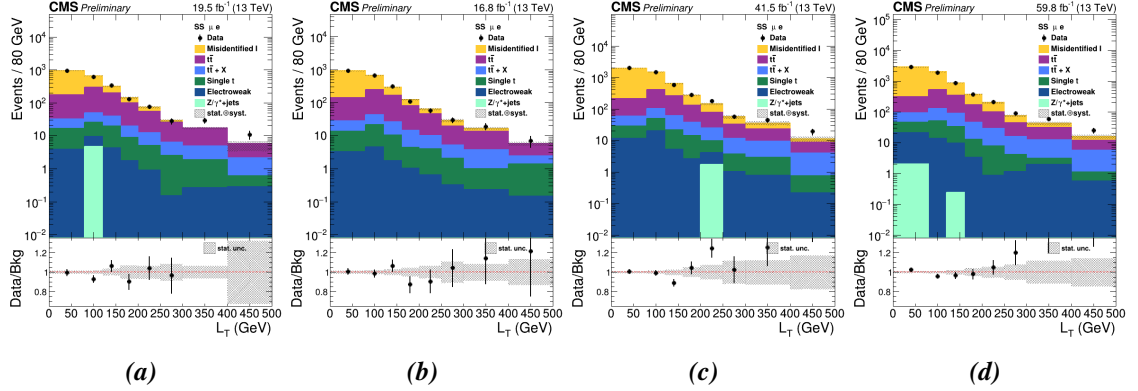


Figure 8.10: Electron FR Self-Closure tests showing the L_T distributions in the μe CR for (a) 2016 pre-VFP, (b) 2016 post-VFP, (c) 2017 and (d) 2018.

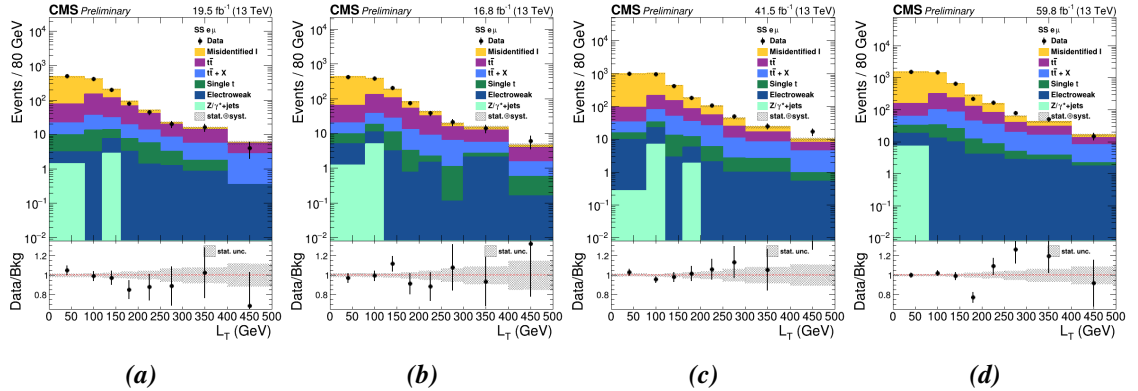


Figure 8.11: Muon FR Self-Closure tests showing the L_T distributions in the $e\mu$ CR for (a) 2016 pre-VFP, (b) 2016 post-VFP, (c) 2017 and (d) 2018.

8.4 Combined Closure Tests in VRs

The ultimate test of the data-driven method of estimating the fake rate contribution comes with the application of the results of the methods in trying to predict the fake lepton background in regions that are independent of the CRs used to measure the fake rate and that have similar composition to the signal regions. This process defines the closure tests in the Verification regions (VRs), which composition-wise are similar but also orthogonal to the SRs. The region $\mu\mu e$ is introduced to simultaneously test the $f_{jet \rightarrow \mu}$ and $f_{jet \rightarrow e}$, while the $\mu e\tau_h(0b)$ is used to test all 3 different flavoured FRs at once. For both tests, the 3 lepton scenario of LTEM is used. The $\mu e\tau_h(0b)$ is defined by inverting the b-jet requirement of

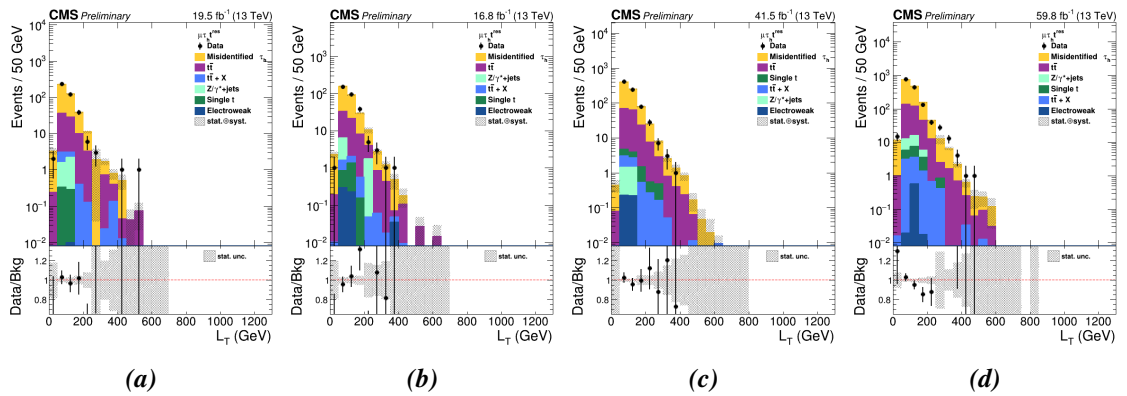


Figure 8.12: Tau FR Self-Closure tests showing the L_T distributions in the $\mu\tau_h t^{\text{res}} p_T^{\text{miss}}$ CR for (a) 2016 pre-VFP, (b) 2016 post-VFP, (c) 2017 and (d) 2018.

the $\mu e \tau_h$ SR, ensuring orthogonality between the two, and at the same time lowering the p_T cuts for both τ_h and jet objects by 10 GeV in order to increase statistics. The $\mu \mu e$ region is defined by asking an additional low p_T (< 10 GeV) μ in the event on top of the μe CR event selections. These requirements are driven by the need to have VRs orthogonal to all SRs and CRs at the same time but also as close as possible to them, both kinematically- and process composition-wise. For example, in $\mu \mu e$ additional μ is introduced to help select as many $t\bar{t}$ events in which both top quarks decay leptonically as possible with additional jets that could fake either a μ or an e . A summary of the complete set of event selection criteria applied to obtain these $\mu e \tau_h(0b)$ and $\mu \mu e$ VRs are summarised in Table 8.1.

8.4.1 Closure test in $\mu \mu e$ VR

As in Sec. 8.3, the prompt e , μ and τ_h are obtained from simulations, while the non-prompt (misidentified) lepton contribution is predicted by weighting the anti-isolated leptons sample according to Eq. 57. Selected results are shown in Fig. 8.13, where one can see that there is a reasonably good agreement normalisation- and shape-wise for the L_T distribution, where the predictions are within statistical uncertainties from the data.

8.4.2 Closure test in $\mu e \tau_h(0b)$ VR

As before, following the same procedure as in Sec. 8.4.1, Fig. 8.13 shows the DNN output of the algorithm that was trained for Signal/Background discrimination (see Sec. 9) and is used as fit discriminant for signal extraction (see Sec. 11). An overall reasonable agreement is observed across Run2, with the vast majority of bins showing consistent predictions within statistical uncertainties from the data.

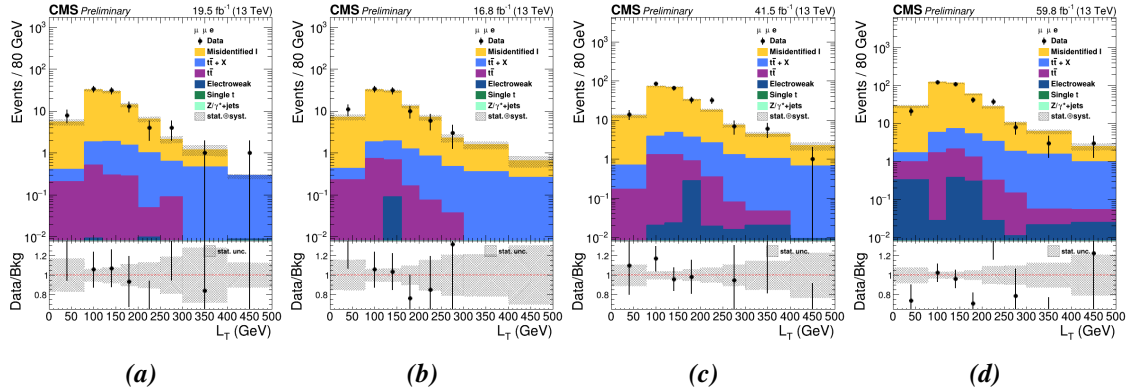


Figure 8.13: Closure tests showing the L_T distributions in the μe VR for (a) 2016 pre-VFP, (b) 2016 post-VFP, (c) 2017 and (d) 2018.

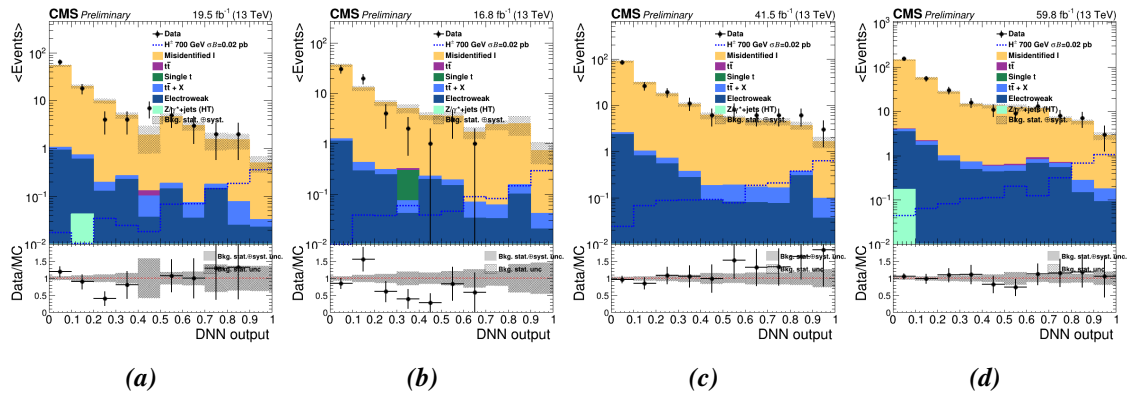


Figure 8.14: Closure tests showing the DNN output distributions in the $\mu e \tau_h(0b)$ VR for (a) 2016 pre-VFP, (b) 2016 post-VFP, (c) 2017 and (d) 2018.

8.5 Other backgrounds

In the preceding subsections we discussed how the misidentified ℓ ($e/\mu/\tau_h$) background, which dominates both the $2\ell^{sf}\tau_h$ and $2\ell^{df}\tau_h$ final states, is measured with a data-driven method. The remaining backgrounds consist of events with prompt $e/\mu/\tau_h$, or events with an electron or muon being misidentified as a τ_h ($\ell \rightarrow \tau_h$). These are mostly comprised of $t\bar{t}$, $t\bar{t}X$, while the other production processes have little to no contribution. Under the assumption that the prompt $e/\mu/\tau_h$ are adequately modeled in the aforementioned simulation samples, and thus events with prompt $e/\mu/\tau_h$ are estimated directly from simulations. This background accounts for events with all three prompt $e/\mu/\tau_h$. The estimation of the $\ell \rightarrow \tau_h$ background, which has a comparatively small contribution to the SR, is also estimated from simulation.

9 DNN Classifier for Signal Extraction

Machine learning (ML) techniques have gained prominence in HEP analyses, owing to the increasing volume of collision data produced by the CMS detector and the complexity of event topologies. From event triggering to object identification and detector simulation, ML is leveraged to improve HEP searches. Unlike traditional cut-based methods, ML combines information from multiple variables to discriminate between signal and background events. The primary ML methods used in HEP are boosted decision trees (BDT) and deep neural networks (DNN). Deep learning, a subset of ML, utilizes complex hierarchical representations to process data, inspired by the structure of the human brain. A DNN, for instance, consists of multiple layers of interconnected neurons, each layer transforming the input data into more abstract representations. Training a DNN involves repetitive adjusting of its parameters to minimize the difference between the predicted and true values, typically using gradient-based optimization algorithms. Common tasks in HEP include classification, where inputs are categorized into distinct classes, and regression, where the algorithm predicts continuous values. Performance evaluation is conducted on separate test datasets, with algorithms considered reliable if they perform consistently on both training and test datasets. The training dataset is typically divided into training and validation subsets, with the latter used to fine-tune hyperparameters and assess model performance.

The selections currently used in this analysis have been optimised by varying the most important selections around their default value and comparing the expected limits. For both $2\ell^{sf}\tau_h$ and $2\ell^{df}\tau_h$ scenarios, an event-based parameterized Deep Neural Network (DNN) classifier [92] has been developed in order to enhance the separation between signal and background. The parameterization is performed based on the m_{H^\pm} true mass.

A simplified interpolation of a fully connected DNN is shown in 9.1. The two drawings on the left, show the case of separate training per m_{H^\pm} , which means that for each available H^\pm mass point, a different DNN training should be performed. On the contrary, instead of doing that, one needs to perform just a single DNN training, using the m_{H^\pm} as an additional input parameter, represented as θ in the right hand side drawing. The latter leads to a parameterized DNN and in order to achieve this, one should give at least 2 datasets of different values of the selected input parameter on which the parameterization is going to be performed.

Given the fact that the signal for all final states, i.e. $e e \tau_h$, $\mu \mu \tau_h$ and $\mu e \tau_h$, is expected to be $e - \mu$ flavour symmetric, most of the background as well, was decided to use $e - \mu$ as the same object for the DNN training, after ensuring that there was not any significant asymmetry in the DNN outputs based on the light lepton type used. Additionally, in order to ensure orthogonality between the datasets used to train the algorithm and the datasets on which the classifier is applied to, datasets from different data-taking periods are used

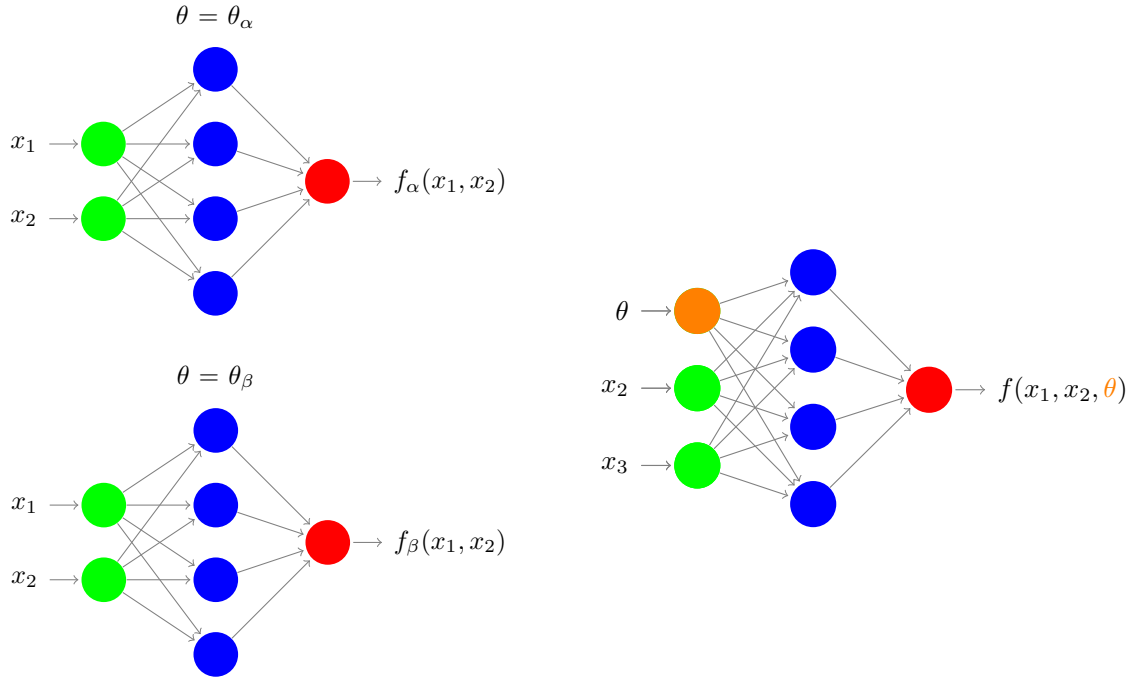


Figure 9.1: Simple interpolation of a fully connected DNN, where individual networks are trained with a single value of parameter θ (left) and trained with the possible values of θ as input features (right), thus parameterized.

to evaluate the DNN classifier performance (e.g. the algorithm that is used for 2018 data is trained and tested using 2016 and 2017 simulated samples). As background, all samples described in Table 4.6 are used to train for the background, weighted according to their cross-section, as explained below. Furthermore, as already noted, there are signal samples for five different $m_{H^0(h^0)}$ (80, 90, 125, 200, and 300 GeV) and a different m_{H^\pm} spectrum is available for each of them. Therefore, a separate parameterized DNN should be trained. The full set of the 14 variables used as input variables to train the individual networks is shown in 9.1. A brief description is provided for each one of them along with a description of the $D\zeta_0$ and $D\zeta_1$.

In order to use all major background samples noted in Table 4.6, namely $t\bar{t}, t\bar{t} + X, SingleTop, W + jets, Z/\gamma^* + jets, Di/Tribosons$, one should correctly weight events of different datasets. All datasets come with a cross section related normalization factor (F_i^{norm}). For a given dataset i , with cross section $xsec_i$ and produced with a total number of events N_i^{all} , the F_i^{norm} is defined as:

$$F_i^{norm} = \frac{xsec_i}{N_i^{all}} \quad (61)$$

This means that in order to use as a single input all available statistics from various background processes of different cross sections, keeping the composition unchanged, the number of events of each sample should be multiplied by the F_i^{norm} . For DNN though, additional

normalization should be performed. For M datasets, each dataset i has a specific number of events passing all selections, N_i and a specific F_i^{norm} . By defining N_{tot} as:

$$N_{tot} = \sum_i (N_i), w_{tot} = \sum_i (F_i^{norm}) \quad (62)$$

N_{tot} should remain unchanged in order to use the events as input to the DNN. This means that a re-weight of all events based on F_i^{norm} without changing the N_{tot} should be made.

$$\sum_i (w_i * N_i) = N_{tot} \quad (63)$$

$$w_i = \frac{(N_{tot} * F_i^{norm})}{(N_i * w_{tot})} \quad (64)$$

Eq. 64 proportionally distribute the total weight N_{tot} among the datasets i based on their individual weights F_i^{norm} , while maintaining the relative weights within each dataset, keeping the total number of events unchanged.

9.1 DNN Input Variables

Table 9.1 shows a list of all variables used in the DNN training. Among them, the $D\zeta$ variable needs to be described in details. $D\zeta$ is a variable related to the momentum vector of a given light lepton (e/μ), the selected τ_h and E_T^{miss} . Equations 65-68 explain step-by-step how this variable is calculated starting from the bisector of the 3-momentum of the light lepton and the τ_h . A schematic interpretation can also be found in Fig. 9.2. This variable is commonly used in analyses involving SM Higgs decays involving τ_h and E_T^{miss} . It is often employed to distinguish signal events ($H^0 \rightarrow \tau^+\tau^-$) from background events by exploiting the alignment of E_T^{miss} with the visible decay products of the hadronically decaying tau leptons. The value of 1.85 was chosen based on studies optimizing the separation between signal and background in $H^0 \rightarrow \tau^+\tau^-$ analysis, involving τ_h .

$$\overrightarrow{bisector} = bisector(\vec{p}_T^{\tau}, \vec{p}_T^l) = |\vec{p}_T^{\tau}| * \vec{p}_T^{\tau} + |\vec{p}_T^l| * \vec{p}_T^l \quad (65)$$

$$P_{\zeta}^{vis} = (\vec{p}_T^{\tau} + \vec{p}_T^l) \cdot \frac{\overrightarrow{bisector}}{|bisector|} \quad (66)$$

$$P_{\zeta} = (\vec{p}_T^{\tau} + \vec{p}_T^l + \overrightarrow{E_T^{miss}}) \cdot \frac{\overrightarrow{bisector}}{|bisector|} \quad (67)$$

$$D_{\zeta} = P_{\zeta} - 1.85 * P_{\zeta}^{vis} \quad (68)$$

Number	Variable	Description
1	H_T	scalar p_T sum of all selected jets in the event
2	E_T^{miss}	magnitude of missing transverse momentum vector
3	$N_{b_{\text{jets}}}$	number of b-tagged jets passing medium pf deep flavour discriminator WP
4	$p_T^{\tau_h}$	transverse momentum of the τ_h object
5	$\Delta R(l_0, l_1)$	pseudo-solid angle between the two leptons in the $\eta - \phi$ plane
6	$p_T^{l_0}/L_T$	ratio of the transverse momentum of the leading lepton and the L_T
7	$p_T^{l_1}/L_T$	ratio of the transverse momentum of the sub-leading lepton and the L_T
8	m_{l_0, τ_h}	invariant mass of the leading lepton and τ_h
9	m_{l_1, τ_h}	invariant mass of the sub-leading lepton and τ_h
10	D_{ζ_0}	a variable based on momentum vector of the leading lepton, τ_h and E_T^{miss}
11	D_{ζ_1}	a variable based on momentum vector of the sub-leading lepton, τ_h and E_T^{miss}
12	$p_T^{j_0}/H_T$	ratio of the transverse momentum of the leading jet and the H_T
13	$p_T^{j_1}/H_T$	ratio of the transverse momentum of the sub-leading jet and the H_T
14	$\Delta R(j_0, j_1)$	pseudo-solid angle between the two leading jets in the $\eta - \phi$ plane

Table 9.1: List of variables included in the training of the parameterized DNN.

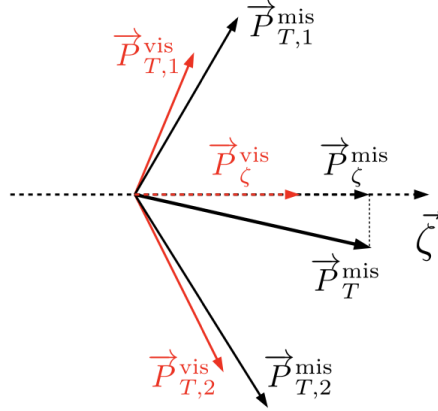


Figure 9.2: Schematic interpretation of the D_ζ variable, which is related to the momentum vector of a given light lepton (e/μ), the selected τ_h and the E_T^{miss} .

The variables are chosen to provide the best discrimination against background, while also being uncorrelated to each other. The latter statement is shown to be valid in both signal and background samples by inspecting the correlation matrix plots in Fig. 9.4. The normalised distributions of these variables are shown in Fig. 9.3 for the signal and background processes for the 2017-2018 eras. The distributions look similar for all year combinations. In Appendix A, the distributions for $m_{H^0(h^0)} = 80\text{GeV}$ can be found, for both low and high m_{H^\pm} , again for the combination of 2017-2018 samples.

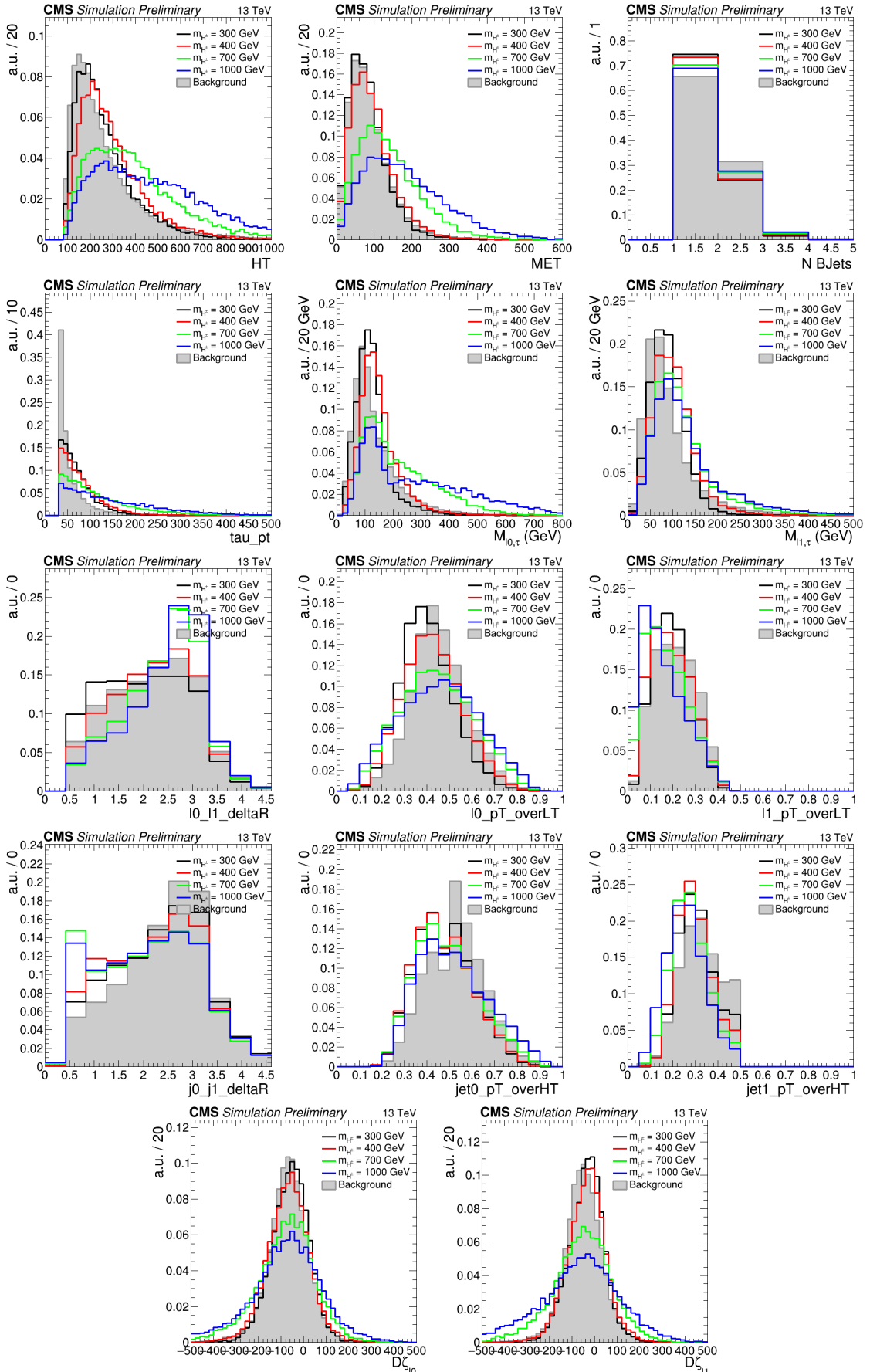


Figure 9.3: Distributions of the input variables used for the parameterized DNN training, normalised in unity, presented for $m_{H^0(h^0)} = 200 \text{ GeV}$.

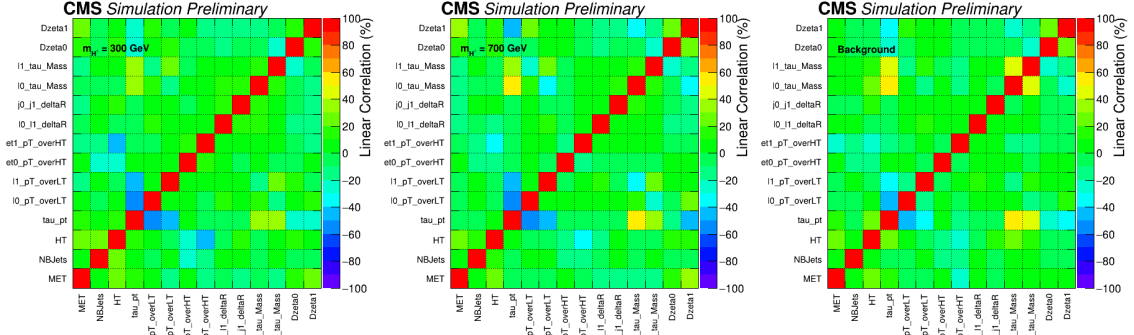


Figure 9.4: Correlation matrices for input variables for $m_{H^0(h^0)} = 200 \text{ GeV}$ in 2017+2018 training, presented for $m_{H^\pm} = 300 \text{ GeV}$ (left), $m_{H^\pm} = 700 \text{ GeV}$ (middle) and background (right).

9.2 DNN Architecture and Features

The DNN method is provided by KERAS [93] and TENSORFLOW [94] software packages while the architecture and features used for the creation of the custom parameterized DNN are presented in Table 9.2.

Option	Value	Description
DNN tool	keras	tool for constructing a neural networks
Optimizer	adam	stochastic gradient descent method
learning rate	0.001	step size at each training iteration while moving toward an optimum of a loss function
activation function	ReLU	introduces the non-linearity property and solves the vanishing gradients issue
layers	3	number of hidden layers of the neural network
neurons	32	number of neurons per hidden layer
max epochs	1000	number of complete iterations of the network
batch size	65536	number of samples processed before the model is updated
training-testing	70%-30%	percentage of events used for training and testing

Table 9.2: Architecture and features of custom parameterized DNN.

The parameterization is performed using a distinct set of m_{H^\pm} values for each available $m_{H^0(h^0)}$. Following optimization tests, the final sets of m_{H^\pm} values used as input for each parameterized DNN training were determined and are summarized in Table 9.3. For low $m_{H^0(h^0)}$ values, two separate trainings were performed, one targeting low m_{H^\pm} values and another targeting high m_{H^\pm} values.

9.3 DNN Performance and Response

The performance of the parameterized DNN algorithm is expressed as a Receiver Operating Characteristic (ROC) curve that shows the background against signal efficiency. ROC curves are produced for all available signal mass points and years and are presented in Fig. 9.5, for the 2017-2018 combined training used in the 2016 analysis.

$m_{H^0(h^0)}$	m_{H^\pm} spectrum	m_{H^\pm} used for parameterization
80 (low m_{H^\pm})	170-300	[170,220,300]
80 (high m_{H^\pm})	400-2000	[400,500,700,1000]
90 (low m_{H^\pm})	185-300	[185,220,300]
90 (high m_{H^\pm})	400-2000	[400,500,700,1000]
125 (low m_{H^\pm})	220-300	[220,250,300]
125 (high m_{H^\pm})	400-2000	[400,500,700,1000]
200	300-1000	[300, 400, 700, 1000]
300	400-1000	[400, 500, 700, 1000]

Table 9.3: Values of m_{H^\pm} given as input to the training the parameterized DNN. All values are reported in units of GeV.

The distributions of the predicted DNN response for various H^\pm mass hypotheses for the $m_{H^0(h^0)} = 200$ GeV are presented in Fig. 9.6 for the 2017-2018 combined training. A similar gradual separation is observed for the other two year combinations and the other four $m_{H^0(h^0)}$, as shown in Fig. 9.7 for a similar set of H^\pm mass hypotheses but for $m_{H^0(h^0)} = 90$ GeV.

The separation of the H^\pm signal from the background is most challenging at low m_{H^\pm} and/or low $m_{H^0(h^0)}$, because of the fact that the signal and background processes show very similar kinematical and topological characteristics, something visible in Fig.9.8. Additionally, for low $m_{H^0(h^0)}$ and high m_{H^\pm} , the $m_{H^0(h^0)}$ is expected to be very energetic resulting to more collimated decay products that can't match the selection requirements of this study.

9.4 Fit discriminant

The output of the DNN is selected as the fit discriminant for all final states ($ee\tau_h$, $\mu\mu\tau_h$, and $\mu e\tau_h$) because it provides the highest signal discrimination against background compared to any other variable evaluated. The choice of the DNN output as the final fit discriminant was driven by extensive optimization studies, which confirmed its robustness and DNN's ability to capture complex correlations and nonlinearities. Pre-fit distributions of the DNN output are shown in Sec. 11.1, where systematic uncertainties are applied as detailed in the next chapter.

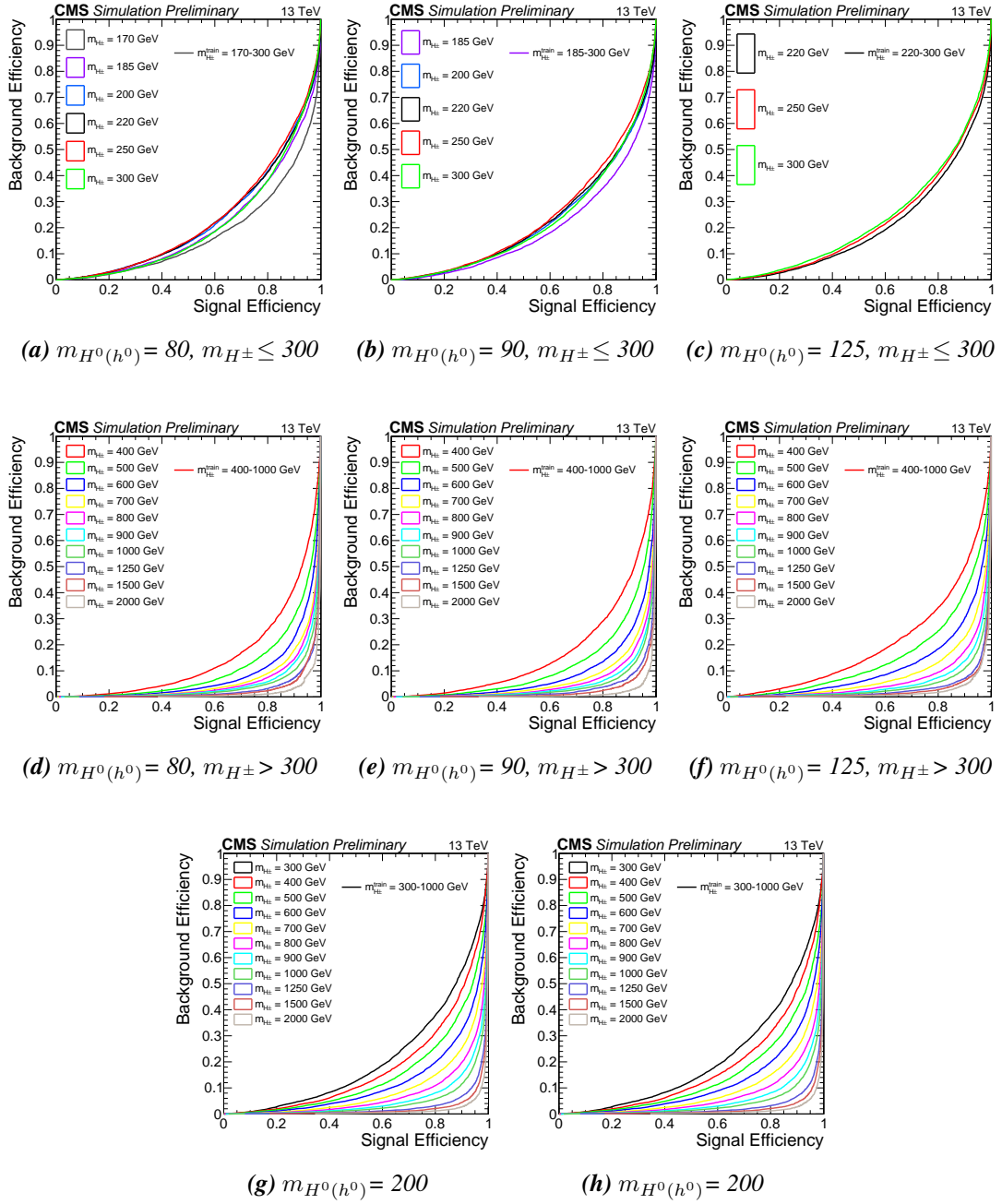


Figure 9.5: ROC curves for the DNN that was trained using the 2017-2018 samples to be used in the 2016 analysis. Mass points in sub-plot labels are reported in GeV.

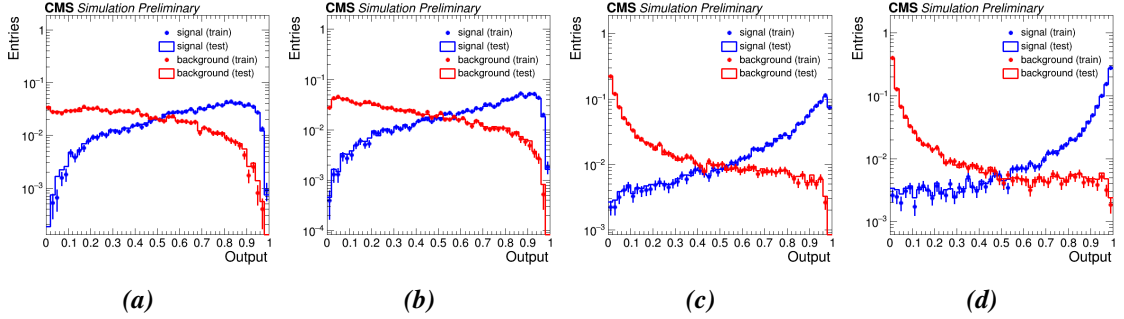


Figure 9.6: The DNN response for signal and background, shown for the $m_{H^0(h^0)} = 200 \text{ GeV}$ - (a) $m_{H^\pm} = 300 \text{ GeV}$, (b) 400 GeV , (c) 700 GeV and (d) 1 TeV signal samples, for both training and testing scenarios. The DNN was trained with the combination of 2017-2018 samples, in order to be used on 2016 samples.

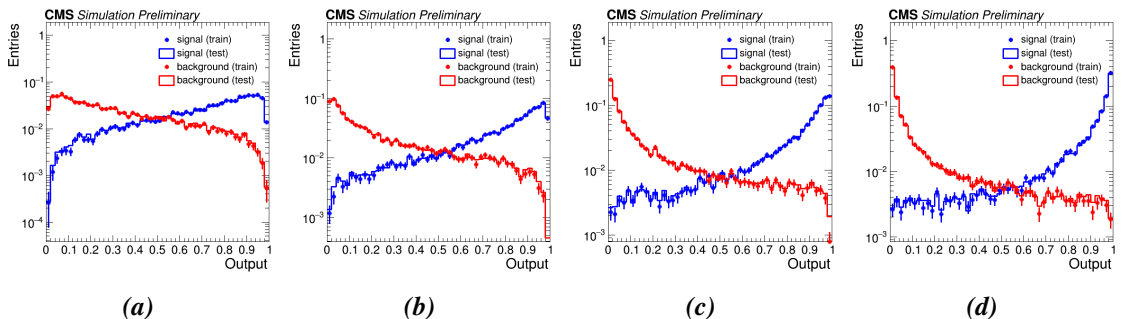


Figure 9.7: The DNN response for signal and background, shown for the $m_{H^0(h^0)} = 90 \text{ GeV}$ - (a) $m_{H^\pm} = 400 \text{ GeV}$, (b) 500 GeV , (c) 700 GeV and (d) 1 TeV signal samples, for both training and testing scenarios. The DNN was trained with the combination of 2017-2018 samples, in order to be used on 2016 samples.

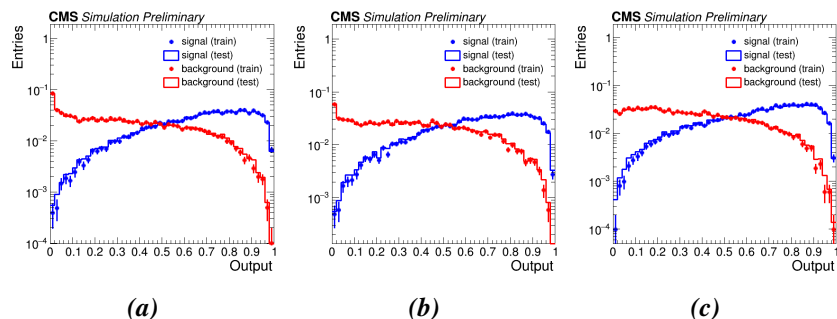


Figure 9.8: The DNN response for signal and background, shown for the $m_{H^0(h^0)} = 90 \text{ GeV}$ - (a) $m_{H^\pm} = 185 \text{ GeV}$, (b) 220 GeV and (c) 300 GeV , for both training and testing scenarios. The DNN was trained with the combination of 2017-2018 samples, in order to be used on 2016 samples.

10 Systematic Uncertainties

This section outlines the various sources of systematic uncertainties that could impact the shape of the fit discriminant, the rate of final yields, or even both, along with their respective contributions to the overall uncertainty.

10.1 Luminosity uncertainty

The CMS luminosity monitoring suggests uncertainties of 1.2%, 2.3%, and 2.5% for the 2016, 2017, and 2018 data-taking periods, respectively [95]. These uncertainties are partially correlated across the datasets due to variations in the luminosity measurement schemes employed during these periods.

10.2 Pileup reweighting uncertainty

The systematic uncertainty arising from pileup modeling is estimated by shifting the mean of the inelastic pp cross section distribution, with variations of $\pm 5\%$ [96]. Following this variation, the simulated events are reweighted and this is propagated to the final fit discriminant, the variation of which is recorded. Any deviations observed from the nominal distribution are then considered as systematic uncertainties.

10.3 Prefiring uncertainty

The prefiring problem arises when the Level-1 trigger is mistakenly activated by misaligned primitives, causing it to associate them with the bunch crossing preceding a particular event in the CMS detector. This issue was notably observed in 2016 and 2017, primarily due to calibration errors in the ECAL endcap. To tackle this problem, prefiring rates, which vary based on the kinematics of jets, are used to calculate an event-based efficiency, as suggested in Ref. [97]. The associated uncertainties in this measurement contribute to the prefiring uncertainty in the final results, which is reflected as a shape uncertainty in the fit discriminant.

10.4 Trigger efficiency uncertainties

The uncertainties associated with the trigger scale factors are determined based on the uncertainties of the trigger efficiency measurements obtained from both data and simulation, as presented in Sec.7. These uncertainties are then propagated to the final fit discriminant distribution as shape uncertainties. To assess the impact of the trigger scale factors on the fit

discriminant distribution, two distributions are generated for the trigger in use, one for the up and one for the down variation. These distributions serve as shape nuisances in the analysis.

10.5 Lepton reconstruction and identification efficiency

In order to perform corrections for the difference in the lepton identification efficiencies between data and MC, appropriate SFs are applied to the simulation samples. The uncertainties of the muon and electron identification SFs are the resulting up and down variations that served as shape nuisances, after propagated to the final fit discriminant distribution as shape uncertainties.

10.6 Tau identification and energy scale uncertainties

For the DeepTau v2.1 identification, a p_T -dependent identification SF is adopted, while for the correction of the energy scale of the various τ_h candidates, a DM-dependent Tau Energy Scale (TES) SF is applied, following the related TAU-POG recommendations for Run-2 [85]. In both cases, the individual bins are varied separately and propagated as uncorrelated shape uncertainties to the final fit discriminant.

10.7 JES, JER and UES uncertainties

The systematic uncertainty related to the JES is evaluated by independently shifting the energy scale of the selected hadronic jets by $\pm 1\sigma$ variations. These up/down variations are propagated after all selections to the final fit discriminant, accounting for both shape and normalization impacts. The effect of the systematic uncertainty related to the energy resolution of hadronic jets on the other hand, is estimated by smearing the reconstructed jets in simulation in such a way that their p_T resolution matches the one observed in data. This is achieved by increasing or decreasing their energy around their nominal value, following the related JetMET POG recommendations [98]. The events are then re-analysed and the resulting normalisation and shape changes in the fit discriminant, represent the final shape uncertainties. The uncertainty due to the scale of the remaining unclustered component of the E_T^{miss} is estimated using the related tools provided by the JetMET group [99].

10.8 B-tagging uncertainties

The uncertainty of the per-event b-tagging SF is calculated by variations on the per-jet SF, derived as described in Sec. 5.3.6, and the b-tagging or b-mistagging efficiencies for jets of different p_T and flavor. It is calculated in analytical form by applying the error propagation

law to the per-event SF formula, constructed based on the per-jet b-tagging efficiency SFs provided by the b tagging POG, for both b and light flavor jets.

During the uncertainty calculation, some assumptions and considerations are taken into account. First of all, the per-jet SFs associated with the efficiency of correctly identifying (tagging) a jet as a b-jet when it truly originates from a b-quark (f_{tag}) and with the mistagging rate, which refers to the probability of incorrectly tagging a jet as a b-jet when it originates from a light-flavor quark (u, d, s) or a gluon (f_{mistag}), can be safely assumed to be uncorrelated. Additionally, the per-jet tag/mistag efficiencies can be treated as uncorrelated, because the SFs are measured in a μ +jets sample while the efficiencies are calculated from a simulated sample where isolated muons are vetoed. In the datacards which are used as input for the limit calculation, the uncertainties related to b-tagging and b-mistagging, are assumed to be uncorrelated and thus treated as two separate sources of uncertainty.

10.9 Misidentified ℓ ($e/\mu/\tau_h$) measurement uncertainty

The systematic uncertainties arising from the LTEM Misidentified ℓ ($e/\mu/\tau_h$) estimation are driven by the observed non-closure in the $\mu e \tau_h(0b)$ VR (Fig. 8.14). For each bin i of the DNN output, a scale factor ($SF_i^{\text{non-closure}}$) is computed as the ratio between data and prediction. Since there are 65 different DNN output distributions corresponding to different m_{H^\pm} mass points, a weighted average of these SFs is calculated for each i bin across all 65 distributions.

The weighted average for each bin is computed as follows:

$$SF_i^{\text{non-closure}} = \sum_{j=1}^{65} (SF_{ij} \times w_{ij}) , \quad w_{ij} = \frac{N_{ij}}{\sum_{k=1}^{65} N_{ik}} \quad (69)$$

where i runs over the bins of the DNN output distribution, and j runs over the 65 DNN output distributions. Here, SF_{ij} represents the Data/Prediction ratio for the i -th bin in the j -th DNN output distribution. The weight w_i is defined as the number of data events N_{ij} in the i -th bin and j -th DNN output distribution, normalized overall the sum of all i -th bins of the 65 distributions, ensuring that bins with higher statistics contribute more.

The resulting $SF_i^{\text{non-closure}}$ values are then used to define a shape uncertainty that is included as a nuisance parameter in the analysis, with each bin contributing independently. This approach ensures that the systematic deviations observed in the verification region are propagated accurately into the final results.

10.10 Theoretical uncertainties

The theoretical uncertainty on the production cross section primarily stems from the uncertainties related to the parton distribution functions (PDF), the renormalization and factorization scale and the strong coupling constant α_S . These uncertainties affect the overall cross section of the various processes, resulting to an impact on the acceptance of the event selection. Additionally, for processes involving single top and $t\bar{t}$ production, the uncertainty arising from the top quark mass is also considered. To evaluate the systematic effects on event acceptance due to renormalization and factorization scales, the scales are independently varied by a factor of two. However, extreme cases where they differ by more than a factor of two are excluded. The scale uncertainty is determined by capturing the maximum variation relative to the nominal fit distribution. The combined uncertainty for the $t\bar{t}$ cross section, encompassing scale, top mass, and PDF plus α_s uncertainties, is approximately $^{+6.2\%}_{-6.6\%}$ for $s = \sqrt{13}$ TeV [62, 100].

10.11 Summary of Systematic Uncertainties

A summary of the values of the various systematic uncertainties is showed in Table 10.1 for the $\mu e \tau_h$ analysis with 2018 data and for $m_{H^0(h^0)} = 200$ GeV - $m_{H^\pm} = 900$ GeV. The uncertainties affecting the shape, noted with a check mark (\checkmark), are estimated by quantifying a specific variation through a scalar value and integrating over both the varied and nominal DNN output distributions, determining the ratio between the two.

	Shape ✓	Signal	Misidentified e, μ, τ_h	Genuine e, μ, τ_h and $e/\mu \rightarrow \tau_h$			
				$t\bar{t}$	Single t	$t\bar{t}+X$	Electroweak
Integrated luminosity 2018	—	1.5	—	1.5	1.5	1.5	1.5
Integrated luminosity correlated	—	2.0	—	2.0	2.0	2.0	2.0
Integrated luminosity correlated (2017, 2018)	—	0.2	—	0.2	0.2	0.2	0.2
Pileup 2018	✓	1.6	—	1.3	< 0.1	0.4	4.4
Trigger timing inefficiency ECAL 2018	✓	< 0.1	—	< 0.1	< 0.1	< 0.1	< 0.1
Trigger timing inefficiency Muon 2018	✓	< 0.1	—	< 0.1	< 0.1	< 0.1	< 0.1
Trigger efficiency	✓	0.2	—	0.2	< 0.1	0.2	0.2
muon identification	✓	< 0.1	—	< 0.1	< 0.1	< 0.1	< 0.1
electron identification	✓	3.5	—	1.7	< 0.1	3.6	1.5
τ_h identification $p_T = 30\text{--}35\text{ GeV}$	✓	< 0.1	—	0.7	< 0.1	0.4	1.4
τ_h identification $p_T = 35\text{--}40\text{ GeV}$	✓	0.1	—	0.5	< 0.1	0.3	< 0.1
τ_h identification $p_T \geq 40\text{ GeV}$	✓	2.1	—	1.5	< 0.1	1.7	1.1
τ_h energy scale DM0	✓	0.2	—	< 0.1	< 0.1	0.1	0.3
τ_h energy scale DM1	✓	0.3	—	0.4	< 0.1	0.3	0.3
τ_h energy scale DM10	✓	0.3	—	0.4	< 0.1	0.3	0.3
τ_h energy scale DM11	✓	0.3	—	0.4	< 0.1	0.3	0.3
$e \rightarrow \tau_h$ misidentification	✓	0.2	—	0.7	< 0.1	0.1	< 0.1
$\mu \rightarrow \tau_h$ misidentification	✓	< 0.1	—	< 0.1	< 0.1	< 0.1	< 0.1
Jet energy scale	✓	2.2	—	15	< 0.1	2.2	0.9
Jet energy resolution	✓	1.4	—	4.6	< 0.1	1.3	0.5
MET unclustered energy scale	✓	< 0.1	—	< 0.1	< 0.1	< 0.1	< 0.1
b jet identification	✓	2.0	—	2.4	< 0.1	2.9	3.4
b jet mistagging	✓	2.7	—	0.6	< 0.1	0.9	2.1
Fake lepton non-closure shape syst	✓	—	13	—	—	—	—
Top quark mass ($t\bar{t}$)	—	—	—	2.8	—	—	—
Top quark mass (single t)	—	—	—	—	2.2	—	—
QCD acceptance (H^\pm)	—	5.0	—	—	—	—	—
QCD Scales ($t\bar{t}$)	—	—	—	+2.4 -3.5	—	—	—
QCD Scales (single t)	—	—	—	—	2.5	—	—
QCD acceptance (top)	—	—	—	2.0	—	2.0	—
QCD Scales (EW)	—	—	—	—	—	—	3.2
PDF + α_s acceptance (H^\pm)	—	+1.7 -0.4	—	—	—	—	—
PDF+ α_s ($t\bar{t}$)	—	—	—	4.2	—	—	—
PDF+ α_s (single t)	—	—	—	—	4.7	—	—
PDF+ α_s acceptance (Top)	—	—	—	+0.3 -2.0	—	+0.3 -2.0	—
PDF+ α_s (EW)	—	—	—	—	—	—	4.4
Theoretical α_s (ttH)	—	—	—	—	—	1.0	—

Table 10.1: The prefit systematic uncertainties (in %) for the background processes and the signal for $m_{H^0(h^0)} = 200\text{ GeV}$ and $m_{H^\pm} = 900\text{ GeV}$, evaluated for the $\mu e \tau_h$ with 2018 data. Nuisance parameters with a checkmark (✓) also affect the shape of the DNN output spectrum.

11 Results

In the following sections the pre-fit distributions in the SR of the $2\ell^{sf}\tau_h$ and $2\ell^{df}\tau_h$ final states are presented in Sec. 11.1.2 and Sec. 11.1.1, respectively. The expected exclusion upper limits for all $m_{H^0(h^0)}$ are presented in Sec. 11.2.2 while the pulls and impacts of the statistical and systematic uncertainties are discussed in Sec. 11.3. Finally, the Goodness-of-fit (GOF) of the model along with related GOF distributions are presented in Sec. 11.4.

11.1 Pre-fit distributions in the SR

In this subsection, the pre-fit distributions of the parameterized DNN output served as final fit discriminant are presented, in both $2\ell^{sf}\tau_h$ and $2\ell^{df}\tau_h$ final states, for all 3 years of Run2 and for the various $m_{H^0(h^0)}$ and m_{H^\pm} combinations. To prevent human bias, the results in this section are currently blinded, hiding data in regions where distributions are sensitive to signal presence, in the high-DNN score region in this case. The signal shown in each individual plot corresponds to the true mass hypothesis used to evaluate the discriminant. The misidentified ℓ ($e/\mu/\tau_h$) background is derived using the data-driven technique explained in Sec. 8, while the rest of the background contributions are consist of three prompt lepton events and are estimated purely from simulations. In all subsequent figures, vertically shaded and hashed areas denote statistical and combined (stat. \oplus syst.) uncertainties of the expected background contributions. The ratio plot showcases these uncertainties with light and dark grey bands, respectively. The low-DNN score region is unblinded since the signal strength is minimal and it is done to make sure that the method works in this region. In this low-DNN score region, data and simulation are in agreement within statistical and systematic uncertainties.

11.1.1 The $2\ell^{df}\tau_h$ final states

The prefit distributions of the DNN output used as final fit discriminant, are presented in Figs. 11.1–11.4, for the $2\ell^{df}\tau_h$ final state. The $m_{H^0(h^0)} = 200$ GeV is selected to be presented in the main body while the distributions for the other 4 $m_{H^0(h^0)}$ can be found in Appendix B.

11.1.2 The $2\ell^{sf}\tau_h$ final states

In this subsection, the prefit distributions of the DNN output for $ee\tau_h$ (Figs. 11.5–11.8) and $\mu\mu\tau_h$ (Figs. 11.9–11.12) final states are presented. As in the $2\ell^{df}\tau_h$ case, the $m_{H^0(h^0)} = 200$ GeV is selected to be presented in the main body while the distributions for the other 4 $m_{H^0(h^0)}$ can be found in Appendix C and Appendix D, for $ee\tau_h$ and $\mu\mu\tau_h$, respectively.

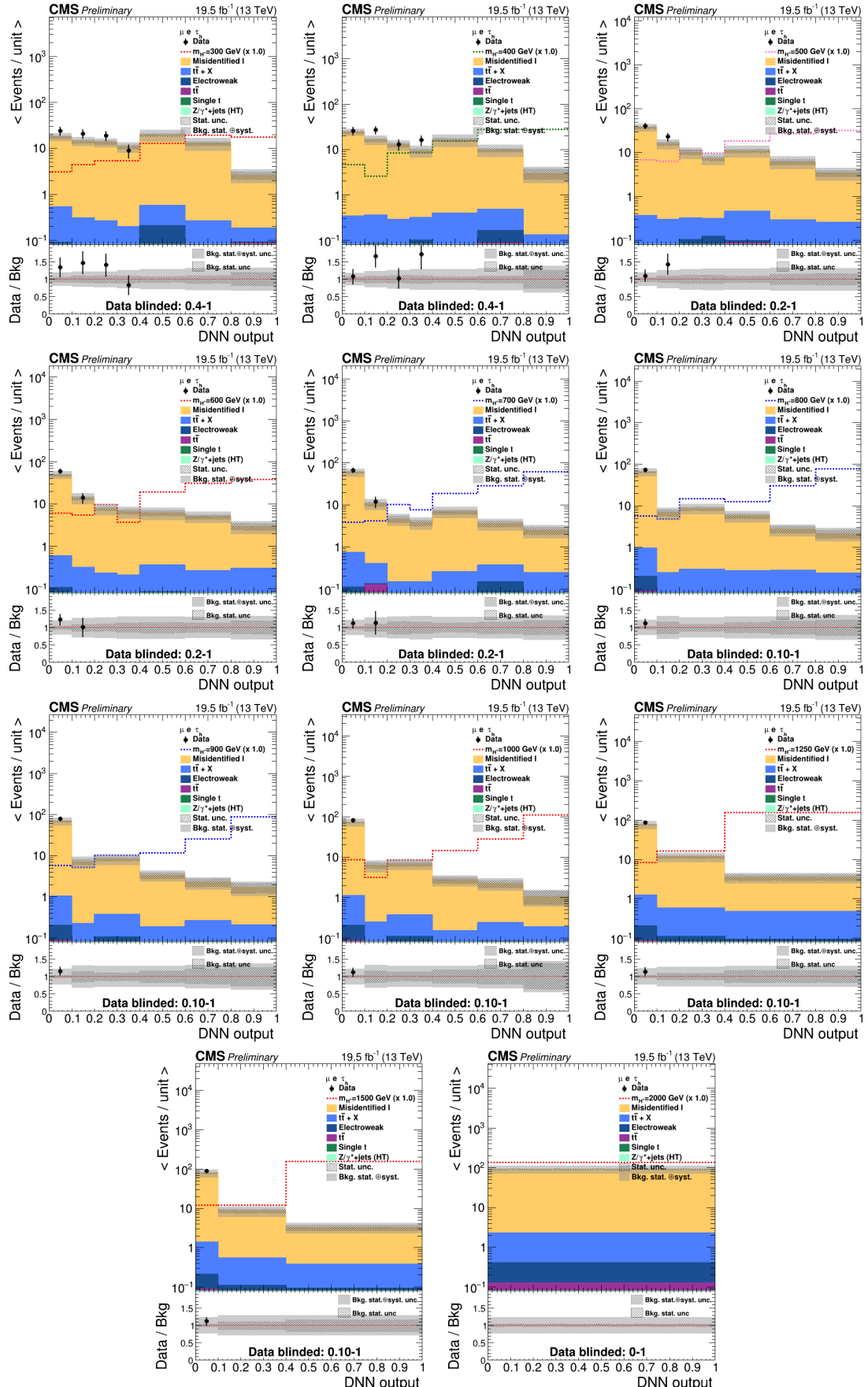


Figure 11.1: Distributions of the parameterized DNN output in $2\ell^{df}\tau_h$ final state for $m_{H^0(h^0)} = 200$ GeV and all available m_{H^\pm} using 2016 pre-VFP data.

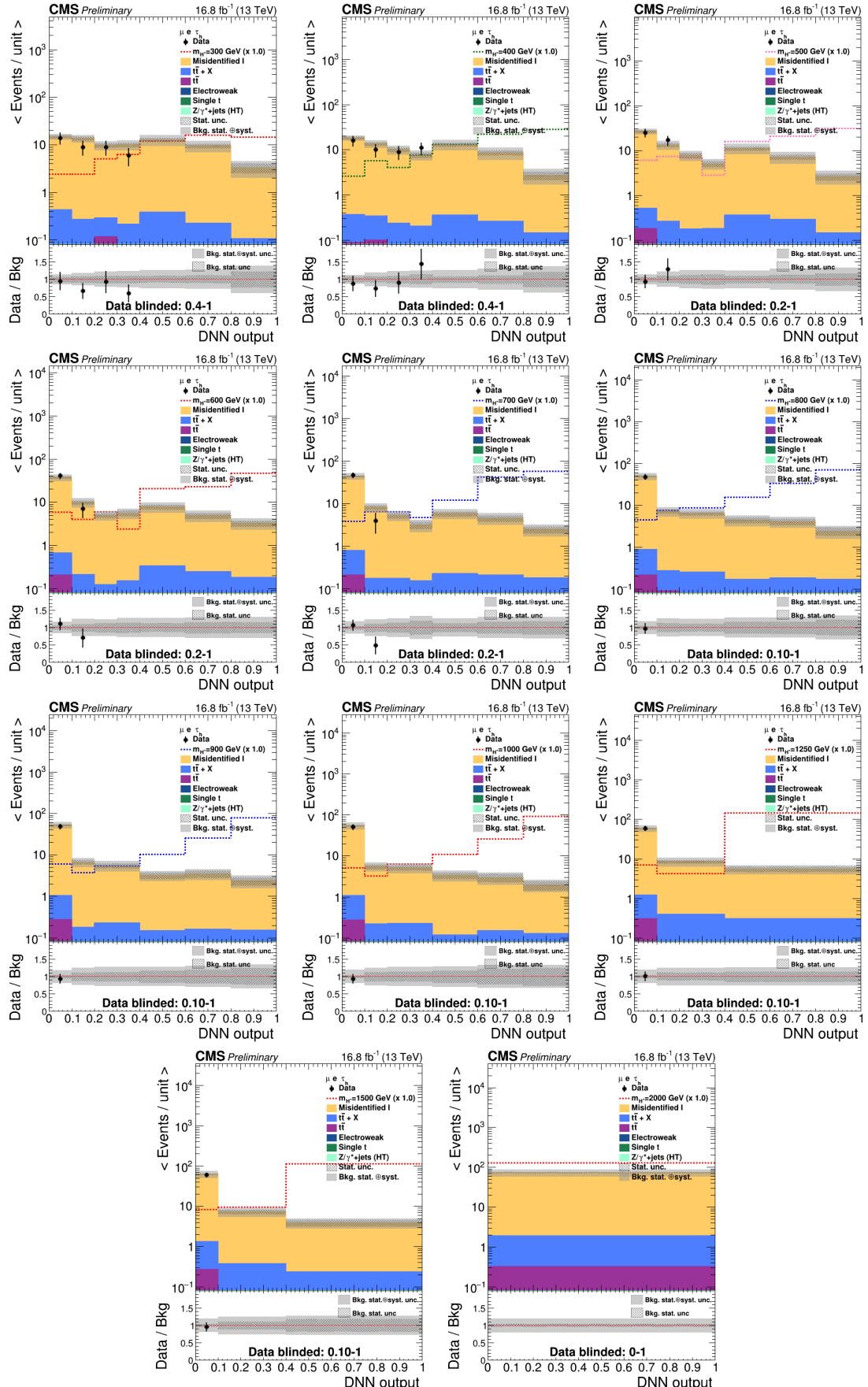


Figure 11.2: Distributions of the parameterized DNN output in $2\ell^{df}\tau_h$ final state for $m_{H^0(h^0)} = 200$ GeV and all available m_{H^\pm} using 2016 post-VFP data.

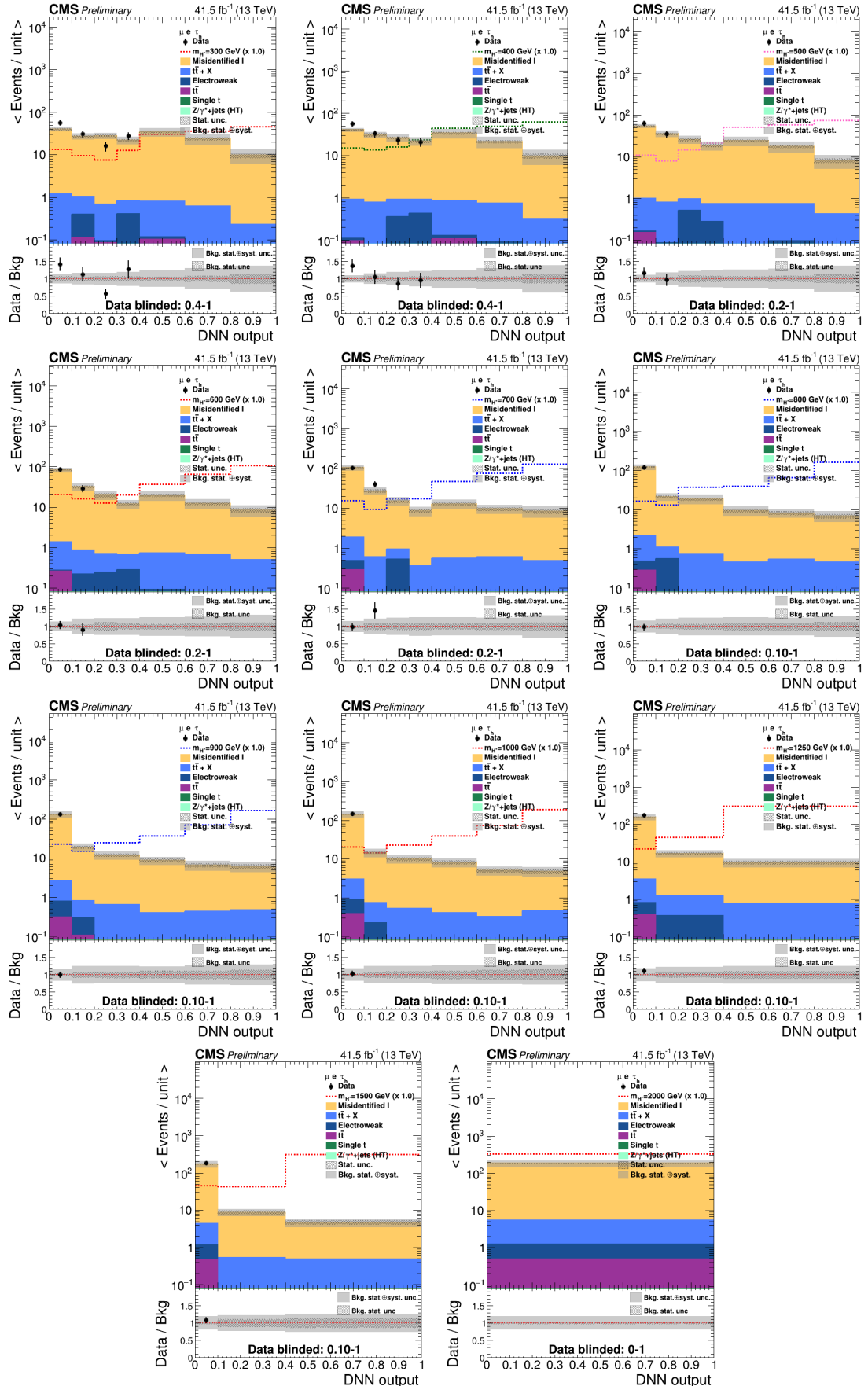


Figure 11.3: Distributions of the parameterized DNN output in $2\ell^{df}\tau_h$ final state for $m_{H^0(h^0)} = 200$ GeV and all available m_{H^\pm} using 2017 data.

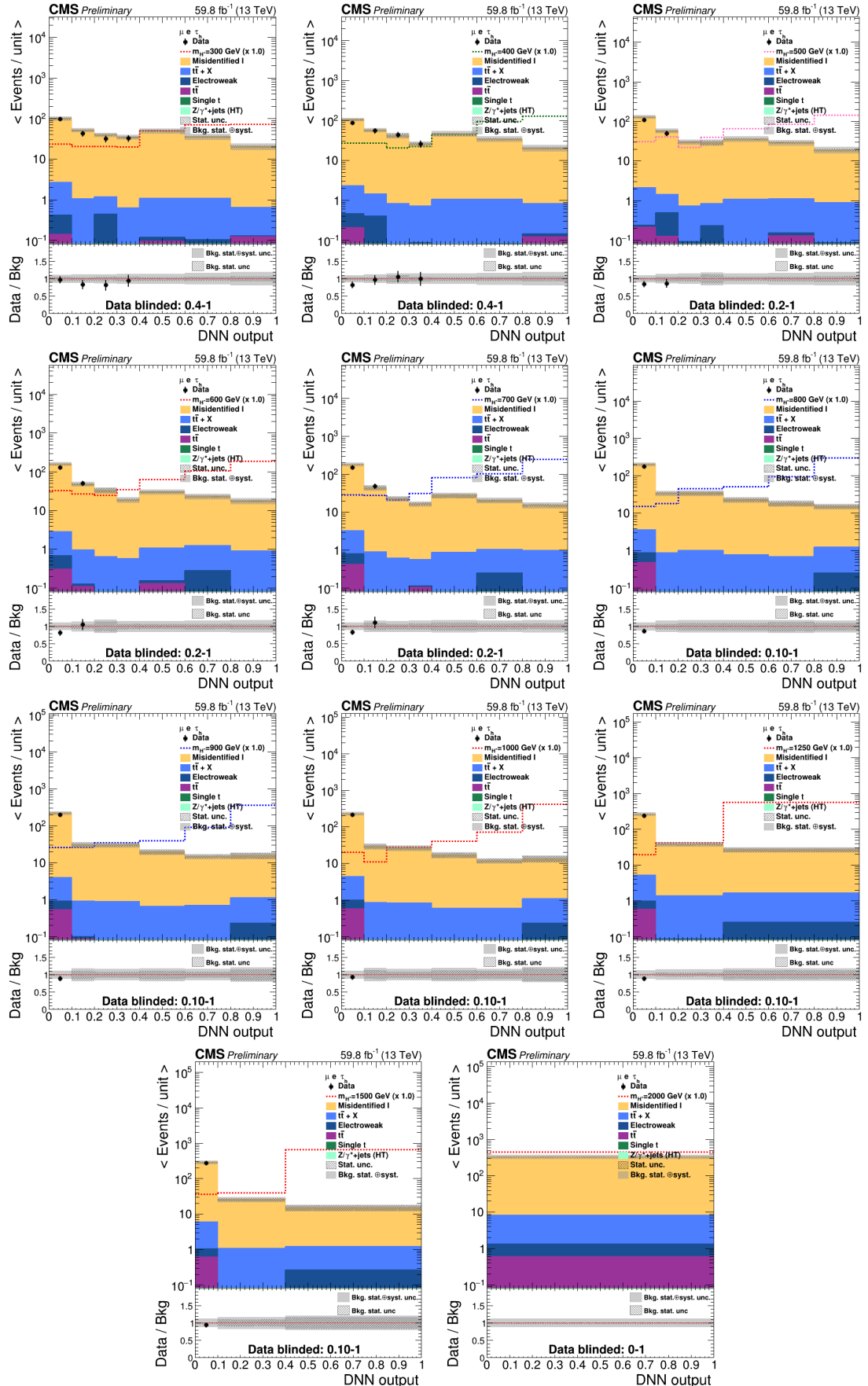


Figure 11.4: Distributions of the parameterized DNN output in $2\ell^{df}\tau_h$ final state for $m_{H^0(h^0)} = 200$ GeV and all available m_{H^\pm} using 2018 data.

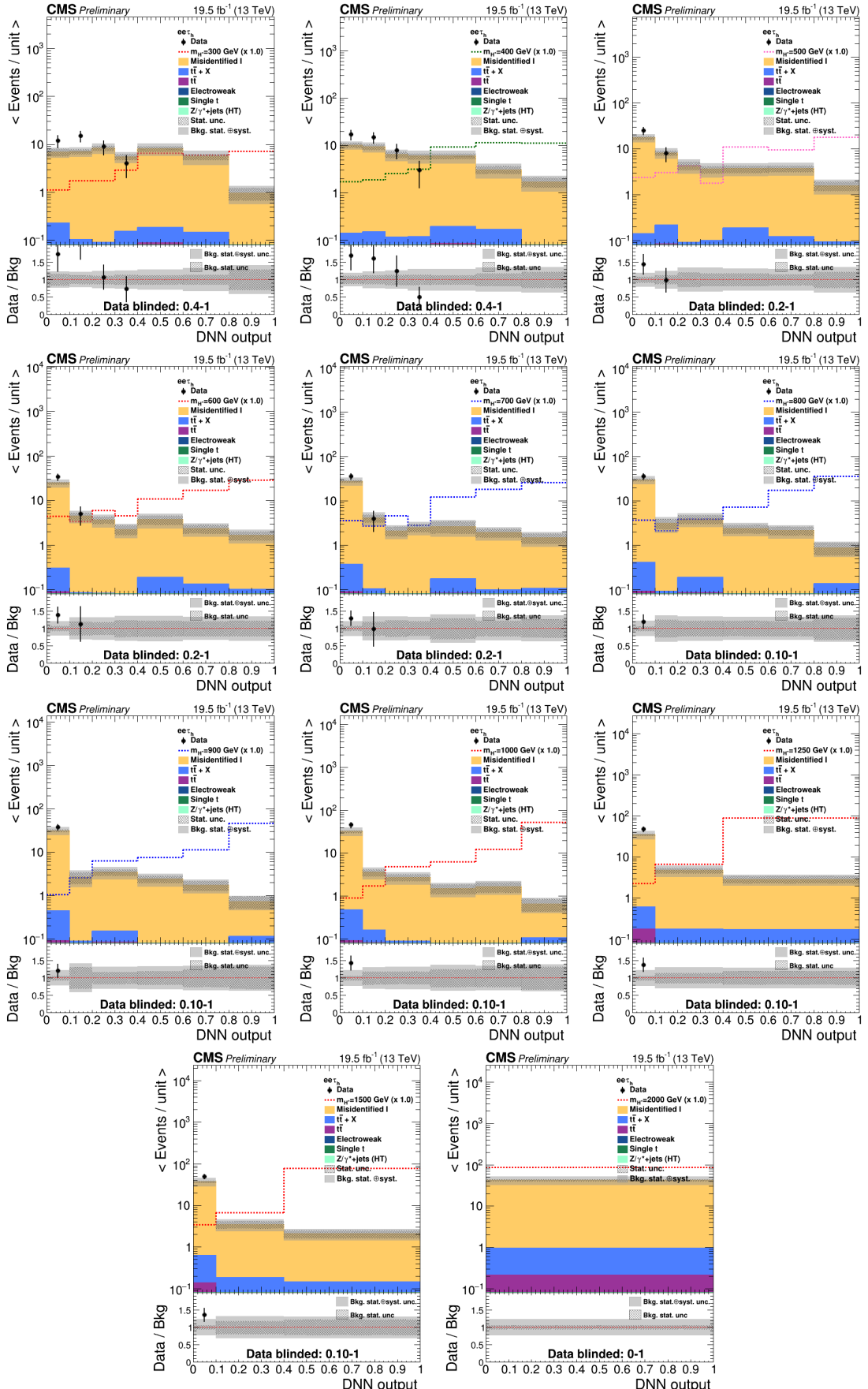


Figure 11.5: Distributions of the parameterized DNN output in $ee\tau_h$ final state for $m_{H^0(h^0)} = 200 \text{ GeV}$ and all available m_{H^\pm} using 2016 pre-VFP data.

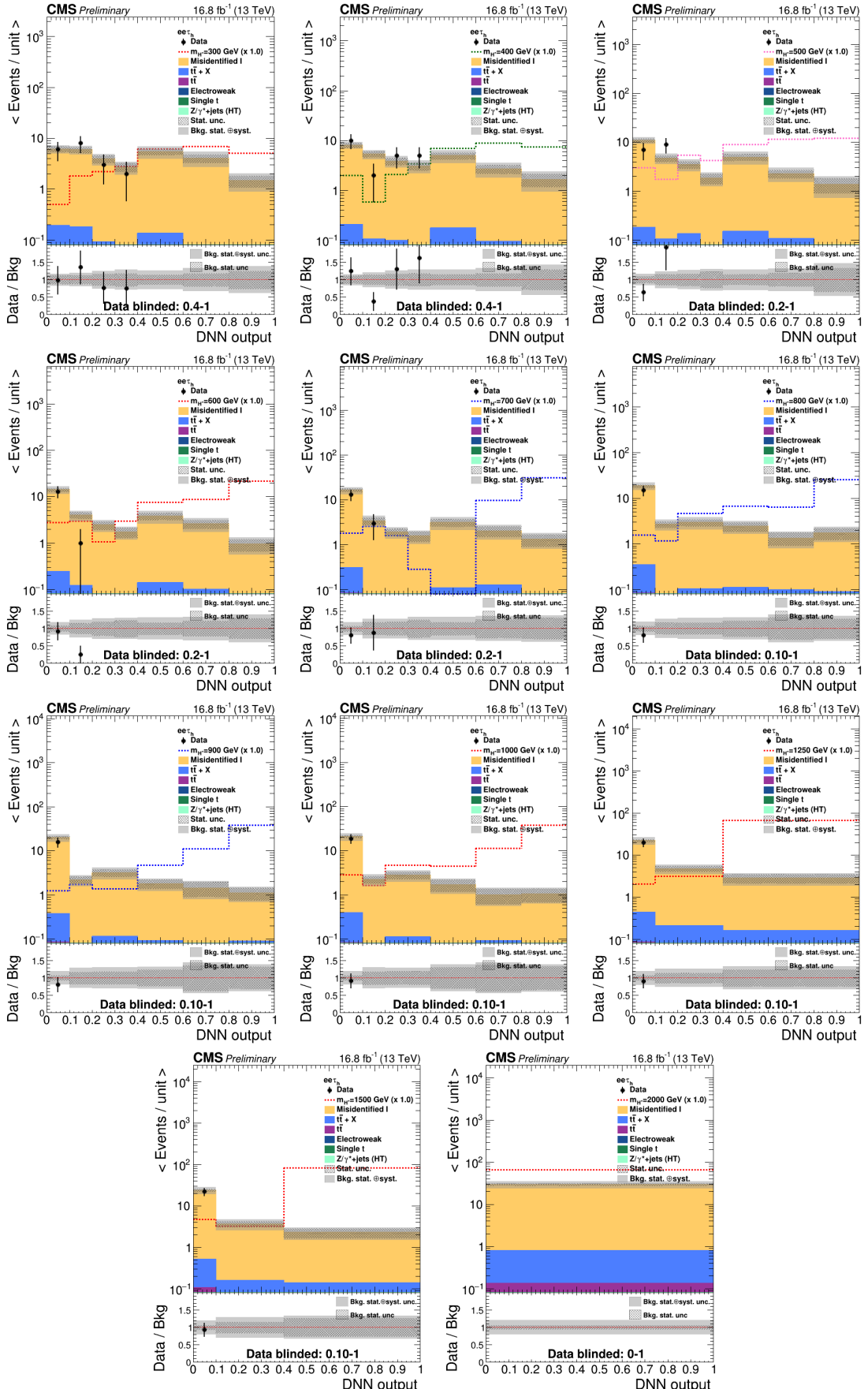


Figure 11.6: Distributions of the parameterized DNN output in $ee\tau_h$ final state for $m_{H^0(h^0)} = 200 \text{ GeV}$ and all available m_{H^\pm} using 2016 post-VFP data.

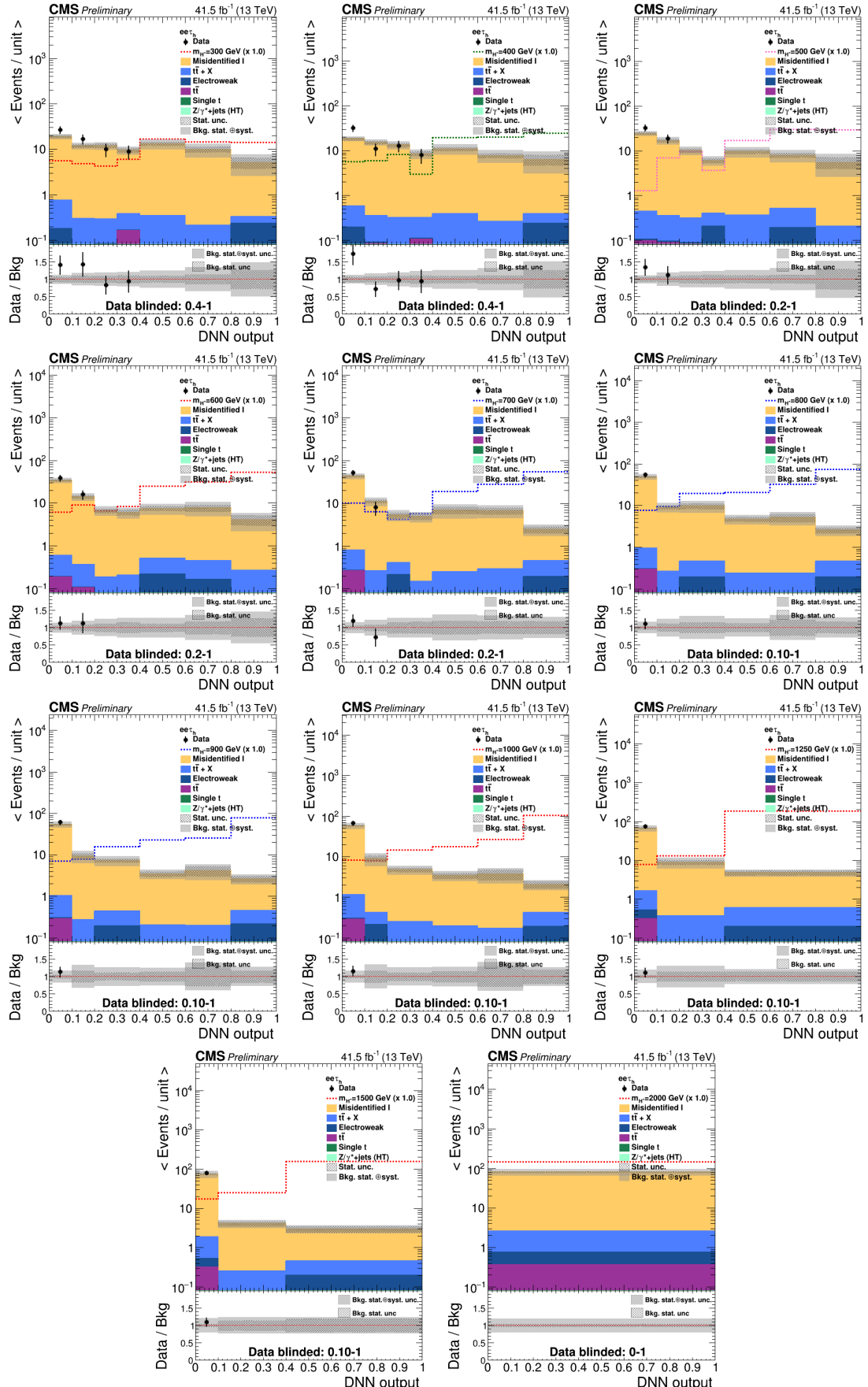


Figure 11.7: Distributions of the parameterized DNN output in ee τ_h final state for $m_{H^0(h^0)} = 200$ GeV and all available m_{H^\pm} using 2017 data.

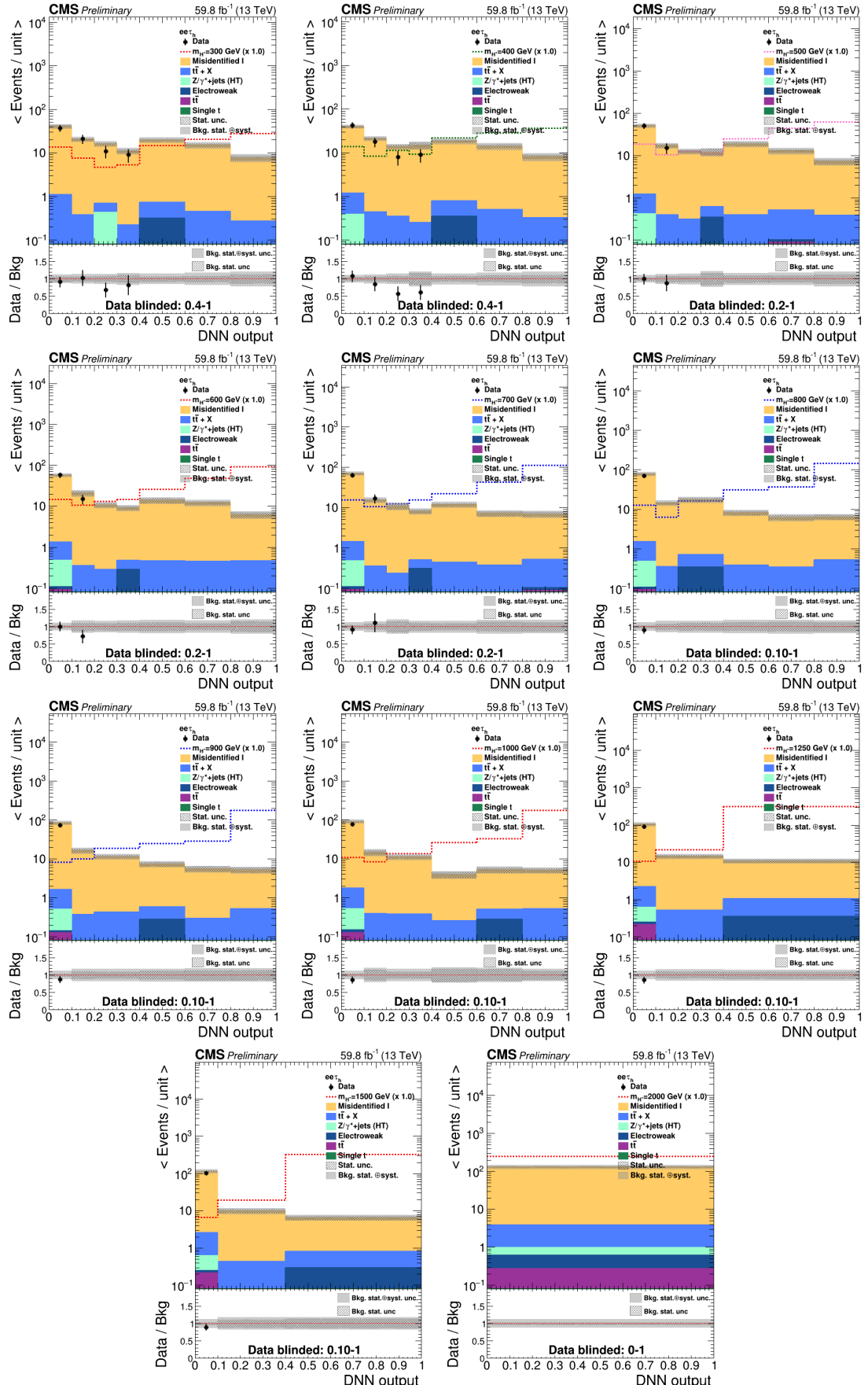


Figure 11.8: Distributions of the parameterized DNN output in $ee\tau_h$ final state for $m_{H^0(h^0)} = 200$ GeV and all available m_{H^\pm} using 2018 data.

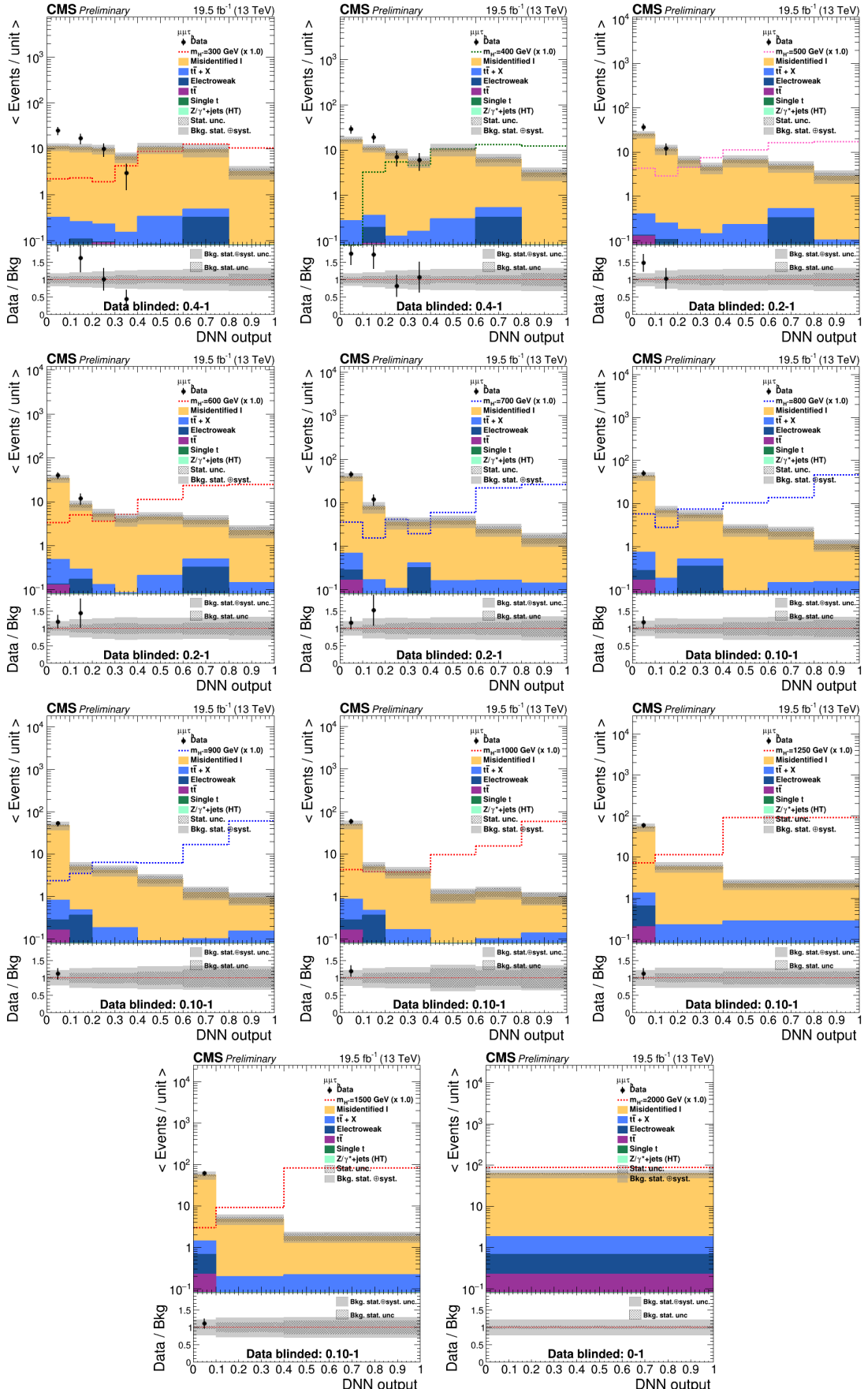


Figure 11.9: Distributions of the parameterized DNN output in $\mu\mu\tau_h$ final state for $m_{H^0(h^0)} = 200$ GeV and all available m_{H^\pm} using 2016 pre-VFP data.

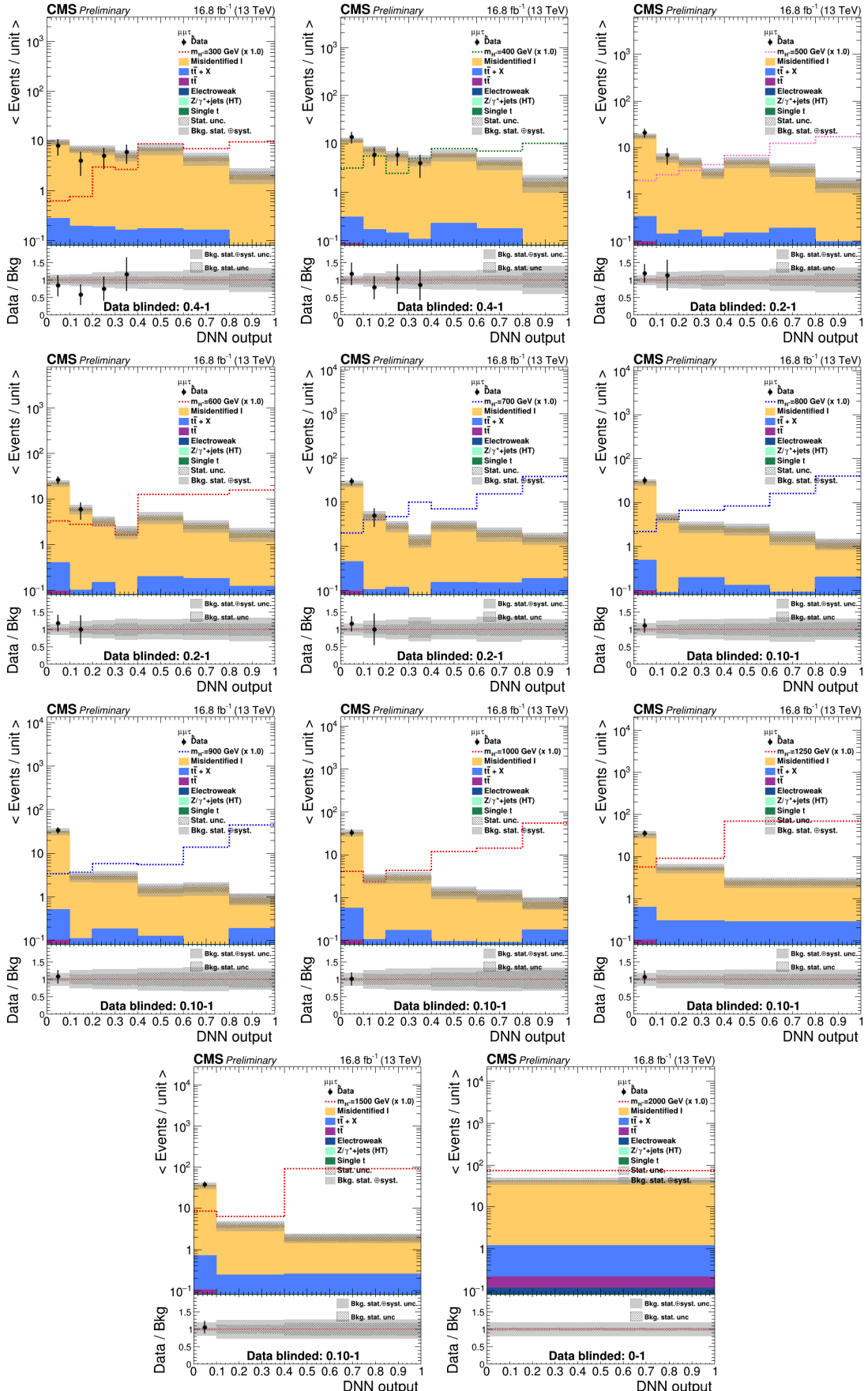


Figure 11.10: Distributions of the parameterized DNN output in $\mu\mu\tau_h$ final state for $m_{H^0(h^\pm)} = 200$ GeV and all available m_{H^\pm} using 2016 post-VFP data.

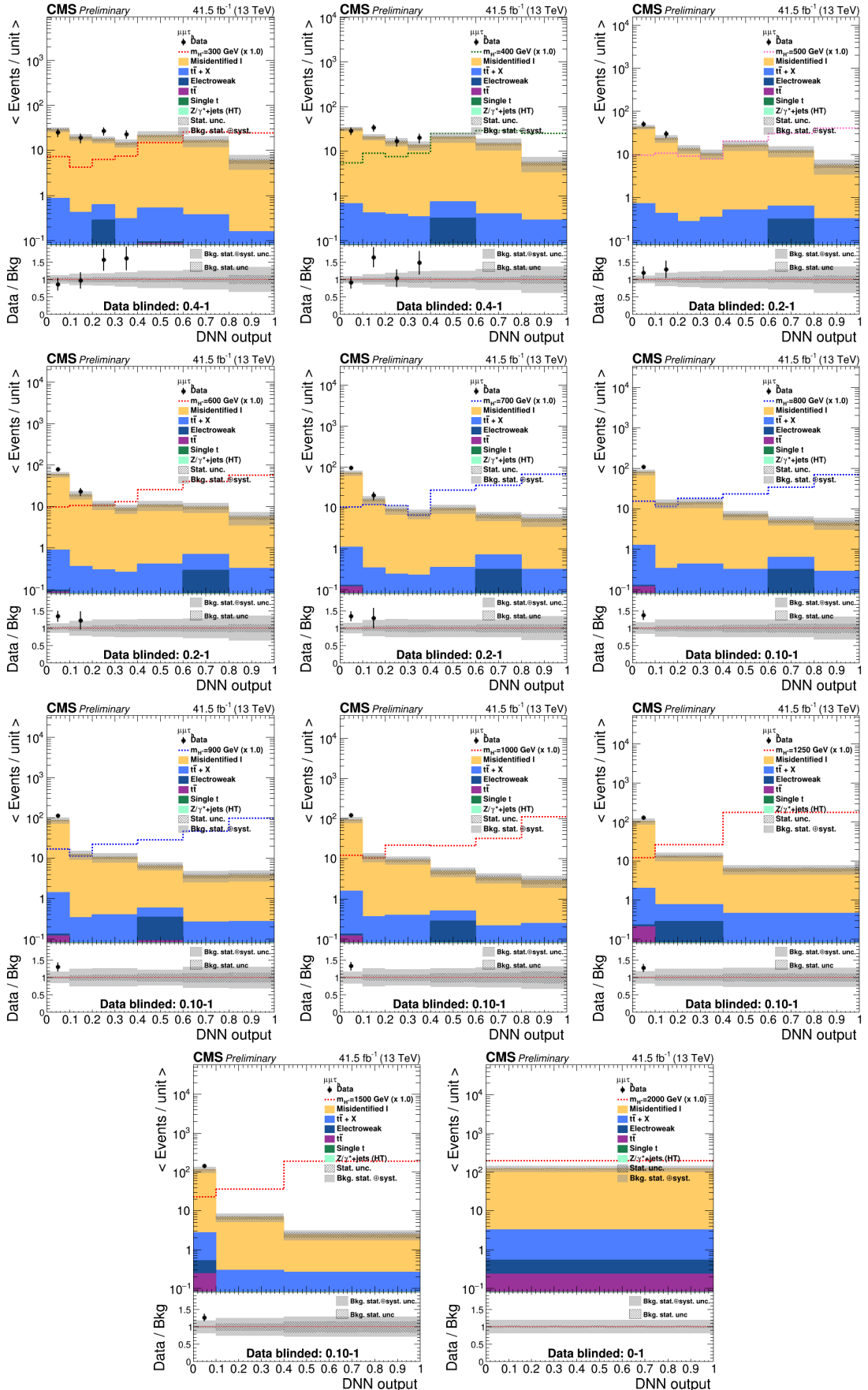


Figure 11.11: Distributions of the parameterized DNN output in $\mu\mu\tau_h$ final state for $m_{H^0(h^0)} = 200$ GeV and all available m_{H^\pm} using 2017 data.

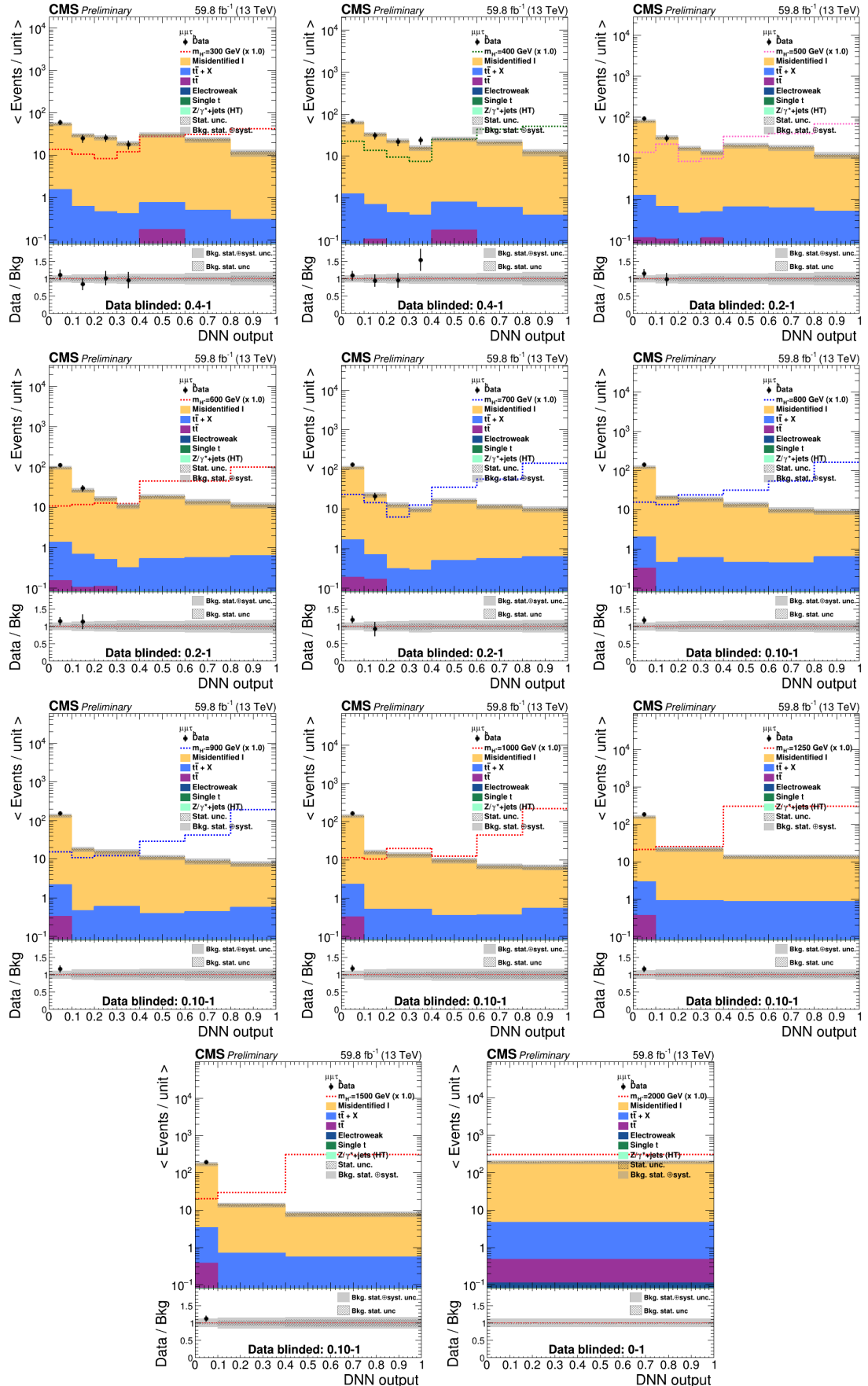


Figure 11.12: Distributions of the parameterized DNN output in $\mu\mu\tau_h$ final state for $m_{H^0(h^0)} = 200$ GeV and all available m_{H^\pm} using 2018 data.

11.2 Expected exclusion upper limits

The 95% upper limits are determined as a binned Maximum Likelihood (ML) fit on the distributions of the DNN output, for the $2\ell^{sf}\tau_h$ ($ee\tau_h$ - $\mu\mu\tau_h$) and $2\ell^{df}\tau_h$ final states, respectively. In the following sections, a brief introduction for the statistical method used for calculating the expected exclusion upper limits is presented in Sec. 11.2.1 and the expected exclusion limits are presented in Sec. 11.2.2. Finally, the impact of the nuisance parameters on the results are described in Sec. 11.3 while the distributions related to the Goodness-of-fit are displayed in Sec. 11.4.

11.2.1 Statistical method for calculating the expected exclusion upper limits for H^\pm production

The method used for the upper limit calculations for charged Higgs production is known as modified frequentist CLs criterion. This method uses a test statistic based on profile likelihood ratios and includes systematic uncertainties via nuisance parameters (NPs). The CMS Higgs combination tool, Combine [103], is used, which is based on the RooStats software [104]. The upper limits are found by fitting the data from each final state using a binned maximum likelihood approach.

Both $2\ell^{df}\tau_h$ and $2\ell^{sf}\tau_h$ final states utilize a DNN classifier for signal-background discrimination. The likelihood function, Eq. 70, combines Poisson probabilities with probability density functions of NP's, Θ :

$$\mathcal{L}(\text{data}|\mu, \Theta) = \prod_i \text{Poisson}(\text{data}_i|s_i(\mu, \Theta) + b_i(\Theta)) \times \prod_j p(\tilde{\Theta}_j|\Theta_j) \quad (70)$$

where data_i is the number of observed data events, while the $s_i(\mu, \Theta)$ and $b_i(\mu, \Theta)$ are the expected numbers of the signal and background events respectively, all in a given i bin. The Poisson probability for bin i is defined as

$$\text{Poisson}(\text{data}_i|s_i(\mu, \Theta) + b_i(\Theta)) = \frac{(s_i(\mu, \Theta) + b_i(\Theta))^{n_i}}{n_i!} \exp(-s_i(\mu, \Theta) - b_i(\Theta)) \quad (71)$$

The probability density functions describe how likely a true value of a NP is equal to Θ_i , given the best estimate $\tilde{\Theta}_j$ from a measurement. The μ parameter, known as the signal strength modifier, is what the limit is based on. The test statistic \tilde{q}_μ quantifies the compatibility with the background-only hypothesis through the profile likelihood ratio:

$$\tilde{q}_\mu = -2 \ln \frac{\mathcal{L}(\text{data}|\mu, \hat{\Theta}_\mu)}{\mathcal{L}(\text{data}|\hat{\mu}, \hat{\Theta})} \quad (72)$$

The observed $\tilde{q}_\mu^{\text{obs}}$ and the best NP values for signal-plus-background and background-only hypotheses are extracted by maximising the Eq. 70. Upper limits are determined by defining p -values for these hypotheses, with distributions obtained through Monte Carlo simulated toy experiments.

The upper limit for μ at the 95% confidence level is determined when $\text{CLs}(\mu) = 0.05$, as these limits are one-sided by definition. A decaying exponential function is used to evaluate $\text{CLs}(\mu) = 0.05$ from the tested μ values. The compatibility test, CLs , is expressed as:

$$\text{CLs}(\mu) = \frac{\text{CLs} + b(\mu)}{\text{CLs}(\mu)} \leq \alpha \quad (73)$$

For heavy charged Higgs boson searches, H^\pm production involves top and bottom quark fusion. Thus, the signal event count $s_i(\mu, \Theta)$ is expressed as:

$$s_i(\mu, \Theta) = \mu \times s_{HW\tau\tau,i}(\Theta) \quad (74)$$

with μ given by:

$$\mu = \sigma_{pp \rightarrow t(b)H^\pm} \times \mathcal{B}(H \rightarrow HW) \times (H \rightarrow \tau\tau) \quad (75)$$

Statistical uncertainties are modeled using the Barlow-Beeston-lite approach [105] (also known as autoMCstats). This approach minimizes the number of parameters needed in the fit. Statistical uncertainties are permitted to vary independently across distribution bins and irrespective of signal or background samples. Measures are taken to ensure stable behavior, especially in bins with zero expected events due to limited statistics. This stability is replicated in simulated sample distributions where statistical uncertainty is less than the sample's statistical resolution.

11.2.2 Expected upper limits for $2\ell^{df}\tau_h$ - $2\ell^{sf}\tau_h$ combination

In general, in the analysis process, the production of limits is often conducted in a blinded manner to minimize potential biases and maintain the integrity of the study. This means that instead of using the actual observed data events, an Asimov dataset is employed. The Asimov dataset is a hypothetical dataset constructed using the best estimates of the expected background and signal contributions. It serves as a representative sample that mimics the expected behavior of the data under the background-only hypothesis or a specific signal model, allowing the evaluation of the sensitivity and performance of an analysis without

revealing actual experimental outcomes. This approach ensures that the analysis remains unbiased and objective, providing a reliable foundation for the subsequent interpretation of results.

In this study, the combined expected upper limits are presented, blinded, using the Asimov dataset, dependent on the $\tan\beta$ and $\sin(b - a)$ values of the 2HDM, used to produce the signal samples (see Sec. 4.2.5). For $m_{H^0(h^0)} = 125, 200$ and 300 GeV, $\tan\beta$ is set to be equal to 10 and $\sin(b - a)$ to 1, while for $m_{H^0(h^0)} = 80$ and 90 GeV, the values of the $\tan\beta$ and $\sin(b - a)$ are equal to 5 and 0, respectively. The combined limit for the full Run2 data, using the full available mass range of m_{H^\pm} (300 GeV - 2TeV) for $m_{H^0(h^0)} = 200$ GeV is presented in Figs. 11.13 and also tabulated in Table 11.1.

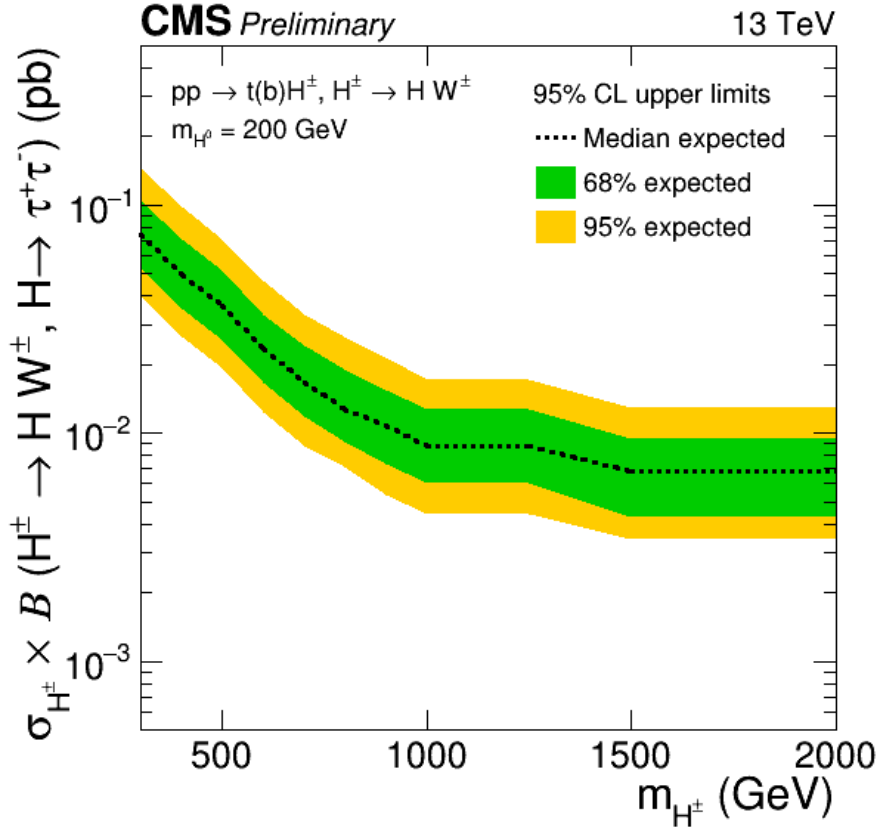


Figure 11.13: Combined expected upper limit of the $2\ell^{sf}\tau_h$ and $2\ell^{df}\tau_h$ final states with full Run2 data and $m_{H^0(h^0)} = 200$ GeV. The dotted black line shows the median expected limit, while the 68% and 95% confidence intervals are presented with the green and yellow bands, respectively.

The combined expected upper limits for the other 4 $m_{H^0(h^0)}$, 80 , 90, 125 and 300 GeV are presented in Fig. 11.14, also produced with full Run2 data. They are also tabulated and presented in Appendix E along with all individual limits, as produced per each final state and Run2 year, separately.

m_{H^\pm} (GeV)	Expected limit					Observed limit
	-2σ	-1σ	median	$+1\sigma$	$+2\sigma$	
300	0.03943	0.05247	0.07422	0.10499	0.14459	Blinded
400	0.02646	0.03521	0.04980	0.07045	0.09766	Blinded
500	0.01920	0.02555	0.03613	0.05169	0.07078	Blinded
600	0.01245	0.01657	0.02344	0.03315	0.04626	Blinded
700	0.00882	0.01174	0.01660	0.02401	0.03311	Blinded
800	0.00714	0.00922	0.01270	0.01917	0.02646	Blinded
900	0.00537	0.00739	0.01074	0.01554	0.02143	Blinded
1000	0.00439	0.00604	0.00879	0.01271	0.01709	Blinded
1250	0.00439	0.00604	0.00879	0.01271	0.01709	Blinded
1500	0.00342	0.00427	0.00684	0.00945	0.01299	Blinded
2000	0.00342	0.00427	0.00684	0.00945	0.01299	Blinded

Table 11.1: The $2\ell^{sf}\tau_h$ and $2\ell^{df}\tau_h$ combined upper limit for $m_{H^0(h^0)} = 200$ GeV, at 95% CL on $\sigma_{pp \rightarrow t(b)H^\pm} \times \mathcal{B}(H^+ \rightarrow H^0 W^+) \times (H^0 \rightarrow \tau^+\tau^-)$ as a function of m_{H^\pm} , with full Run 2 data.

11.3 Impacts of the Nuisance Parameters

The measurement of the correlation between the Signal Strength (\hat{r}) and the Nuisance Parameters is done by calculating the impact of these NP on the Signal Strength itself. This impact of a given nuisance θ , is defined as the $\Delta\hat{r}$ shift caused by shifting θ to its $\pm 1\sigma$ post-fit values, keeping all other parameters to their nominal values. In general, in the case of highly ranked impacts coming from statistical sources (see prob_binhplus in Fig. 11.15), as in this study, leads to the conclusion that the sensitivity is mostly driven by lack of statistics. The direction of the $\pm 1\sigma$ impacts on (\hat{r}) indicates whether the parameter is correlated or anti-correlated with it. This measurement is essential for understanding the importance of all NP based on their effect on the signal strength uncertainty.

The pulls and impacts on the NP values are estimated using the MultiDimFit method of the Combined Software [106] and produced with the Asimov dataset with the expected signal cross section set to 1 pb . The impacts presented in Fig. 11.15 are estimated for the $m_{H^0(h^0)} = 200$ GeV and $m_{H^\pm} = 800$ GeV mass hypothesis, combined for $2\ell^{sf}\tau_h$ and $2\ell^{df}\tau_h$ final states. Only the first thirty NPs are shown, in descending order of significance based on the signal strength uncertainty ($\Delta\hat{r}$).

11.4 Goodness of fit

The compatibility of model with the observed data is tested through the Goodness of Fit (GOF) method. In this study, since is all done blinded, a pseudo-data dataset is produced by

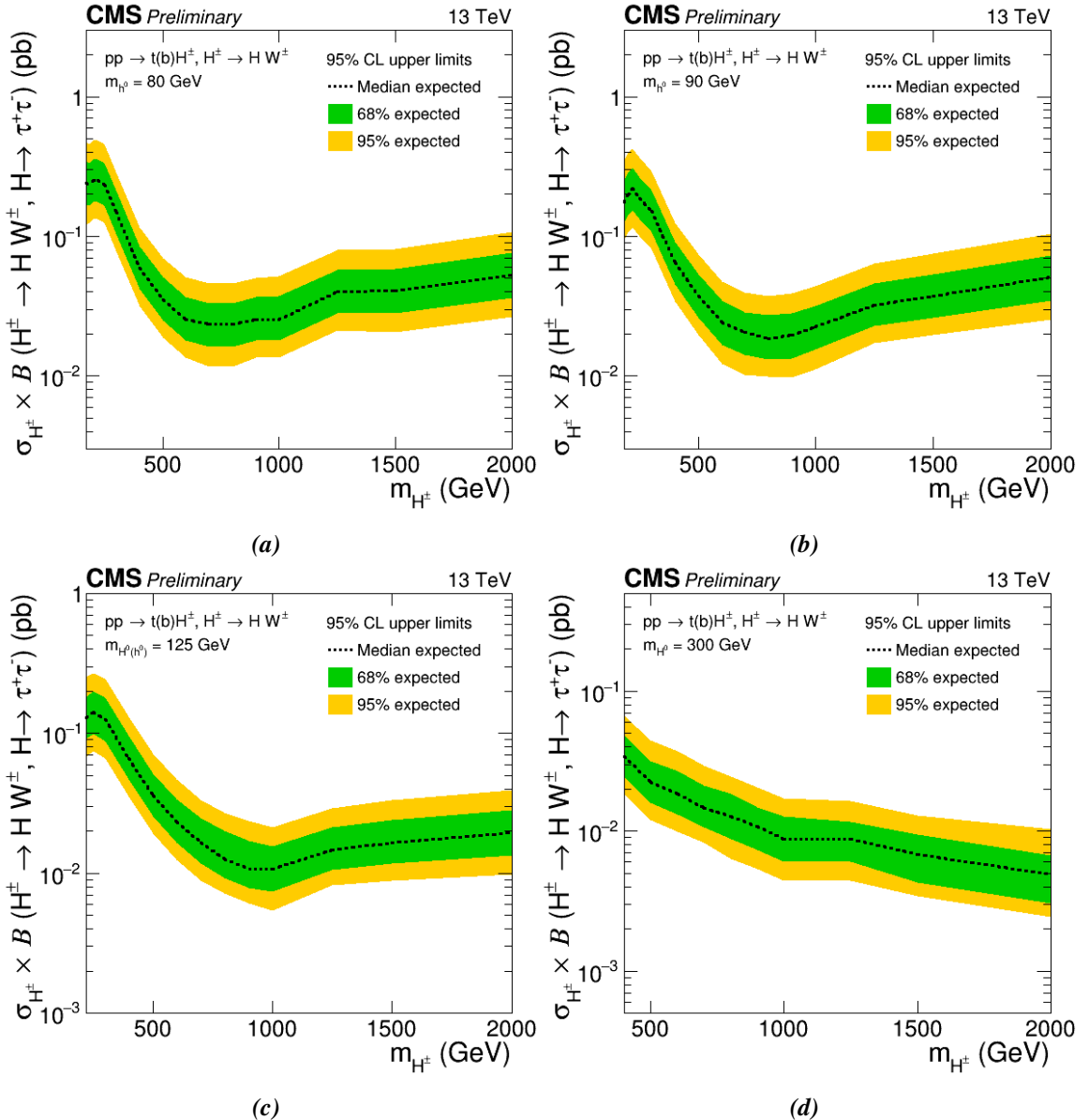


Figure 11.14: Combined expected upper limit of the $2\ell^{sf}\tau_h$ and $2\ell^{df}\tau_h$ final states with full Run2 data. The dotted black line shows the median expected limit, while the 68% and 95% confidence intervals are presented with the green and yellow bands, respectively. The limits are presented for $m_{H^0(h^0)}$ values of (a) 80 GeV, (b) 90 GeV, (c) 125 GeV and (d) 300 GeV.

varying the background contributions within uncertainty. The GOF method is done with the so-called saturated model. By defining test-statistic t as:

$$t = -2 \ln \lambda = 2 \sum_i \left[f_i - d_i + d_i \ln \left(\frac{d_i}{f_i} \right) \right], \quad (76)$$

where d_i is the i^{th} measured data and f_i is the model prediction. The ratio between the model expectation f_i and observation d_i is known as the "likelihood ratio". This allows for an arbitrary combination of binned channels with arbitrary constrains. Using the observed value of the test-statistic, t_0 , and the corresponding distribution obtained from toy experiments,

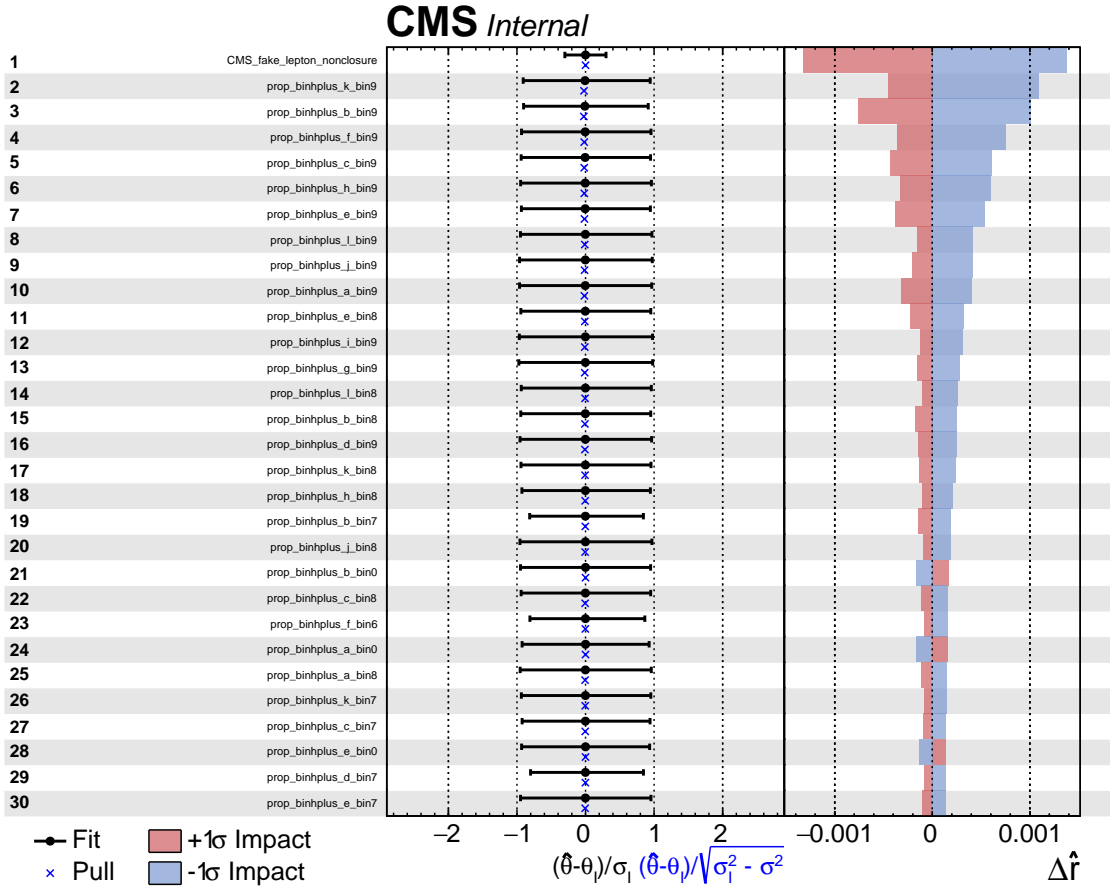


Figure 11.15: Pulls (left column) and Impacts (right column) for the $2\ell^{sf}\tau_h$ and $2\ell^{df}\tau_h$ combination and all three years, using the Asimov dataset. The signal assumption is the $m_{H^0(h^0)} = 200$ GeV and $m_{H^\pm} = 800$ GeV mass hypothesis, assuming 1pb signal cross section.

$f(t)$, the p – value is defined as :

$$p\text{-value} = \int_{t=t_0}^{+\infty} f(t) dt \quad (77)$$

The closest to one this p-value is, the stronger the indication that the results of the analysis are reasonable while the criterion for a failed test is the scenario of a p -value to be less than 0.05. The GOF distributions are shown in Figs. 11.16–11.20 for all available $m_{H^0(h^0)}$ and some of the H^\pm mass hypotheses. These GOFs are produced for the combination of all final states and eras, estimated with 500 toy experiments as presented by the red-line distributions. The observed t_0 value estimated with the pseudo-data dataset is presented by the blue vertical line. The t_0 value is compatible with the expectation from toy experiments, in all $m_{H^0(h^0)}$ - m_{H^\pm} combinations.

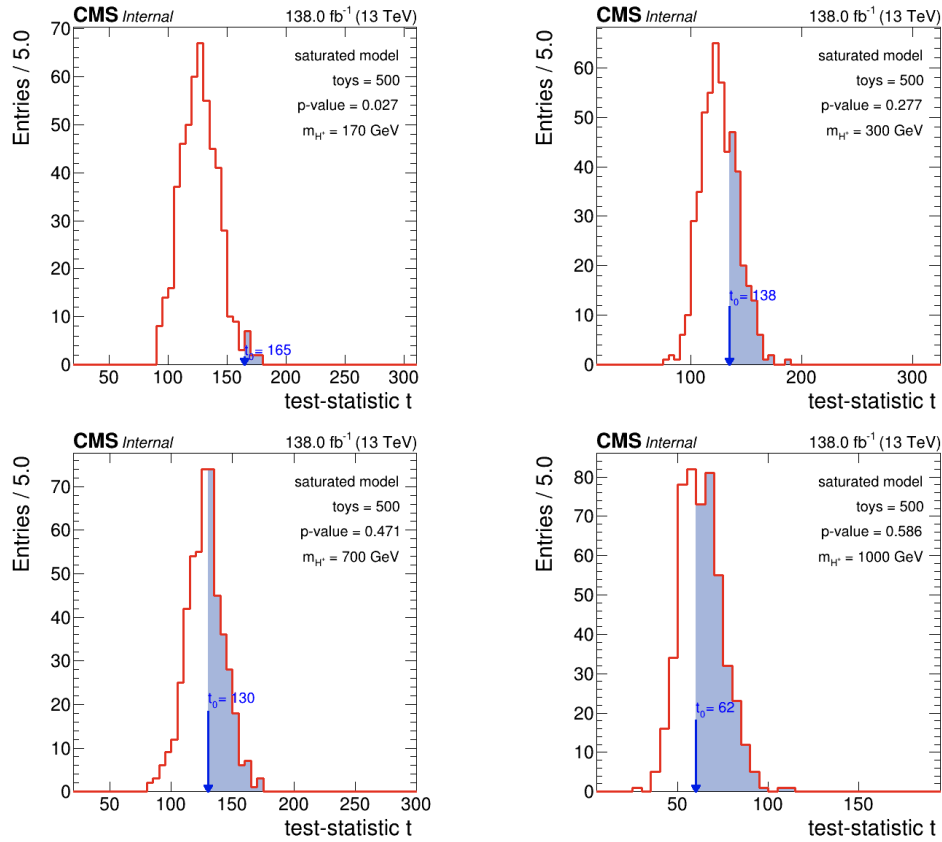


Figure 11.16: The Goodness-of-fit for the combination of all final states and eras obtained with the saturated algorithm, using pseudo-data for $m_{H^0(h^0)} = 80 \text{ GeV}$ and different m_{H^\pm} values.

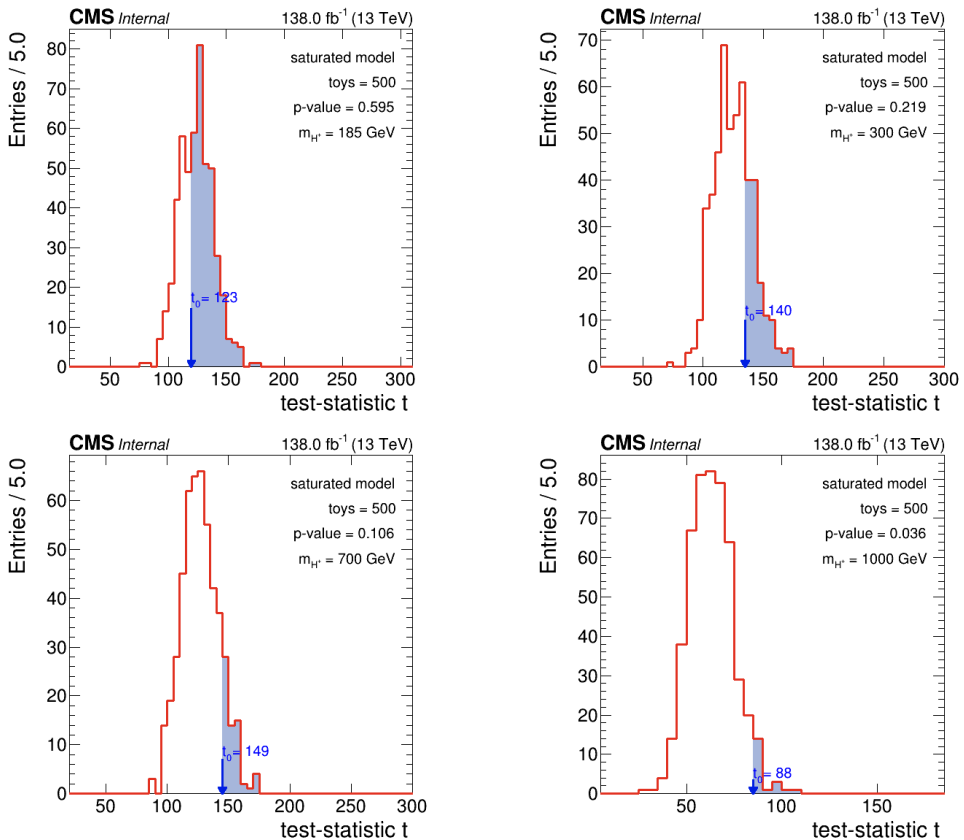


Figure 11.17: The Goodness-of-fit for the combination of all final states and eras obtained with the saturated algorithm, using pseudo-data for $m_{H^0(h^0)} = 90 \text{ GeV}$ and different m_{H^\pm} values.

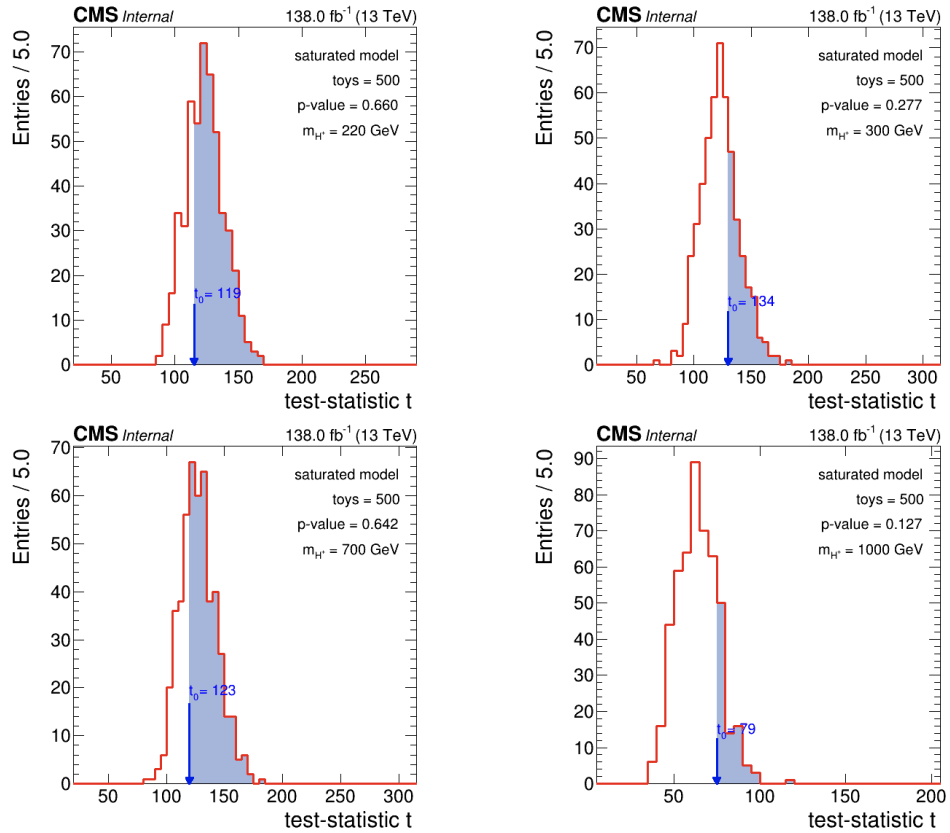


Figure 11.18: The Goodness-of-fit for the combination of all final states and eras obtained with the saturated algorithm, using pseudo-data for $m_{H^0(h^0)} = 125 \text{ GeV}$ and different m_{H^\pm} values.

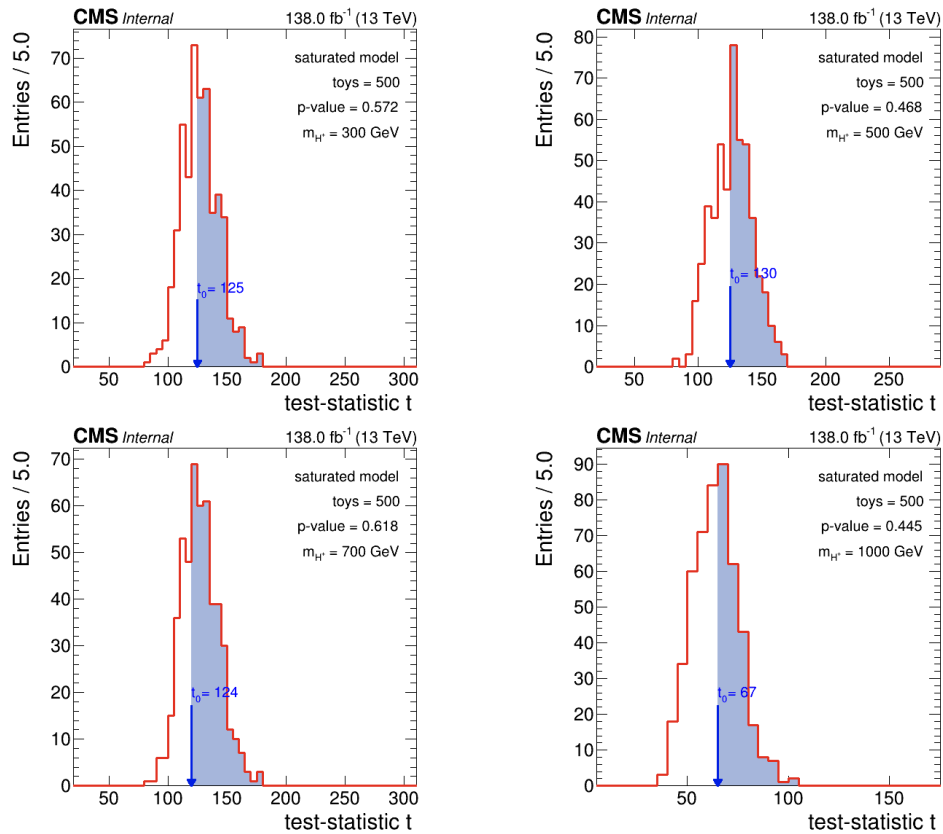


Figure 11.19: The Goodness-of-fit for the combination of all final states and eras obtained with the saturated algorithm, using pseudo-data for $m_{H^0(h^0)} = 200 \text{ GeV}$ and different m_{H^\pm} values.

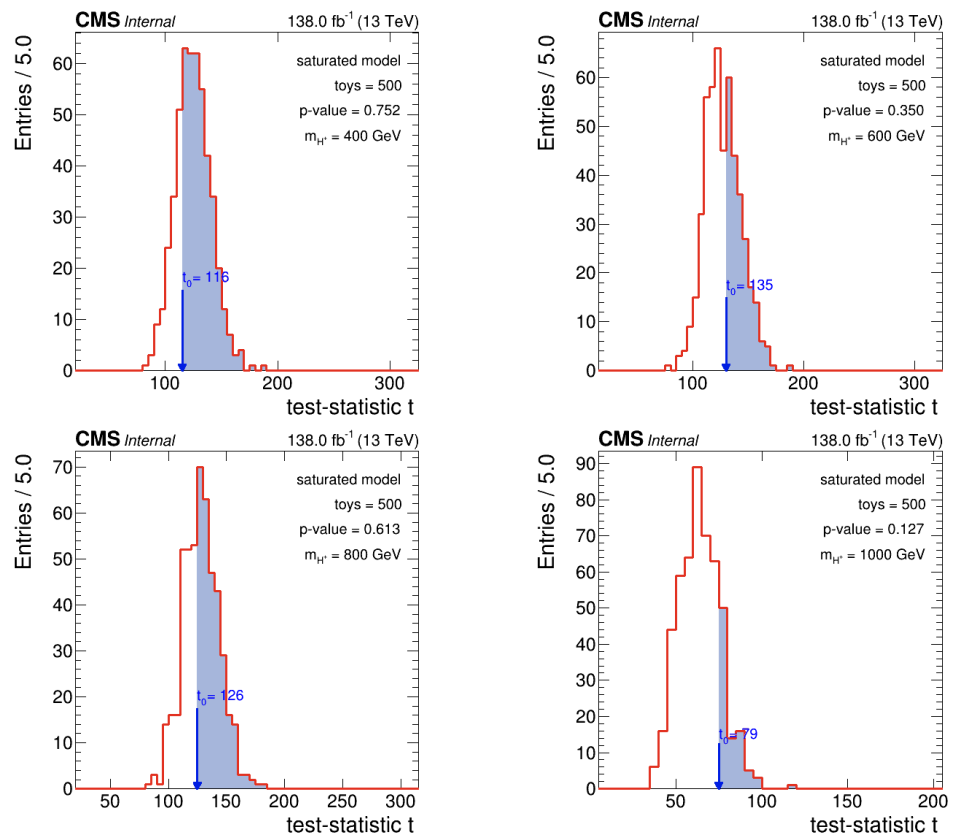


Figure 11.20: The Goodness-of-fit for the combination of all final states and eras obtained with the saturated algorithm, using pseudo-data for $m_{H^0(h^0)} = 300 \text{ GeV}$ and different m_{H^\pm} values.

12 Conclusions

The search for a Charged Higgs boson in events produced by the CMS experiment at the LHC has been conducted using the full Run-II dataset. In most extensions of the Standard Model (SM), the Higgs sector must be expanded by introducing additional singlets, doublets, or even triplets of Higgs fields. The simplest extension is the Minimal Supersymmetric Standard Model (MSSM), which incorporates a Two-Higgs-Doublet Model (2HDM) by introducing an additional Higgs doublet. As a result, four additional Higgs bosons are predicted, two of which are charged (H^\pm). Among the possible decay channels, the $H^\pm \rightarrow H^0(h^0)W^\pm$ process dominates across all 2HDM types, for both small and large values of $\tan\beta$. The subsequent decay $H^0(h^0) \rightarrow \tau^+\tau^-$, enables an extensive search for H^\pm .

This analysis focuses on final states with two light leptons and a hadronically decaying τ -lepton, considering combinations of five $H^0(h^0)$ mass points and a range of H^\pm mass points. The observables in these final states include two light leptons, a hadronically decaying τ -lepton, missing transverse energy (E_T), and at least three jets, with at least one jet tagged as a b-jet. The efficiencies of the single-lepton triggers used in the analysis are measured through two independent approaches, with data-to-simulation scale factors derived and applied to simulated samples. The difference between scale factors obtained from the two methods is treated as a systematic uncertainty.

The main background processes in these final states are categorized into events containing prompt and non-prompt leptons. A dedicated data-driven technique is applied for the estimation of the non-prompt lepton contributions, providing reliable background predictions. Comprehensive closure tests in control and validation regions are performed to ensure the validity of this method.

To enhance signal-background discrimination, a mass-parameterized Deep Neural Network (DNN) classifier was developed and optimized. The DNN output serves as the final fit discriminant, allowing exclusion upper limits to be set on the product of the H^\pm production cross-section and its branching ratio into $H^0(h^0)W^\pm$. All measurements are blinded to mitigate potential human bias. The current analysis complements the one published by CMS [79], by completing all measurable final states and covering a wide range of parameter space of the $H^\pm - H^0(h^0)$. The expansion of the published analysis to cover the full $H^\pm - H^0(h^0)$ mass spectrum, as well as the implementation of the data-driven method established in this analysis, are expected to enhance the overall sensitivity. Following comprehensive cross-checks of the employed methods, the unblinding procedure will be initiated, allowing for the investigation of any potential excesses beyond the expected SM background. Additionally, a more extensive search across the $H^\pm - H^0(h^0)$ mass spectrum, along with the inclusion of refined event selection criteria, such as the inclusion of boosted di-tau jets, could further improve the sensitivity and strengthen the exclusion upper limits.

Looking ahead to Run 3, the increased luminosity and energy will significantly boost the discovery potential in searches for extended Higgs sectors, including charged Higgs bosons, especially in the more challenging mass regions where signal events are expected to be rare. The improved detector capabilities and more refined analysis techniques will allow for a more precise investigation of both existing and new phase-space regions, potentially uncovering signals that were previously inaccessible. As the datasets grow, the sensitivity to rare processes and new physics signatures will increase, offering a promising avenue for exploring scenarios beyond the Standard Model.

References

- [1] CMS Collaboration, *Observation of a new boson at a mass of 125 GeV with the CMS experiment at the LHC*, Phys. Lett. B716 (2012) 30-61, arXiv: 1207.7235.
- [2] ATLAS Collaboration, *Observation of a new particle in the search of the Standard Model Higgs boson with the ATLAS detector at the LHC*, Phys. Lett. B716 (2012) 1-29, arXiv: 1207.7214.
- [3] CMS Collaboration, *Measurements of Higgs boson production cross sections and couplings in the diphoton decay channel at $\sqrt{s} = 13$ TeV*, JHEP, 2021, arXiv:2103.06956.
- [4] A.Purcell, *Go on a particle quest at the first CERN webfest. Le premier webfest du CERN se lance à la conquête des particules*, BUL-NA-2012-269, 35/2012, <https://cds.cern.ch/record/1473657>
- [5] Kenneth S. Krane, *Introductory Nuclear Physics*, 272-315.
- [6] R.P. Feynman *Quantum electrodynamics* Westview Press, New Ed. Edition (1998). ISBN 978-0201360752
- [7] Greiner, Walter, Schafer, Andreas *Quantum Chromodynamics* Springer. ISBN 0-387-57103-5
- [8] Peter W. Higgs *Broken Symmetries and the Masses of Gauge Bosons*, Phys. Rev. Lett., 13:508–509, Oct 1964
- [9] F. Englert and R. Brout. *Broken Symmetry and the Mass of Gauge Vector Mesons*, Phys. Rev. Lett., 13:321–323, Aug 1964
- [10] J. Ellis, M.K. Gaillard and D. V. Nanopoulos *A Historical Profile of the Higgs Boson. An Updated Historical Profile of the Higgs Boson*, The Standard Theory of Particle Physics, ISSN 1793-1339, 2016, <https://doi.org/10.48550/arXiv.1504.07217>
- [11] J. Bahcall, *Solving the Mystery of the Missing Neutrinos*, 2004, arXiv:physics/0406040
- [12] C. Waltham, *Neutrino oscillations for dummies*, arXiv: preprint physics/0303116 (2003)
- [13] S. P. Martin, *A Supersymmetry Primer*, Advanced Series on Directions in High Energy Physics, WORLD SCIENTIFIC, 1998, arXiv:hep-ph/9709356v5, http://dx.doi.org/10.1142/9789812839657_0001
- [14] G. Branco et al., *Theory and phenomenology of two-Higgs-doublet models*, Phys. Rept. 1043 516 (2012) 1, doi:10.1016/j.physrep.2012.02.002, arXiv:1106.0034

- [15] H. Bahl, T.Stefaniak and J. Wittbrodt, *The forgotten channels: charged Higgs boson decays to a W^\pm and a non-SM-like Higgs boson*, 2021, 2103.07484, doi:10.1007/JHEP06(2021)183
- [16] A. Djouadi, *The anatomy of electroweak symmetry breaking Tome II: The Higgs bosons in the Minimal Supersymmetric Model*, ISSN: 0370-1573, 2008, arXiv:hep-ph/0503173, <http://dx.doi.org/10.1016/j.physrep.2007.10.005>
- [17] *The Large Hadron Collider Project*, <http://lhc.web.cern.ch/lhc/>
- [18] L. Evans and P. Bryant, *The LHC machine*, 2008 JINST 3 S08001
- [19] The CMS Collaboration et al, *The CMS experiment at the CERN LHC*, 2008 Journal of Instrumentation v3, <http://stacks.iop.org/1748-0221/3/i=08/a=S08004>
- [20] CMS Collaboration, *Precise Mapping of the Magnetic Field in the CMS Barrel Yoke using Cosmic Rays*, JINST 5 (2010) T03021, doi:10.1088/1748-0221/5/03/T03021, arXiv:0910.5530
- [21] V. Khachatryan et al., *The CMS trigger system*, JINST, vol. 12, no. 01, p. P01020, 2017
- [22] CMS Collaboration, *Description and performance of track and primary-vertex reconstruction with the CMS tracker*, JINST 9 (2014) P10009, arXiv:1405.6569, <http://dx.doi.org/10.1088/1748-0221/9/10/P10009>
- [23] G. L. Bayatian *et al.* [CMS], *CMS Physics: Technical Design Report Volume 1: Detector Performance and Software*, CERN-LHCC-2006-001
- [24] CMS Collaboration, *The CMS electromagnetic calorimeter project: Technical Design Report*, CERN-LHCC-97-033
- [25] P. Adzic et al., *Energy resolution of the barrel of the CMS electromagnetic calorimeter*, JINST 2 (2007) P04004, doi:10.1088/1748-0221/2/04/P04004
- [26] Rocca, P. and Riggi, Francesco, *The Use of Avalanche Photodiodes in High Energy Electromagnetic Calorimetry*, 2011, isbn:978-953-307-163-3, doi:10.5772/14574
- [27] V.D. Elvira, *Measurement of the Pion Energy Response and Resolution in the CMS HCAL Test Beam 2002 Experiment*, CMS-NOTE-2004-020, CERN, Geneva (2004), <http://cds.cern.ch/record/800406>
- [28] CMS Collaboration, CMSHCAL, *Design, Performance, and Calibration of CMS Hadron Endcap Calorimeters*, CMS-NOTE-2008-010, CERN, Geneva (2008), <https://cds.cern.ch/record/1103003>

- [29] S. Chatrchyan et al., *The performance of the CMS muon detector in proton-proton collisions at $\sqrt{s} = 7\text{TeV}$ at the LHC*, JINST, vol. 8, p. P11002, 2013, <http://dx.doi.org/10.1088/1748-0221/8/11/P11002>
- [30] CMS Collaboration, *Particle-flow reconstruction and global event description with the CMS detector*, arXiv:1706.04965
- [31] CMS Collaboration, *Particle-Flow Event Reconstruction in CMS and Performance for Jets, Taus, and MET*, CMS-PAS-PFT-09-001 (2009)
- [32] R. Fruhwirth, *Application of Kalman filtering to track and vertex fitting*, Nuclear Instruments and Methods A262(1987), p.444-450
- [33] K. Rose, *Deterministic Annealing for Clustering, Compression, Classification, Regression and related Optimisation Problems*, Proceedings of the IEEE 86 (1998), doi:10.1109/5.726788
- [34] R. Fruhwirth, W. Waltenberger, and P. Vanlaer, *Adaptive vertex fitting*, J. Phys. G, 34 (2007) N343, doi:10.1088/0954-3899/34/12/N01
- [35] S. Baffioni & al., *Electron Reconstruction in CMS*, CMS NOTE 2006/040
- [36] CMS Collaboration, *Performance of electron reconstruction and selection with the CMS detector in proton-proton collisions at $\sqrt{s} = 8\text{ TeV}$* , JINST 10 (2015) P06005, arXiv:1502.02701
- [37] CMS Collaboration, *Performance of the CMS muon detector and muon reconstruction with proton-proton collisions at $\sqrt{s}=13\text{ TeV}$* , JINST V13, 2018, 1748-0221, <http://dx.doi.org/10.1088/1748-0221/13/06/P06015>, arXiv:1804.04528v2
- [38] CMS Collaboratio, *Performance of photon reconstruction and identification with the CMS detector in proton-proton collisions at $\sqrt(s) = 8\text{ TeV}$* , JINST v10, 2015, 1748-0221, <http://dx.doi.org/10.1088/1748-0221/10/08/P08010>, arXiv:1502.02702
- [39] K. Rehermann and B. Tweedie, *Efficient Identification of Boosted Semileptonic Top Quarks at the LHC*, JHEP 1103 (2011) 059 doi:10.1007/JHEP03(2011)059, arXiv:1007.2221
- [40] CMS Collaboration, *Determination of jet energy calibration and transverse momentum resolution in CMS*, JINST 6 (2011) P11002, arXiv:1107.4277
- [41] E. Bols, J. Kieseler, M. Verzetti, M. Stoye, and A. Stakia, *Jet flavour classification using DeepJet*, JINST, v15, P12012, 2020, doi : 10.1088/1748-0221/15/12/P12012, arXiv: 2008.10519

- [42] CMS Collaboration, *Identification of hadronic tau lepton decays using a deep neural network*, JINST, 2022. arXiv:2201.08458
- [43] GEANT4 Collaboration, *GEANT4: A Simulation toolkit*, Nuclear Instruments and Methods A506(2003) p.250–303, doi:10.1016/S0168-9002(03)01368-8
- [44] A. Giammanco, *The Fast Simulation of the CMS Experiment*, Journal of Physics, Conference Series513 (2014) 022012, doi:10.1088/1742-6596/513/2/022012
- [45] NNPDF Collaboration, *Parton distributions from high-precision collider data*, The European Physical Journal C, v.77, 1434-6052, no. 10, 2017, doi:10.1140/epjc/s10052-017-5199-5, <http://dx.doi.org/10.1140/epjc/s10052-017-5199-5>
- [46] Stefan Höche, *Introduction to parton-shower event generators*, 2015, arXiv:1411.4085
- [47] Bellm, Johannes and others, *Herwig 7.0/Herwig++ 3.0 release note*, Eur. Phys. J. C, v76, 2016, arXiv:1512.01178, CERN-PH-TH-2015-289, doi: 10.1140/epjc/s10052-016-4018-8
- [48] CMS Twiki, *Loss of Hit Efficiency due to HIP*, Available at <https://twiki.cern.ch/twiki/bin/viewauth/CMS/SiStripHitEffLoss>
- [49] Alwall, J. and Frederix, R. and Frixione, S. and Hirschi, V. and Maltoni, F. and Mattelaer, O. and Shao, H. -S. and Stelzer, T. and Torrielli, P. and Zaro, M., *The automated computation of tree-level and next-to-leading order differential cross sections, and their matching to parton shower simulations*, JHEP, v.07, 2014, p.079, CERN-PH-TH-2014-064, CP3-14-18, LPN14-066, MCNET-14-09, ZU-TH-14-14, doi: 10.1007/JHEP07(2014)079
- [50] Nason, Paolo, *A New method for combining NLO QCD with shower Monte Carlo algorithms*, JHEP, v.11, 2004, doi:10.1088/1126-6708/2004/11/040
- [51] Frixione, Stefano and Nason, Paolo and Oleari, Carlo, *Matching NLO QCD computations with Parton Shower simulations: the POWHEG method*, JHEP, v.11, 2007, "BICOCCA-FT-07-9, GEF-TH-21-2007", doi: 10.1088/1126-6708/2007/11/070
- [52] Alioli, Simone and Nason, Paolo and Oleari, Carlo and Re, Emanuele, *A general framework for implementing NLO calculations in shower Monte Carlo programs: the POWHEG BOX* , JHEP, v.06, 2010, "DESY-10-018, SFB-CPP-10-22, IPPP-10-11, DCPT-10-22", doi: 10.1007/JHEP06(2010)043
- [53] Agostinelli, S. and others, GEANT4, *GEANT4: a simulation toolkit*, Nucl. Instrum. Meth. A", v.506, 2003, doi:10.1016/S0168-9002(03)01368-8"
- [54] Allison, J and others, GEANT4, *Geant4 developments and applications*, IEEE Trans. Nucl. Sci., v.53, 2006, doi:10.1109/TNS.2006.869826

- [55] Sjöstrand, Torbjorn and Ask, Stefan and Christiansen, Jesper R. and Corke, Richard and Desai, Nishita and Ilten, Philip and Mrenna, Stephen and Prestel, Stefan and Rasmussen, Christine O. and Skands, Peter Z., *An Introduction to PYTHIA 8.2*, Comput. Phys. Commun., v.191, 2015, doi: 10.1016/j.cpc.2015.01.024
- [56] A. M. Sirunyan, et al., *Performance of Pythia 8.2 with CP5 tuning in LHC Run II simulations*, Eur. Phys. J. C, v.79, p.743, 2019, doi:10.1140/epjc/s10052-019-7272-8
- [57] Khachatryan, Vardan and others, *Event generator tunes obtained from underlying event and multiparton scattering measurements*, CMS, Eur. Phys. J., C76, 2016, doi: 10.1140/epjc/s10052-016-3988-x
- [58] Frederix, Rikkert and Re, Emanuele and Torrielli, Paolo, *Single-top t-channel hadroproduction in the four-flavour scheme with POWHEG and aMC@NLO*, JHEP, v.09, 2012, doi: 10.1007/JHEP09(2012)130
- [59] Artoisenet, Pierre and Frederix, Rikkert and Mattelaer, Olivier and Rietkerk, Robbert, *Automatic spin-entangled decays of heavy resonances in Monte Carlo simulations*, JHEP, v.03, 2013, doi: 10.1007/JHEP03(2013)015
- [60] Re, Emanuele, *Single-top Wt-channel production matched with parton showers using the POWHEG method*, Eur. Phys. J. C, v.71, 2011, doi: 10.1140/epjc/s10052-011-1547-z
- [61] Hartanto, Heribertus B. and Jager, Barbara and Reina, Laura and Wackerlo, Doreen, *Higgs boson production in association with top quarks in the POWHEG BOX*, Phys. Rev. D, v.91, 2015, doi: 10.1103/PhysRevD.91.094003
- [62] LHC Twiki, *ATLAS-CMS recommended predictions for top-quark-pair cross sections using the Top++v2.0 program*,
<https://twiki.cern.ch/twiki/bin/view/LHCPhysics/TtbarNNLO>, Revision 21
- [63] CMS Twiki, *ATLAS-CMS recommended predictions for single-top cross sections using the Hathor v2.1 program*, Revision 36,
<https://twiki.cern.ch/twiki/bin/view/LHCPhysics/SingleTopRefXsec>
- [64] CMS, *Commissioning of the Particle-Flow Reconstruction in Minimum-Bias and Jet Events from pp Collisions at 7 TeV*, <http://cdsweb.cern.ch/record/1279341>, CMS-PAS-PFT-10-002, v.10/002, 2010
- [65] Khachatryan, Vardan and others, *Reconstruction and identification of τ lepton decays to hadrons and ν_τ at CMS*, JINST, v.11, 2016, doi:10.1088/1748-0221/11/01/P01019
- [66] CMS Twiki, *Standard Model Cross Sections for CMS at 13 TeV*, Revision 25,
<https://twiki.cern.ch/twiki/bin/viewauth/CMS/StandardModelCrossSectionsat13TeV>

- [67] CMS Twiki, *How to Compute Cross Sections with the GenXSecAnalyzer*, Revision 17, https://twiki.cern.ch/twiki/bin/view/CMS/HowToGenXSecAnalyzer-#Running_the_GenXSecAnalyzer_on_a
- [68] CERN, *CERN Yellow Reports: Monographs, Vol 2 (2017): Handbook of LHC Higgs cross sections: 4. Deciphering the nature of the Higgs sector*, 2017, doi:10.23731/CYRM-2017-002, <https://e-publishing.cern.ch/index.php/CYRM/issue/view/32>
- [69] CMS Twiki, *MET Filter Recommendations for Run II*, Revision 144, https://twiki.cern.ch/twiki/bin/view/CMS/MissingETOptionalFiltersRun2-#MET_Filter_Recommendations_for_R
- [70] CMS Twiki, *Public CMS Luminosity Information*, <https://twiki.cern.ch/twiki/bin/view/CMSPublic/LumiPublicResults>
- [71] CMS Collaboration, *Performance of reconstruction and identification of τ leptons decaying to hadrons and ν_τ in pp collisions at $\sqrt{s} = 13$ TeV*, JINST, v13, 2018, doi:10.1088/1748-0221/13/10/P10005, arXiv:1809.02816
- [72] CMS Twiki, *Tau Physics Object Group, tau ID developers*, <https://github.com/cms-tau-pog/TauIDSFs/tree/master/data>
- [73] CMS Twiki, *E/gamma POG-Energy Scale and Smearing*, https://twiki.cern.ch/twiki/bin/viewauth/CMS/EgammaMiniAODV2-#Energy_Scale_and_Smearing
- [74] CMS Twiki, *MET Corrections and Uncertainties for Run-II*, https://twiki.cern.ch/twiki/bin/viewauth/CMS/MissingETRun2Corrections#-xy_Shift_Correction_MET_phi_modu
- [75] CMS Twiki, *Methods to apply b-tagging efficiency scale factors*, Revision 27, <https://twiki.cern.ch/twiki/bin/view/CMS/BTagSFMMethods>
- [76] CMS Twiki, *b Tag & Vertexing Physics Object Group*, Revision 272, <https://twiki.cern.ch/twiki/bin/view/CMS/BtagPOG>
- [77] CMS Twiki, *Recommendation for Using b-tag Objects in Physics Analyses*, <https://btv-wiki.docs.cern.ch/ScaleFactors/>
- [78] CMS Twiki, *Usage of b/c Tag Objects for 13 TeV Data in 2016 and 80X MC*, Revision 18, https://twiki.cern.ch/twiki/bin/viewauth/CMS/BtagRecommendation80X-#Data_MC_Scale_Factors

- [79] CMS Collaboration, *Search for a charged Higgs boson decaying into a heavy neutral Higgs boson and a W boson in proton-proton collisions at $\sqrt{s} = 13 \text{ TeV}$* , JHEP, 2023, 1029-8479, doi:10.1007/jhep09(2023)032
- [80] K. Rose, *Deterministic annealing for clustering, compression, classification, regression, and related optimization problems*, Institute of Electrical and Electronics Engineers (IEEE), v86, 1998, p.2210–2239, <http://dx.doi.org/10.1109/5.726788>
- [81] CMS Twiki, *E/gamma Physics Object Group*,
<https://twiki.cern.ch/twiki/bin/view/CMS/EgammaPOG>
- [82] CMS Twiki, *Multivariate Electron Identification for Run2*, Revision 43
<https://twiki.cern.ch/twiki/bin/view/CMS/MultivariateElectronIdentificationRun2-#Recommended>
- [83] CMS Collaboration, *Performance of CMS muon reconstruction in pp collision events at $\sqrt{s} = 7 \text{ TeV}$* , JINST, v7, 2012, doi:10.1088/1748-0221/7/10/P10002, arXiv:1206.4071
- [84] CMS Twiki, *Muon Physics Object Group*,
<https://twiki.cern.ch/twiki/bin/view/CMS/MuonPOG>
- [85] CMS Twiki, *Tau ID recommendations for Run-2: 2016, 2017, and 2018*,
<https://twiki.cern.ch/twiki/bin/viewauth/CMS/TauIDRecommendationForRun2>
- [86] CMS Twiki, *JetMET Physics Object Group*,
<https://twiki.cern.ch/twiki/bin/view/CMS/JetMET>
- [87] CMS Collaboration, *Pileup mitigation at CMS in 13 TeV data*, CMS Physics Analysis Summary, 2019, CMS-PAS-JME-18-001, <https://cds.cern.ch/record/2683784>
- [88] CMS Collaboration, *Jet energy scale and resolution in the CMS experiment in pp collisions at 8 TeV*, JINST, 2016, arXiv:1607.03663
- [89] CMS Collaboration, *Search for a charged Higgs boson decaying into a heavy neutral Higgs boson and a W boson in proton-proton collisions at $\sqrt{s} = 13 \text{ TeV}$* , pp.7-8, JHEP, 2023, 1029-8479, doi:10.1007/jhep09(2023)032
- [90] CMS Twiki, *E/gamma Recommendations for 2017 Data*, Revision 36,
https://twiki.cern.ch/twiki/bin/view/CMS/Egamma2017DataRecommendations-#Single_Electron_Triggers
- [91] H. Saka,C. G. Tully, *Search for Third Generation Scalar Leptonquarks Decaying to Top Quark-Tau Lepton Pairs in pp Collisions*, CMS AN, 2012/289

- [92] Baldi, Pierre and Cranmer, Kyle and Faucett, Taylor and Sadowski, Peter and Whiteson, Daniel, *Parameterized neural networks for high-energy physics*, The European Physical Journal C, vol. 76, 2016, 1434-6052,
<http://dx.doi.org/10.1140/epjc/s10052-016-4099-4>
- [93] Chollet, Fran ois and others, *Keras: Deep learning library for theano and tensorflow*,
<https://keras.io>
- [94] Mart n Abadi and others, *TensorFlow: Large-Scale Machine Learning on Heterogeneous Systems*, 2015, <https://www.tensorflow.org/>
- [95] CMS Twiki, *Luminosity Physics Object Group*, Revision 66,
<https://twiki.cern.ch/twiki/bin/view/CMS/TWikiLUM>
- [96] CMS Twiki, *Estimating Systematic Errors Due to Pileup Modeling*, Revision 11,
<https://twiki.cern.ch/twiki/bin/view/CMS/PileupSystematicErrors>
- [97] CMS Twiki, *Reweighting recipe to emulate Level 1 ECAL and Muon prefiring*,
<https://twiki.cern.ch/twiki/bin/viewauth/CMS/L1PrefiringWeightRecipe>
- [98] CMS Twiki, *JER Scaling factors and Uncertainty for 13 TeV*, Revision 58,
https://twiki.cern.ch/twiki/bin/viewauth/CMS/JetResolution#JER_Scaling_factors_and_Uncertai
- [99] CMS Twiki, *Official Prescription for calculating corrections and uncertainties on Missing Transverse Energy (MET)*, Revision 92,
<https://twiki.cern.ch/twiki/bin/view/CMS/MissingETUncertaintyPrescription>
- [100] Czakon, Micha  and Fiedler, Paul and Mitov, Alexander, *Total Top-Quark Pair-Production Cross Section at Hadron Colliders Through $O(\alpha_S^4)$* , Phys. Rev. Lett., 2013,
arXiv:1303.6254, doi: 10.1103/PhysRevLett.110.252004
- [101] Read, L., *Presentation of search results: the CL_s technique*, J. Phys. G, v.28, 2002,
doi:10.1088/0954-3899/28/10/313
- [102] Junk, Thomas, *Confidence level computation for combining searches with small statistics*, Nucl. Instrum. Meth. A, v.434, p.435, 1999, doi:10.1016/S0168-9002(99)00498-2,
arXiv:hep-ex/9902006
- [103] CMS Twiki, *Documentation of the RooStats-based statistics tools for Higgs PAG*,
<https://twiki.cern.ch/twiki/bin/view/CMS/SWGuideHiggsAnalysisCombinedLimit>
- [104] Moneta, L. and Cranmer, K. and Schott, G. and Verkerke, W., *The RooStats project*, 2010, arXiv:1009.1003,
<http://pos.sissa.it/cgi-bin/reader/conf.cgi?confid=93>

REFERENCES

- [105] Barlow, Roger J. and Beeston, Christine, *Fitting using finite Monte Carlo samples*, Comput. Phys. Commun., v.77, 1993, p.219-228, doi:10.1016/0010-4655(93)90005W
- [106] CMS Twiki, *Non standard features of the Higgs PAG limit setting tool*, Revision 42, <https://twiki.cern.ch/twiki/bin/viewauth/CMS/HiggsWG>

A DNN Input Variables

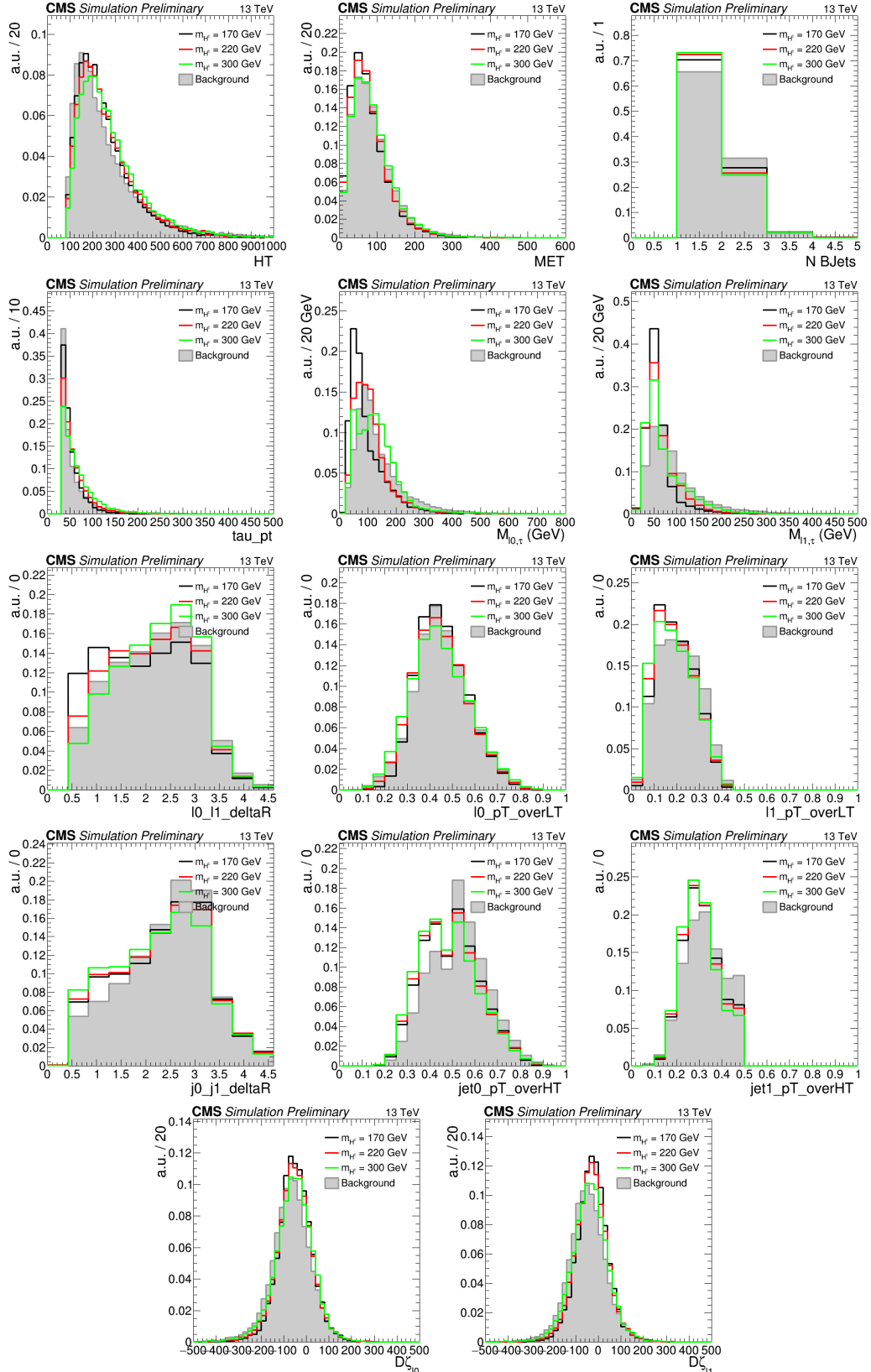


Figure A.1: Distributions of the input variables used for the parameterized DNN training, normalised in unity, presented for $m_{H^0(h^0)} = 80\text{GeV}$ and low $m_{H^\pm} (\leq 300\text{ GeV})$.

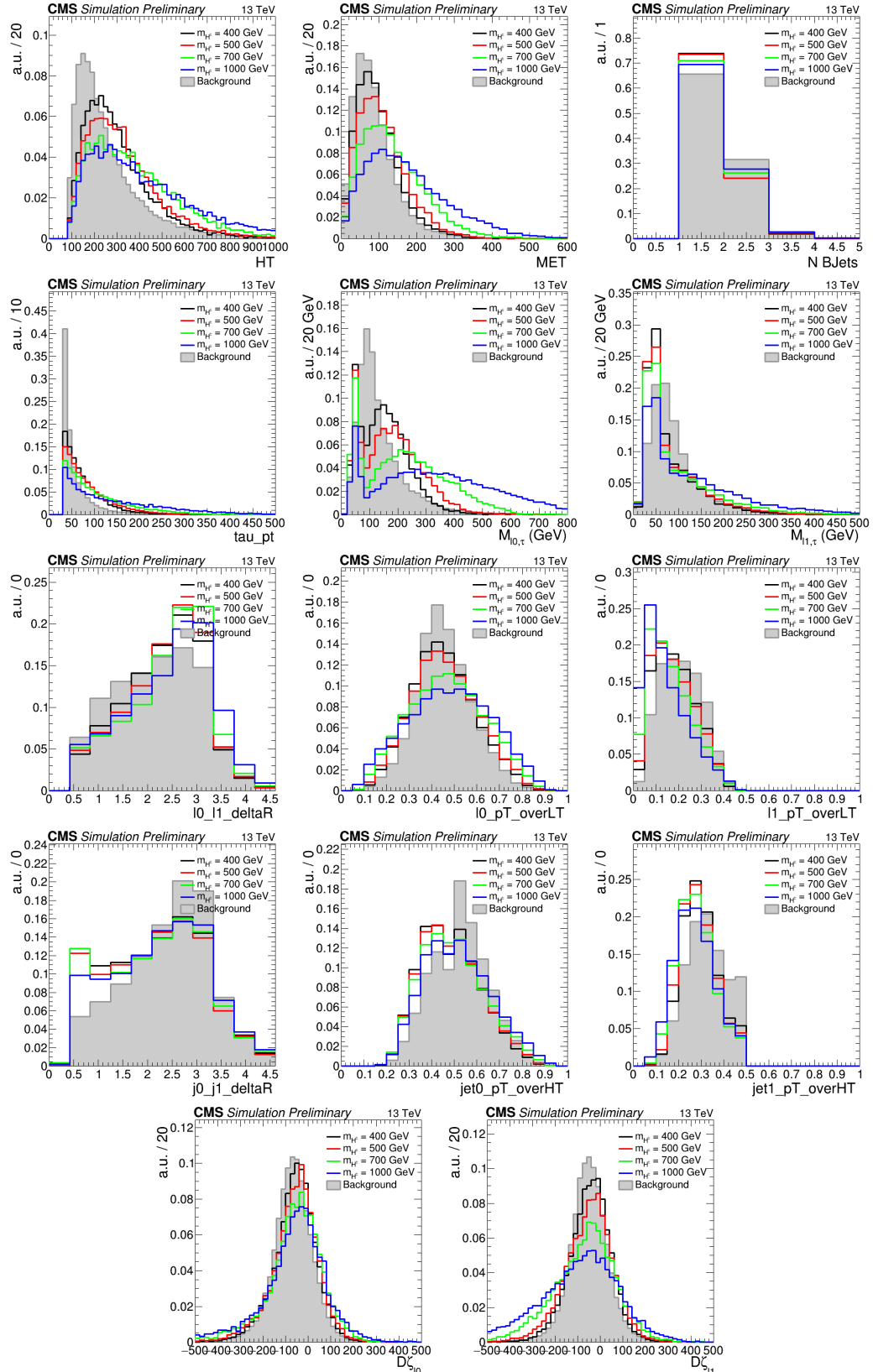


Figure A.2: Distributions of the input variables used for the parameterized DNN training, normalised in unity, presented for $m_{H^0(h^0)} = 80 \text{ GeV}$ and high $m_{H^\pm} (> 300 \text{ GeV})$.

B Fit Discriminant in MuETau

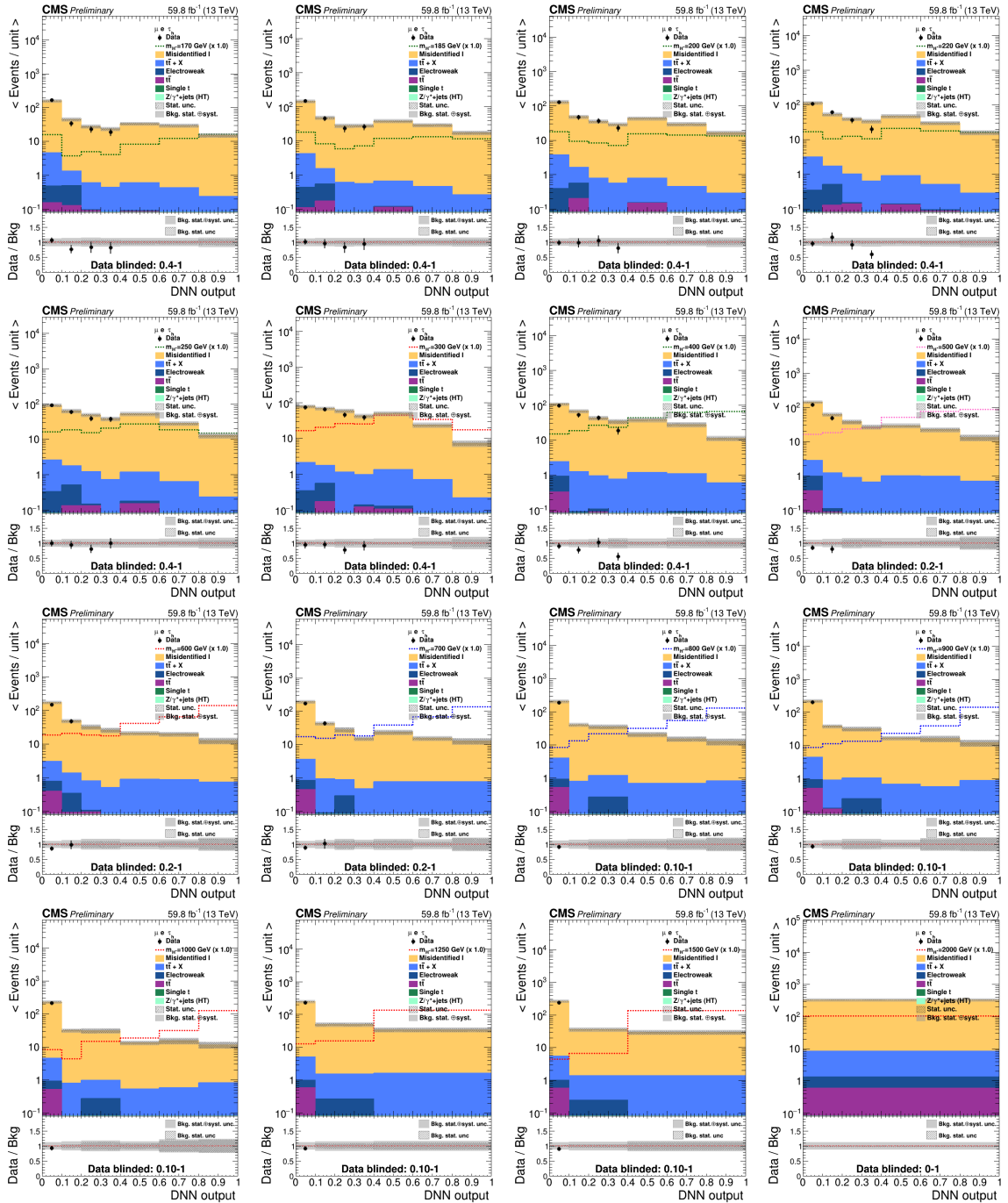


Figure B.1: Pre-fit distributions of the parameterized DNN output in $2\ell^{df}\tau_h$ final state, for $m_{H^0}(h^0) = 80$ GeV and various m_{H^\pm} using 2018 data.

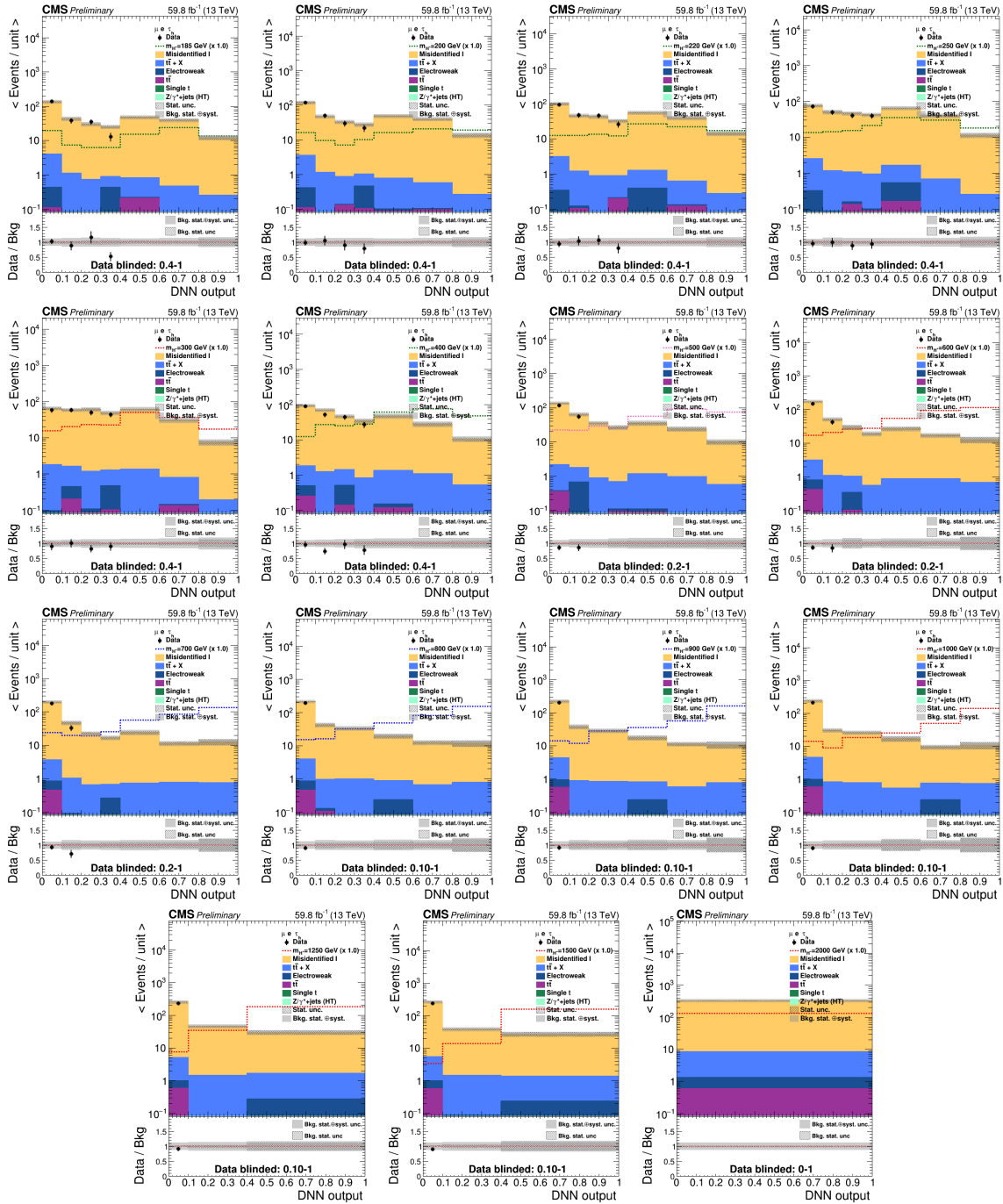


Figure B.2: Pre-fit distributions of the parameterized DNN output in $2\ell^{df}\tau_h$ final state, for $m_{H^0}(h^0) = 90$ GeV and various m_{H^\pm} using 2018 data.

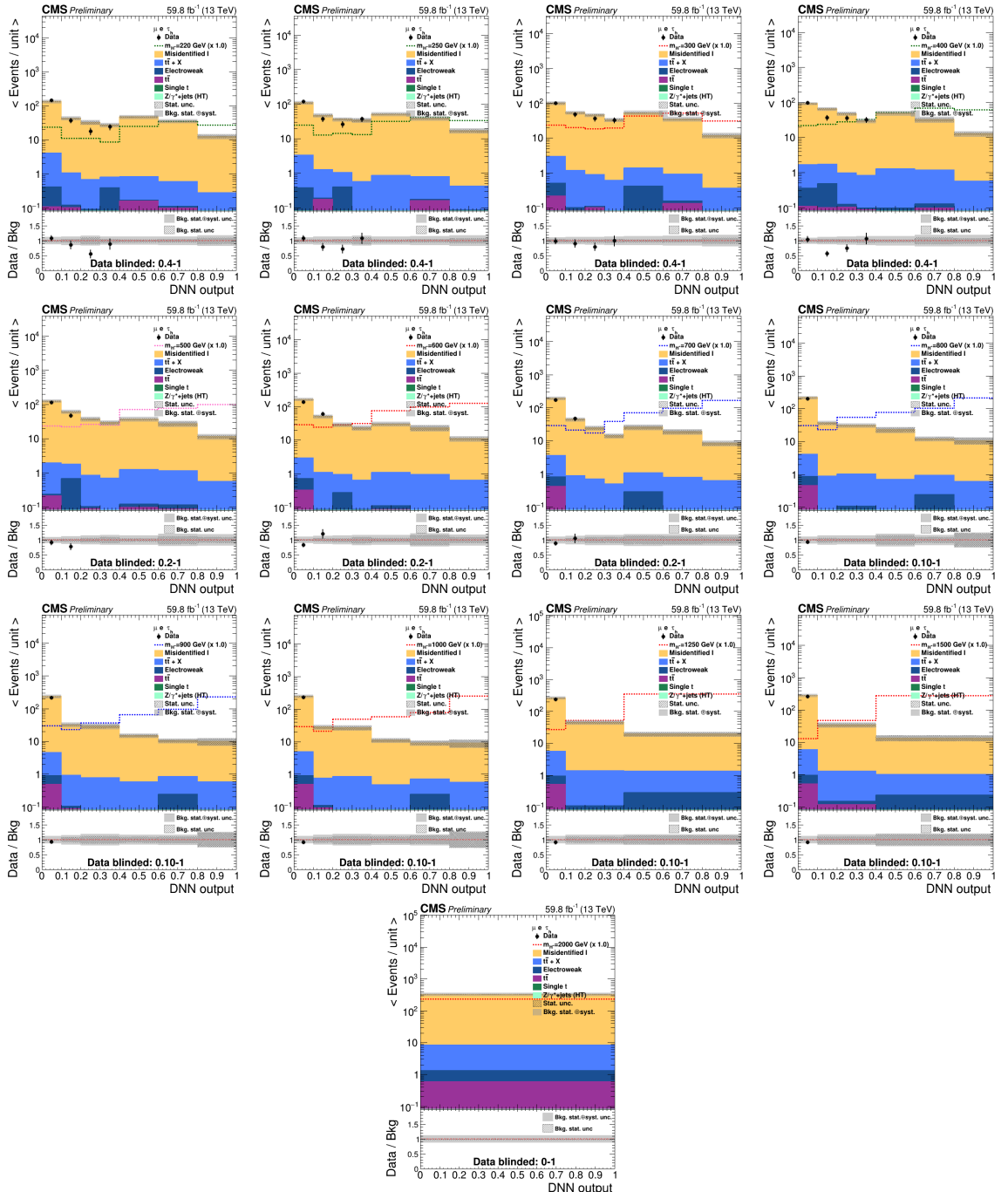


Figure B.3: Pre-fit distributions of the parameterized DNN output in $2\ell^{df}\tau_h$ final state, for $m_{H^0}(h^0) = 125$ GeV and various m_{H^\pm} using 2018 data.

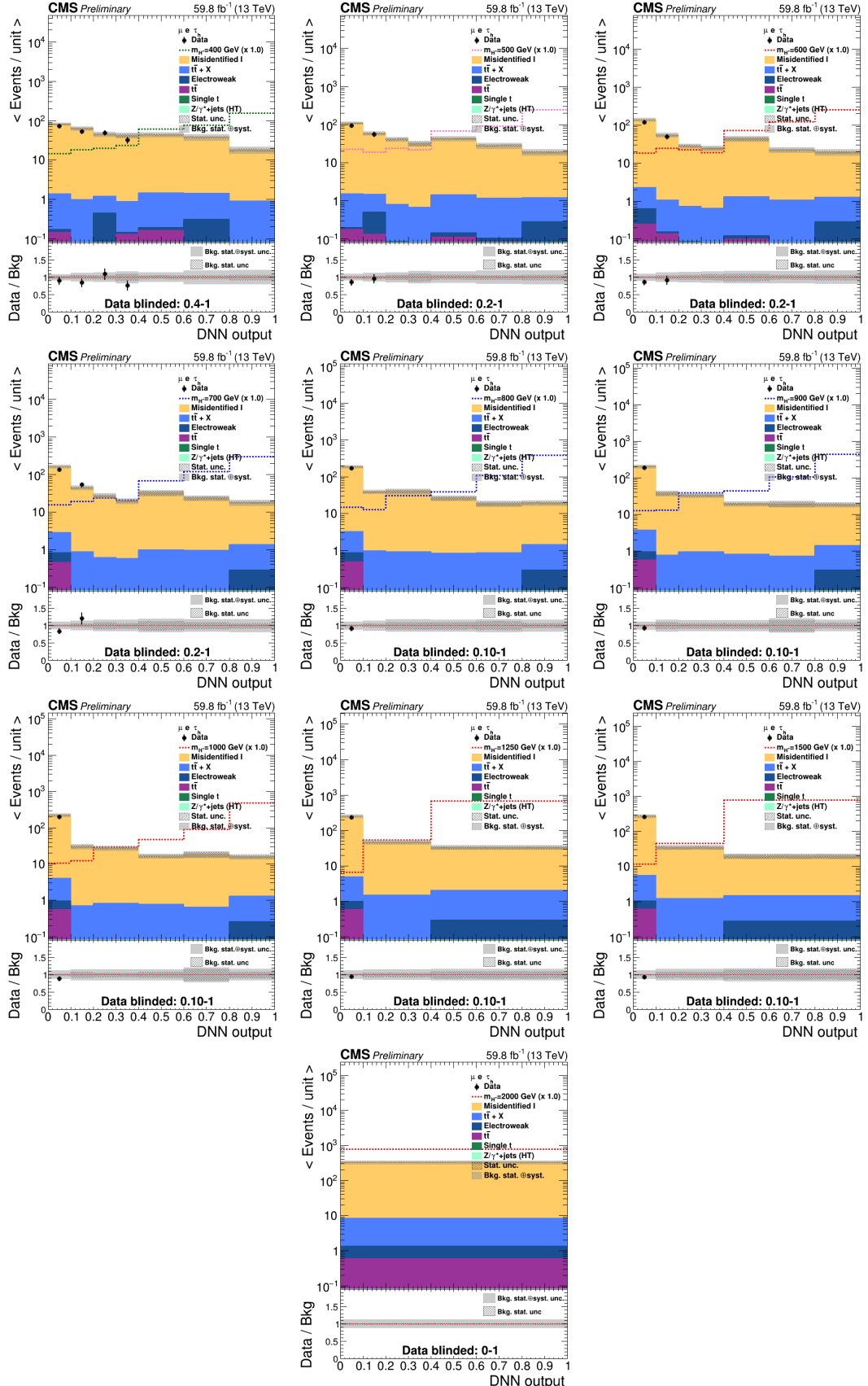


Figure B.4: Pre-fit distributions of the parameterized DNN output in $2\ell^{df}\tau_h$ final state, for $m_{H^0}(h^0) = 300 \text{ GeV}$ and various m_{H^\pm} using 2018 data.

C Fit Discriminant in EETau

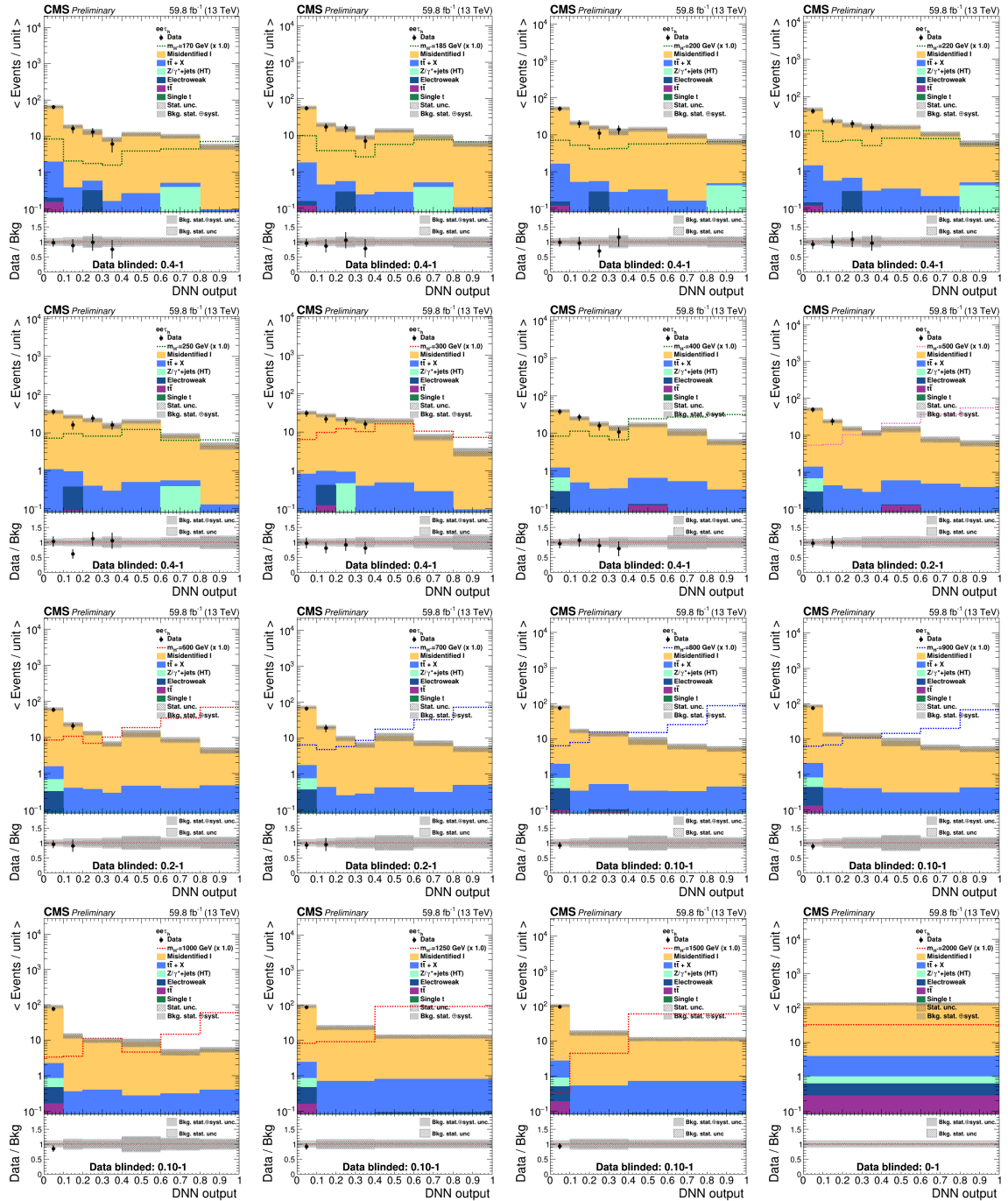


Figure C.1: Pre-fit distributions of the parameterized DNN output in $ee\tau_h$ final state, for $m_{H^0}(h^0) = 80 \text{ GeV}$ and various m_{H^\pm} using 2018 data.

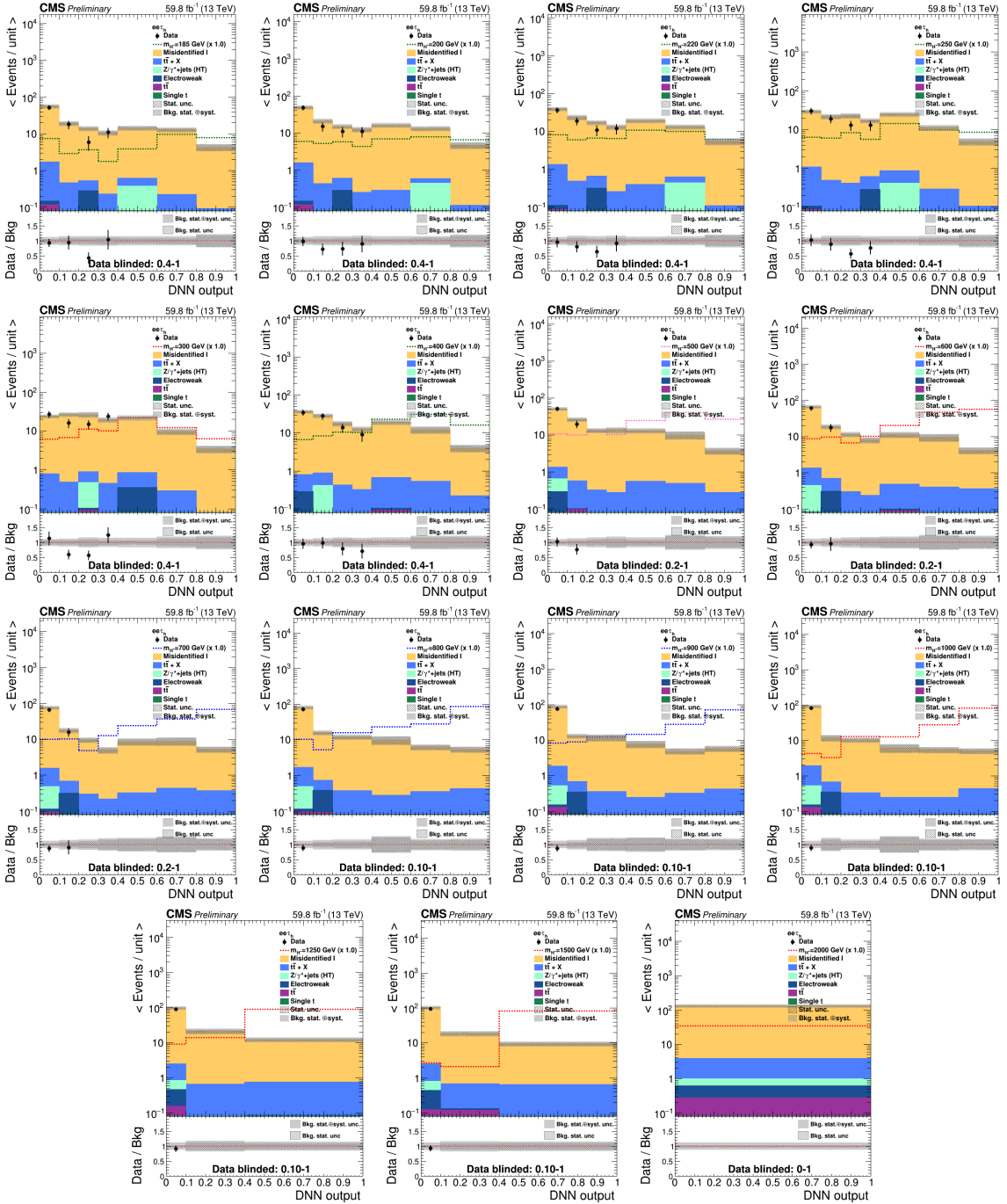


Figure C.2: Pre-fit distributions of the parameterized DNN output in ee τ_h final state, for $m_{H^0}(h^0) = 90$ GeV and various m_{H^\pm} using 2018 data.

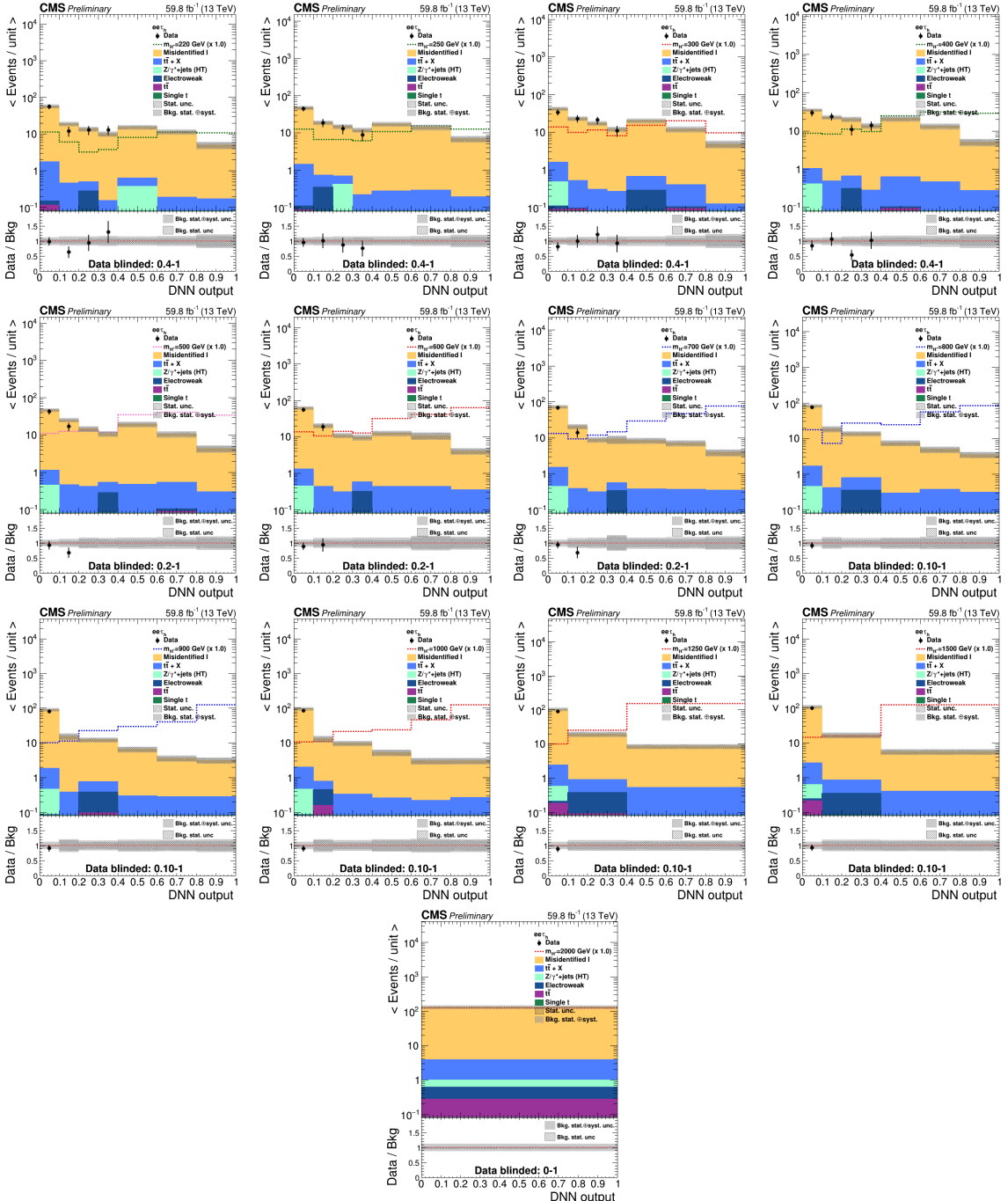


Figure C.3: Pre-fit distributions of the parameterized DNN output in $ee\tau_h$ final state, for $m_{H^0}(h^0) = 125$ GeV and various m_{H^\pm} using 2018 data.

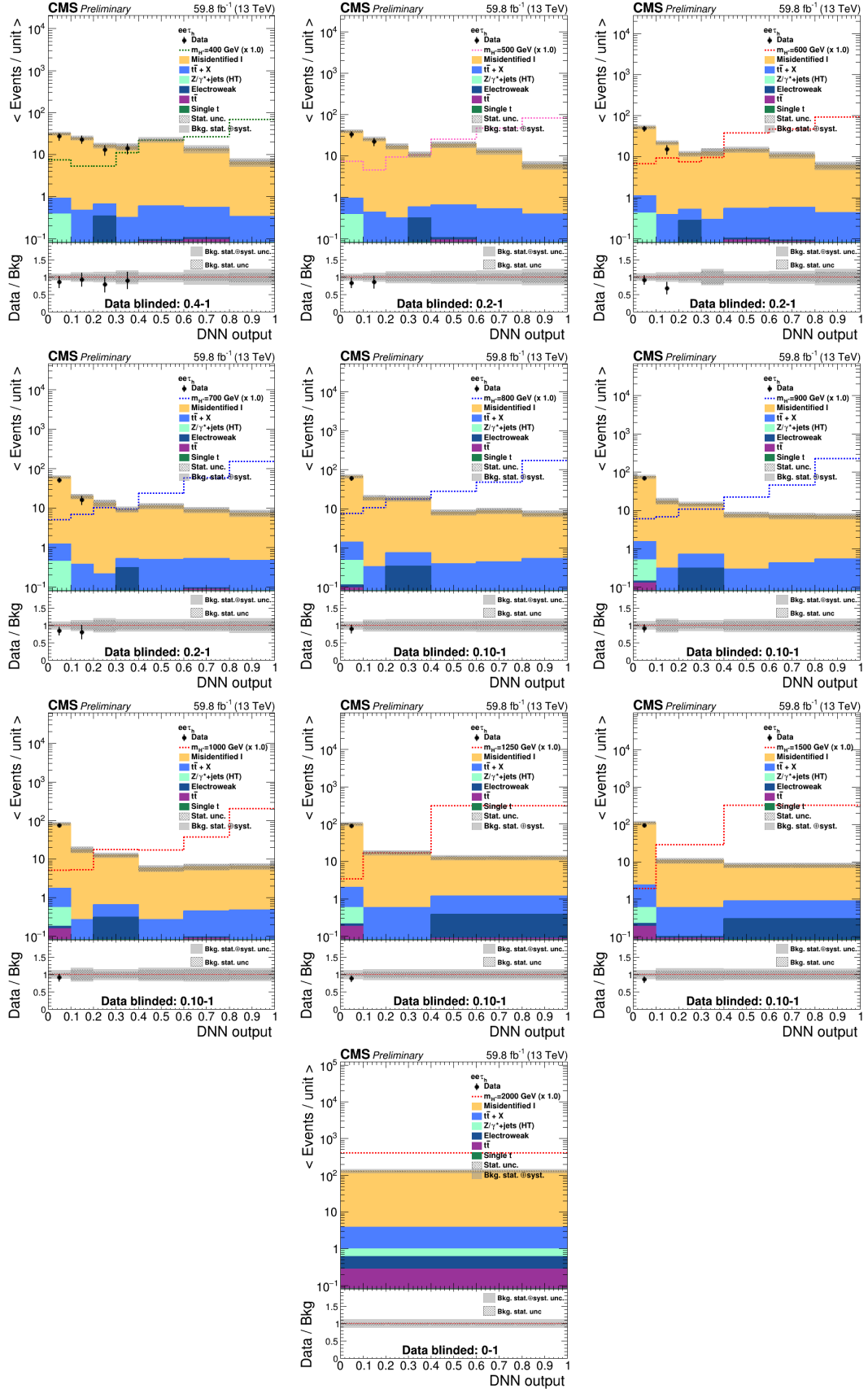


Figure C.4: Pre-fit distributions of the parameterized DNN output in $ee\tau_h$ final state, for $m_{H^0}(h^0) = 300 \text{ GeV}$ and various m_{H^\pm} using 2018 data.

D Fit Discriminant in MuMuTau

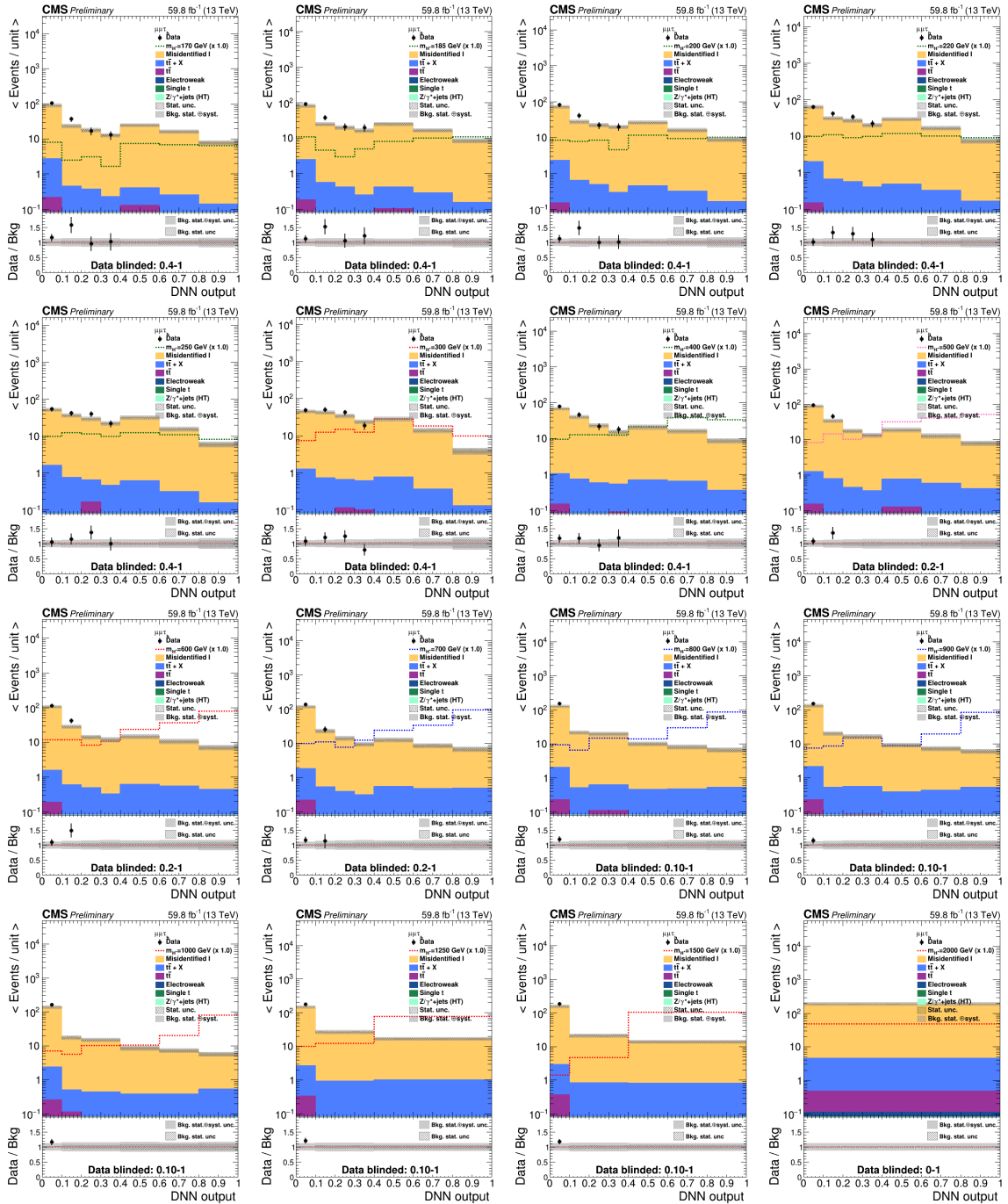


Figure D.1: Pre-fit distributions of the parameterized DNN output in $\mu\mu\tau_h$ final state, for $m_{H^0}(h^0) = 80 \text{ GeV}$ and various m_{H^\pm} using 2018 data.

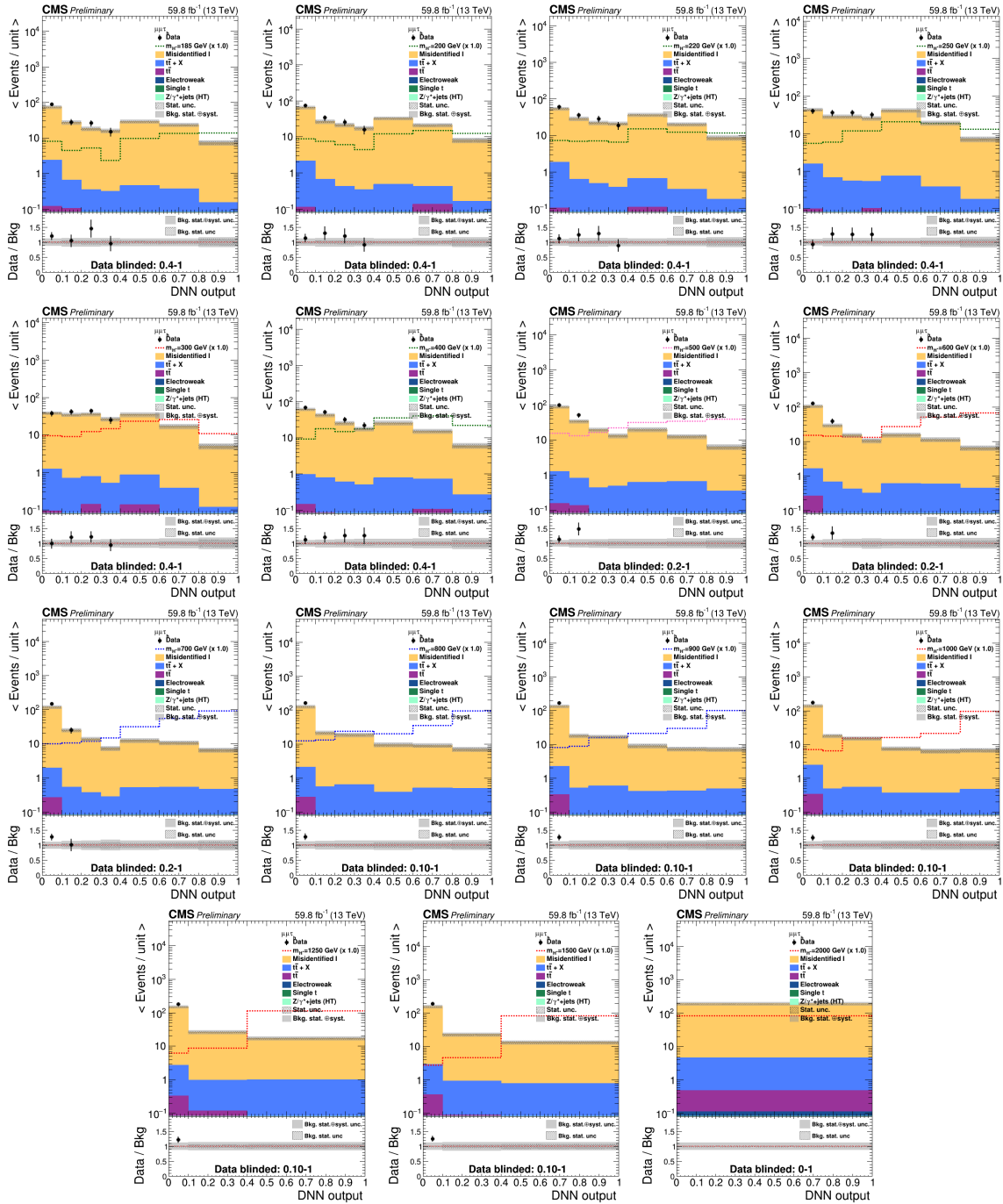


Figure D.2: Pre-fit distributions of the parameterized DNN output in $\mu\mu\tau_h$ final state, for $m_{H^0}(h^0) = 90\text{ GeV}$ and various m_{H^\pm} using 2018 data.

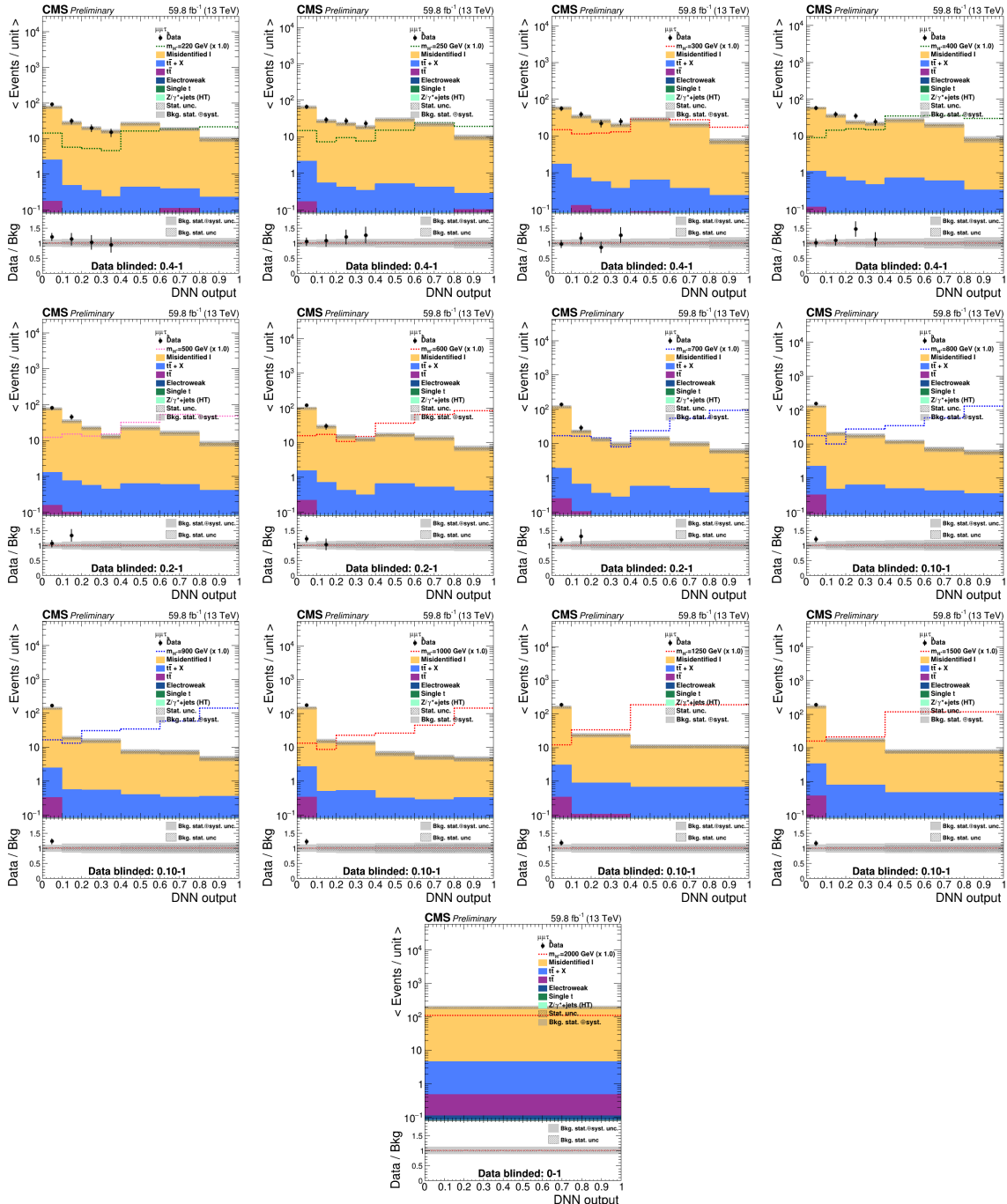


Figure D.3: Pre-fit distributions of the parameterized DNN output in $\mu\mu\tau_h$ final state, for $m_{H^0}(h^0) = 125$ GeV and various m_{H^\pm} using 2018 data.

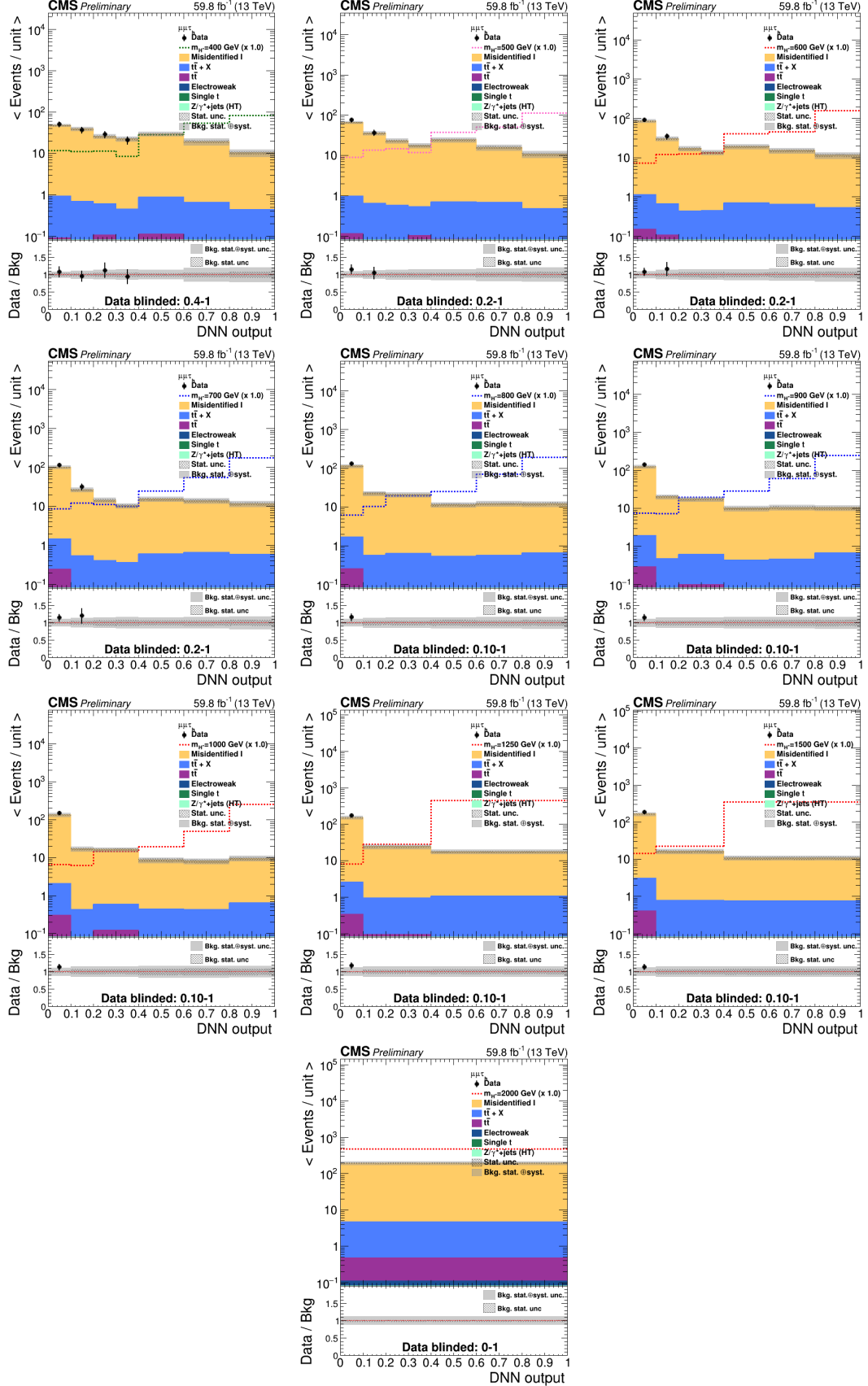


Figure D.4: Pre-fit distributions of the parameterized DNN output in $\mu\mu\tau_h$ final state, for $m_{H^0}(h^0) = 300$ GeV and various m_{H^\pm} using 2018 data.

E Limits

m_{H^\pm} (GeV)	Expected limit					Observed limit
	-2σ	-1σ	median	$+1\sigma$	$+2\sigma$	
170	0.12109	0.16650	0.24219	0.34259	0.47182	Blinded
185	0.12451	0.16571	0.23438	0.33527	0.45912	Blinded
200	0.13281	0.17676	0.25000	0.35762	0.48972	Blinded
220	0.13281	0.17676	0.25000	0.35364	0.48387	Blinded
250	0.12451	0.16571	0.23438	0.33527	0.45912	Blinded
300	0.07886	0.10495	0.14844	0.21234	0.28891	Blinded
400	0.03165	0.04212	0.05957	0.08521	0.11669	Blinded
500	0.01868	0.02486	0.03516	0.05085	0.07012	Blinded
600	0.01349	0.01795	0.02539	0.03673	0.05127	Blinded
700	0.01172	0.01611	0.02344	0.03315	0.04626	Blinded
800	0.01172	0.01611	0.02344	0.03315	0.04626	Blinded
900	0.01349	0.01795	0.02539	0.03673	0.05064	Blinded
1000	0.01349	0.01795	0.02539	0.03754	0.05179	Blinded
1250	0.02127	0.02831	0.04004	0.05791	0.07986	Blinded
1500	0.02051	0.02820	0.04102	0.05867	0.08138	Blinded
2000	0.02637	0.03625	0.05273	0.07628	0.10781	Blinded

Table E.I: The $2\ell^{sf}\tau_h$ and $2\ell^{df}\tau_h$ combined upper limit for $m_{H^0(h^0)} = 80$ GeV, at 95% CL on $\sigma_{pp \rightarrow t(b)H^\pm} \times \mathcal{B}(H^+ \rightarrow H^0 W^+) \times (H^0 \rightarrow \tau^+ \tau^-)$ as a function of m_{H^\pm} , with full Run 2 data.

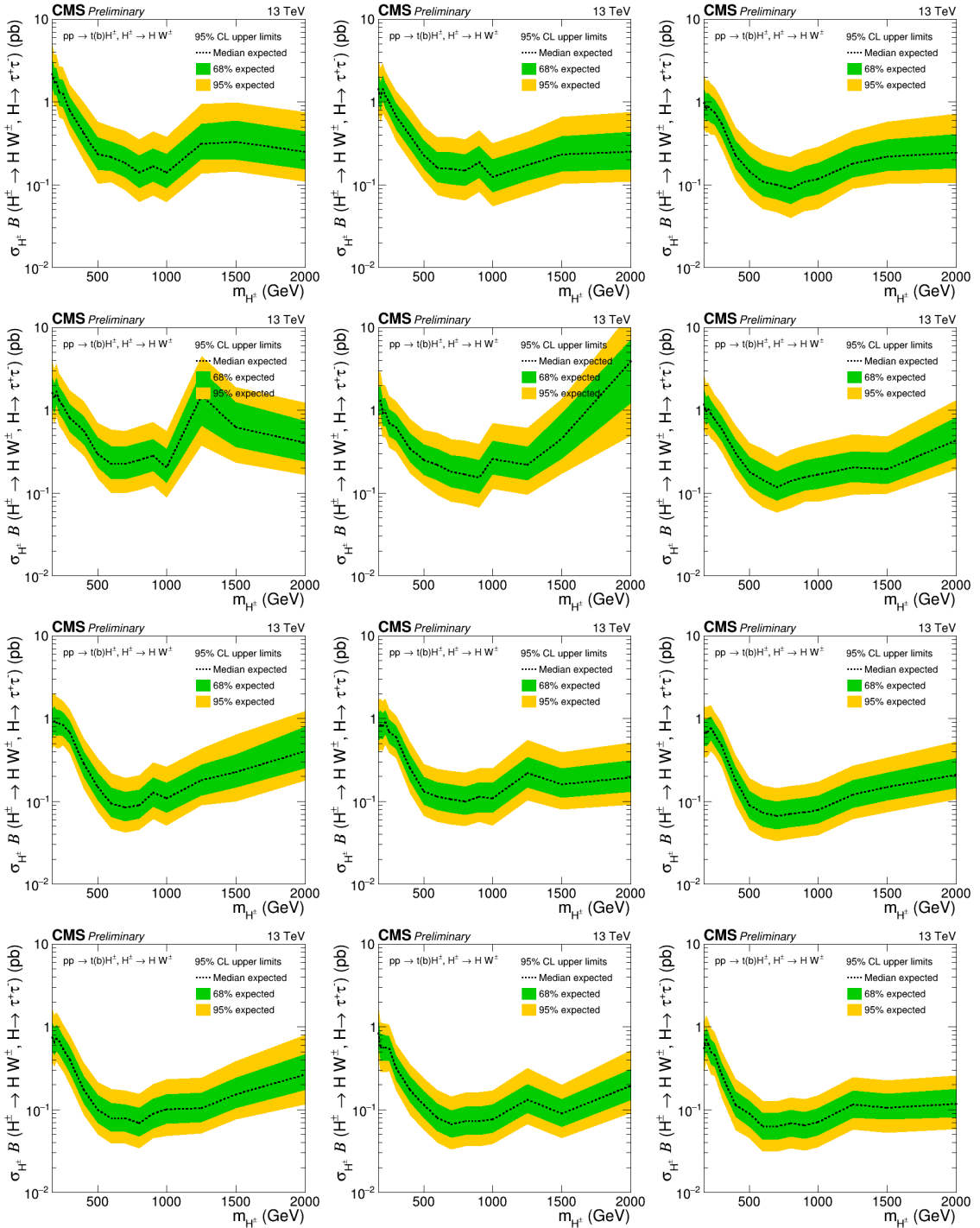


Figure E.1: Expected upper limit for $m_{H^0(h^0)} = 80$ GeV, per final state per data-taking year. The $ee\tau_h$, $\mu\mu\tau_h$, and $\mu e\tau_h$ limits are presented in the 1st, 2nd, and 3rd column, respectively, while the 2016 pre-VFP, 2016 post-VFP, 2017, and 2018 limits are in the 1st, 2nd, 3rd, and 4th row, respectively. The dotted black line shows the median expected limit, while the 68% and 95% confidence intervals are presented with the green and yellow bands, respectively. The non-smooth behavior observed, particularly for the 2016 pre- and post-VFP periods, is attributed to low statistics. Sensitivity tends to plateau or even degrade for $m_{H^\pm} > 1$ TeV, which is expected because, at high masses, the decay products become boosted and thus more collimated. In this scenario, an analysis incorporating boosted di-tau jets could potentially improve sensitivity. The slight bump at low masses is related to the performance of the DNN training (see Sec. 9.3).

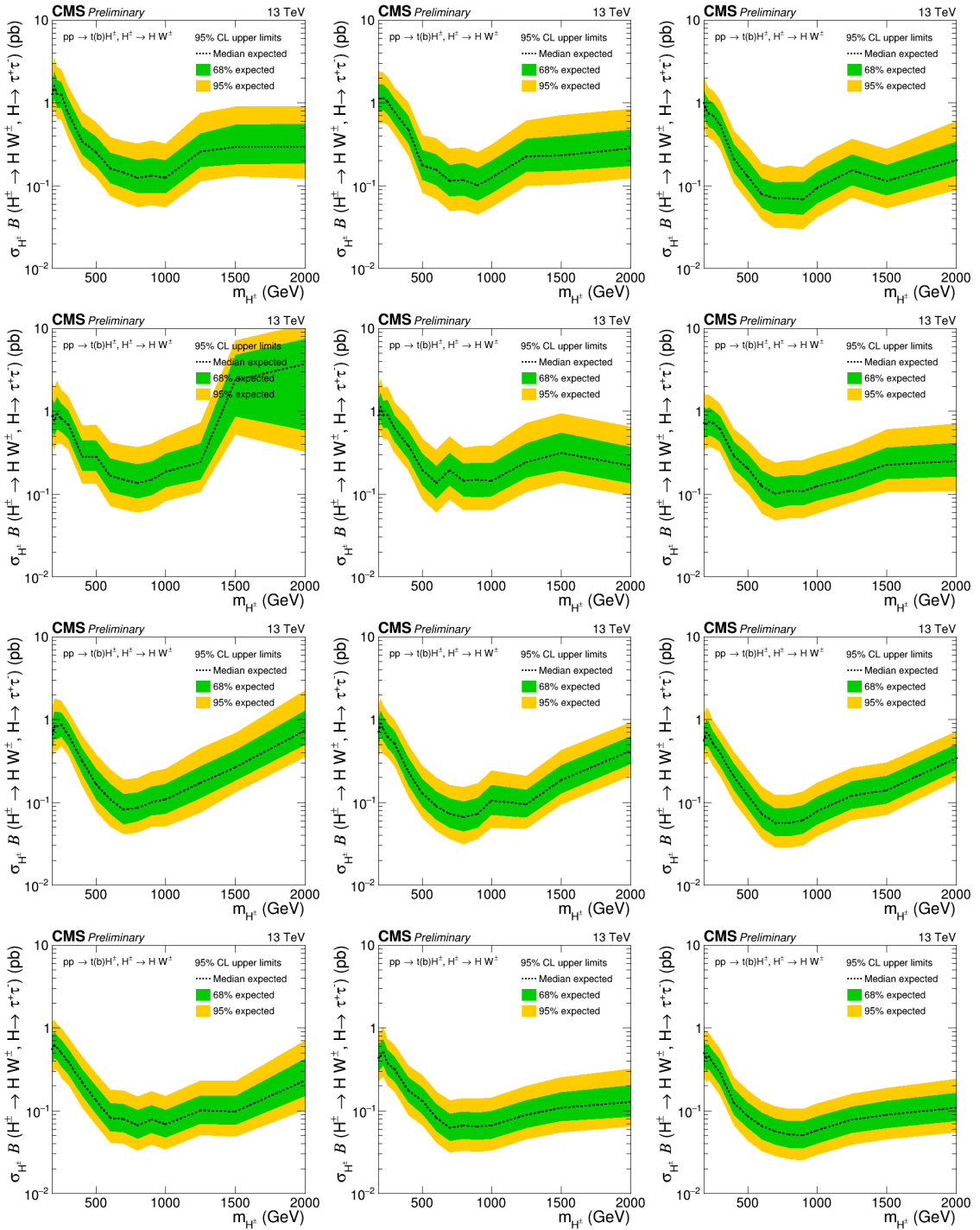


Figure E.2: Expected upper limit for $m_{H^0(h^0)} = 90$ GeV, per final state per data-taking year. The $ee\tau_h$, $\mu\mu\tau_h$, and $\mu e\tau_h$ limits are presented in the 1st, 2nd, and 3rd column, respectively, while the 2016 pre-VFP, 2016 post-VFP, 2017, and 2018 limits are in the 1st, 2nd, 3rd, and 4th row, respectively. The dotted black line shows the median expected limit, while the 68% and 95% confidence intervals are presented with the green and yellow bands, respectively. The unusual behavior observed in the limit plots is discussed in Fig. E.1, and the same explanation applies here as well.

m_{H^\pm} (GeV)	Expected limit					Observed limit
	-2σ	-1σ	median	$+1\sigma$	$+2\sigma$	
185	0.09546	0.12704	0.17969	0.25704	0.35425	Blinded
200	0.10583	0.14085	0.19922	0.28498	0.39275	Blinded
220	0.11621	0.15466	0.21875	0.30943	0.42616	Blinded
250	0.09961	0.13257	0.18750	0.26523	0.36528	Blinded
300	0.08093	0.10771	0.15234	0.21307	0.29125	Blinded
400	0.03424	0.04557	0.06445	0.09117	0.12557	Blinded
500	0.01971	0.02624	0.03711	0.05368	0.07402	Blinded
600	0.01221	0.01678	0.02441	0.03453	0.04756	Blinded
700	0.01025	0.01410	0.02051	0.02836	0.03951	Blinded
800	0.00986	0.01312	0.01855	0.02743	0.03740	Blinded
900	0.00977	0.01343	0.01953	0.02825	0.03896	Blinded
1000	0.01123	0.01544	0.02246	0.03177	0.04433	Blinded
1250	0.01712	0.02279	0.03223	0.04610	0.06394	Blinded
1500	0.01971	0.02624	0.03711	0.05368	0.07494	Blinded
2000	0.02539	0.03491	0.05078	0.07345	0.10381	Blinded

Table E.2: The $2\ell^{sf}\tau_h$ and $2\ell^{df}\tau_h$ combined upper limit for $m_{H^0(h^0)} = 90$ GeV, at 95% CL on $\sigma_{pp \rightarrow t(b)H^\pm} \times \mathcal{B}(H^+ \rightarrow H^0 W^+) \times (H^0 \rightarrow \tau^+\tau^-)$ as a function of m_{H^\pm} , with full Run 2 data.

m_{H^\pm} (GeV)	Expected limit					Observed limit
	-2σ	-1σ	median	$+1\sigma$	$+2\sigma$	
220	0.06848	0.09114	0.12891	0.18234	0.25113	Blinded
250	0.07471	0.09943	0.14062	0.19892	0.27039	Blinded
300	0.06641	0.08838	0.12500	0.17881	0.24486	Blinded
400	0.03528	0.04695	0.06641	0.09605	0.13079	Blinded
500	0.01920	0.02555	0.03613	0.05169	0.07078	Blinded
600	0.01245	0.01657	0.02344	0.03390	0.04675	Blinded
700	0.00882	0.01174	0.01660	0.02454	0.03346	Blinded
800	0.00714	0.00922	0.01270	0.01998	0.02697	Blinded
900	0.00604	0.00780	0.01074	0.01691	0.02380	Blinded
1000	0.00537	0.00739	0.01074	0.01554	0.02143	Blinded
1250	0.00824	0.01064	0.01465	0.02119	0.02922	Blinded
1500	0.00882	0.01174	0.01660	0.02401	0.03311	Blinded
2000	0.00977	0.01343	0.01953	0.02825	0.03896	Blinded

Table E.3: The $2\ell^{sf}\tau_h$ and $2\ell^{df}\tau_h$ combined upper limit for $m_{H^0(h^0)} = 125$ GeV, at 95% CL on $\sigma_{pp \rightarrow t(b)H^\pm} \times \mathcal{B}(H^+ \rightarrow H^0 W^+) \times (H^0 \rightarrow \tau^+\tau^-)$ as a function of m_{H^\pm} , with full Run 2 data.

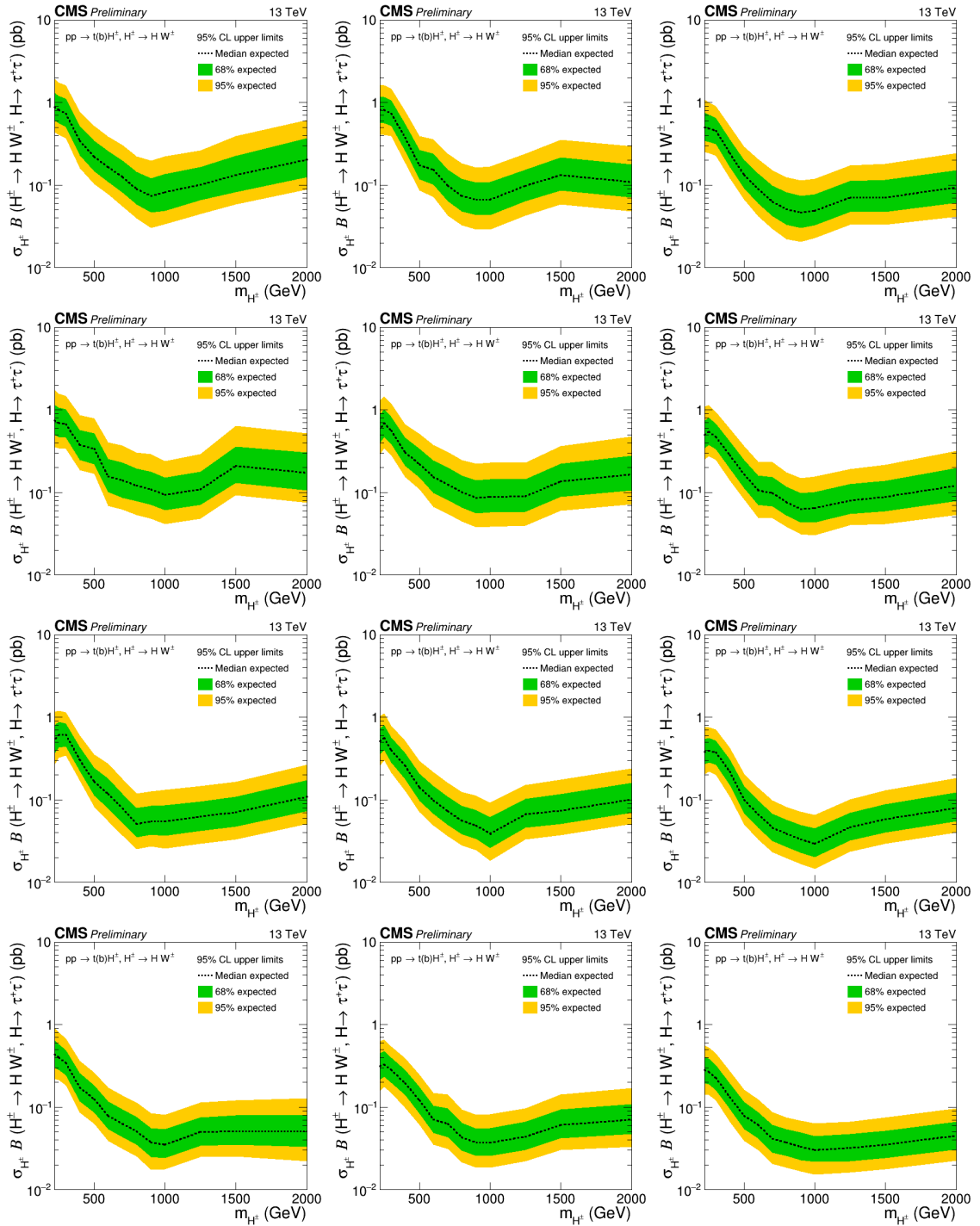


Figure E.3: Expected upper limit for $m_{H^0(h^0)} = 125$ GeV, per final state per data-taking year. The $ee\tau_h$, $\mu\mu\tau_h$, and $\mu\epsilon\tau_h$ limits are presented in the 1st, 2nd, and 3rd column, respectively, while the 2016 pre-VFP, 2016 post-VFP, 2017, and 2018 limits are in the 1st, 2nd, 3rd, and 4th row, respectively. The dotted black line shows the median expected limit, while the 68% and 95% confidence intervals are presented with the green and yellow bands, respectively. The unusual behavior observed in the limit plots is discussed in Fig. E.1, and the same explanation applies here as well.

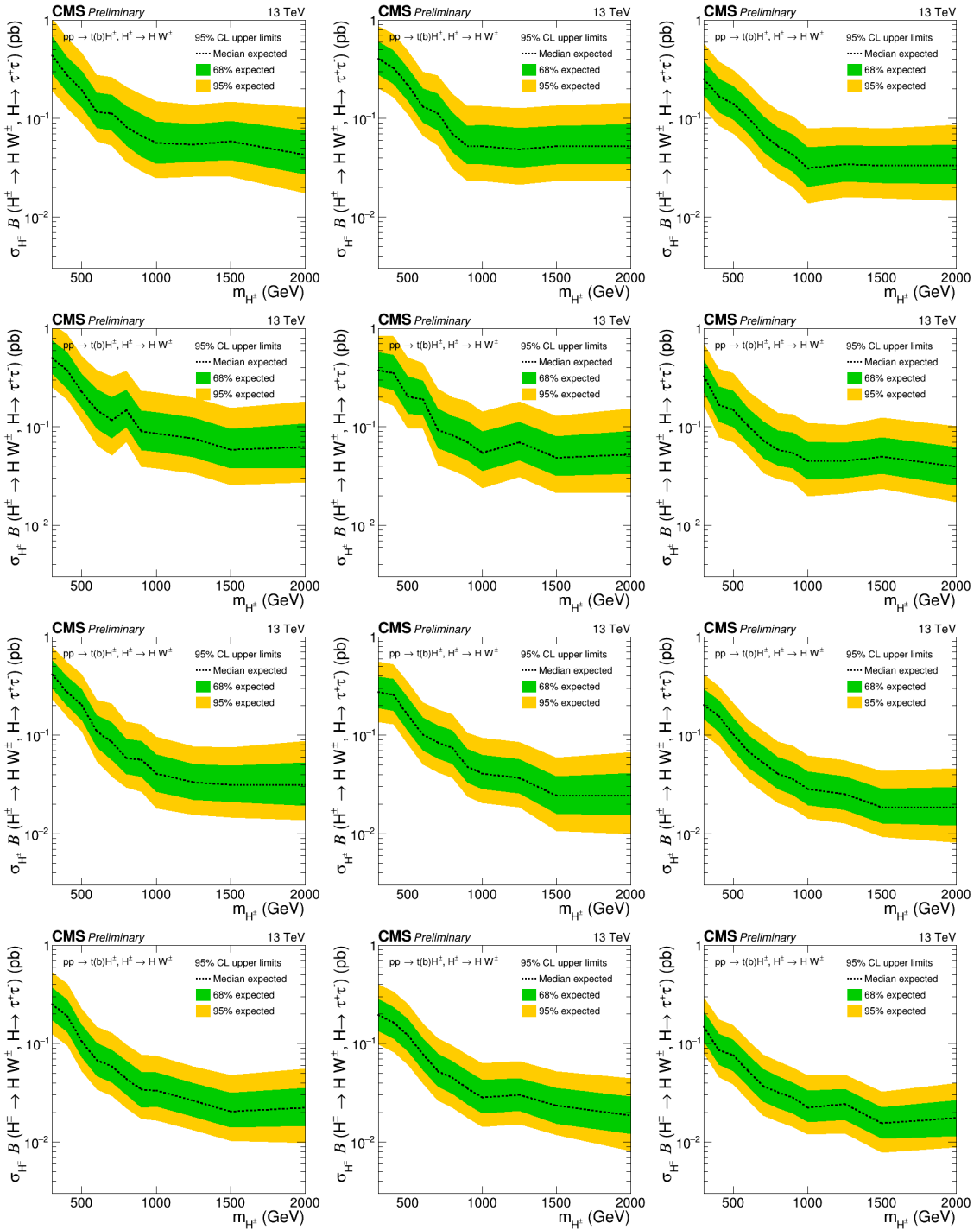


Figure E.4: Expected upper limit for $m_{H^0(h^0)} = 200$ GeV, per final state per data-taking year. The $ee\tau_h$, $\mu\mu\tau_h$, and $\mu\tau_h$ limits are presented in the 1st, 2nd, and 3rd column, respectively, while the 2016 pre-VFP, 2016 post-VFP, 2017, and 2018 limits are in the 1st, 2nd, 3rd, and 4th row, respectively. The dotted black line shows the median expected limit, while the 68% and 95% confidence intervals are presented with the green and yellow bands, respectively. The unusual behavior observed in the limit plots is discussed in Fig. E.1, and the same explanation applies here as well.

m_{H^\pm} (GeV)	Expected limit					Observed limit
	-2σ	-1σ	median	$+1\sigma$	$+2\sigma$	
300	0.03943	0.05247	0.07422	0.10499	0.14459	Blinded
400	0.02646	0.03521	0.04980	0.07045	0.09766	Blinded
500	0.01920	0.02555	0.03613	0.05169	0.07078	Blinded
600	0.01245	0.01657	0.02344	0.03315	0.04626	Blinded
700	0.00882	0.01174	0.01660	0.02401	0.03311	Blinded
800	0.00714	0.00922	0.01270	0.01917	0.02646	Blinded
900	0.00537	0.00739	0.01074	0.01554	0.02143	Blinded
1000	0.00439	0.00604	0.00879	0.01271	0.01709	Blinded
1250	0.00439	0.00604	0.00879	0.01271	0.01709	Blinded
1500	0.00342	0.00427	0.00684	0.00945	0.01299	Blinded
2000	0.00342	0.00427	0.00684	0.00945	0.01299	Blinded

Table E.4: The $2\ell^{sf}\tau_h$ and $2\ell^{df}\tau_h$ combined upper limit for $m_{H^0(h^0)} = 200$ GeV, at 95% CL on $\sigma_{pp \rightarrow t(b)H^\pm} \times \mathcal{B}(H^+ \rightarrow H^0 W^+) \times (H^0 \rightarrow \tau^+ \tau^-)$ as a function of m_{H^\pm} , with full Run 2 data.

m_{H^\pm} (GeV)	Expected limit					Observed limit
	-2σ	-1σ	median	$+1\sigma$	$+2\sigma$	
400	0.01816	0.02417	0.03418	0.04835	0.06659	Blinded
500	0.01193	0.01588	0.02246	0.03177	0.04433	Blinded
600	0.00986	0.01312	0.01855	0.02684	0.03701	Blinded
700	0.00824	0.01064	0.01465	0.02119	0.02922	Blinded
800	0.00635	0.00873	0.01270	0.01836	0.02469	Blinded
900	0.00537	0.00739	0.01074	0.01485	0.02042	Blinded
1000	0.00439	0.00604	0.00879	0.01271	0.01709	Blinded
1250	0.00439	0.00604	0.00879	0.01159	0.01632	Blinded
1500	0.00342	0.00427	0.00684	0.00945	0.01299	Blinded
2000	0.00244	0.00305	0.00488	0.00675	0.01029	Blinded

Table E.5: The $2\ell^{sf}\tau_h$ and $2\ell^{df}\tau_h$ combined upper limit for $m_{H^0(h^0)} = 300$ GeV, at 95% CL on $\sigma_{pp \rightarrow t(b)H^\pm} \times \mathcal{B}(H^+ \rightarrow H^0 W^+) \times (H^0 \rightarrow \tau^+ \tau^-)$ as a function of m_{H^\pm} , with full Run 2 data.

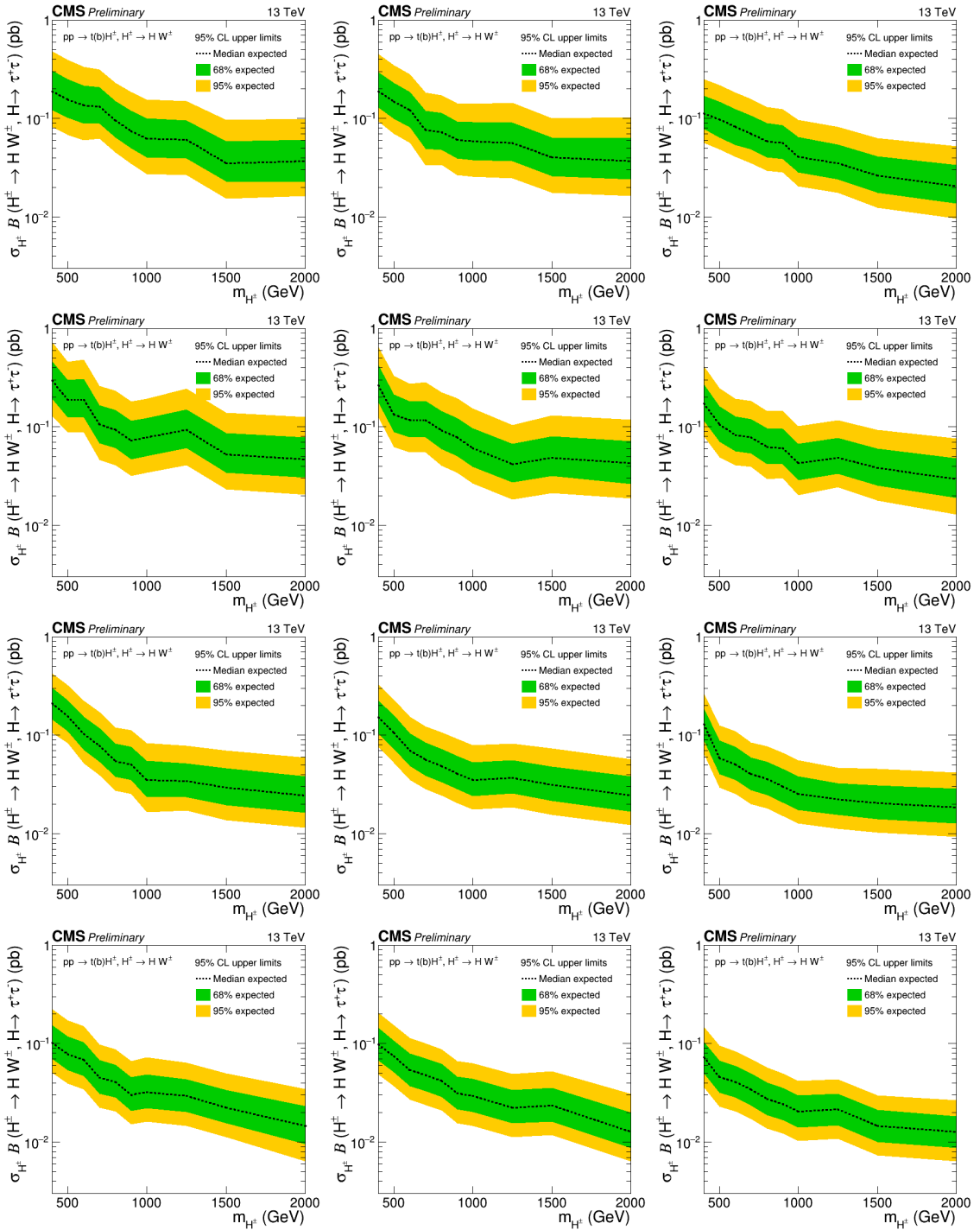


Figure E.5: Expected upper limit for $m_{H^0(h^0)} = 300$ GeV, per final state per data-taking year. The $ee\tau_h$, $\mu\mu\tau_h$, and $\mu\epsilon\tau_h$ limits are presented in the 1st, 2nd, and 3rd column, respectively, while the 2016 pre-VFP, 2016 post-VFP, 2017, and 2018 limits are in the 1st, 2nd, 3rd, and 4th row, respectively. The dotted black line shows the median expected limit, while the 68% and 95% confidence intervals are presented with the green and yellow bands, respectively. The unusual behavior observed in the limit plots is discussed in Fig. E.1, and the same explanation applies here as well.